SCUOLA DI DOTTORATO
UNIVERSITÀ DEGLI STUDI DI MILANO-BICOCCA

Dipartimento di / Department of

Scienza dei materiali

Dottorato di Ricerca in / PhD program Scienza e nanotecnologia dei materiali Ciclo / Cycle XXV

Surfactant enhanced synthetic strategies for luminescent nanomaterials and stabilized colloids

Cognome / Surname Mecca Nome / Name Sara

Matricola / Registration number 778793

Tutore / Tutor: Prof. Luca Beverina

Coordinatore / Coordinator: Prof. Marco Bernasconi

ANNO ACCADEMICO / ACADEMIC YEAR 2022/2023

Contents

Overview

At first glance, it might look like the present thesis is based on two distinct and unconnected topic: colloidal nanocrystals and stabilized micelles. Looking more carefully, we can see that colloidal perovskites nanocrystals and micelles formation and their further in solution stabilization build upon similar mechanisms, as schematized in Figure 1. An ensemble of molecules with dual nature (polar and apolar, covalently linked together), whose characteristics dictated by the surrounding environment, creates new objects, maintained stable in solution through their action. There a lot of possibilities and the combined choice of these molecules and the medium acts both on final object intrinsic properties and its interaction with the outer world. "Ligands" and "surfactants" are nothing but two different names for species that have the same role. Ligands are composed by a charged (in this present case, ammonium or carboxylate) portion that takes actively part in the nanocrystals growing surface structure, affecting it. Through their length and steric hindrance, ligands can create nanocrystals inks or compact self-assemblies, stabilize the growth of a surface termination respect to another, induce formation of nanoplatelets instead of nanocubes and protect the crystalline structure to which they are attached. Surfactants, on the other hand, can spontaneously generate an associative new pseudophase, that is not an independent object, but exists only as supramolecular cooperative ensemble. They can be linear or branched, polymers or small molecules, ionic or neutral: all these parameters act on the dimensions, dynamics, stability to different conditions, interaction with other species of the outcoming assembly. With stabilization, these properties can be maintained constant in every condition. The first part of this thesis deals with the development of a robust, versatile and highly scalable method for the colloidal synthesis for $CsPbBr_3$ nanocrystals. The protocol remains well-controlled also when extended gradually to the unprecedented scale of 3,6 L, thanks to the original introduction of a rotor-stator turbo emulsifier, combined with a careful selection of the solvents and the capping ligands. We thus firstly corroborated the improvement with respect to generally used magnetic stirring, showcasing its requirement when working with volumes that exceed 1 L. Successively, we deeply studied the impact of processing parameters on the properties of colloidal dispersions to gain a full insight and completely rule over the synthetic mechanism: increased medium viscosity, temperature, employment

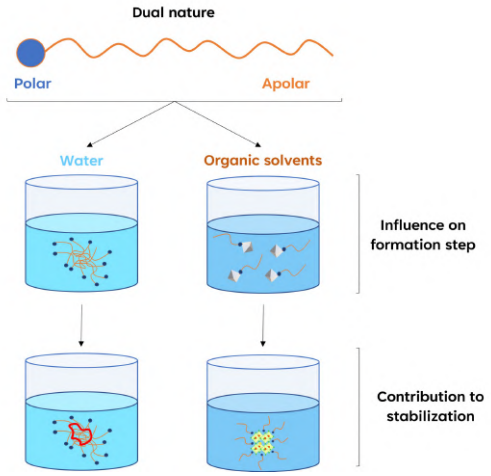

Figure 1 Cartoon that highlights the similar mechanism upon which both micelles stabilization and colloidal nanocrystals build: action of an ensamble of amphiphiles in a specific medium.

of different acid and amine ligands, reliability also with different halogen and halogen mixed precursors, both during and post synthesis. We also demonstrated the capability of recovering solvents and excess reagents – with particular emphasis for the toxic lead – and recycling without impact on the overall quality of the final material. This feature critically improves the sustainability of this class of materials, particularly regarding to the production of heavy metal contaminated wastes. Finally we preliminary tested these materials in solar cells, deducing better compatibility with indoor target and patented a new type of nanocomposite scintillator able preserve its properties to gamma irradiation doses up to 1 MGy. We aim at enhancing the photovoltaic compatibility involving also different A cations in the synthetic process (methylammonium and formammidinium) and optimizing the ligand quantity in the final product. Nanocomposite scintillator fast response can be improved by $CsPbCl_3$ employment. Further extending the application library to other fields such as photocatalysis and direct X-rays detectors is interesting as well. The second part of this dissertation concerns the assembly of soft and stable nano-host objects from an amphiphilic environment. The literature pertaining this field reports examples of micelles based on complex polymeric designer surfactants stabilized by crosslinking of a polymerogenic unit contained in their structure, resulting in stiff and rigid objects suitable for very specific applications. We developed a different approach based on the combination of commercially available, cheap, non-toxic surfactant as Tween 80 and an easy polymerogenic additive (co-surfactant) bearing the polymerogenic unit (methacrylate), in some cases a photoinitiator, a crosslinker that can tune the "network density" and UV. The in-situ photopolymerization of the co-surfactant while dispersed within micelles forms a semi-interpenetrated network that "mechanically hinders" the chains, freezing the specific association colloid formed. Such study is intimately coupled with surfmer localization descending from its polarity. The final materials are intended for catalysis, controlled release and imaging applications. We firstly optimized efficiency of photopolymerization process under 365 nm irradiation acting on different aspects: employment of microflow chemistry conditions, coupling a more efficient photoinitiator with a proper sensitizer, introducing a more polar and compatible with pegylated shell photoinitiator, enhancing the homogenization during irradiation with magnetic stirring. Secondly, we extended the generality of the method designing and using two further co- surfactants with different polarities, with 254 nm irradiation to avoid the necessity of photoinitiation and directly exciting methacrylate group. For all species, 100 % yield was observed and the obtained dispersion demonstrated to resist to organic solvent dissolution. We are planning to "equip" these objects with embedded palladium and phosphine species and use them as reaction catalysts. With a little conceptual jump ahead, the in-situ formation of a polymer that hinders surfactants chains and forms a nano-object can be extendend. If the polymer is able also to form specific interactions with reactive substrates, this can be exploited to activate them for specific reactions. We chose Poly(9,9-dioctyl)fluorene (PFO) synthetized through mini-emulsion Suzuki Miyaura polymerization, where the Pd source that allowed the formation of PFO is itself the embedded catalyst for further reactions. The dispersion is directly employed as reaction medium for a Suzuki-Miyaura test reaction to compare the results obtained with palladium on carbon heterogeneous catalyst. PFO demonstrated to form better quality dispersions, almost zero palladium leaching, and complete NMR conversion, without homocoupling detected. We are planning to further extend the reaction library and to deepen the preliminary results about catalyst reuse. The common frame of these two topics is the synthesis via wet methods of colloids having applications as functional materials.

Acknowledgments

Firstly, a heartfelt major thanks to my supervisor Prof. Luca Beverina, for his entusiastic and contructive support and to all LaSMo group for the creation of a dynamic shareful working environment, that went beyond merely professional improvement. I had the pleasure of working with Giorgio Patriarca, who performed all ^{1}H NMR with noteworthy patience. I am extremely grateful to Prof. Giovanni Maria Vanacore and Dr Melissa Saibene for the collection and analysis of HRTEM images. Special thanks to Prof. Sergio Brovelli, Dr Valerio Pinchetti and Andrea Erroi for the essential and detailed optical characterizations. Thanks should also go to Prof. Anna Vedda and Dr. Francesca Cova for the expert characterization of radioluminesce. I'd like to acknowledge Prof. Thomas Brown and Suresh Podapangi from University of Roma-Tor Vergata, to give me the opportunity to visit their facility and to preliminary test my materials in solar cells. I would like to extend my sincere thanks to Prof. Gianfranco Pacchioni and Dr. Giovanni Di Liberto for the interesting computational studies performed. I would remiss if not mentioning Dr. Maria Tringali for all the ICP-OES analyses. Lastly, I want to mention my acknowledgment for Prof. Roberto Lorenzi that measured XRF of my samples.

Chapter 1

Bright stars of the actual scientific scene: colloidal perovksites nanocrystals

1.1 Introduction

1.1.1 Meet perovskites

"Perovskite" refers to a class of minerals with general composition ABX_3, where A and B are cation with respectively bigger and smaller ionic radius and X anion (usually oxygen or an halogen). They show the characteristic crystalline structure of $CaTiO_3$, the first natural perovskites (PVK) discovered: a body centered cubic cell, that can be visualized as a 3D lattice composed by $[BX_6]^{-4}$ octahedrons sharing vertexes (180 °) and A cation in cuboctahedral sites (Figure 1.1). At low temperatures or in presence of cations with large

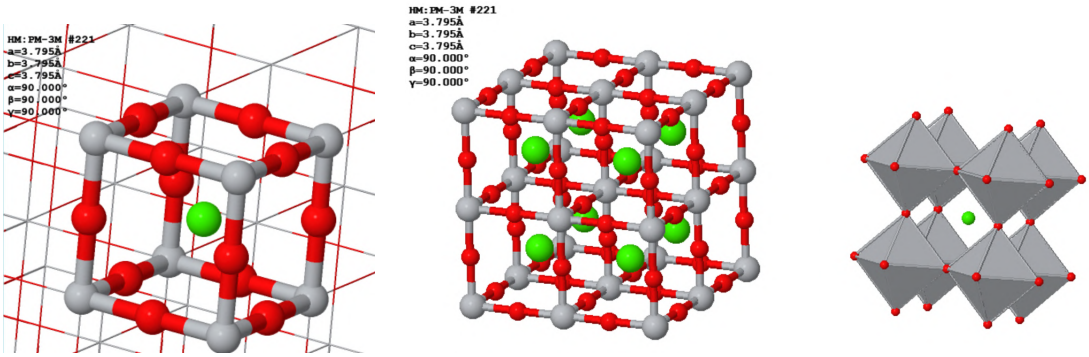

(a) **(b)** **(c)**

Figure 1.1 Crystalline structure of $CaTiO_3$, reference perovskites: cation A ($Ca_2{}^+$) is represented in grey, B ($Ti_4{}^+$) in green e X ($O_2{}^-$) in red. (a) Unit cell with lattice parameters; (b) 3D extension of unit cell; (c) alternative way to visualize crystalline structure, through $[BX_6]^{4-}$ ochtaedra sharing sides with cation A in cuboctahedral sites.Images are created with ChemTube3D.

ionic radius, lower symmetries are also possible, such as tetragonal and orthorhombic, due to octahedral angle distortion. This structure raised great interest in scientific community thanks to correlated properties (piezoelectricity,[1] high dielectric constant[2] and ferroelectricity[3]). This attention led to attempts in combination of great number of cations and anion to find new stable PVK. Although nature offers us a certain number of

examples, synthetic PVK are the leading type. It was demonstrated that ionic radii of A,B and X are fundamental for crystalline structure stability. An experimental parameter, Goldschmidt tolerance factor,[4] was introduced to predict whether PVK structure can be obtained from a specific set of ions:

$$t = \frac{r_A + r_B}{\sqrt{2}(r_B + r_X)} \tag{1.1}$$

where r_A, r_B and r_X are ionic radii of respectively A, B and X. The interval within t value necessarily but not sufficiently has to range lies from 0,81 and 1,1: below, B cation is too small and re-arranges in a different crystalline structure, whereas above PVK lattice is unstable due to excessive distortion. Among all the characteristics, it's worth to mentioned one of the most famous, characteristic of oxygen-deficient triple oxide form YBCO ($YBa_2Cu_3O_7$): superconductivity.[5] Their very breakthrough took place when Miyasaka et al., in 2009, introduced for the very first time organohalide PVKs ($MAPbBr_3$ and $MAPbI_3$) as visible light sensitizer in photolectrochemical cells,[6] although with a starting efficiency of only 3,8 %. In less than a decade, their employment became viral, the efficiency raised until 23,7 % in 2018:[7] improvement that took more than 20 years for silicon solar cells. The latest record efficiency reported is very recent and is 24 %, while retaining 87 % of its original output capability after 2400 hours of operation at 55 °C.[8] The fact that is one of the most hot topic of our century is also demonstrated by a study performed on research publication trends from 2009-2019.[9] Such an intensive study about these materials lead to the discovery/development of a great number of different type of PVKs. The scientific community, and we as well, focused mainly on lead halide type (LHP).

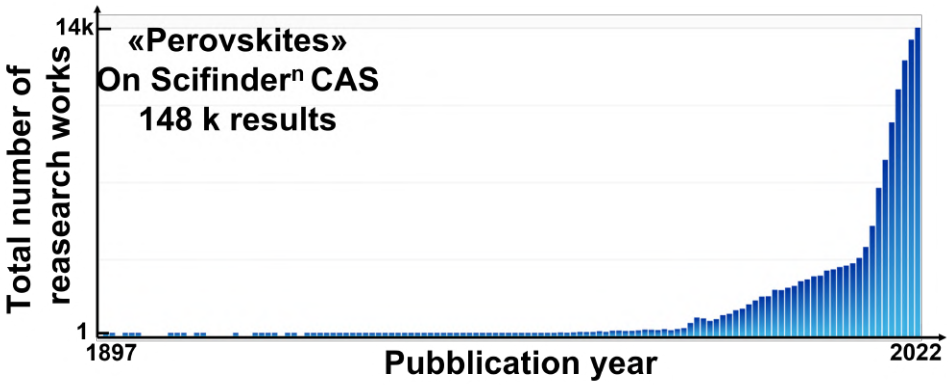

Figure 1.2 Trend in total number of research works about perovskites as function of the pubblication year, from 1897 (1) to 2022 (14k). The total number in this time interval is 148k. Reported data are estimated from Scifinder$_n$ CAS.

1.1.2 Main protagonists: lead halide perovskites

For this specific class PVKs, A cation can be cesium, methylammonium or formamidinium (hybrid type), B cation is lead and X is chloride, bromide, iodide or their mixture.[10] Species that have Goldschmidt tolerance factor next to the limit, such as $FAPbI_3$ and $CsPbI_3$, show easy phase transition (also at room temperature - RT) towards lower symmetry crystalline structures (orthorhombic or even hexagonal) that are called "yellow" phases (optically inactive).[11] The entire class builds upon ionic interaction that makes them both

highly crystalline (and thus easy to obtain), favors post-synthetic treatment (as halogen exchange[12]) but at the same time makes them particularly sensitive to moisture and polar solvents.[13]

1.1.2.1 General optical properties

The leading characteristic of lead halide PVKs lies in their optical properties, determined by a unique electronic structure. The detailed description is beyond the scope of this chapter but it's worth to know that valence band is mainly formed by p-type orbitals from the halogen, combined with s-type orbitals of lead, whereas conduction band generates from combination of the former with lead p-type orbitals.[14] As a consequence, halogen variation induce a prevalent shift on valence band. For example, $CsPbX_3$ species can tune their emission wavelength from 410 nm (X = Cl) to 512 nm (X = Br) even up to 685 nm (X = I): this passage can be gradual if mixed compositions are employed.[15]

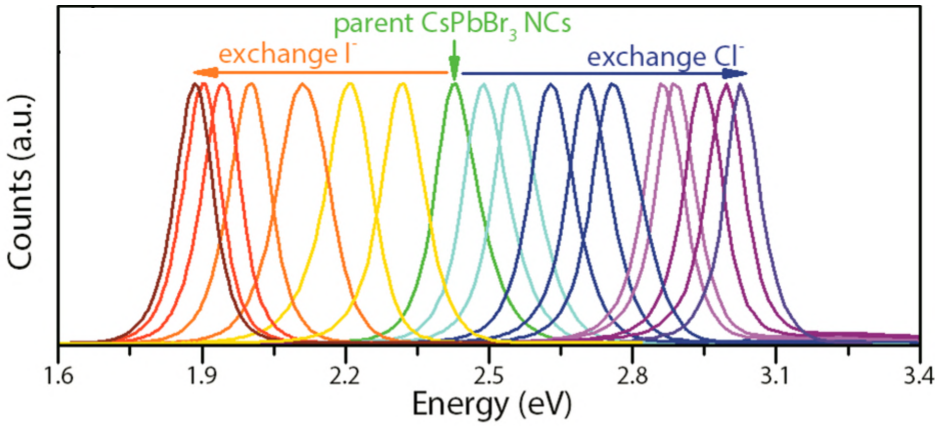

Figure 1.3 PL emission tuning from 3 eV ($CSPbCl_3$) to 1,8 eV ($CsPbI_3$) obtained by mixed halogen compositions.[15]

From this point of view, it seems that cation A contribution to spectral features is negligible. On the contrary, its dimension and position bend octahedral structure, modifying X-B-X angle that affects band-gap.[16] In particular, an increase in cation A space extension leads to a general red-shift in bandgap of resulting LHP. For this reason, by exploiting different halogen concentrations, $MAPbX_3$ materials can cover from 407 to 734 nm[17] and $FAPbX_3$ are able to emit up to 784 nm.[17] Photoluminescence (PL) spectral width, defined by full width at half maximum (FWHM), theoretically doesn't depend on halide and it is around 70-110 meV.[18] Nevertheless, PL spectra are more often reported in function of wavelengths and, in this scale, the interval depends on spectral position. The result is that FWHM for Cl species is around 10 nm, whereas for I is up to 40 nm*. A key feature of LHP is the extremely high photoluminescence quantum yield (PLQY), ascribable to intrinsic elevated defect tolerance (around 80-90 %)[20](ref near 100%, near unity). This is true only for bromide and iodide derivatives: chloride materials scarcely reach 20 %[21].[22] Such cutting-edge optoelectronic properties made LHP appealing for a large number of different applications.[23] In literature, we can find examples of employment in lasers,[24] light emitting devices,[25] transistors,[26] photocatalysis[27],[28] photodetectors[29] and

*Since wavelength and energy are related through an inverse relationship, for signal acquisition evenly spaced data intervals in wavelength are unevenly spaced in energy. The proper conversion is accomplished through a Jacobian transformation.[19]

obviously photovoltaic.[30] Although the PVKs era began with hybrid materials, their lower stability with respect to all-inorganic cesium counterpart pushed our focus mainly towards the latter. For this reason, from this moment on, the description will be centered on $CsPbX_3$.

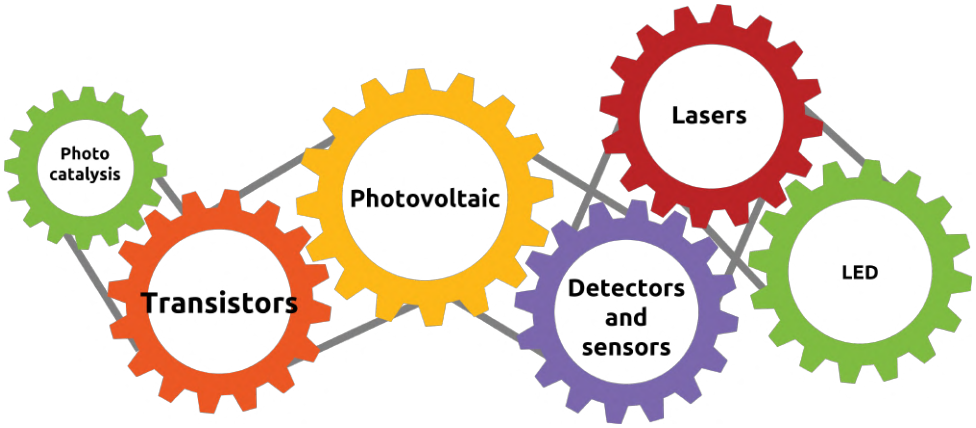

Figure 1.4 Main applications of lead halide perovskites.

1.1.2.2 Quantum confined structures

Another fundamental aspect, experimented by all semiconductive material, is confinement effect. When one, two or even all three dimensions of a crystal are decreased below exciton Bohr radius, optoelectronic properties change. This value in fact represents the extension of probability distribution of electron and hole pair in an exciton. When size is below, electron and hole wavefunctions experiment confinement and assume quantized energy levels.[31] The Coulombian repulsion increases and so does exciton binding energy, resulting in more sharp absorption (ABS) edges.[32] Moreover, spectral features blue-shift and starts to depend on specific size. In LHP exciton Bohr radii varies from 5 nm for $CsPbCl_3$ to 12 nm for $CsPbI_3$: these dimensions are easily obtained varying synthetic conditions and exploiting templating effect of colloidal ligands. With recent results, synthesis can be pushed until monolayer-thickness control.[33] In addition to halogen exchange, nanostructuring a material allows to manipulate optical properties. For this intriguing aspect, low dimensional species as nanoplateletes (2D), nanowires (1D) and quantum dots (0D) are far more analyzed than bulk 3D phase.

Nanoplatetelets are defined by confinement in one dimension. The most interesting aspect is that the number of monolayers that compose the NP structure can be precisely correlated to quantized values of energy gap by computational studies.[34] This peculiarity allows to predict ABS and PL features when exact structure is known, and vice versa. Nanowire structures are less stable, especially in colloidal form, and have the tendency to coalesce. The consequence is elimination of confinement and red-shift of optical properties.[35] As a consequence these species are more employed for fundamental shape evolution studies rather than for effective application. LHP quantum dots are confined in each direction. The theoretical minimum size correspond to a single $[PbX_6]^{4-}$ octahedron, which band gap falls in deep UV (3.4 eV for X = iodide and 4.4 eV for X = Cl).[36] The cesium-rich phase, Cs_4PbBr_6, since composed by octahedrons that do not share sides but are separated by cesium ions, shows optical properties similar to single cluster. In present work, attention is focused mainly on 2D and 0D materials.

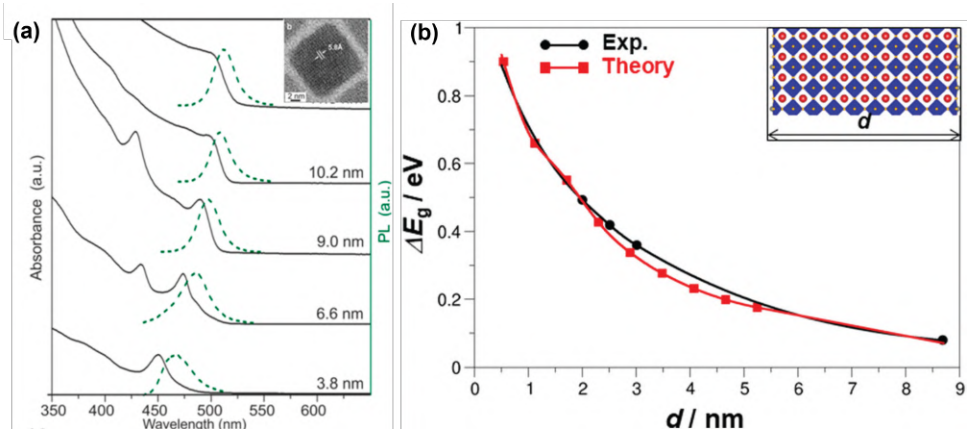

Figure 1.5 (a) ABS and PL spectra of $CsPbBr_3$ NCs with different sizes.[15] (b) Experimental (black dots and line) and calculated (red squares and line) band gap deviation from the bulk value for $CsPbBr_3$ nanoplatelets. d = thickness of the system.[34]

1.1.2.3 Colloidal synthetic methods

Thanks to outstanding interest for these materials, a lot of effort has been spent over the years to develop synthetic procedures.[37] They can be obtained either with in-situ protocols, such as direct crystallization of precursor on substrates, or through colloidal procedures. The former seems at first more compelling, but there is a lack of control on final material properties and, in addition, it usually bases on spin-coating technique[38] that can't be industrially employed. Colloidal methods are more compatible with further commercialization aim and allow to carefully control conditions and thus output. In solution colloidal syntheses background for LHP is literally immense. The most employed synthesis is "hot injection" method[15] , which allows to obtain materials with high-quality optical properties, but under harsh synthetic conditions, like inert atmosphere and high reaction temperatures. Moreover, it is not compatible with the need of a great amount of output material, as such synthetic conditions are not easily controlled on gram-scales. To overcome such limitations, RT synthetic procedures have been explored, ligand-assisted reprecipitation process (LARP) being the most known approach. In 2016, Li et al.[40] adapted the LARP - previously developed only for the synthesis of $MaPbX_3$ PVKs[17] - to the preparation of $CsPbX_3$ nanocrystals (NCs). This process is simple and efficient and doesn't require heating. Unfortunately, the preparation of high quality materials is developed on use of aprotic dipolar solvents like dimethylformamide (DMF) or dimethylsulfoxide (DMSO), whose acceptance in the chemical industry is dwindling.[41] Moreover, the process does not scale up flawlessly, again due to concentration profiles. Akkerman et al.[39] recently proposed an easy procedure to work at RT (and laboratory conditions)

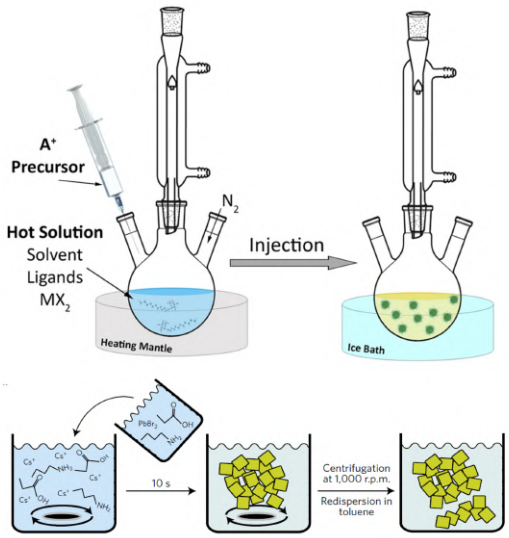

Figure 1.6 Schematic representation of the hot injection method[15] and synthetic procedure reported by Akkerman et al.[39]

with more friendly solvents (isopropanol and hexane) in a scalable way. They chose as capping ligands propionic acid and butylamine, proper for device application but not so colloidally stable for further in solution studies. This method has been intensively reported, employed and in some cases also modified. Capping ligands can be replaced through post-synthetic ligand exchange to more colloidal suitable one, as oleyamine.[42] Anyway, this means an additional tedious step. They have already been replaced during synthesis with others more common in literature. Di Stasio's group[43] obtained PVK nanoplatelets with a similar procedure, substituting propionic acid and butylamine with octyl acid and octylamine as ligands and cesium carbonate with cesium acetate as the Cs^+ precursor. Sorrentino et al.[44] modified Akkerman synthesis tuning Cs/Pb precursors ratio to obtain 3D nanocubes or 2D and 3D PVKs mixtures. Wu et al.[45] proposed a very similar synthesis involving propionic acid/oleylamine as capping ligands and diamine bromides with different chain lengths as additional halogen precursors, to respect the stoichiometry. However their approach involves DMF as solvent. Basically, from 2015 to our days, a huge library of different ligands has been tested and analysed in PVKs synthesis, both at high and low temperatures, in terms of their effect on morphology, stability and optical properties.

1.1.2.4 Few words about lead issue

Despite excellent efficiencies and straightforward possibilities for upscaling to industrial production, lead-based composition induce significant concerns that restrict full blooming of this technology[4647].[48] Its toxicity for human health and negative environmental impact are
used was banished as additive to fuels and it still composes lead-acid batteries and solder. Both United States environmental protecting agency (EPA) and the European Restriction of Hazardous Substances Directive (RoHS) produced specific law and regulations about tolerable amount (1000 ppm by weight in a solid device, much higher than cadmium limit of 100 ppm).[49] Hence, scientific community is spending a lot of efforts to develop a proper alternative to substitute lead cation, not giving up optoelectronic quality. From the beginning, $Sn_2{}^+$ has been a qualified candidate,[50] but tin-based PVKs are not as stable as the Pb-analogues. Moreover, tin is not so much better than lead when speaking about toxicity. An alternative way to face this issue can be a more careful control of the life cycle assessment: reduce environmental impact of the synthetic process with recycle of unreacted species, introduction of specific measures for workers, encapsulation of photovoltaic module for prevent leakage and a correct way to dispose cells in their after-life can be a solution.[51] Some improvements in this direction have yet been made,[52] especially towards polymeric encapsulation.[53] Although a lot of work has still to be made, there are reason to be optimistic.[54] Regarding our specific laboratory work, we have focused on the first part of the process, that has been so far too much overlook in academic studies, even if some attempts has started to appear.[55]

1.2 Aim of the work

My original involvement in the perovskite research field was rooted in a more typical topic for a group generally working in structure-property relationships in polyconjugate organic material for optoelectronic applications. I developed a class of ligands designed to bind two dimensional PVKs (2D PVKs) and achieve a triplet-triplet annihilation up-conversion (TTA-UC) process featuring a PVK as the sensitizer and the ligand as the emitter. To prepare the 2D PVK, I tried to reproduce a LARP synthetic process developed by a former PhD student, without however obtaining the same results. I therefore decided to employ the established hot-injection method, choosing the procedure from Protesescu et al.[15] to prepare nanoctrystals (NCs) instead of 2D PVK. In this case, I succeed in obtaining good quality materials, but I also realized that such procedure is straightforward only when little amount of material is needed. Since I required a bigger quantity of NCs to make all the tests I had in mind, I switched again to the easy, RT procedure developed by Akkerman et al.[39] The use of butylamine (BuAm) ligand, however, represented quite a step back: the process was valuable, but the colloidal stability of the obtained material was too poor for my intents. We thus resolved to develop our own synthetic strategy having in mind a specific set of features: reliability, capability to afford colloidally stable materials with specific morphology and crystal structure, ease of scaling up to litres of colloidal solution level and operational simplicity. We profited from the solid experience of the group in colloidal and formulation chemistry to develop the original PVK synthesis described in this work. We further deepened our understanding of the effect of different conditions during (homogenization, halogen and ligands nature, viscosity, temperature) and after (anion exchange, solvents, storage, deposition) the process, especially on the morphology of the output material, to completely rule over the protocol. In fact in the meantime, the panel of our intended application widened, from TTA-UC to direct our NCs as active material in perovskites solar cells and nanoscintillator detectors. The achieving of one-pot unprecedented amount (8 g) of high quality materials is a clear boost for application investigations, making possible to reach pre-industrial prototype devices as well. The whole procedure is the main finding of a recent patent application.

1.3 Synthetic protocol

The literature describing the state of art of cesium LHPs synthesis is vast, as described in section 1.1.2.3. From a quick overview, it seems that almost every possible pathway has been tested and every kind of material obtained. Nevertheless, we struggled to adapt existing procedures to the preparation of 1 L batches of colloidally stable dispersions that could be reproducibly obtained and feature a minimal shelf life enabling to carry out an entire experimental campaign without the need of repeating the procedure. As disclosed in section 1.2, the starting point of this journey in PVKs synthetic field was the literature procedure of Akkerman et al.,[39] which we adapted to our needs, making our process original and successful. The first change is the substitution of short BuAm ligand - more appropriate for the preparation of devices and featuring a very limited colloidal stability – with oleylamine (OAm). In their work, Yang et al.[56] found out that ligands with poor packing capability (for example, because of the presence of a cis double bond instead of a purely linear chain) lead to NCs with improved colloidal stability, and better suited for solution characterizations. The second variation is the addition of an additional bromide source, tetrabutylammonium bromide (TBAB). It is composed by a bulky cation (see molecular structure in experimentals, Figure 1.48) that does not fit into the crystalline PVKs structure and can't thus be intercalated into it. The reason behind this choice is that working in an halogen rich environment is reported to decrease detrimental bromide vacancy, typical of PVK NCs, especially on surfaces.[57] Finally, the key modification of the entire process has been the original introduction of a turbo-emulsifier homogenizer instead of classical magnetic stirring. This instrument is renowned in formulation chemistry to help in refining emulsions[58] and generally mixing efficiently high volumes of liquids. It is composed by a motor group that can fit different types of dispersing tool, depending on the desired application (Figure 1.7(b), more details in experimentals, Table 1.11). It has never been used in NCs synthesis before, but we proved that its introduction is beneficial (see section 1.5.1). It exploits a very fast rotor-stator effect inside the dispersing tool that allows a very fast and efficient mix of large volumes. The process is here briefly described for the minimum scale of 60 mL (for further details, see experimentals).

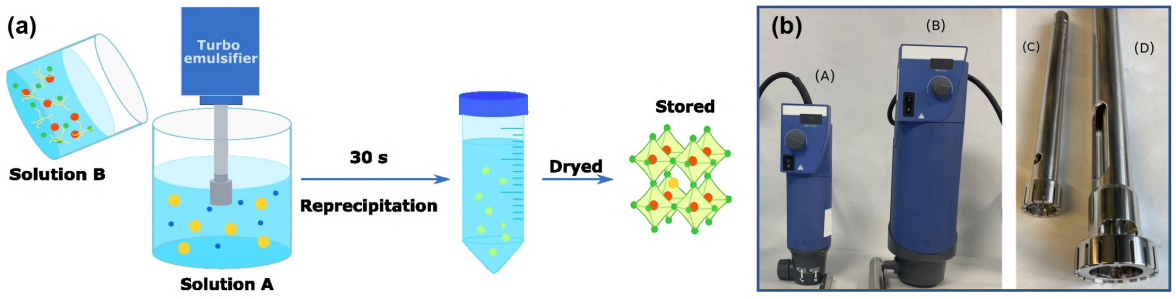

Figure 1.7 (a)Synthetic procedure scheme: the cesium propionate solution A in heptane/isopropanol 2:1 v/v is put under turbo-emulsifier homogenization while the $PbBr_2$ and TBAB mixture in OAm/propionic acid 1:1 mol/mol with isopropanol is added and let homogenize for 30 s. The procedure is carried out in laboratory atmosphere and at room temperature. The as prepared solution is repreciptated with isopropanol and the solid product is recovered by centrifugation, dried under vacuum and weighted to be stored. (b) The motor group IKA ULTRA-TURRAX DIGITAL 25 (A) and 50 (B) and the respective dispersing tools S25N-25G (C) and S250N-G45M (D).

Solution A is prepared by dissolving Cs_2CO_3 (0,1 mmol) in propionic acid (PA, 1,33 mmol, 0,1 mL) and then diluted in 60 mL of Heptane/isopropanol (Hept/iPrOH, 2:1 v/v).

Solution B consists in $PbBr_2$ (1 mmol) and TBAB (1 mmol) dissolved at 80 °C in a mixture of OAm (2,9 mL, 9 mmol) and PA (0,7 mL 9 mmol) with 0,7 mL of iPrOH. When solution B is cooled down to RT, it is added into solution A under turbo-emulsifier homogenization (15k rotations per minute - RPM). Immediate color change is observed, with the mixture becoming highly fluorescent. The mixture is let homogenize for 30 seconds, then 30 mL of iPrOH are added, triggering the transformation of the original clear bright yellow solution into a dispersion. The precipitated NCs are recovered by centrifugation (4500 RPM, 2 min): the solid product is dried under vacuum and the supernatant is stored for further recovery of unreacted species (see section 1.7). The former is thus easily isolated as a colloidal solid and weighted (with this minimum scale, 120 mg of final material can be obtained). This solid can be stored either as powder in glove box or in toluene solution (at a concentration of 10 mg/mL) (discussed in section 1.4.2).

1.4 Perovskites like to change: output material evolution

We soon discovered that the solid output material is composed by cluster-like metastable PVKs, firstly, from its structured ABS spectrum (Figure 1.8 (a)). As aforementioned (section 1.1.2.2), when PVKs dimensions are under the Bohr's exciton radius, as for all optically active nanoparticles (NPs), the spectroscopic signature varies and it is thus detectable and correlating with the shortest length. In fact, from this moment on, we will exploit ABS profile as fingerprint of the material structure. We noticed that the ABS shows more than one peak under the classical bulk value of 520 nm, and thus performed a gaussian deconvolution using Fityk (Figure 1.8(b)). Neglecting the big gaussian at shorter wavelengths that stands for the high density of state region, we found four distinct contributions to the whole spectrum. There are many papers published that correlate PVK energy gap and thickness: we considered the theoretical expression derived from Diliberto et al.,[34] that demonstrated to fit very well with experimental values, and plotted our results. We can clearly see (Figure 1.8(d)) that our families ranges from 3 to 7 monolayers thickness (with monolayer is intended a single unit cells "sheet"). Normalized PL intensity deconvolution (Figure 1.8(c)) shows three main emission peaks at 458 nm, 474 nm and 498 nm that are compatible with ABS of respectively populations 2, 3 and 4. Population 1 is too few to effectively see its emission by itself and, through excitation migration or reabsorbtion process, it probably contributes to lower energy peaks. For the same reason, the more intense peak is the more red shifted one (peak 3). Considering that for cubic phase approximation the unit cell extension is around 0,59 nm, the NCs lower dimension (that is the one that imprints ABS features) should range between 2 and 4 nm. We confronted this conclusion with transmission electron microscopy (TEM) images and the corresponding statistical analysis on dimensions (Figure 1.8(e-g)). The pristine material is half way between rods and "bricks". We can hypothesize that the more rectangular objects are nothing but the nanorods lying on the TEM grid with "face" instead of edge. By drop casting in fact, the NCs randomly arranges over the grid surface. The modest but perceivable difference in contrast can support this speculation. The shortest dimension distribution, fitted with a gaussian function, tells us that the mean statistical value is 3,8 $\pm$ 2 nm, completely compatible with the prediction from ABS.

We thus speculated that the formation of small NCs is ascribable firstly to RT conditions (more kinetically then thermodinamically driven) and moreover to the fact that after

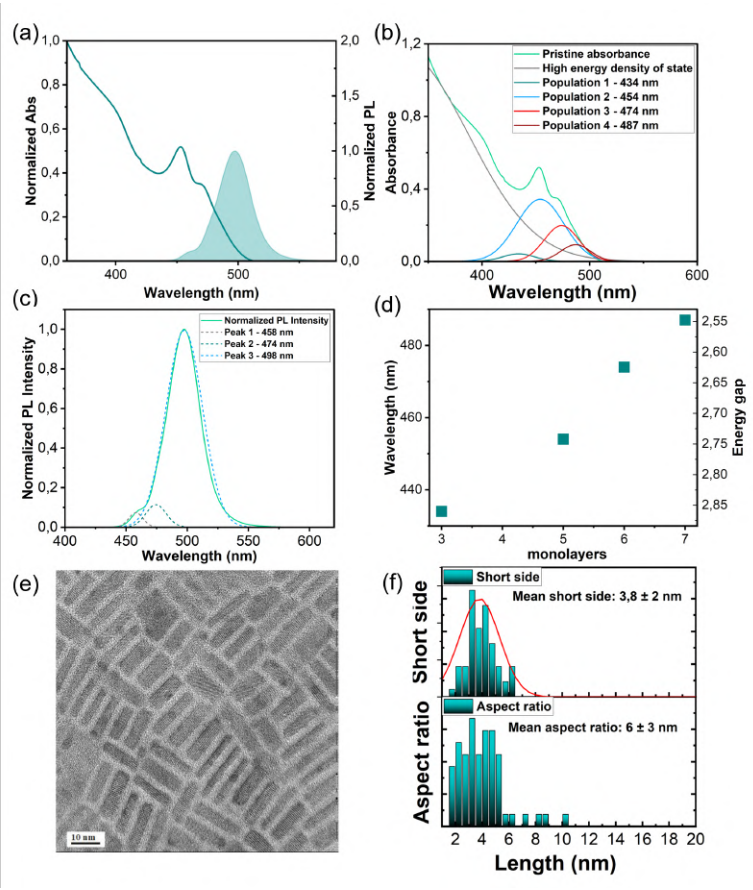

Figure 1.8 (a) Normalized absorbance and photoluminescence spectra of the crude $CsPbBr_3$ NCs as dispersed in hept at 0,1 mg/mL (λ_{exc}= 365 nm). Deconvolution of normalized (b) ABS and (c) PL spectra with multiple gaussians fitting performed with Fityk. (d) Graph of the correspondence between ABS maximum wavelenght of the different deconvolved gaussian on the left (and the corresponding value of energy gap on the right) and the calculated number of monolayers composing the perovskites. This values are derived from Diliberto et al. theoretical relation.[34] (e) High resolution TEM (HRTEM) image of the pristine NCs and the corresponding distributions of dimension of (f) the shortest side, fitted with a gaussian curve (top), and aspect ratio (bottom), both with the mean value and the standard deviation. (70 NPs)

reprecipitation, they are temporarily embedded in a ligands-rich medium, where diffusion is very slow. It is in fact well known that the repreciptation step, necessary to recover the colloidally well-dispersed NCs from the reaction medium, gives back a product with an excess of ligands that "demix" along with NPs. Generally, the output is thus further purified with washing steps that contribute to damage the NCs if the capping ligands do not interact strong enough.[59] In our work, we decided to exploit this feature instead of considering it as a limitation. In fact, for some applications in which the presence of dielectric ligands around the $CsPbX_3$ material is not a problem (section 1.8.2), we can use the crude product directly in the device preparation and preserve the final NCs. In our conditions, the reaction is kinetically driven and the ligand pair, PA and OAm (in form of propionate and oleylammonium), keeps the obtained NCs well dispersed. These conditions induce the formation of different size-limited populations. To recover them, we induce the precipitation by addition of iPrOH, which is a bad solvent for OAm as well, the less soluble of the pair. As previously mentioned, in these preliminary tests we used this specific amine to investigate the process, but we think that this method can be extended to other amines as well. The recovered material is a soft colloidal solid.

From thermogravimetrical analysis (TGA) the amount of organic part varies between 20 and 35 wt%. In particular, from Figure 1.9, we notice that the use of acetone to repreciptate instead of IPrOH reduces ligands precipitation (light blue curve versus light green one), probably for higher solubility of OAm in this solvent (confirmed by an experimental test): this aspect however at the same time plays against material recovery. If we perform our synthetic procedure on a 120 mL volume batch and after homogenization we split it in two 60 mL parts, reprecipitating them with the same amount (30 mL) on one side of iPrOH and on the other one of acetone, we recover respectively 58 mg and 46 mg of NCs. Considering the inorganic percentage of the two samples (calculated as wt% residue at 500 °C), the NCs yield is still lower (respectively 76% and 79%, meaning 44 mg versus 36 mg). Therefore, the small difference in the organic wt% doesn't validate the use of acetone, and we kept on repreciptating with iPrOH. By the way, this measurement confirms our hypothesis on OAm different solubility as reason behind the large amount of organic ligands in the sample. We furthermore can't forget that the obtained NCs are really small (as we have evaluated from ABS and confirmed from TEM images), and this lead to high surface to volume ratio and thus more ligands necessary to stabilize them. Also, the ^{1}H NMR of obtained solid in deuterated benzene confirms the abundant presence of OAm/PA mixture (Experimentals 1.10.5.4, Figure 1.48). We then evaluated the material behaviour in different conditions: conservation in solid state, redispersion in different solvents at diverse concentrations, exposure to temperature.

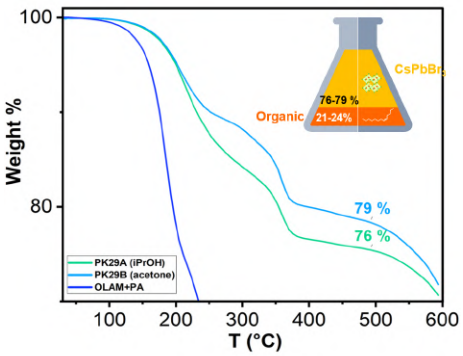

Figure 1.9 Thermogravimetrical analysis of OAm/PA 1:1 mol ratio (dark blue curve), PK29A reprecipitated with iPrOH (light green curve) and PK29B with acetone (light blue curve).

1.4.1 Solvents driven evolution

We ascertained that OAm solubility (and when over the surface of NCs, its tendency to be solvated) plays a fundamental role in the "interaction" of NCs with the surrounding solvent medium, starting from and imprinting on the way they are recovered from the crude mixture. We then decided to test its behaviour in different solvents over time. The most straightforward as well as efficient way to test colloidal stability is to disperse the NCs directly in a solvent filled quartz cuvette and start collecting ABS and PL spectra immediately and for about 24 hours, while keeping the dispersion under magnetic stirring. In all of the cases, even though the samples went through drastic morphological and structural evolutions, we have been able to monitor the process using optical techniques as at all stages the NCs remained homogeneously dispersed in the solvents. As solvents, we selected hept and toluene (tol). The solvents are reported in order of increasing capability of oleylamine solvation (and also polarity, for the basic rule - and also experimental evidence - that "like dissolves like", and we are dealing with an amine/ammonium). This two low-boiling solvents are also often used for ink preparation. The ABS and PL spectra are collected for 24 hours. Both ABS features (Figure 1.10(a) and (c)) evolve with time, but toluene effect is faster. In fact, yet for as-dispersed toluene sample (0 min) the smallest population (453 nm) is characterized by a decreased ABS and the modifications during 24 hours are modest. For heptane dispersed sample, we can clearly recognize the original

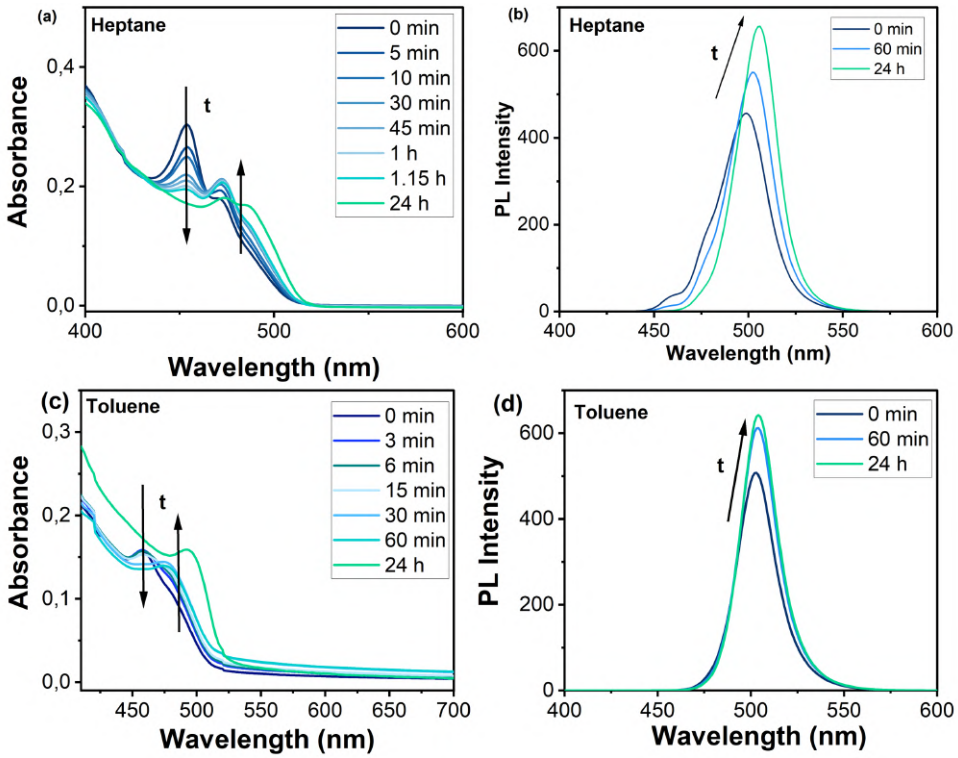

Figure 1.10 As-prepared $CsPbBr_3$ NCs evolution of optical features under dispersion in solvent (0,1 mg/mL) in heptane (upper graphs, respectively (a) ABS and (b) PL) and in toluene (bottom graphs, respectively (c) ABS and (d) PL) (λ_{exc}= 365 nm).

three populations previously described after 1 hours as well. Moreover, after 24 hours, the sample is still characterized by two ABS peaks, and not only one as for sample in toluene. To further deepen this aspect, we plotted the absoprtion values of the two sample at different wavelengths (458 nm, 476 nm and 493 nm - selected considering deconvolution of as prepared NCs ABS spectrum, Figure 1.8(a)) for both sample as function of redispersion time. Absorption values of 476 nm and 493 nm peaks increased over the time with a trend that is similar in both samples. The former, after one hour, start to slow down, whereas the latter increases until reaching at 24 h maximum value. Population represented by 458 nm peak instead decreases at the same time. After 24 hours, its value is higher than the starting one anyway. This behaviour suggest that smaller NCs coalesce toward the formation of bigger species. Not only the most red shifted (and thus bigger) objects ,in the initial 60 min of dispersion stirring, increases its absorption, but also the population with intermediate dimensions. The occurring evolution could be dominated by exchange of matter from different NCs, instead of simple coalescence. PL spectra corroborate ABS trend: the red-shift for toluene sample is of only 2 nm (from 502 nm to 504) and the shape indicates prevalent emission from only one species from the start. In heptane, at 0 min we can discriminate between different families emission, the most red-shifted one is the only emitting after 24 hours. The most interesting characteristic anyway is that in both cases PL Intensity increases over the time along with evolution. Generally, coalescence and Ostwald ripening of NCS in solution are associated with decreased material quality.[60] On the contrary, in our case the evolution process triggered by solvents seems to enhance luminescence. The details of such process are not known. A possible explanation is connected with the overall decrease of the surface to volume ratio due to the increase in the average dimension of the crystals during aging. This process involves merging of smaller

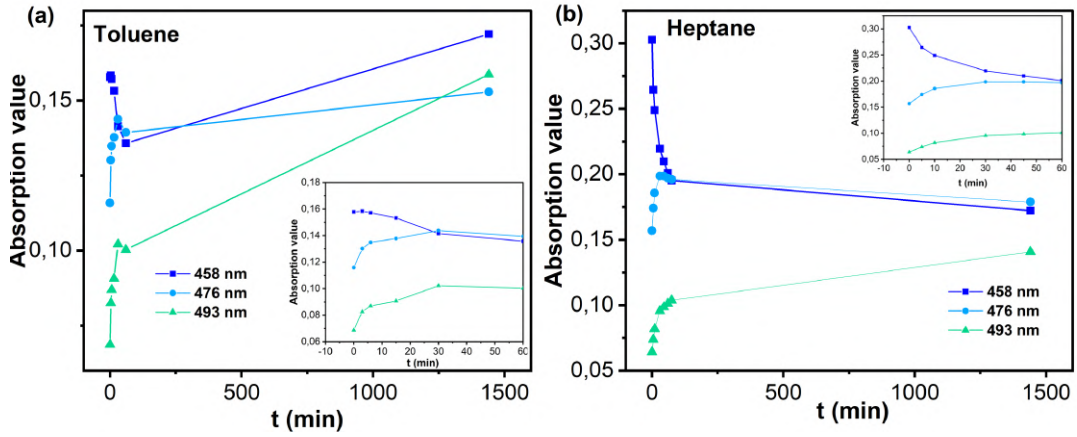

Figure 1.11 Absorption values trend at different wavelengths (458, 476 and 493 nm) as function of time for $CsPbBr_3$ NCs dispersed in toluene (a) and (b) heptane (0,1 mg/mL). Zoom from 0 to 60 minutes in the inset.

NCs as well as diffusion of materials from smaller to bigger ones. As all such processes involves erosion of existing surfaces, there could be preferential restructuring/evolution of those having a higher concentration of defects and therefore a higher energy/lower stability. Probably, the presence of excess ligands favours this reconstruction in a way that preserves surfaces from defectiveness, generally related to bromide vacancies. This process is exploited ahead in section 1.8.2. The outcome is characterized by bulk-like optical features (absorption edge at about 500 nm, PL maximum around 511 nm, Figure 1.12 (d)), correlated with shortest dimension now equal or longer than 8,5 nm (considering that dimension as the exciton Bohr radius[15]). The other important aspect is that the evolution process starts with more families with different dimensions and optical features to end up with the only thermodinamically favoured one. There's in fact only one absorption edge and photoluminescence peak and the full width at half maximum is smaller. TEM images and dynamic light scattering (DLS) comparisons confirm that the material has "grown". From Figure 1.12 (c), it is possible to notice that the long side distribution remains almost the same (around 13-14 nm), whereas the short side doubles. Also the aspect ratio noticeably decreases, from 6 to 1,6. We can thus hypothesize that the starting nanorods coalesce "face by face" when solvents solubilize the ligands excess between them. We can't properly define these final NCs neither nanoplatelets (there isn't one dimension too shorter than the other two) nor nanocubes: from this moment on, we will address them as nanobricks (NBs). The hypotetized process is depicted in Figure 1.12 (a) and the corresponding TEM images seem to corroborate it. The volume distribution fit from dynamic light scattering analysis (DLS,), performed in a 1 cm path quartz cuvette both on as-dispersed material and after 24 hours of magnetic stirring at 0,1 mg/mL in toluene, is reported in Figure 1.12(b) (more details in the experimentals 1.10.5.1). At first glance, it seems counterintuitively that not evolved sample (green curve) contains bigger species respect to evolved one (red curve). Nevertheless, in our model the pristine nanorods are kinetically trapped in a ligands-rich matrix, creating an higher dimension aggregate. With solvent solubilization of this "shell", the effective redispersion and then the "matter redistribution" to the thermodynamically favored form takes place, producing bigger and well dispersed NBs. The distribution in fact becomes narrower and more centeredof the excess ligand, the nanocrystals are allowed to evolve to bigger structures via Oswald ripening, in our case leading to well dispersed NBs. The distribution in fact becomes

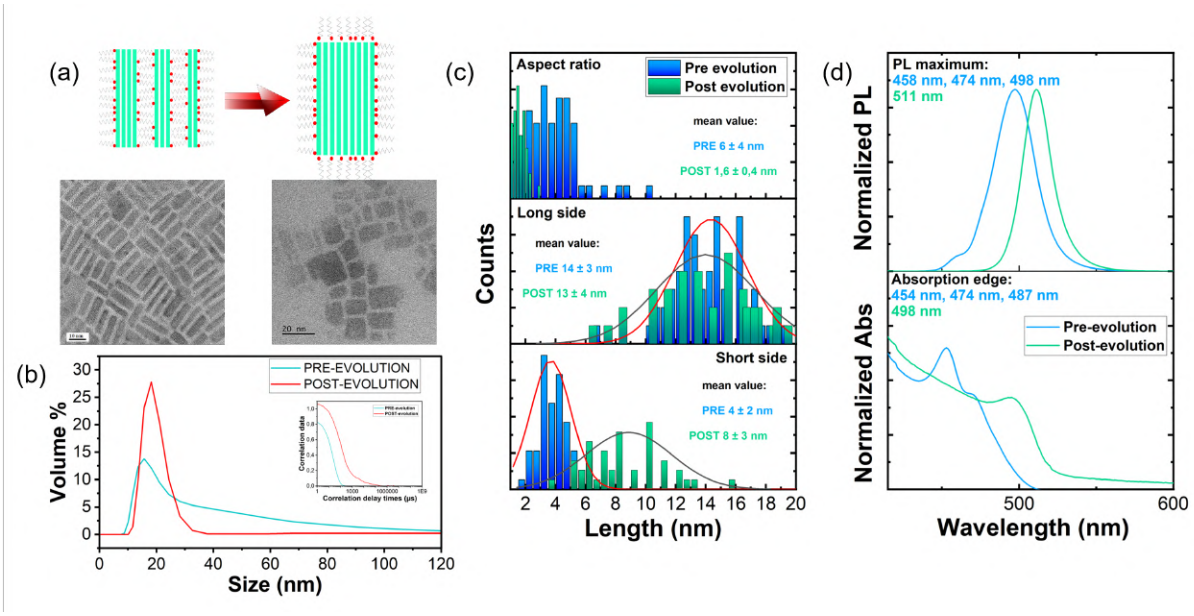

Figure 1.12 (a) Cartoon that represents our hypotesis about output material evolution in solvents and the corresponding TEM images. (b) Volume distribution fit from dynamic light scattering analysis (DLS) of the pre (green curve) and post (red curve) evolution samples. (c) Statistical analysis of the different dimensions (shortest and longest side) fitted with gaussians and the aspect ratio of both pre (blue) and post (green) evolution samples (80 NPs). (d) Normalized absorption and photoluminescence spectra comparison between pre (blue curve) and post (green curve) evolution samples. (0,1 mg/mL in toluene, λ_{exc}= 365 nm).

sharper. The correlograms in the inset agree with this interpretation: the evolved one starts higher than one, probably because with more dispersed objects scattering increases, but the shape is indicatively retained. There is also a slower tail, probabily due to NCs that grew too much.

1.4.2 Conservation in solid state

The question arises quite naturally: if the precursor NCs evolve, faster or slower, when in contact with solvents, what happens to them when they remain in solid state for prolonged times? This aspect is especially important to establish the correct way to stock the synthesized powders without damaging them if not readily used, especially considering that our synthetic procedure allows to obtain large quantities of material (see section 1.5.1.3). We tested two different storage protocols: a) storage under inert atmosphere and in the absence of moisture in refrigerated flask (4 °C); and b) storage at RT, without any further protection for moisture. For the former (sample A), we dried a transparent glass vessel with a Bunsen burner while under nitrogen flux, filled it with the material and stored it in the fridge (4 °C) of an Argon-filled glove box. For the latter (sample B), we used the same vessel but without drying and in air RT. After 2 months of storage, we compared the properties. At first glance (Figure 1.13), sample A retained the original light yellow look, conversely sample B features the segregation of a white phase not initially observed. The ABS and PL spectra exhibited comparable features. TEM images told us another story: both samples were redispersed in toluene (10 mg/mL), diluted at 0,1 mg/mL, stirred overnight, and deposited. Sample A was still composed by our characteristic rectangular NBs in every part, with the same lattice distance. In sample B instead we detected some peculiar hexagonal structures, never observed before. According

to the literature, the characteristics of new phase are consistent with the formation of a non luminescent Cs_4PbBr_6 phase[36] featuring $[PbBr_6]^{4-}$ octahedra that do not share sides and traps the luminescence. This modification is clearly detrimental for applications requiring efficient PL. Why does this happens? Given our previous results about ligands abundance around the NCs and the exchange that this species show in solution that makes the pristine material grow, we formulated an hypothesis. Oleylammonium bromide and lead oleate are somewhat loosely bound to the surface of the NCs, particularly when water is present. The prolonged exposure of the sample to temperatures up to 30 °C, environmental moisture and illumination can induce the extraction of bromide and lead by the free ligands, leaving behind a material that rearranges in a cesium-rich phase. This phenomenon is particularly relevant for the exposed surface of the sample. Probably the core remains the starting $CsPbBr_3$ produced at the beginning but contaminated. In conclusion, this analysis was definitely useful to assure that the best way to store these materials is with protocol of sample A: in solid state in a dried, under Argon inert atmosphere and refrigerated vessel to fully prolong their starting quality.

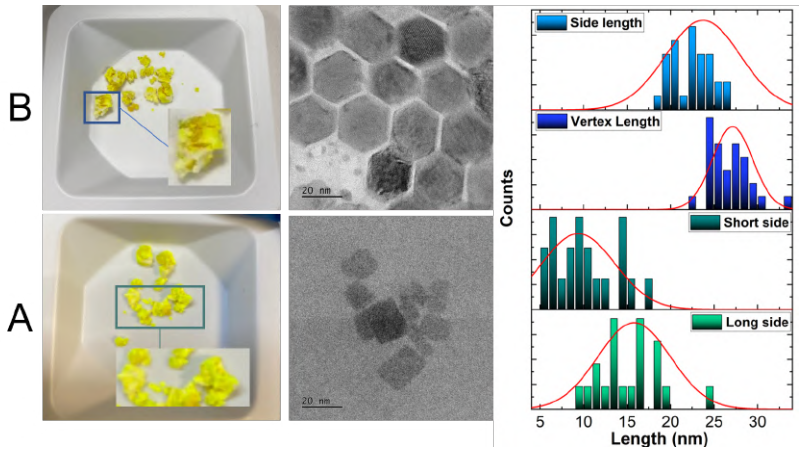

Figure 1.13 Photographs, TEM images and distribution of dimensions for sample B (upper) and A (bottom) (50 NPs).

1.4.3 Temperature effect

Due to the soft ionic nature of $CsPbBr_3$, they are renowned to undergo easy temperature transitions that are often detrimental for optical applications.[61] This contributes to their description as "heat sensitive". As previously stated, we originally developed our colloidal dispersions for optical applications, yet in order to fully exploit their characteristics we also tested their properties in dry solid films of interest for solar cells and OLEDs. In particular, we decided to test their behaviour as spin coated film at a direct exposure to an hot plate at 90 °C for increasing times from 1 to 5 minutes. This annealing passage is in fact often exploited to evaporate completely the solvents. According to our previous experience, we expected that the temperature annealing could bring about coalescence, not necessary a negative effect in view of solid state charge transport, but could also affect the nature of the crystalline phase. Firstly, we tested different spin coating conditions to select the best one for our purpose. We prepared perovskites dispersions in toluene at a test concentration of 10 mg/mL and spin-coated 100 µL onto a 2,5 x 2,3 cm glass. We selected 1000, 1500 and 2000 RPM for 45 seconds, under a nitrogen flux of 4 bar. The sample is then let aged for 2 minutes under nitrogen flux to be sure that the solvent is evaporated.

We collected ABS and PL spectra and compared them (Figure 1.14(b)) without normalization to evaluate the different resulting optical densities. As expected, lower spin coating velocities led to bigger amount of material deposition, characterized by a higher

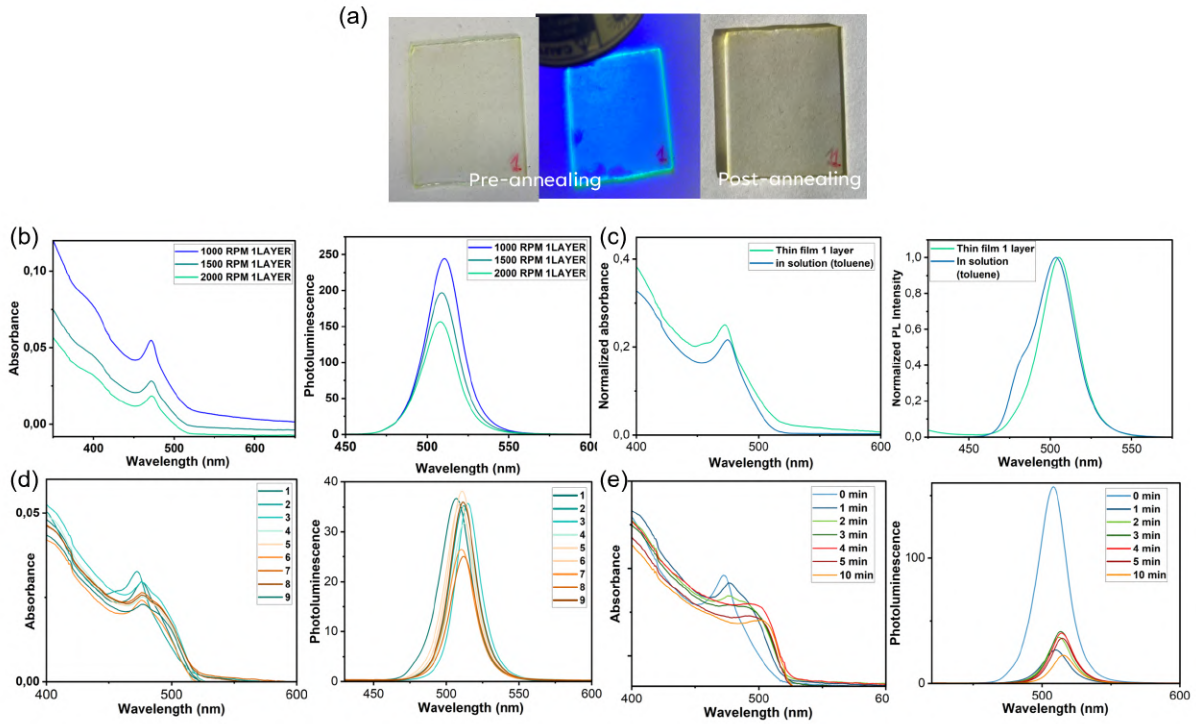

Figure 1.14 (a) Photographs of NCs deposited films before (under solar and UV illumination) and after annealing time (90 °C) of 1 minute; ABS and PL (b) at different spin coating velocities, (c) in solution and in thin film (1 layer, normalized), (d) at increasing number of layer depositions with 1 minute of annealing and (e) at increasing annealing time on 1 layer.(λ_{exc}= 365 nm)

optical density and at the same time more pronounced scattering tail, with the same starting solution concentration. However, lower velocities afforded films of poorer quality. We thus decided to choose 2000 RPM. Secondly, we analyzed the different characteristics between in solution and thin film samples (Figure 1.14(c)). Almost no differences are detectable in normalized ABS features: there are more families with different dimensions in both and only an expected higher scattering tail for solid state sample. Normalized PL shows differences between solution and solid state samples: in solution there is a blue-shifted emission peak from high energy gap populations that in solid state is absent. In thin film conditions in fact, shorter distances between different NCs favour excitation migration to lower energy conduction bands of bigger species. At this point, we considered two different approaches: the effect of a constant annealing time (1 minute) on progressive number of layers deposition and, vice versa, the effect of increasing annealing times on a fixed number of layers (1 layer). For the former, the procedure consisted in depositing each layer, collecting ABS and PL spectra, annealing on the hot plate at 90 °Cfor 1 minute, collect spectra again and depositing another layer, and so on, until the ninth. The resulting ABS (Figure 1.14(d)) is not proportional to the number of layers: probably every deposition partially dissolves the previous one. This suggests that annealing time of 1 minute is not sufficient to compact the layer. We thus turned our attention to increasing annealing times: we deposited one layer and then collected ABS/PL after every minute of treatment until 5 minutes and then after 10. ABS clearly shows that the evolution towards bigger NCs along with the red shift. The scattering increases marginally. After five minutes, the optical density decreases, meaning that prolonged temperature treatments can be detrimental. Even if PL spectra seem not to be completely reliable, it is noticeable

that annealing strongly reduces luminescence (probably due to formation of non-radiative defects during solid state coalescence). We can thus conclude that annealing procedure at 90 °Cis tolerated by the material (with this thickness of 0,1 mm) up to a maximum annealing time of 5 minutes (provided that PL is not a target).

Finally, along with steady state optical characterization, we analysed the possible differences in crystalline structure with powder X-ray diffraction (PXRD) before and after annealing process. We deposited the material onto the glass sample holder through drop casting (70 mg/mL), collected the diffractogram, heated the sample directly in the PXRD holder on the hot plate for 10 minutes (thickness 0,3 mm) and then let it cool down to RT under nitrogen flux. Finally, we repeated the measure again. The two diffractograms are reported with the correspondent Lorentzian fit of each peak (see experimentals, equation 1.7) in Figure 1.15. The fitting allows to accurately obtain the peak centre and the FWHM that can be correlated, through Scherrer equation (see experimentals, equation 1.8), to grain or, as in the present case, crystallites dimension. The values are reported in Table 1.1. Firstly, it's evident that the temperature treatment does not influence the crystalline phase: the peaks are in the same position of the diffractograms. The crystalline structure is compatible with cubic phases, but we can't exclude the co-presence of an orthorhombic one (more intense peaks are really similar, Figure 1.15), condition that moreover finds support in literature for these low-dimensional materials.[60] From this moment on, for simplicity we will consider cubic phase approximation when needed. Both morphology and crystalline structure are consistent with other low temperature protocols and ligand-rich conditions, that usually favour the formation of nanoplatelets instead of nanocubes[57].[62]The shift toward higher 2-theta from pre to post annealed samples is modest (on average 0,07 deg) but systematic and compatible with bigger crystalline domains: the only slight increase is comprehensible if we think that we are dealing with NCs that grow from 4 to 8 nm. The FWHM also lightly decreases (inversely proportional to the dimensions) and from its analysis through Scherrer equation, on average the crystallites evolved from 6,5 to 7,9 nm. The values are probably not exact due to other factors that act on peaks width and position in this kind of colloidal NCs samples (i.e. not perfectly flat for difficult deposition procedure, abundant presence of amorphous ligands), but their trend matches with the other results and our assumption. In not normalized diffractograms, there is no difference between relative intensity of the different peaks, meaning that the evolution process is not anisotropic.

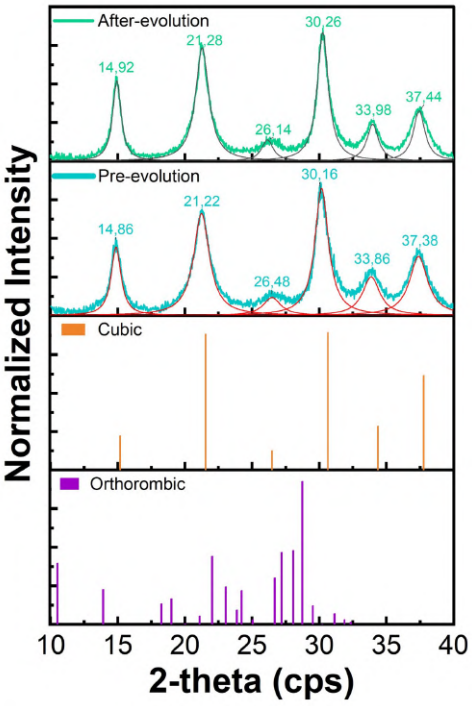

Figure 1.15 Powder X-ray diffractograms of both pre (light blue curve in the lower frame) and post annealing (light green curve in the upper frame) samples. Lorentzian fit and the 2-theta degrees of main peaks are reported.

In conclusion, heat is confirmed another parameter for NPs evolution.

Table 1.1 Peak center, FWHM and Scherrer equation derived crystallite size from PXRD on pre and post evolution samples.

Sample	Peak (deg)	FWHM (deg)	Scherrer dimension (nm)
Pre	14, 87	0, 88	9, 5
	21, 23	1, 42	5, 95
	26, 48	1, 58	5, 4
	30, 17	1, 22	7, 05
	33, 86	1, 56	5, 56
	37, 39	1, 64	5, 34
Post	14, 93	0, 76	11, 02
	21, 28	1, 2	7, 04
	26, 14	1, 06	8, 04
	30, 26	1	8, 6
	33, 97	1, 04	6, 4
	37, 43	1, 04	6, 26

1.5 Impact of processing parameters on the properties of colloidal dispersions.

Having suitably characterized the nature of the as synthetized materials and its evolution during storage and handling, we turned to the generality of our synthesis in terms of processing parameters (the nature of stirring method most of all, but also temperature and viscosity of solvents employed) as well as composition of the final phase as a function of the reagents we employed. The effect of all such variations was monitored during synthesis and through comparison of the optical and morphological features of the output materials.

1.5.1 Homogenization method

My team previous expertise in formulation chemistry (and also my personal one built on a parallel project presented in chapter 2) taught me that an efficient and high-speed homogenization method is central in through and reproducible mixing of solutions and dispersions, both on small quantities, and progressively more with larger ones. In the PVK synthesis field, the most common stirring methods employed are high speed magnetic or mechanical stirring, but neither of them is really suitable when very large volumes are tackled (i.e. more than 2 L). In these cases, a turbo-emulsifier homogenizer, that exploits a rotor-stator effect (Figure 1.7(b)) is often needed.[58] When dealing with colloidal NCs synthesis, especially $CsPbBr_3$ that forms very rapidly and are characterized by optically inactive phases, avoiding the formation of concentration profiles in the synthetic process is fundamental. The use of this type of instrument is completely unknown in field of colloidal NCs synthesis and thus its introduction is original.

1.5.1.1 60 mL scale

For this reason, we firstly decided to corroborate its compatibility performing the same reaction with both classical magnetic stirring (and from now on, the output material will be referred to as MSSs - magnetically stirred samples) and turbo-emulsifier (TESs - turbo-emulsified samples) on the minimum batch employed of 60 mL. For the former we set 1000 RPM, the maximum value for our stirring plates, and for the latter 15000

Table 1.2 Every entry represents a type of sample (TES and MSS) for which are reported the volume of solution employed, the dried recovered amount of material, the ABS edge, the maximum of PL, the corresponding FWHM and the aspect ratio with its standard deviation. The data are comparable at every scale.

Entry	Volume (mL)	Output (mg)	ABS edge (nm)	PL maximum (nm)	FWHM (nm)	Aspect ratio
TES	60	120	493	511	22	$1,6 \pm 0,4$
	1200	2800	489	513	24	$1,8 \pm 0,8$
MSS	60	97	490	510	21	$1,4 \pm 0,3$
	1200	2700	491	512	20	$1,4 \pm 0,4$

RPM, half of the maximum rotating velocity, for the same time interval, with all the other conditions unchanged (reported extensively in 1.3). We deeply analysed in section 1.4.1 that the obtained material from our developed synthetic protocol changes and evolves, especially in solvents depending on time and concentration, but once reached the final form, it maintains well-defined properties. Thus, to enable a comparison between the TES and MSS, we made all characterizations on evolved material, after standardized redispersion in toluene conditions: 0,1 mg/mL concentration and overnight stirring.

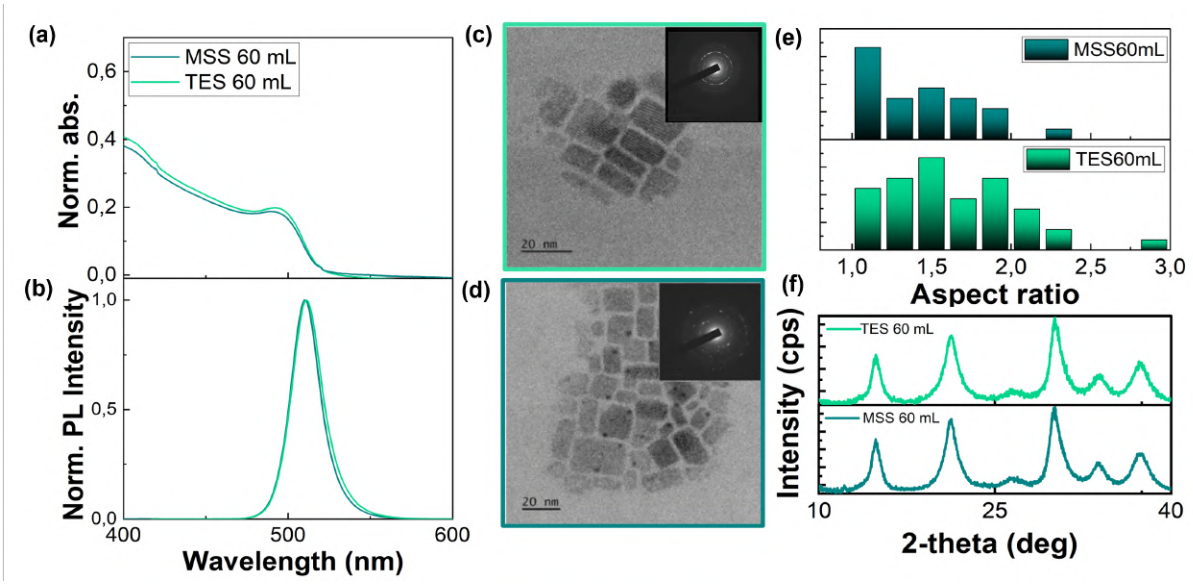

Figure 1.16 Normalized (a) ABS and (b) PL spectra (0,1 mg/mL in toluene, λ_{exc}= 365 nm), (c)-(d) HRTEM images and single area electron diffraction (SAED) in the insets, (e) aspect ration distribution analysis (both on 50 NPs) and (f) PXRD of TES and MES on 60 mL batch volume.

Figure 1.16 shows that, on a 60 mL scale, magnetic and high shear homogenization provides NBs with comparable characteristics in terms of photophysical properties, shape, dimensions and crystalline phase (Table 1.2).

Both samples exhibit superimposable ABS profile with a clear edge at about 496 nm and PL centred around 510 nm (Figure 1.16 (a)-(b)), concordant with the evolved sample values. The FWHM is also very similar and the same can be deduced for PL decay in time (Figure 1.16(b) in the inset, Table 1.2). The absolute PLQY too was comparable around 65%. The TEM images (Figure 1.16 (c)-(d)) and the corresponding statistical analysis of aspect ratio (Figure 1.16 (e)) reveal that the latter is always higher than 1 (exact value 1,6 ± 0,4). The long side is around 13 nm ± 4 nm and the short one around 8 nm ± 3

nm, even if for MSS values are slightly higher (respectively 17 ± 4 nm and 11 ± 6 nm, see experimentals, Figure 1.46). Considering random deposition of the NCs on every side, we can conclude that also thickness is within the same dimensional range: it can be either around 8 nm or 13 nm. Also the crystalline phase is the same and the PXRD peak are completely superimposable both with 2-theta maximum and FWHM (Figure 1.16(f)). In terms of NCs output quantity, the control experiment (magnetically stirred) produced 97 mg of solid, whilst the turbo emulsified one 120 mg. (64% and 78% respectively of estimated yield calculated from the inorganic part deduced with TGA respect to the amount of starting quantity of limiting reactant caesium – Figure 1.9).

1.5.1.2 1200 mL scale

Having validated the method on a typical laboratory scale, we linearly scaled up all components of the reaction up to a 1200 mL mixture volume, without any other change in the protocol. This scale allowed us to obtain 2.8 g of output material with turbo-emulsifier and 2.6 g with magnetic stirring. At such a large scale, the results obtained working with magnetic stirring and turbo-homogenization vary dramatically. Indeed, if in terms of steady state optical properties the two methods afford comparable samples (also behaving identically to those prepared at the 60 mL scale, Figure 1.17 (a)-(b), Table 1.2), the structural TEM analysis provides a very different scenario (Figure 1.17 (c)-(d)).

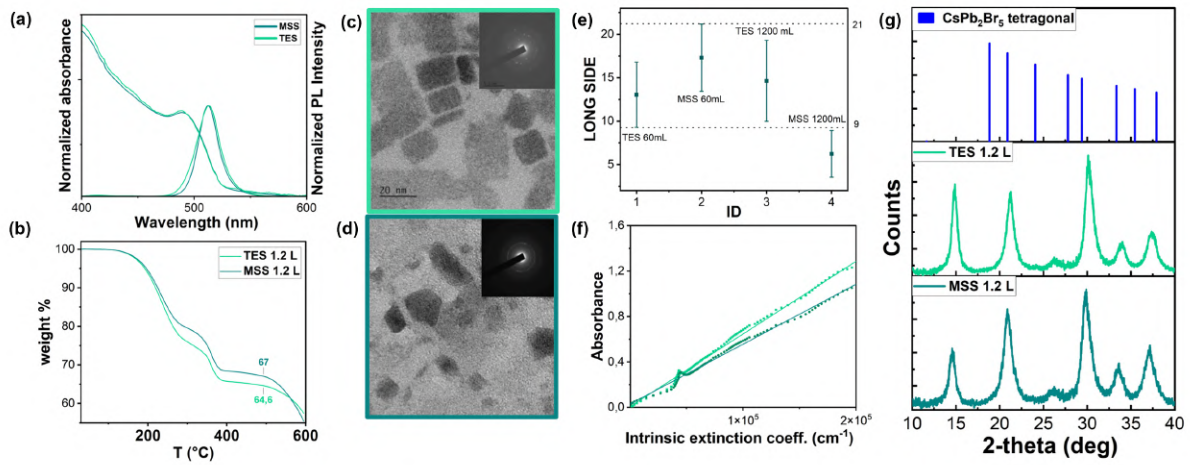

Figure 1.17 (a) Normalized ABS and PL spectra ofPVK NCs inks obtained from 1200 mL batches with TES (light green line) and MSS (dark green line)(0,1 mg/mL in toluene, λ_{exc}= 365 nm). (b) TGA analysis of both samples. HRTEM images and SAED inset of samples obtained respectively with (c) turbo-emulsification and (d) magnetic stirring. (e) Plot of the long side statistical mean value for TES and MSS at 60 mL and 1200 mL scales (50 NPs). (f) ABS at the specific wavelength and concentration (489 nm, 0,125 mg/mL) in function of the intrinsic extinction coefficient, calculated by De Roo et al[63] and their linear regression for both TESs (light green) and MESs (dark green). (g) PXRD of TES and MSS samples compared with standard $CsPb_2Br_5$ tetragonal phase (PDF Card No.: 00-054-0753).

While the TES-NCs are essentially comparable with those produced at the smaller scale (average long side is the same, Figure 1.17 (c)-(e)), showing the recognizable and regular shape of nanobricks, the TEM image of the MSS is, in this case, extremely dissimilar (Figure 1.17 (d)). The PVK NCs are still distinguishable and crystalline, yet they span a wider range of shapes and dimensions. Figure 1.17 (d) clearly shows their extreme shape irregularity and also the presence of extraneous, apparently not crystalline, contrast aggregates we did not observe in any other sample. The aspect ratio and the statistics

Table 1.3 For each sample (TES and MSS 1,2 L) weight of analyzed sample, % Cs, % Pb and Pb/Cs ratio are reported from ICP-OES analysis.

Sample	Weight (mg)	% Cs	% Pb	Pb/Cs
TES 1.2 L	112	10,9	21,3	1,2
MSS 1.2 L	111	11,6	22,3	1,2

of TES-NCs are not preserved, especially the average long side (Figure 1.17 (e)) and the profile is rather flake-like than rectangular. This aspect suggests that, even though the amount of material we isolated in the two procedures was comparable, the actual NCs yield is higher in the case of TES. To further elucidate this intriguing aspect, we compared the optical density of NCs solutions with identical nominal concentration obtained with TES and MSS samples. According to the method of De Roo et al.,[63] that precisely correlates ABS to concentration through the introduction of intrinsic extinction coefficient, calculated by them for a wide range of wavelengths and independent of the NC size in some conditions, we plotted the ABS at a specific wavelength (489 nm, next to the ABS edge) and at a given concentration of the two solutions in function of the intrinsic extinction coefficient (Figure 1.17(f)). The data sets (from 320 nm to 550 nm) are satisfactorily represented by the linear trend model used (see experimental 1.10.5.2). The resulting slope, that is demonstrated to be proportional to the effective NCs concentration in solution, is considerably higher in the case of TES sample. This behaviour confirms that the actual concentration of NBs in MSS sample is smaller than in the case of TES one. The deviation from linearity between 458 and 512 nm is probably related to the fact that we produced NBs ,instead of perfect bulk cubes, that contribute to more pronounced ABS in that specific region before the bulk ABS edge. We further characterized the two samples by TGA and ICP-OES to evaluate the ligand concentration and to characterize the Cs/Pb ratio (Table 1.3).

The two samples gave similar results. There are two possible interpretations about the nature of the extraneous material detected in TEM images of 1200 mL MSS: oleylammonium-rich lead bromide clusters or very small Cs_4PbBr_6 0D clusters representing unevolved $CsPbBr_3$ precursors. Our data cannot discriminate between the two possible phases, in any case representing an undesired outcome of the reaction. Disregarding the details in the compositions, the extraneous material can't be generated by other reasons than concentration profiles during formation, leading to the nucleation of stoichiometries other than the target $CsPbBr_3$. Such inhomogeneities are particularly detrimental for low temperature protocols where kinetics is dominant over thermodynamics. The use of turbo emulsifier provides a very rapid and efficient mixing, immediately leading to the ideal stoichiometry of all regents within the whole reaction volume and almost exclusive nucleation of the target material, making reliable also work in the range of almost 3 g of output material.

1.5.1.3 Reliability and remarkable scalability of the procedure

The lack of reproducibility is a known issue of literature procedure for the synthesis of inorganic and hybrid PVK, especially when scaling up a procedure originally devised to produce materials on the mg scale. Aiming at further showcasing the robustness of our method, we progressively increased the reaction volume of TES to 120, 240, 300, 900, 1200 and 3600 mL.

Figure 1.18(a) shows the normalized ABS and PL spectra of all the different samples. Table 1.4 shows the corresponding optical parameters (PL maximum, FWHM, ABS edge),

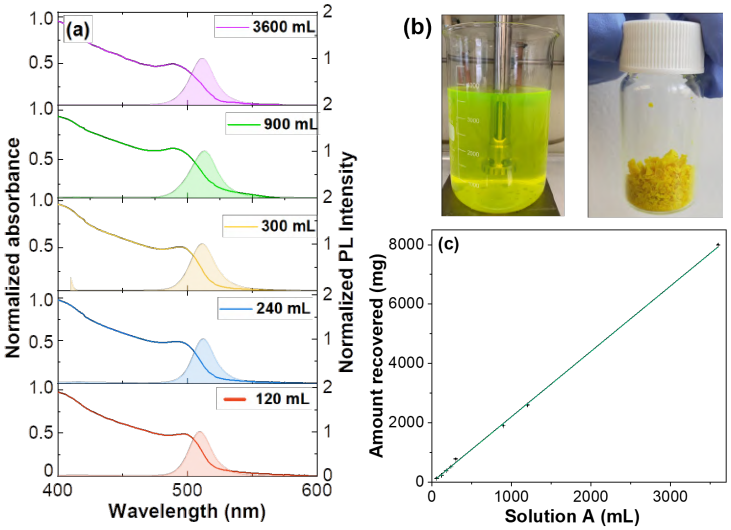

Figure 1.18 (a) Normalized ABS (full lines) and PL spectra (filled area curves) of five samples of different scales that show comparable features (0,1 mg/mL in toluene, λ_{exc}= 365 nm). (b) Photograph of the obtained 3.6 L volume raw mixture. (c) Linear regression of the volume of solution A in function of the dried recovered amount of NCs.

Table 1.4 Every entry represents a TES for which are reported the volume of solution A employed, the dried recovered amount of material, the maximum of PL and the corresponding FWHB. The data are comparable at every scale.

Entry	Scale (mL)	Recovered amount (g)	$\frac{Amount}{Volume}$ (mg/mL)	PL Max (nm)	FWHM (nm)
1	60	0,12	2	510	21
2	120	0,230	1,9	508	26
3	240	0,510	2,1	510	20
4	300	0,78	2,6	510	20
5	900	1,9	2,1	512	25
6	1200	2,6	2,2	508	24
7	3600	8	2,2	511	25

together with the amount of collected material. The different batches show comparable optical properties, which confirms reliability of this method at every selected scale.

The TEM imaging also gives comparable results while scaling up (experimentals, 1.47). An immediate way to compare the yield of numerous samples is the relative comparison between the amounts of material recovered following the same procedure. From table 1.4, data plotted in function of the employed batch size can be satisfactorily modelized with a linear fit (Figure 1.18(c)):

$$y = (6,4 \times 10^{-12} \pm 2 \times 10^{-13}) + (2,2 \pm 0,03)x$$

$$R^2 = 0,99$$

Between 7 differently scaled reaction (from 60 ml to 3600 ml) that span from 120 mg of output material to the unprecedent 8 g, the R^2 of the fitted model remains very high (0,99), suggesting that this process is reliable and robust. As a further confirmation of the robustness of the method, it is even possible to use the slope of the fitting straight line to correctly dimension a specific synthesis with respect to the target amount of material required. Thus, with this novel synthetic procedure, it is not only possible to reach the unprecedented scale of 8 g of final dry material in a single well-controlled preparation,

when working at the 3.6 L reaction volume, but also to gain the original advantage of planning and achieving the desired amount of NCs just using the corresponding specific conditions.

1.5.2 Different anions

As previously mentioned in introduction part (section 1.1.2.1), one of the most outstanding LHP NCs characteristic is the predisposition to compositional tuning, allowing the corresponding optical properties to span all over the UV-VIS range. In my project, I deepened the effect on synthetic process and output material of different halide precursors ($PbBr_2$, $PbCl_2$, PbI_2), also in mixture, maintaining the cations constant. I didn't have time to approach the cation engineering, (i.e. methylammonium/formamidinuim instead of cesium or tin in place of lead) but it is a future perspective to further expand our protocol possibilities.

1.5.2.1 $CsPbCl_3$ and $CsPbBr_xCl_{3-x}$

Firstly, we decided to approach the synthesis of $CsPbCl_3$ NCs. The synthetic procedure reported in section 1.3 was performed identically except for the employment of $PbCl_2$ instead of $PbBr_2$ (the same molar amount) and obviously the absence of TBAB (experimentals, 1.10.2.2). We tested 60 mL and 120 mL scales, as proof of concept. $PbCl_2$ well dissolves in OAm/PA 1:1 mol mixture. When the lead-rich solution B is added to the caesium propionate solution A under turbo-emulsifier homogenization, any modification is noticeable. After 30 seconds of mixing, the solution remained clear and colourless, without any fluorescence. The addition of the standard iPrOH quantity doesn't induce instantaneous precipitation. After 30 minutes the mixture starts to become slightly turbid. After 24 hours, the dispersion was centrifuged as usual (4500 RPM, 2 min), the supernatant discarded and the solid dried. We collected 68 mg of grey colloidal output material with 60 mL batch (Table 1.5) and 125 mg with 120 mL one. The experiment told us that the $CsPbCl_3$ formation kinetic is slower with respect to $CsPbBr_3$. Even if tolerance factor is slightly higher for the former (0,93 respect to 0,92[64]), probably synthetic conditions change the cards on table. A computational in depth-study is planned.

To evaluate their optical features, we redispersed the solid in toluene at the usual concentration of 0,1 mg/mL. The first exciton absorption peak is centred around 398 nm and it seems to be sharper than the bromide one (Figure 1.19 (a)). This phenomenon is usually correlated with more strongly confined excitons.[32] The PL is weaker (the relative quantum yield is around 4%, comparable with literature values,[22] as explained in section 1.1.2.1), with maximum value at 410 nm and the FWHM apparently smaller (13 nm respect to 22 nm, Table 1.5, further details in section 1.1.2.1). The time resolved photoluminescence is really fast (estimated around 100 ps): in these cases, it is necessary to use a streak camera to properly deconvolve the laser finger from the signal and have a more reliable value. The experiment is still in progress at the time of writhing of this thesis. Regarding to the morphological characteristics, the PXRD (Figure 1.19(b)) confirms that the sample has a single phase, compatible with the orthorhombic one (PDF Card No.: 01-075-0411). The analysis of TEM images (Figure 1.19(d) and (f), deposition after overnight stirring at 0,1 mg/mL) reveals that this NCs are modestly smaller and more cubic than the bromide (i.e. mean long side 10 ± 2 nm respect to 13 ± and mean aspect ratio 1,4 ± 0,4 respect to 1,6 ± 0,4). Nevertheless, these differences are negligible and the dimensions obtained are within the same range and thus characteristic of the synthetic

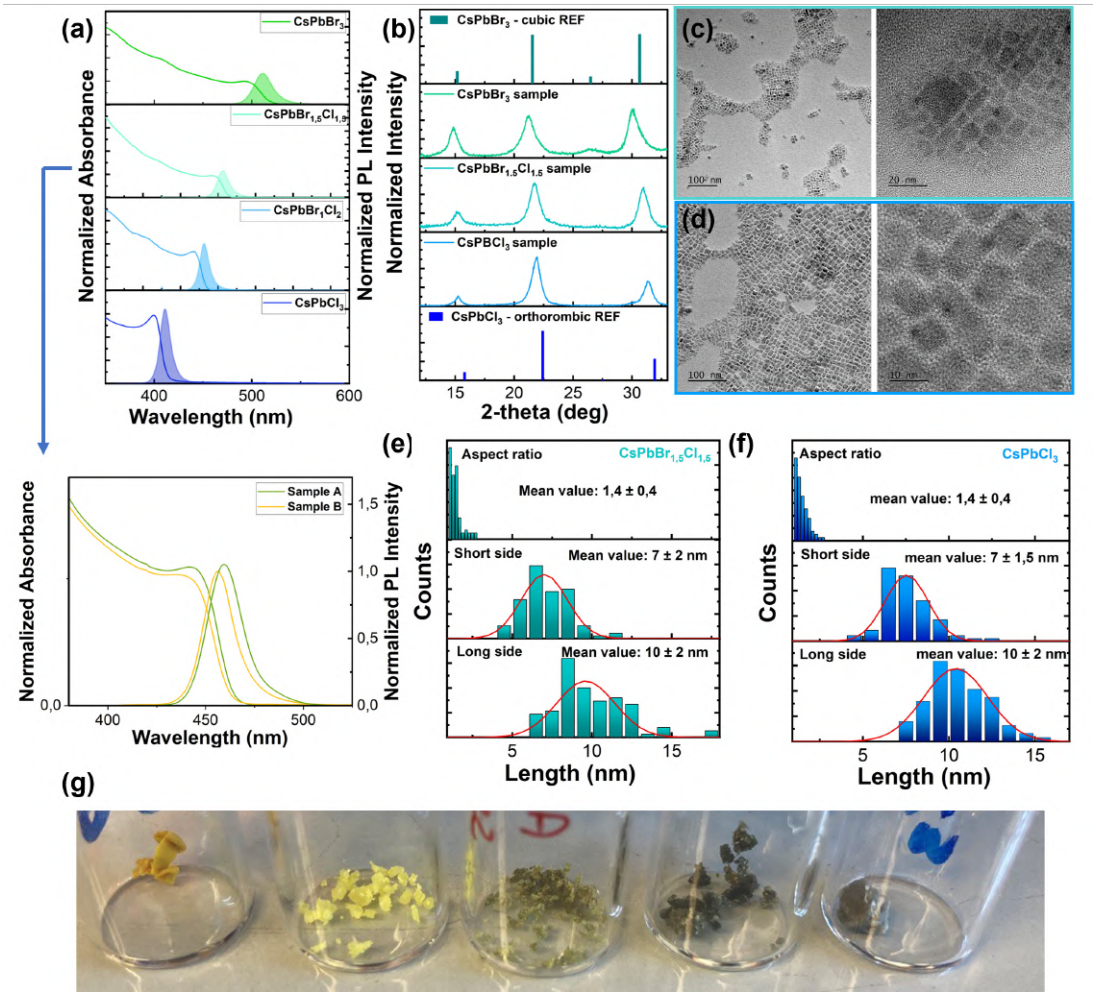

Figure 1.19 (a) Normalized ABS (only curves), PL spectra (filled area curves) (0,1 mg/mL in toluene, λ_{exc}= 350 nm) and (b) PXRD with references (PDF Card No.: 01-075-0411 and PDF Card No.: 01-084-0464) of $CsPbBr_xCl_{3-x}$ samples produced and spectroscopic details about the two batches obtained with nominal concentration of $CsPbBr_{1,5}Cl_{1,5}$. TEM images at low and high magnification and the derived statistical analysis on dimensions of respectively (c)(e) $CsPbBr_{1,5}Cl_{1,5}$ (top) and (d)(f) $CsPbCl_3$ (bottom)(90 NPs). (g) Photograph of different samples obtained in solid state. From left to right: $CsPbBr_3$, $CsPbBr_{1,5}Cl_{1,5}$. sample B, sample A, $CsPbBrCl_2$, $CsPbCl_3$.

procedure. Given the poor PLQY, several literature studies have focus on its improvement. One of the most common methods is the post-synthetic treatment of the dispersed NCs with halide rich species, such as $CdCl_2$. We adapted Mondal et al.[22] procedure and dispersed the NCs at 0,2% mg/mL in toluene, then added 10 mg of $CdCl_2$ and let the mixture stir for 2 hours. The dispersion is centrifuged to remove solid parts and the output reached a PLQY of 40%, one order of magnitude higher than the pristine sample, without any change in ABS and PL position (experimentals, Figure 1.44). Indeed, the PL intensity decay time of treated NCs moves from 100 ps to 2 ns. The reported explanation bases on the fact that post-synthesis added chlorides fill the surface diffused halogen vacancies, the most common defects in lead halide perovskites with high surface area. Moreover, given that between all the chloride salts the cited one is the most performing, it is also hypothesized that cadmium partially intercalates into the crystalline structure without modifying it and its related energy level related properties. We can conclude that our synthetic protocol can be easily extended to high quality $CsPbCl_3$ NCs production as well and it maintains its intrinsic scalability. Considering this promising result, we also

Table 1.5 Main characteristics of $CsPbBrxCl_3-x$ samples with different halogen compositions synthesized on 60 mL scale

Sample	Recovered amount (mg)	ABS edge (nm)	PL Max (nm)	FWHM (nm)	(100) XRD peak (deg)
$CsPbCl_3$	68	398	410	13	$15,2$
$CsPbCl_2Br$	77	420	433	$14,5$	$15,1$
$CsPbCl_{1,5}Br_{1,5}$	78	$439-443$	$457-460$	$18,5-21$	$15,1$
$CsPbBr_3$	120	489	511	23	$14,8$

tested synthetic procedure robustness towards different bromide/chloride proportions. The first attempt was to obtain $CsPbBr_{1,5}Cl_{1,5}$. NCs: we selected 60 mL scale and dissolved in OAm/PA half mole of $PbBr_2$ (183,5 mg) and half mole of $PbCl_2$ (139 mg). In this way, the amount of lead is maintained. Immediately along with solution B addition into solution A under turbo-emulsifier homogenization, the mixture turned yellowish and with iPrOH addition slightly turbid. We centrifuged this first solid (sample A) obtaining 40 mg and then let the supernatant rest for additional 24 hours. More solid precipitated and we recovered further 38 mg (sample B), meaning a total of 78 mg. We compared the steady state optical properties of the two batch (Figure 1.19 zoom (a)): the first exciton ABS peak differs of only 4 nm and in both cases is more broaden and obviously red-shifted (respectively 443 and 439 nm) than the $CsPbCl_3$ one and the same can be deduced for PL (respectively maximum 460 and 457 nm, FWHM 21 and 18,5 nm, Table 1.5). These data suggest that sample A, that precipitates faster, is slightly richer in bromide because it is more redshifted respect to B. This evidence is concordant with the slower kinetic shown by chloride reaction.[12] Also in this case, the morphology and dimensions are completely comparable with the other obtained material (Figure 1.19).

Another test was the combination of $PbCl_2$, as source of lead and chloride, with the TBAB, as the only source of bromide. We also wanted to elucidate whether the fact that the bromide is provided by a counter ion other than lead could affect the kinetic but not the inserted halogen proportions. In our opinion, this method could be a more controlled way to "dope" the $CsPbCl_3$ NCs with bromide. We decided to address the $CsPbBrCl_2$ composition and to keep Pb^{2+} constant (1 mmol respect to 0,2 mmol of Cs^+) because the change in Pb^{2+}/Cs^+ ratio affects crystalline morphology and thus spectral features (i.e. its increase pushes towards more confined 2D species[65]). We dissolved 1 mmol of $PbCl_2$ and 1 mmol of TBAB in OAm/PA: in these conditions, the halogens are in excess respect to the previous case but keep the desired proportion Cl/Br 2:1. After injection step, the mixture turned from colourless to pale yellow, slightly blue luminescent under UV illumination (365 nm). The iPrOH addition triggered the formation of a precipitate that is recovered as in the previous case (sample C, 67 mg), meanwhile the supernatant is let resting for 24 hours and centrifuged again (sample D, 10 mg). In this case, suggesting that the process is speeded up even if there's less reactive chloride in place of bromide. This could be due to the large chloride excess, driving the formation of kinetically less favoured of $CsPbCl_3$ phase. The optical analysis (Table 1.5 and Figure 1.19 (a)) confirms that the features are comparable with the literature value for this Cl/Br ratio.

In conclusion, the procedure enables the chloride-bromide compositional changes, even when careful tuning of the final composition is required, and the use of TBA is useful for this purpose without introducing further lead excess.

1.5.2.2 $CsPbI_3$

The extension towards $CsPbI_3$ comes quite naturally. These materials are renowned in literature to be the least stable of the three[66] but also the ones with the spectrum more compatible with the solar one for photovoltaic applications.[67] Also in this case, we dissolved only PbI_2 (1 mmol, 461 mg) in OAm/PA mixture without any problem and added this solution to 60 mL of caesium propionate one. The reaction turns immediately intense yellow and turbid, then darkens a bit towards orange to stabilize its colour to opaque pale yellow at the end of the 30 s. The changes in colour suggest that a reaction takes place. Given that the mixture already presented a thick precipitate, we collected this first solid, added the standard volume of iPrOH to the supernatant and let it rest overnight. We obtained 77 mg of an intense yellow, very hard to detach from centrifuge vial surface, first solid with an almost imperceptible dark orange border (Figure 1.20 (b) in the inset), and a negligible similar solid from the second centrifugation. At first sight, the aspect was not the expected one: it is reported in literature that the emissive γ "black" phase is deep red, the not-optically active orthorombic δ "yellow" one is instead indeed yellow.[11] We optically and morphologically characterized the output: ABS and PL spectra (Figure 1.20(b)) confirm that the product is non-fluorescent and with ABS features ascribable to isolated $[PbI_6]^{4-}$ octahedra[68,69] PXRD clearly shows that the product can contain PbI_2 but it is in majority composed by the orthorhombic $CsPbI_3$ phase (Figure 1.20 (a)). It is not extremely surprising, given that RT synthetic conditions are more prone to give orthorhombic structures[11] (because generally more thermodynamically stable at "low" temperatures, when the difference is noticeable). We tested if the transition phase happens at reflux toluene temperature (110 °C) but, as suggested in literature, such temperature not sufficient.[66] With present conditions, our procedure is thus not suitable for the synthesis of such materials but the fact that it doesn't give back the reactants but a different phase of the desired product is nevertheless a good starting point. We have in mind to both try to change solvents to make it possible to raise the temperature (see section 1.5.4), adding sort of "templating agents" during the synthesis (i.e. tetrabutylammonium iodide or others) and forming a film with this material and make it change its phase directly in film form with post-synthetic annealing. In any case, we exploited an alternative post-synthetic strategy to access this compound (see section 1.6.1).

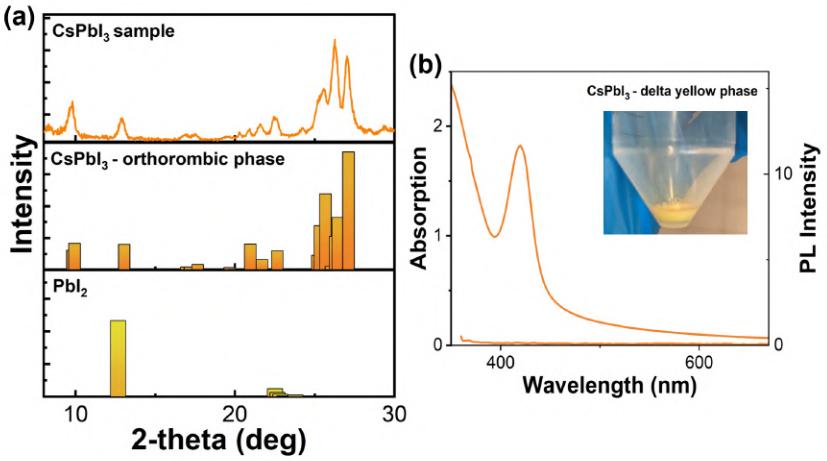

Figure 1.20 (a) ABS and PL spectra (concentration: 0,1 mg/mL, λ_{exc}= 365 nm) of $CsPbI_3$ attempt and photograph of the obtained solid in the inset. (b) PXRD of $CsPbI_3$ attempt sample with orthorhombic non-emissive $CsPbI_3$ phase and PbI_2 diffractograms as references (respectively PDF Card No.: 01-074-1970 and PDF Card No.: 01-073-1288).

1.5.3 Viscosity

The diffusion coefficients of the various chemical species employed in a colloidal synthesis can have a deep impact on the properties of the final materials, particularly when working on a large scale and with experimental procedures requiring the rapid injection of a solution in a mixture of solvents and antisolvents. The viscosity of the solvents employed can thus profoundly impact on the results, by slowing all diffusion processes at comparable temperature. Also, the use of solvents with high viscosity and high boiling point enables carrying out the reaction at high temperature (as discussed in the next paragraph). We thus decided to study the behaviour of the protocol when varying both solvents from hept and iPrOH to higher viscosity and higher boiling point analogues. Instead of the former, the obvious choice was octadecene (ODE), already highly used in literature NCs synthetic procedures.[15] Substituting iPrOH was more challenging: in the end, Dowanol DPnP™(Dow) was selected. It's a commercial dipropylene glycol n-propyl ether produced by Dow company, usually employed for coatings, resins and cleanings formulation.[70]

We measured the viscosity of the two solvents mixture with amine/acid ligands 1:1 mol ratio in the same amount used for reaction using a Brookfield viscosimeter and all relevant values are reported in Table 1.6. While working at RT, the use of the high boiling point solvents doubles the viscosity of the reaction mixture. The procedure was thus adapted as follow: $PbBr_2$ was dissolved in OAm/PA 1:1 mol ratio with a small amount of Dow and then added to a 60 mL caesium propionate solution in ODE/Dow 2:1. TBAB was not employed to exclude possible further influences on viscosity (TBA salts are known thickening agents). During the first seconds under turbo-emulsifier homogenization, the solution becomes yellow. At the end of the mixing process, the mixture is blue luminescent under UV irradiation (365 nm). In contrast to the standard procedure, we did not dilute the obtained solution with iPrOH, but we directly diluted it in toluene (20:1 v/v) and recorded ABS and PL spectra. We did not proceed to the standard isolation protocol due the observed deep blue fluorescence. Such an emission hints at very small NCs we could not in any case isolate by centrifugation. After 5 and 15 minutes, we collected PL again. As it is possible to evaluate from Figure 1.21(a), the first exciton peak at about 445 nm is strongly blue-shifted and thus confined under the exciton Bohr radius and other populations are present and broaden it. The PL maximum is concordant around 464 nm: the most interesting thing is that it increases over time and red-shifts. This suggests evolution in sample according to a growth mechanism. To further slowdown this process and have a better insight, we decided to substitute PA with oleic acid (OA). We were aware that the use of a long acid ligand acts on NCs morphology, generally pushing them towards more 2D structure: this aspect was already investigated in previous literature[5765] and tested by ourselves in Section 1.5.5. Its use is also essential to further apply the procedure

Table 1.6 Comparison between main characteristics of different solvents employed in synthetic procedure.

Solvents	Boiling point (°C)	Viscosity (mPa s, 25 °C)	Dipole moment (D)
Heptane	98	0,4	0,0
Isopropanol	82,6	2,4	1,7
Hept/iPrOH 2:1		0,9	
Octadecene	315	4,1	0,4
Dowanol DPnP™	213	11,4	
ODE/Dow 2:1 with PA		2,2	
ODE/Dow 2:1 with OA		2,2	

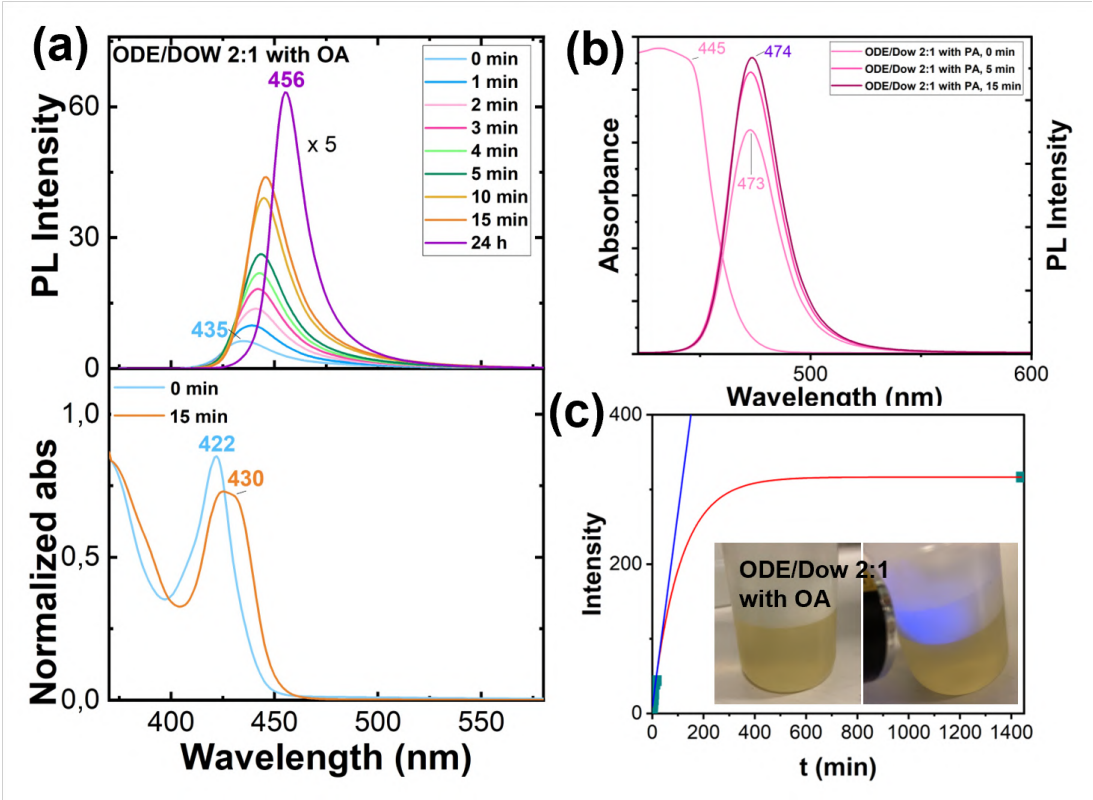

Figure 1.21 (a) Normalized ABS and PL spectra of samples obtained with ODE/Dow 2:1 and oleic acid as ligand, monitored for 24 hours (concentration: 0,1 mL of crude mixture in 2 mL of toluene, λ_{exc}= 350 nm). (b) Normalized ABS and PL spectra of samples obtained with ODE/Dow 2:1 and PA as ligand, monitored for 15 minutes (concentration: 0,1 mL of crude mixture in 2 mL of toluene, λ_{exc}= 350 nm). (c) PL intensity maximum as function of time: the overall trend is fitted with an exponential function, whereas starting values well fit with a linear function. In the inset, photographs of crude mixture obtained with ODE/Dow 2:1 and oleic acid under solar and UV (365 nm) illumination.

to temperatures higher than 100 °C(Section 1.5.4): PA is too low boiling (141 °C) respect to OA (360 °C). We checked viscosity again and the value was nearly unchanged with respect to the corresponding mixture containing PA. The synthesis was performed as above-mentioned. The resulting mixture is characterized by a pale yellow colouration and a very weak PL(Figure 16 (b)). We checked both absorption and PL of 0,1 mL of crude mixture in 2 mL of toluene every minute for 5 minutes, then at 10, 15 minutes and 24 hours for the latter (Figure 1.21(c)). The maximum PL value increases up to 5 times and red-shifts of 20 nm. Also, absorption red-shifts and broadens. This could be due to coalescence of crystal nuclei formed and then blocked in the reaction medium, make it possible by more efficient diffusion in a higher viscosity regime. If we plot the intensity as a function of time, the trend is well fitted by an exponential function:

$$I_{PLmax} = 316 - (308)e^{(-0,001)t}$$

$$R^2 = 0,999$$

where I_{PLmax} is the PL intensity maximum and t is time (min). This behaviour suggests that shortly after redispersion in toluene, these nuclei grow faster probably because they are abundant, then the process starts to slow down with their probability to meet until it reaches the new equilibrium. If this is the case, the nucleation could be slowed down by reaction medium viscosity and species get again to grow when the viscosity starts to

decrease. This means that the initial intensity increases with the shortest dimension growth, hypothesizing that no other defective process acts on the radiative pathway. The growth in dimension can be approximately correlated to medium viscosity by Stokes-Einstein equation

$$I_{PLmax} \propto L_{shortest-size} \propto \frac{k_B T}{6\pi\eta(t, miscibility, concentration)D} \tag{1.2}$$

where $L_{shortest-size}$ is the length of shortest side, k_B is Boltzmann constant (1,38 x $10^{-23} JK^{-1}$), T is temperature, $\eta(t, miscibility, concentration)$ is viscosity that depends on time, miscibility and relative concentration of two liquids and D is diffusion coefficient (it depends on object composition, shape, medium) . Given that we are dispersing a little quantity of our crude solution in a determined amount of toluene, the process will depend also on their miscibility and relative concentration too.

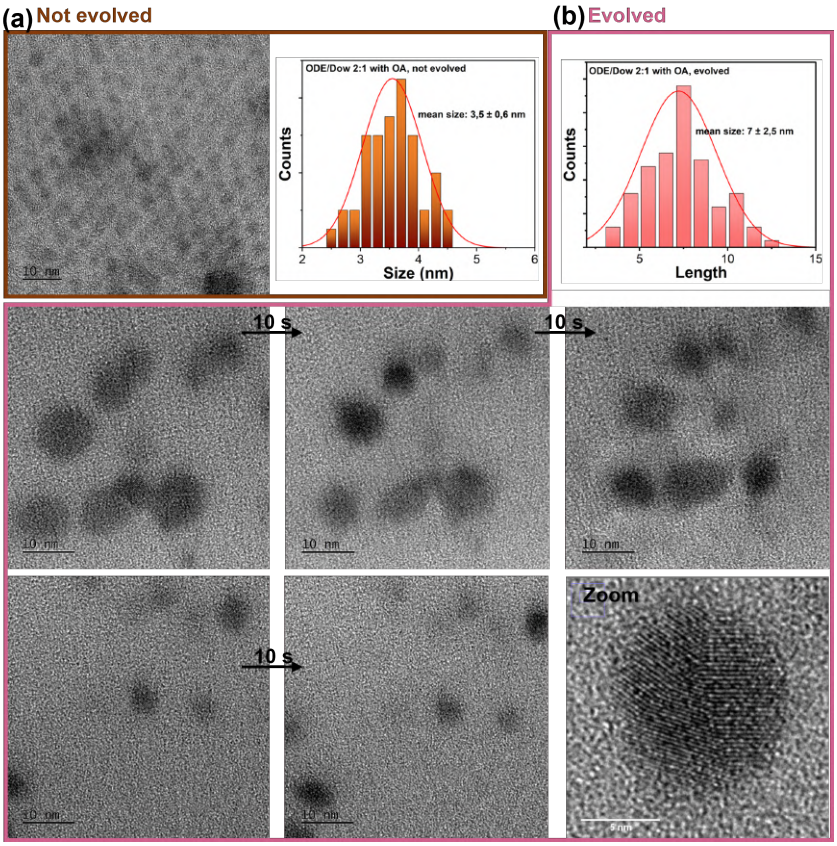

Figure 1.22 TEM images of (a) non-evolved sample and (b) evolved sample and their statistical analysis of dimensions. For the latter, images acquired after 10 s of electron beam irradiation and a zoom of a polycrystalline objects are reported.

To evaluate the initial and final species involved, we collected TEM images of the second sample and analysed the statistical distribution of size as redispersed in toluene (to facilitate deposition on TEM grid) and after some hours at the previously mentioned concentration. In the first case, a big amount of very small, spherical well-ordered objects (mean size around 3,5 ± 0,6 nm, concordant with obtained absorption edge) are clearly recognizable (Figure 1.22 (a)). In the second case, the dimension increases as expected (mean value around 7 ± 2,5, Figure 1.22 (b)), the shape becomes more irregular and so for the number of species and their distance. This distribution confirms our hypothesis about growth trend but it is not concordant with the ABS edge. The most interesting

aspect is that some of them are polycrystalline even if so small: in the zoomed TEM image three different crystalline orientations are observable but the lattice spacing, thus the exposed face, is the same (0,3 nm). This could explain the more blue-shifted experimental ABS. Moreover, the nano-objects seem to be particularly sensitive to the electron beam: if we expose them for 10 s and then other further 10 s, their morphology changes and in some cases, crystallinity increases (Figure 1.22, first and second case of images acquired at different and progressive exposure times). This phenomenon can be a consequence of local heat or solvent removal by the electron beam that act on the evolution too. In conclusion, reactions performed in a high viscosity medium lead to a precursor of the target PVK-NCs. All the reagents are there, as well and nucleation seed, but time is required to observe complete evolution towards the emissive phase. According to such features, we rechristened such materials as "latent" PVK, hinting at the features of thermally activable “latent” pigments.[71] Our results are of practical interest for the in situ synthesis of PVK-NCs in high viscosity medium like concentrated polymeric solution and even solution of polymers in the corresponding monomer, commonly employed in cell cast polymerization. We will elaborate on this point in the section dedicated to the use of the NCs in scintillation applications (section (1.8.2)).

1.5.4 Temperature

To make our synthetic procedure safe, easy to perform and scale up, we optimized it at RT. Nevertheless, we also evaluated the effect of temperature in the morphology and composition of the outcome material.

1.5.4.1 High temperature

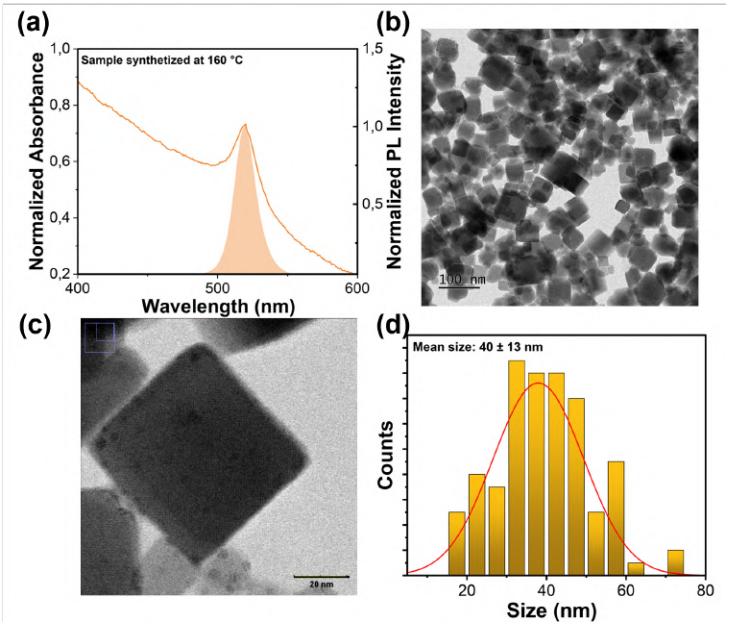

Figure 1.23 (a) Normalized ABS and PL spectra (concentration: 0,1 mL of toluene dispersion diluted with 2 mL of fresh toluene , λ_{exc}= 350 nm, 1 mm cuvette), TEM images at low (b) and (c) high magnification and (d) the derived statistical analysis of dimensions of samples obtained at 160 °C.

As aforementioned, one of the most diffused synthetic protocol for NCs production is hot-injection, performed at high temperatures (between 150 °C and 220 °C)[15] and with cuboids as general output. This morphology can be modified towards the preparation of nanoplatelets decreasing Cs/Pb molar ratio, increasing the amount of carboxylic ligand or lowering the reaction temperature[57]:[65] all these parameters act on thermodynamic stability of the different faces and their termination, favouring one growing direction with respect to another. Our low viscosity RT original procedure takes place in kinetically driven conditions (that only in a further evolution phase go towards thermodynamic equilibrium) and this aspect disadvantages the formation of cubes and favours polydispersity. We have already demonstrated (Section 1.5.3) that increased viscosity slows this phenomenon, producing more spherical objects. What about increasing the temperature? In this case, if we consider Stokes-Einstein equation, we are acting on the numerator and then boosting diffusion and dimensions. We maintained the solvents and acid ligand adaptations introduced in the previous section and reproduced the synthesis with the only difference of mixing the two solutions while they're heated at 160 °C with a silicone oil bath on a hot plate (60 mL scale). The mixture becomes immediately intense yellow, fluorescent and turbid. The addition of iPrOH triggers further precipitation and the solid is collected by centrifugation. It is not possible to completely dry the product because of the high boiling point solvents used: we were thus not able to evaluate the solid recovered amount nor the yield. We directly redispersed all the output in 20 mL of toluene and collected ABS,

PL spectra and TEM images. Figure 1.23(a) highlights that the sample highly scatters and the first exciton peak is compatible with bulk regime. It is surprisingly sharp, even if it's usually more common to see this in confined structures. The PL is perfectly resonant with ABS peak and with a FWHM of 18,5 nm. The TEM images and the derived analysis of dimensions distribution (Figure 1.23(b)-(d)) are comparable with the optical results: the output is composed by nanocubes with broad distribution of dimensions well above the bulk limit (40 ± 13 nm). In the high magnification TEM image (Figure 1.23 (c)), the lattice distance is around 0,5 nm, compatible with the cell length $\vec{a}$ in the cubic phase. The high polidispersity could be related to temperature profiles, a problem difficult to tackle even when using efficient mixing tools. We can thus conclude that our protocol is expandable also to high temperature conditions, where thermodynamic growth regime leads to the formation of cubic NCs.

1.5.4.2 Low temperature

Lowering the temperature close to the freezing point of the solvent mixture is an alternative method to slow down diffusion processes with respect to the use of more viscous solvents. Obviously, lowering the temperature has only a small impact on viscosity but strongly reduces solubility of all the species involved, results are thus not directly comparable with those obtained using the alternative solvent mixture. We performed the standard procedure without TBAB (to compare the output with Section 1.5.3 one) on a 60 mL caesium propionate in hept/iPrOH 2:1 maintained at 8 °C. The final mixture is clear and blue fluorescent. Since low boiling solvents allows to recover dried solid product, we reprecipitated with iPrOH addition and, after centrifugation step, 130 mg of dark green solid are obtained. ABS and PL spectra, at this level, are the only characterization performed.

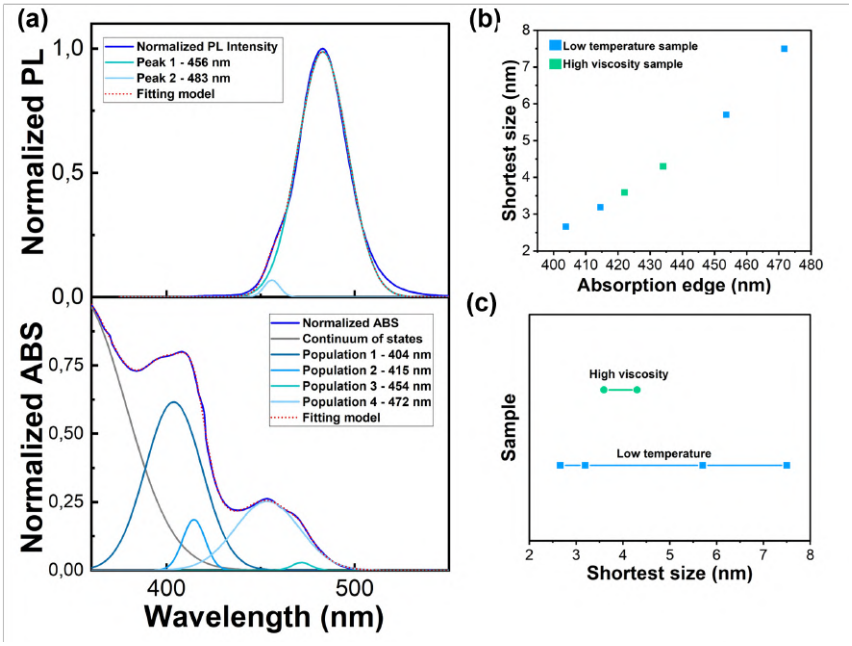

Figure 1.24 (a) Normalized ABS and PL spectra (0,1 mg/mL, λ_{exc}= 350 nm, 1 mm cuvette) both fitted with multiple gaussian functions with Fityk. (b) Expected size in function of ABS edge, derived from theoretical calculation reported by Diliberto et al.[34] and (c) the distribution of shortest sizes of different populations plotted in comparison for this low temperature synthesis (blue dots and line), the increased viscosity one reported in section 1.5.3 (green dots and line).

Both spectra clearly show different small populations involved: we fitted the profile with multiple gaussian functions with Fityk. Neglecting the gaussian that resembles the continuum of states with high energy, we obtained 4 different populations: only PL of the two less energetic ones is observable, as expected considering migration/reabsorption phenomena. If we exploit the theoretical calculation reported by Diliberto et al.[34] that correlates ABS edge (and thus energy gap) with monolayers number (already proven to be comparable with experimental value obtained from TEM images, sections 1.4 and 1.5.3) and multiply this value to the unit cell dimension of cubic phase (0,59 nm), we obtain that the output objects should have dimensions ranging from 2,7 to 7,5 nm. It is important to underline again that it's the shortest dimension to define confinement and thus characteristic spectral signature shifted respect to bulk value: this means that the sizes derived with this method could refer to the shortest length and do not define the others (unless the objects are cubes or spheres and we have demonstrated that except for isotropic viscosity or high temperature effect, this is not usually the case for our kinetic procedure). Comparing these values with the dimensions obtained with the high viscosity case by plotting the expected size as a function of ABS edge (respectively blue and green points and line), we can conclude that the synthesis with lowered temperature induces the formation of smaller but more polydisperse NCs. The heating effect of the high-shear features of turbo-emulsifier can be a possible explanation: temperature cannot be efficiently equalized over the relatively short characteristic time of the processes involved.

1.5.5 Acid ligand

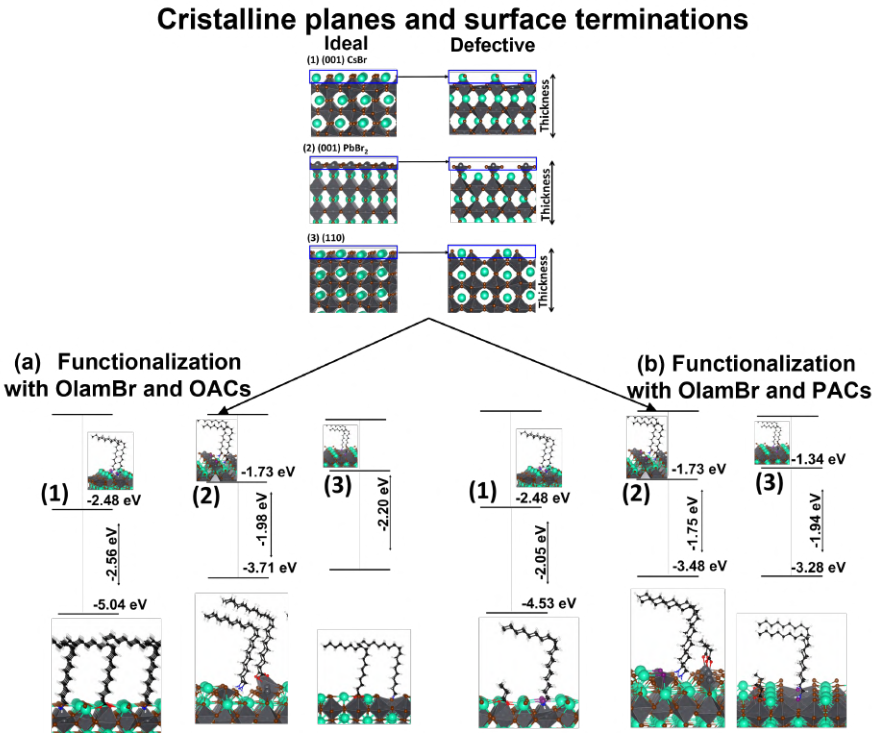

Figure 1.25 Descriptive image of the theoretical model empolyed for calculation. The authors considered from the orthorhombic γ phase of $CsPbBr_3$ defective termination CsBr and $PbBr_2$ of (001) and (110). They functionalized all of them with both oleylammonium bromide(OAmBr)/caesium propionate and OAmBr/caesium oleate and calculated the overall stabilization, here reported as separated contributions.

We developed the standard synthetic procedure (section 1.3) with a specific set of

ligands, OAm and PA: generally in literature species are chosen with the same alkyl chain length, or at least not so different. The most used ligand partner for OAm is in fact OA, already introduced in sections 1.5.3 and 1.23. We resolved thus to test the substitution of PA in standard synthesis with two completely different acids: OA and trifluoroacetic acid (TFA). The latter is a stronger acid with respect to the other mentioned and was employed in the literature works only post-synthesis[59] or in direct thin film formation.[72] In this last work, the authors exploit its uniform electron distribution that favours Pb^{2+} complexation to reduce grain boundaries. Regarding the former, as aforementioned in Section 1.5.4.1, it is reported in the state of art that its presence, especially when in slight excess respect to amine ligand, favours 2D NCs formation.[65] During synthesis, OA is present as oleate species that complex Cs^+ cation, while oleylammonium couples with bromide that was previously bonded to Pb^{2+}. It follows that OA^- actively participate in the formation and growth of CsBr terminated surface. It's demonstrated by computational calculation (carried out on the orthorhombic phase, but compatible with cubic phase too) that the most stabilized face and termination in presence of OA and OAm in 1:1 molar ratio is (001) CsBr terminated (Figure 1.25) (a)). This induces their preferred formation with respect to the others, pushing towards high surface area 2D nanoplatelets. They compared the stabilization effect of OAm/Pa 1:1 mol ratio too: the most stabilized termination is the same, although in a less pronounced way. Calculations involving TFA^- are still in program. Experimentally, we adapted the standard protocol to maintain the identical molar amount of acid in every synthesis. The reaction between caesium oleate and $PbBr_2$+TBAB in OAm/OA 1:1 mol ratio produced 100 mg of bright green-yellow solid that was further optically and morphologically characterized. Indeed, TFA/OAm 1:1 mol ratio mixture was not able to dissolve neither $PbBr_2$+TBAB nor $PbBr_2$ alone, even stirring at increased temperature for prolonged time. We resolved in use it in combination with PA 1:1 mol/mol and we managed to obtain complete dissolution and then the reaction (the product is from now now identified as "TFA sample" for brevity).

Figure 1.26(a) clearly shows that both samples are composed by 3-4 different sized populations. After deconvolution process with multiple gaussian functions, we can recognize that absorption spectrum goes from 416 to 460 nm for OA sample and from 435 to 480 nm for TFA one. Correlating the derived energy gap with size as previously done, the shortest dimensions vary in the first case from 3,3 nm to 6,3 and in the second between 4,4 and 8,6 nm. It is clear that OA sample is composed by more confined populations respect to TFA one, which is more similar to PA output (Figure 1.26 (b)). TEM images and their analysed distribution (Figure 1.26 (c) and (d)) place the shortest dimension in the former case at 2,6 $\pm$ 0,6 nm and in the second around 6 nm $\pm$ 3 nm: the values are perfectly comparable with expected ones. In particular, the NCs stabilized with OA deposit face to face and orthogonal to the TEM grid surface: they should be very thin also in the other dimensions because the contrast is very low. On the contrary, the samples stabilized with TFA are like to NCs obtained with PA but smaller and still very thin because also in this case the contrast is low. The distribution in dimensions is very broad both on the basis of ABS and TEM analyses and the comparison of the results from the former between all the three sample suggests that polydispersity is slightly higher for PA. In conclusion, as expected OA is the acid that induces formation of thinner species and TFA, because being used in 50 % molar mixture with PA, modifies marginally the distribution, only slightly pushing it towards decreased dimensions. Polydispersity continues to be a characteristic of all conditions.

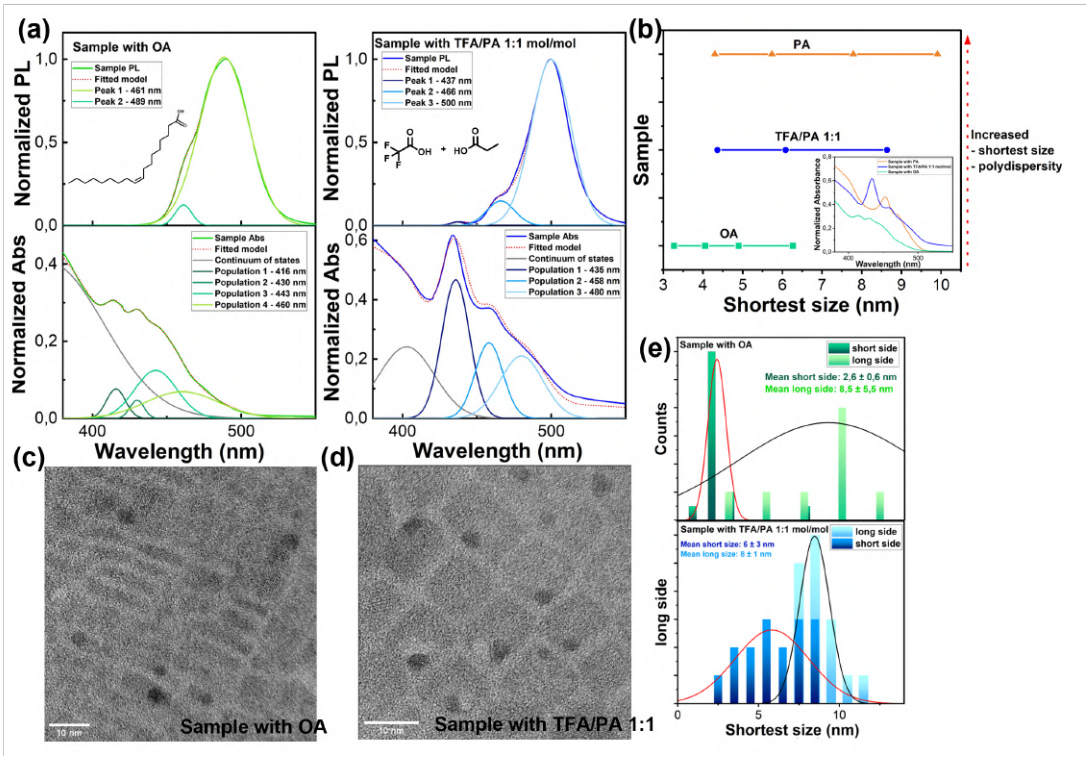

Figure 1.26 (a) Normalized ABS and PL spectra, deconvolved with multiple gaussian functions of both sample with OA and TFA/PA 1:1 mol ratio. (b) Graphical comparison of the shortest sizes of different populations present in samples obtained with OA, TFA/PA 1:1 mol/mol and PA. TEM images of (c) OA and (d) TFA/PA 1:1 mol/mol samples and (e) the derived statistical analysis of dimensions.

1.5.6 Amine ligand

To complete this systematic study, we evaluated the possibility of expanding the library of amines as well. We analysed the compatibility of our synthetic approach with BuAm, in the production of both $CsPbBr_3$ and $CsPbCl_3$ nanocrystals. Thanks to the short alkyl chain, this ligand is preferred in device application requiring good charge transport capabilities.[39] The standard procedure is repeated in the usual way, only changing the mixture employed in lead containing solution with BuAm/PA 1:1 mol/mol. The salts dissolve well. After the injection step, the mixture becomes immediately turbid, even in the chloride case: the short chains of both ligands give poor colloidal stability, enhancing the precipitation from the reaction medium. For $CsPbBr_3$, the scale was 120 mL. 30 mL were separated and further reprecipitated with iPrOH, the remaining 90 mL were not, to evaluate if there's any difference in the amount of recovered material. After centrifugation and drying process, we recovered in both cases colourless and clear supernatants and respectively 91 mg and 220 mg, a total amount of 311 mg. Considering that the first value should be 1/3 of the second, we can conclude that iPrOH still helps a bit. The overall value is higher than the one obtained for the same scale with OAm (230 mg), suggesting, as expected, that recovery of solid material is easier when colloidal stability is poor. The difference in supernatant luminescence (only slightly luminescent with BuAm and strongly blue luminescent with OAm) confirms this speculation: in the latter, too small species are particularly well dispersed to be precipitated by the employed amount of iPrOH. However, an excessive amount of polar solvent can be detrimental for the NCs, thus a trade-off is needed. For BuAm-$CsPbBr_3$, we employed 60 mL scale and added iPrOH to the whole reaction mixture. We considered that this case has a lower kinetic and desired to evaluate

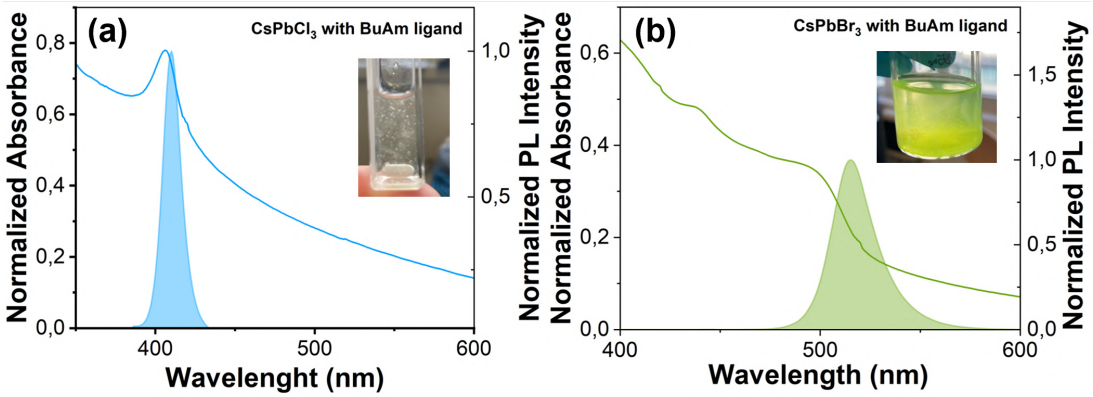

Figure 1.27 Normalized absorbance and pholuminescence spectra (0,1 mg/mL in tolene, λ_{exc} 350 and 365 nm respectively)and sample photograph (in the inset) of respectively (a) BuAm-$CsPbCl_3$ and (b) BuAm-$CsPbBr_3$.

if in these conditions was possible to recover all the output material without waiting for 24 hours. We recovered immediately after synthesis 110 mg, nearly twice as much than the 68 mg obtained after 24 hours with OAm. Unfortunately (but rather predictably), the redispersion of the BuAM-stabilized NCs in toluene was inefficient. This aspect led to poor-quality steady states optical characterizations. Figure 1.27 displays sample photographs in the insets, where it is distinctly recognizable the dispersed powder. Both ABS edges are red-shifted with respect to OAm samples, unveiling that the NCs dimensions are increased and the polydispersity is reduced: probably in solution instability quickens the growth, suppressing "parasite" processes that also broaden the dimensions distribution. In conclusion, these specific materials are surely interesting for device application as active material with request charge separation, even if the ink formation is challenging. Moreover, the success expanded once again our procedure playground, confirming its consistency also for different, and why not, designed amines.

1.6 Post-synthetic treatments

Having thoroughly characterized the synthetic process, we explored the possibility to influence the composition of the NCs by post synthesis elaboration. This approach is well documented in the literature as a way to access materials that cannot be directly prepared with ease. Generally, the most diffused are ligand exchange,[59] halogen exchange,[73] sometimes cation Cs exchange[74] and treatments with salts that heal defectiveness[22] (as already reported for $CsPbCl_3$ with $CdCl_2$ in Section 1.5.2.1). Post synthesis modification further enhance the already vast potentialities of hybrid perovskite materials in optoelectronics applications.

1.6.1 Halogen exchange

Between all the possibilities, we drove our attention to iodide exchange because we didn't manage to obtain the desired phase with direct synthesis. We employed the material that was closer to the target one and on which we were more confident, $CsPbBr_3$ NBs. We exploited the well-known soft ionic nature of these materials that makes this process easier with respect to the other ionic salts renowned for optoelectornics: this exchange happens fast around the surfaces and re-equilibrate inside the crystalline structure spontaneously.

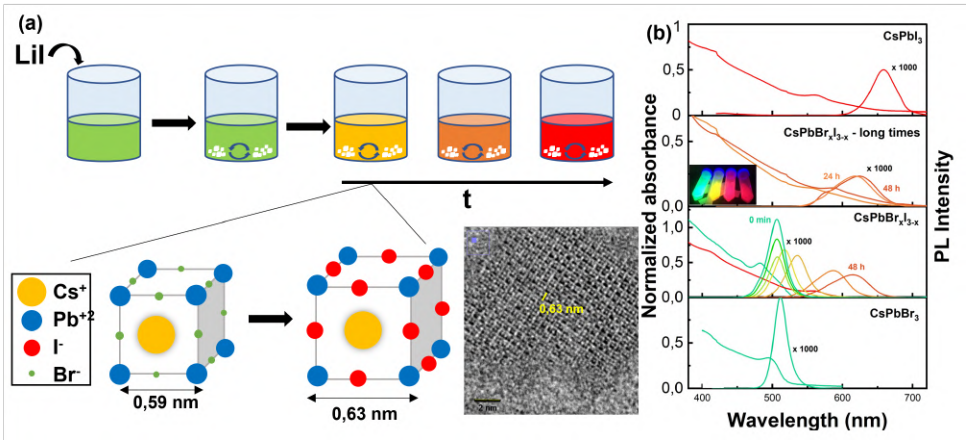

Figure 1.28 (a) Schematic picture of the anion exchange procedure employed: a specific amount of LiI salt was directly added to a toluene $CsPbBr_3$ dispersion (5 mg/mL) and put under magnetic stirring. The "doping" takes place over the time until the new equilibrium is reached. The unit cell (represented for cubic phase for simplicity) rearranges from the smaller bromide ($\vec{a}$=0,59 nm) to the bigger iodide one ($\vec{a}$=0,63 nm), as underlined in the TEM image of our samples. (b) Normalized ABS and PL Intensity spectra of evolved $CsPbBr_3$, exchanged sample 1 from the beginning (pristine $CsPbBr_3$) to the end of the process, exchanged sample 2 at longer times and $CsPbI_3$ (from bottom to top).

The amount of halogens (and thus the final optical properties) can be finely tuned with the concentration of the added salt. We exploited LiI: some works report a beneficial effect also from lithium possible intercalation.[75] Considering that $CsPbI_3$ NCs are the less stable of the three, we paid particular attention to moisture: LiI is slightly hygroscopic so it was previously dehydrated by heating it under vacuum with direct flame (Bunsen burner) until melting and then cooled down to RT under nitrogen atmosphere. The exchange was carried out in an anhydrous round-bottom flask with 10 mg of $CsPbBr_3$ NCs in 2 mL of anhydrous toluene (1 mg/mL), where LiI were added under nitrogen positive flux under magnetic stirring. We initially tested exchange in an homogeneous medium, previously dissolving LiI in a polar solvent (iPrOH) and then adding the solution to NCS toluene dispersion. This method improves solubility and mixing of reacting species but negatively impacts on the crystalline structure of the perovskite because of the solubilizing effect of iPrOH. As a result, stability is severely compromised. We thus resolved perform the halogen exchange under heterogeneous conditions. LiI salt doesn't dissolve in toluene and the exchange takes place only at its interface. This phenomenon is clearly observable because the white disperse powder starts to develop an outer reddish coloration due to deposition of NCs on the surface. This protocol requires longer reaction times to reach equilibration of halogens present in the reaction mixture due to sizeable diffusion barriers. It should be noted that the tendency of our colloidal NCs to evolve while in dispersion in a given solvent could be helpful in promoting efficient heterogeneous phase doping. We monitored the process via ABS and PL (Figure 1.28 (b)). The PL begins immediately to represent the low energy gap species quickly red-shifting and then slows down. In the second and third stacked layer from the top, we can see that the process is faster at the beginning, precisely when also growth takes place rearranging material, then completes in 48 hours with the final product. In zoomed TEM image

Figure 1.29 Photographs of $CsPbBr_3$ NCs samples doped with LiI and $SnCl_2$ under solar (up) and UV (bottom) illumination.

(Figure 1.28 (a)) the high resolution allows us to measure the interatomic distance between two rows of atom at the same height (we can discriminate a row beneath) and it is 0,63 nm, compatible with the cubic iodide phase. With centrifugation, the remained salt can be removed and the NCs are ready to be used. Moreover, tuning the amount of LiI added, we were able to get various $CsPbBr_xI_{3-x}$ concentration, as can be seen in the inset picture in Figure 1.28 (b). In conclusion, even if we could not directly prepare $CsPbI_3$ NCs with our colloidal procedure, we managed to access the very same structure by post synthesis halogen exchange. We also demonstrated our capability to perform post synthesis transformation of $CsPbBr_3$ in $CsPbCl_3$, in this case $SnCl_3$ as the halogen source (Figure 1.29).

1.7 Waste recovery

In light of the ongoing quest for higher lab-scale quantities, research focus is shifting to thus far overlooked aspects like industrial upscaling and environmental sustainability that are key for future effective large-scale exploitation of these materials. In fact, the first prominent advantage in comparison with other polycrystalline film technologies for opto-electronics is that PVK films are compatible with printing approaches on a wide range of substrates and are composed of earth-abundant materials. Easy colloidal PVK formulation enables easier solution processing from greener and low boiling solvents. Indeed, the wet syntheses of NCs commonly require relatively dilute conditions, surplus reagents and do not lead to the target material with a 100% efficiency. The up-scaling goal was already achieved with the introduction of the turbo-emulsifier, as deeply explained in Section 1.5.1, reaching the unprecedented and pre-industrial scale of 3,6 L (8 g of output solid). Nevertheless, we haven't yet dealt with the sustainability issue. Considering a mass balance between materials involved in synthesis and the product obtained, it is evident that the process produces significant amount of waste (Figure 1.30). In principle, most of such material could be reprocessed and reused. Pioneering works dealing with this issues recently started to appear[5576,77] but it remains essentially an almost unexplored and underestimated field.

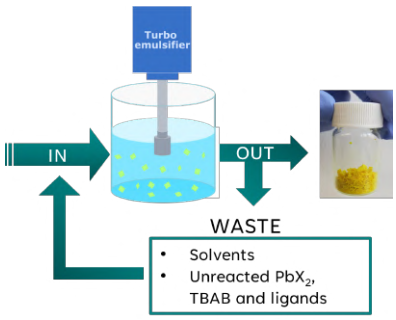

Figure 1.30 Schematic representation of the "circular" synthetic process, that takes advantage of wastes reuse, mainly composed by solvents and unreacted species.

1.7.1 Supernatant mixture characterization

Synthesis involves formation of three different kind of waste: solvents, excess ligands, and unreacted precursors. They all end up in the supernatant after isolation of the solid product by centrifugation. The procedure we developed in this work requires solvents having low boiling point and high volatility thus making recovery by distillation easy and energy efficient. The dried residue contains a mixture of precursors and ligands we were also interested in recycling. Aiming at quantitative evaluation, we tested the recovery procedure on a reaction batch of 240 mL with the standard procedure and deeply characterized the various part: the final goal is to correctly reuse them performing the synthetic procedure with the minimum amount of fresh reactants and establishing a cyclic process in light of a zero-waste approach. We obtained 512 mg of $CsPbBr_3$ NCs and limpid

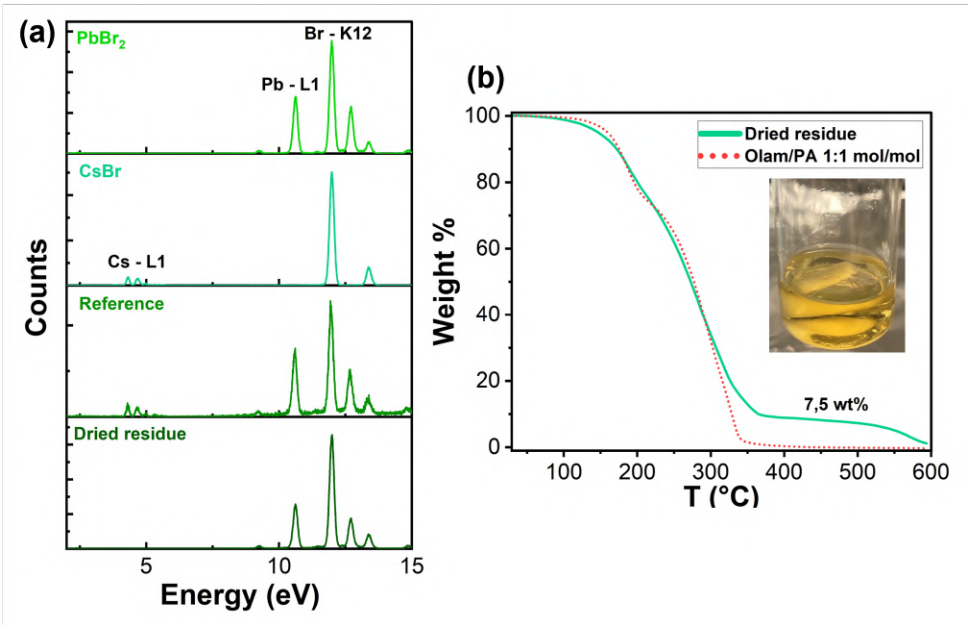

Figure 1.31 (a) X-ray fluorescence (XRF) spectra of dried residue, reference sample composed by weighted $CsCo_3$ and $PbBr_2$ in OAm/PA 1:1 mol/mol, CsBr and $PbBr_2$. (b) TGA of the dried residue respect to ligands mixture and the photograph in the inset.

Table 1.7 Total amount of employed and recovered amount of different species.

Species	Amount	Total amount	Recovered amount
Solid reactants	2, 9 g	15, 6 g	$16,5^{g}$
Ligands	12, 6 g		
Solvents	363 mL	363 mL	354 mL

yellow fluorescent supernatant. The solvents were distilled under reduced pressure and we ended up with 360 mL volume. Heptane and iPrOH form an azeotrope with relative concentration of respectively 46:56 v/v and boiling point of 76,4 °C: we obtained 344 mL with azeotrope concentration (158 mL of Hept and 186 mL of iPrOH) and 15 mL of pure iPrOH from distillation. The recovered solvents contain thus Hept/iPrOH 1:1,26 volume ratio. We analysed this mixture with gas chromatograph-mass spectrometer (GC-MS) to exclude presence of any contaminant and we confirmed that, after this easy recovery treatment, they are ready to be employed again. The dried residue is 15,7 mL of yellow viscous liquid (16 g, d = 1,02 g/mL) where a white fluorescent solid tends to precipitate after prolonged times (some days). It becomes again homogeneous if heated at 80 °C under magnetic stirring for 15 minutes. As all the OAm mixture, it's better to keep it protected from light, because its UV component leads to OAm impurities degradation that make it brownish. We speculate that this mixture is composed by unreacted lead bromide and TBAB residues, excess ligands and a fraction of $CsPbBr_3$ NCs too small to be recovered by centrifugation. Thus, to reuse it in a controlled synthetic procedure, we carefully characterized its composition with X-ray fluorescence (XRF), inductively coupled plasma - optical emission spectroscopy (ICP-OES) and TGA. The former was performed to have a qualitative confirmation of the presence of both lead and caesium. The homogeneous mixture was drop casted over a teflon flat surface (material transparent to X-rays) and the obtained spectrum analysed in comparison with the references $CsCO_3$ and $PbBr_2$ at a known concentration dispersed in the same mixture of OLAM/PA 1:1

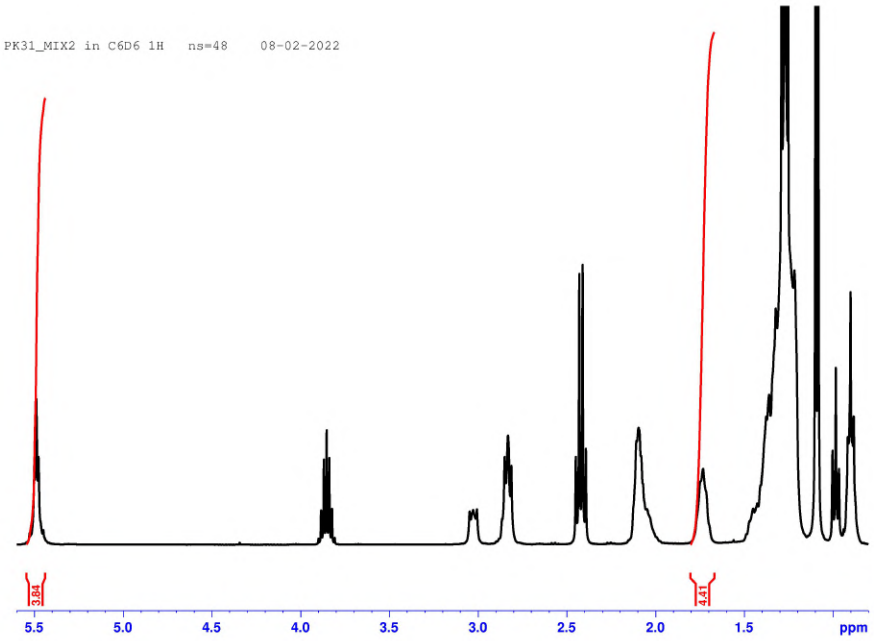

Figure 1.32 (a) ^1H NMR in C_6D_6 of the dried residue: the integrated peaks at 5,5 ppm and 1,7 ppm are respectively of OAm ($-CH{=}CH-$) and PA ($-CH_2-$), in molar ratio of 1:0,9.(b) TGA of the same sample.

mol/mol and CsBr and $PbBr_2$ powders: the two atoms have in fact a very different X-rays absorption cross section and also the viscous medium can affect the X-ray travel. Way far from being quantitative, we wanted to test reliability of the signals. From Figure 1.31 (a) we can observe that lead is surely present, indeed the caesium amount seems to be too low to be detected: it has in fact a very weak X-ray absorption cross section. Luckily, ICP-OES has a very high sensitivity (detection limit for both Pb and Cs is 0,01 mg/mL) and helped us. The analysis revealed a consistent 2,25 wt% of lead and 0,04 wt% of caesium in two different dried residues examined (derived from diverse scales - respectively 240 mL and 3,6 L). It means that the 2,3 wt% of the recovered mixture is composed by lead and caesium: the TGA reports a 500 °C residue of 7,5% that, considering the presence of bromide as counterion (not detectable with our ICP-OES), TBAB salt and some degraded ligands chains, can be considered consistent with ICP-OES data. For determination of OLAM and PA amount present in the mixture, we considered firstly the relative intensity of diagnostic peaks in ^1H NMR in C_6D_6 of the dried residue: the ratio between the integral of 5,5 ppm peak (OLAM protons on double bond) and 1,7 ppm one ($-CH_2-$ of PA) is respectively 1:0,9. PA should be in form of salt but if it assumes the free acid form, its boiling point is low (141 °C) and can be partially evaporated in some passages. Considering that TGA estimates the content of organic compounds in the residue at around 92,5 wt%, we were able combining all the information to give a good account of all the components there present. About TBAB, the NMR signals are too broadened (due to the difficult relaxation of its sterically hindered form) or superimposed to others to be able to use them quantitatively. We can only hypothesize that the amount of TBAB effectively incorporated over the NCs surface is negligible and that it is all present in the residue (7 wt%).

Table 1.8 Amount of different species introduced in reference sample, derived from recovered material and added to perform again the reaction on 120 mL scale.

Species	Reference	Recovered	Addition
Pb	414, 4 mg	142 mg	483 mg
Cs	53, 2 mg	2, 5 mg	51, 8 mg
Hept	80 mL	37, 8 mL	51 mL
iPrOH	40 + 60 mL	37, 8 mL	0, 9 + 60 mL
OLAM	5, 9 mL	3, 6 mL	1, 1 mL
PA	1, 7 mL	1, 4 mL	0, 2 mL
TBAB	644 mg	441 mg?	205 mg

1.7.2 Synthesis with recovered reactants

Once evaluated the amount of reactants present in the dried residue and the relative concentration of hept and iPrOH in the mixture of solvents, we adapted the synthetic procedure in order to add the minimum amount of fresh materials and successfully obtain $CsPbBr_3$ NCs again. We selected 120 mL scale and thus needed 8,4 mL of OAm/PA/iPrOH mixture. We decided to employ 6,6 mL of dried residue (6,3 g): from ICP-OES results it contains already 142 mg of lead (2,25 wt%, 0,68 mmol) and 2,5 mg of caesium (0,04 wt%, 0,019 mmol). We thus added only 483 mg of $PbBr_2$ (1,3 mmol), respect to 734 mg and 2 mmol) and 205 mg of TBAB (0,6 mmol, respect to 644 mg and 2 mmol) , 0,9 mL of iPrOH and the remaining volume of OAm (1,1 mL). Heating under magnetic stirring at 80 °C as previously done, makes the mixture completely clear even when cooled at room temperature, with a slight blue luminescence (derived from the fact that in this case, caesium is already present). Solution A was obtained by diluting 70 mL of recovered solvent mixture (composed by 32,2 mL of hept and 37,8 mL of iPrOH) with 51 mL of fresh hept (57,5 % volume recovered) to reach again the desired hept/iPrOH volume ratio of 2:1. 61,9 mg of Cs_2Co_3 (0,18 mol respect to 0,2 mol) was dissolved in 0,2 mL of PA and then added. After injection of solution B into solution A under turbo-emulsification, the mixture becomes immediately yellow and then turbid, differently from standard procedure. The first solid was centrifuged (sample A, 272 mg) and then the supernatant further reprecipitated with 60 mL of iPrOH and centrifuged again (sample B, 20 mg). From Figure 1.34 (a), we deduce that both samples are very similar to the NCs obtained with the standard procedure (reference sample), indeed sample A has a more bulk-like profile and sample B has a thinner population that absorb at about 440 nm (energy gap 2,8 eV, around 5 nm of shortest expected size). Sample A features bigger crystals and, coherently, a slightly worse colloidal stability. TEM images, TGA and XRD pattern refer to sample A: the mean shortest dimension (Figure 1.34(b) and (c)) is bigger and broaden respect to the reference sample and more like to the evolved species respect to pristine one, even if the NCs where just redispersed in toluene (0,1 mg/mL). XRD peaks full width at half maximum (Figure 1.34(e)) confirms the increased dimension but the phase is retained. From TGA (1.34(d)), the amount of material that

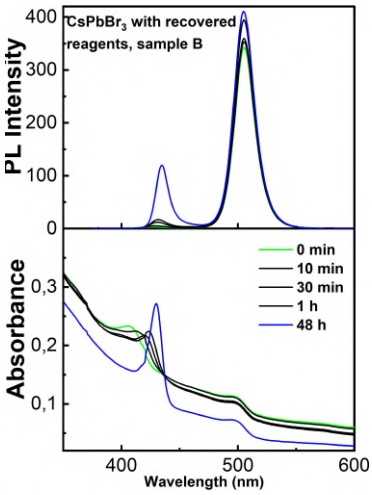

Figure 1.33 ABS and PL spectra of $CsPbBr_3$ NCs obtained with recovered reagents (sample B) over time (concentration in toluene: 0,1 mg/mL, λ_{exc}= 365 nm).

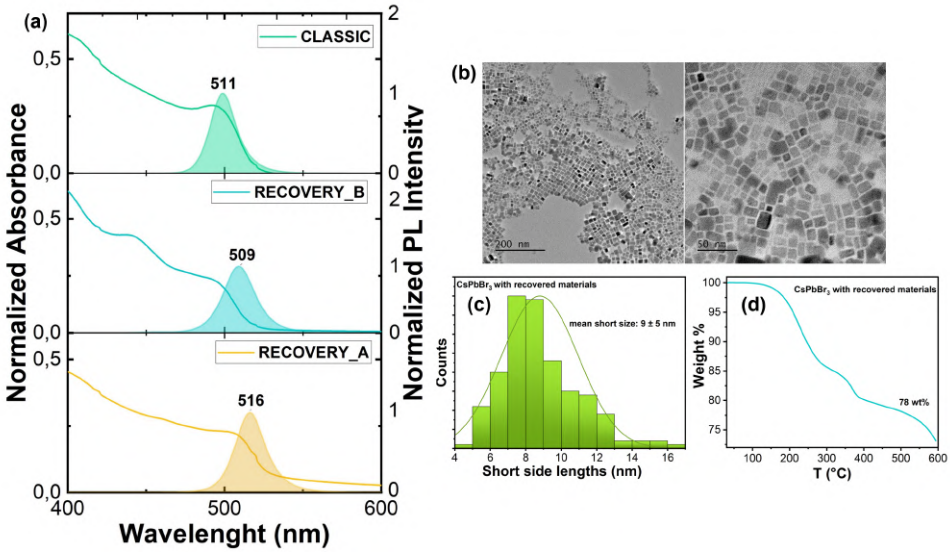

Figure 1.34 (a) Normalized ABS and PL spectra of $CsPbBr_3$ NCs produced with standard procedure and with recovered reactants (sample A from first centrifugation and B from second one) respectively from top to bottom. (b) TEM images at different magnification, (c) statistical analysis of the shortest dimension, (d) TGA and (e) PXRD patterns compared with classical of $CsPbBr_3$ NCs produced with recovered reactants (sample A).

degrades before 490 °C is compatible with the reference sample, probably a bit lower (22 wt%, coherent with bigger dimensions). Sample A doesn't show any evolution of optical properties in time: when it reprecipitates by itself, it is already in its thermodynamically more stable form. For sample B, the story is different: its recovery is induced by addition of iPrOH, as for reference material. When diluted in toluene at the standard concentration of 0,1 mg/mL, it starts to evolve over the time (Figure 1.33): in particular, differently for reference output, the scattering tail decreases and the bulk-like population at 500 nm remains unvaried. The clusters that absorb at 408 nm (around 3 nm of shortest expected dimension), in 48 hours coalesce to give an intense absorption peak at 430 nm (compatible with species with expected shortest size of 4 nm). The PL peak at 434 nm increases along with it, even if blueshifted with respect to the 505 nm one. This suggests that the former emitting population is very copious to avoid reabsorption and migration of excitation. The recovered amount with this behaviour is really poor (only 20 mg) but it is anyway interesting: we can hypothesize that with this synthesis almost all the material precipitates by itself in form of already evolved and thermodynamically stable NCs and only a slight amount is collected in form of small cluster under exciton Bohr's radius. This could mean that with recovered materials, the species are already equilibrated and the encounter and growth happen faster. We have in mind to surely deepen this intriguing aspect. In any case, we successfully demonstrated that using the recovered unreacted species to perform again the NCs synthesis is possible, and the result is consistent in terms of quality and possibly even better in terms of reaction time with respect to the protocol performed starting from fresh reagents. In principle, after this synthesis the supernatant can be recovered again as well.

1.8 Applications

Alongside with very significant findings in terms of fundamental science, lead halide perovskites have also found very relevant practical applications in very diverse research fields, as already mentioned in the introduction. From lasers[24] to photocatalysis,[28] their tuneable properties seem to be adaptable to almost every applications of interest. So far, we explored the performance of our materials in two applications - solar cells and scintillator X-ray detectors - but activities in the development of luminescent solar collectors and OLEDS are planned. The remarkable shelf-life of our perovskite inks represents a further valuable asset for printing applications.

1.8.1 Solar cells

The main application field of PVK materials is solar cells. The impact that such materials had (and still have) on the field is so big that the association of the two terms perovskite and solar cells, is almost automatic (see introduction 1.1.1). We thus tested our colloidal inks in the manufacturing of such devices even if the main material we developed - $CsPbBr_3$ NCs - are renowned to have a relatively large energy gap making their use not perfectly suited, at least for outdoor applications (2,4 eV respect to 1,2 eV of intrinsic silicon,[78] 1,6 eV for $MAPbI_3$[17] and 1,9 eV for $CsPbI_3$,[15] Figure 1.35). This means that they are not able to absorb a consistent part of the solar spectrum, decreasing their performance. They are however suitable for indoor or multijunction application. In principle, our inks are attractive for printing manufacturing and thus particularly for large scale applications where spin coating cannot be applied. Yet, according to the need for colloidal stability, our inks contain a relatively large amount of insulating capping ligand (OAm) that could cause high electric resistance and thus poor photocurrents harvesting. Nevertheless, we decided to preliminary test our material anyway in outdoor PSCs, simultaneously addressing our attention to indoor application that has, as primary target, active layers with higher energy gaps (depending on the different shape of indoor LED lamps spectrum). The information gained as proof of concept will be useful milestones in developing crystalline phases and ligands more suitable for such particular device applications. The investigations performed in Section 1.4.3 on spin coating deposition velocities, effect of increasing annealing time on fixed number of layers and vice versa (Figure 1.14) helped us to select the best deposition and annealing conditions to form a suitable active layer. All devices preparation and measurements were performed at CHOSE (Polo solare organico della regione Lazio), affiliated with the University of Rome-Tor Vergata. The device layered structure is engineered as follow:

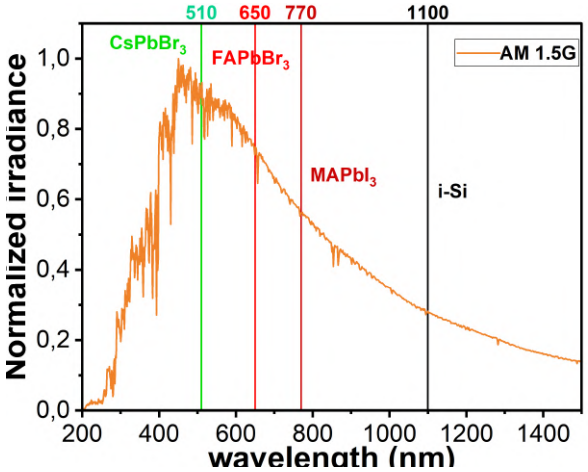

Figure 1.35 Sun normalized irradiance at AM 1.5G (orange curve) with straight vertical lines in correspondence of absorption edges of materials employed as active layers in SCs: $CsPbBr_3$ (green line, 510 nm, 2,4 eV), $FAPbBr_3$ (red line, 650 nm, 1,9 eV), $MAPbI_3$ (dark red line, 770 nm, 1,6 eV) and intrinsic silicon (balck line, 1100 nm, 1,2 eV).

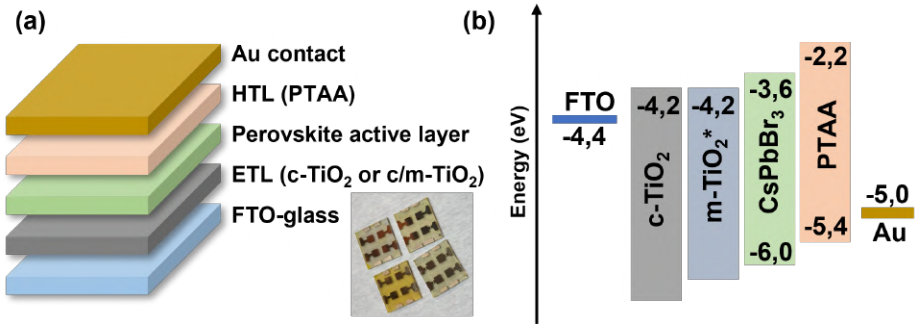

Figure 1.36 (a) The device layered structure expanded (with a photograph in the inset) and (b) the energy levels of the different parts (PTAA literature levels[79]). m-TiO_2 is signed with a star because it is not present in every sample.

1. glass + FTO: in this case, glass employed is thicker (around 2 mm) to bear higher annealing temperature necessary to dope classic ITO with fluorine. Total area: 2,5 cm x 2,5 cm.

2. Back contacts made with Ag paste.

3. Compact-TiO_2 (c-Tio_2)electron transport layer (ETL)and possible further mesoporous-TiO_2 (m-TiO_2) layer deposited by spin coating. For both cases, UV-curing passage (10 min under 400/420 nm irradiation) is needed.

4. Perovskite active layer, either deposited by spin coating, drop casting (our $CsPbBr_3$ NPs) or in-situ crystallized (reference $CsPbBr_3$ and $FAPbBr_3$ polycrystalline samples).

5. PTAA (polytriarylamine) polymer as hole transport layer (HTL), deposited with spin coating from a toluene solution (10 mg/mL, 1 layer).

6. Au contacts, deposited via evaporation with suitable masks (around 100 nm thick).

7. Ag paste.

Our NPs active layer was deposited in glove box (under nitrogen atmosphere) either by spin coating (2000 RPM for 45 s) or drop casting of 10 mg/mL toluene solution. After each layer deposition, an annealing step of 2 minute over a 90 °C hot plate is performed (to evaporate the solvent) and the final annealing lasted 4 minutes (to "sinter" the NPs). We produced devices with 3, 5 and 7 active layers both with only c-TiO_2 and with further m-TiO_2 deposition over the whole surface. Every device presents 4 cells (Figure 1.36(a) in the inset, referred to as A,B,C and D) and it is designed with a code (a number followed by a letter, i.e. 25W), to be uniquely recognizable. We also considered reference devices with in-situ crystallized $CsPbBr_3$ and $FAPbBr_3$ and the same with 1 further layer of our NPs to evaluate their effect on performances. Every device is produced identically twice for statistical purpose. The characterization consisted in J-V measurements under Air Mass 1.5 Global (AM 1.5G) irradiance. Firstly, we wanted to elucidate which type of TiO_2 ETL suits best for our active material. Figure 1.37(a) shows that with the contribution of mesoporous-TiO_2 the short circuit photocurrent (J_{sc}) is higher for every number of layers. The open circuit voltage (V_{oc}) is instead within the same range: it is more related to the energy levels and thus to the nature of material itself. This trend suggest that, with the mesoporous ETL, there is more collection of charges. It can be due to a better

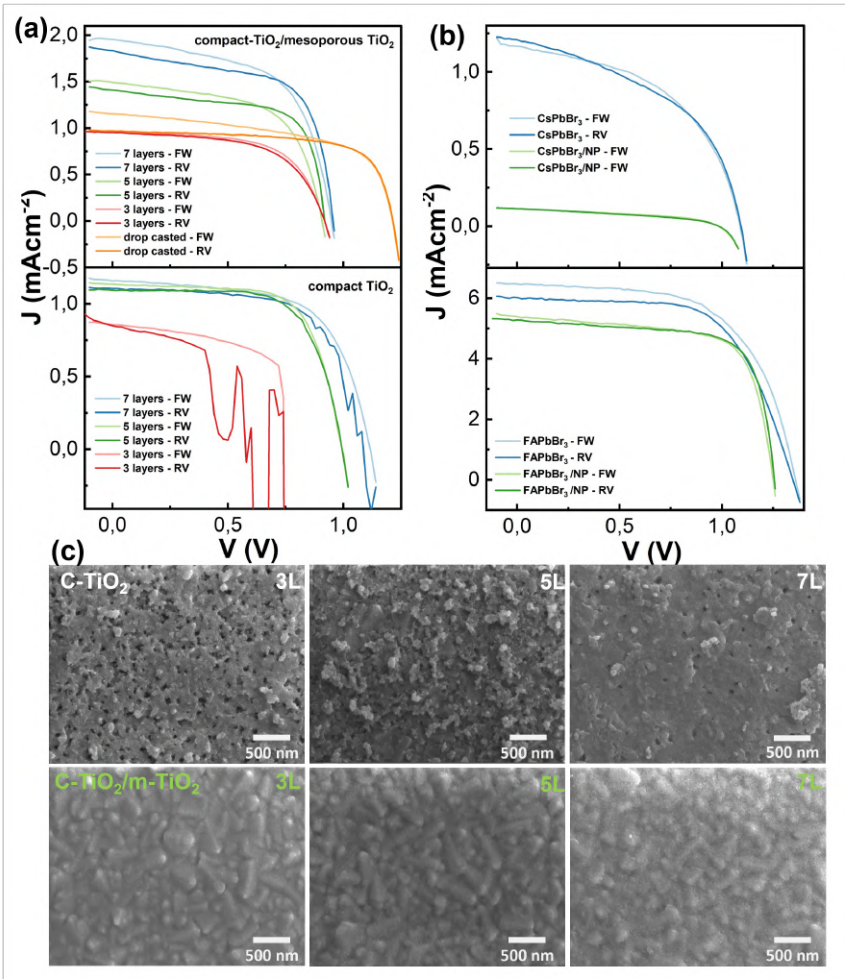

Figure 1.37 Best photocurrent density in function of voltage curves under 1 sun irradiation of (a) 3, 5, 7 layers and drop casted NPs with c-TiO_2 + m-TiO_2 (top) and only c-TiO_2 (bottom) and (b) reference samples ($CsPbBr_3$ (top) and $FaPbBr_3$ (bottom) polycristalline) alone and with 1 layer of our NPs). (c) SEM images of respectively 3,5,7 layers of NPs deposited over c-TiO_2 (top) and c-TiO_2/m-TiO_2(bottom).

interpenetration of NPs with the substrate: the nanometric form could be particularly compatible with small roughness. Looking at SEM images of the two different architectures (Figure 1.37(c)), this hypothesis seems coherent: the layers have a more smoother surface, probably because their accommodation is favoured. Looking at different layers deposition, the (J_{sc}) increases with the number of layers, as expected along with the optical density (proportional to the quantity of active material). For the devices made with compact TiO_2 alone, there is almost no dependency between number of depositions and current, but the V_{oc} is generally larger than in the case of the mesoporous TiO_2. Based on I-V curves alone, it is not possible to drive definite conclusions on the different behaviour of the two ETL, yet it seems reasonable to conclude that compact TiO_2 enables more favorable level alignment (and thus higherV_{oc}) at the cost of the amount of active material deposited. This does not necessarily mean that the absorbing layer is thinner but that the presence of the large OAm ligand prevents the bulk of the layer from displaying any useful photocurrent. Interestingly, the FF of the devices reaches values as high as 70 %, meaning that the material shows a good diode behaviour. The resulting power conversion efficiency (PCE), defined as

$$Efficiency(\eta) = \frac{FillFactor(FF) \cdot V_{oc} \cdot J_{sc}}{IncomingPower(P_{in})} \tag{1.3}$$

is all cases very low (Table 1.9, from 0,4 to 1,1 %), with best result under 1 sun irradiation obtained by depositing by spin coating 7 layers of NPs over m-TiO_2. Considering the reference samples, in-situ $CsPbBr_3$ polycrystalline are produced by dissolving $PbBr_2$ and CsBr (respectively 734 mg and 30 mg) in 2 mL of dimethylsulfoxide (DMSO) overnight and then spin-coating the solution, following this step with a specific annealing treatment that induces crystallization of precursors. The performance of this material on the previously selected as more efficient ETL are poorer with respect to our best combination: V_{oc} is similar because the chemical nature is the same but J_{sc} and FF (and consequently efficiency) are lower (Table 1.9). When a layer of NPs is spin coated over it, V_{oc} remains unvaried as expected but J_{sc} falls critically down: the presence of OAm is the more likely responsible. Moreover, the fact that deposited NPs dispersion is in toluene can partially dissolved/damage the underlying layer. This phenomenon can also happen to our NPS themselves when the HTL (in toluene) is deposited. Further optimization in selection of more suitable orthogonal solvents is required. In order to get a direct comparison of the performances of the colloidal material, we tested using the same device structure a layer of $FAPbBr_3$ PVK grown with a standard in situ crystallization procedure. The J_{sc} we measured is as expected much higher due to the improved photon harvesting, while the V_{oc} is only slightly improved due to the little variation in the level alignment. The addition of a layer of colloidal NPs on top of the $FAPbBr_3$ does not improve current and V_{oc} but has a positive impact on the fill factor, probably because of improved contact with the selective extraction layer. Regarding reproducibility of the different cells, from Figure 1.38 we can clearly observe that m-TiO_2 confirms to be improved respect to only c-TiO_2, with the latter with only 3 layers being the less reliable and the former with 7 layers the sample that has the most constant J_{SC} value. The polycrystalline $CsPbBr_3$ layer is less reproducibile than our inks: in situ formation of the active layers has the advantages of the absence of ligands and the direct formation over the substrate, but still suffers of lack of control during crystallization. The deposition of NPs layer only slightly enhance reliability. For $FAPbbr_3$ phase this process works better and with NPs even more, even if J_{sc} values are decreased. We also performed a second cycle of measurement after 5 minutes under sun simulator irradiation (1 sun)(Figure 1.39): the process has less sever effect than expected but J_{sc} decresed as a probable consequence of some sort of insulating ligand segregation. This preliminary test suggest us to in future consider incapsulation of the device to prolong the performances. To summarize the results we obtained working with solar cells, the use of the colloidal nanoparticles approach is of practical value as the manufacturing of the device is easier. Yet, the introduction of an excess of insulating material limits performances because of limited charge transport capabilities. Also, the peculiar phase we optimized is not suitable for outdoor applications because of both limited photon harvesting and poor performances at high illuminations conditions. Despite this negative aspects, our best ink outperforms the in situ grown materials of identical composition.

The indoor measurements were performed using the same set up, but substituting the solar simulator with a common LED lamp[80] with known dependency between irradiance and distance from the sample. In this case measurement unit is lux (lx, where 1 sun = $1000\,W\,cm^{-2}$ = 120 000 lux[81]) and the incoming power (in denominator of PCE) should be calculated converting lux in $W\,cm^{-2}$. We performed J-V measurements at 200 and 1000 lux. Here are reported (Figure 1.40(a)) only results obtained with m-TiO_2 ETL, , the best one of the two we used for the measurements under sun simulator. It is immediately clear that under indoor conditions all samples work better: at 200 lux there's almost no difference between different number of layers and at 1000 lux is still very modest, non

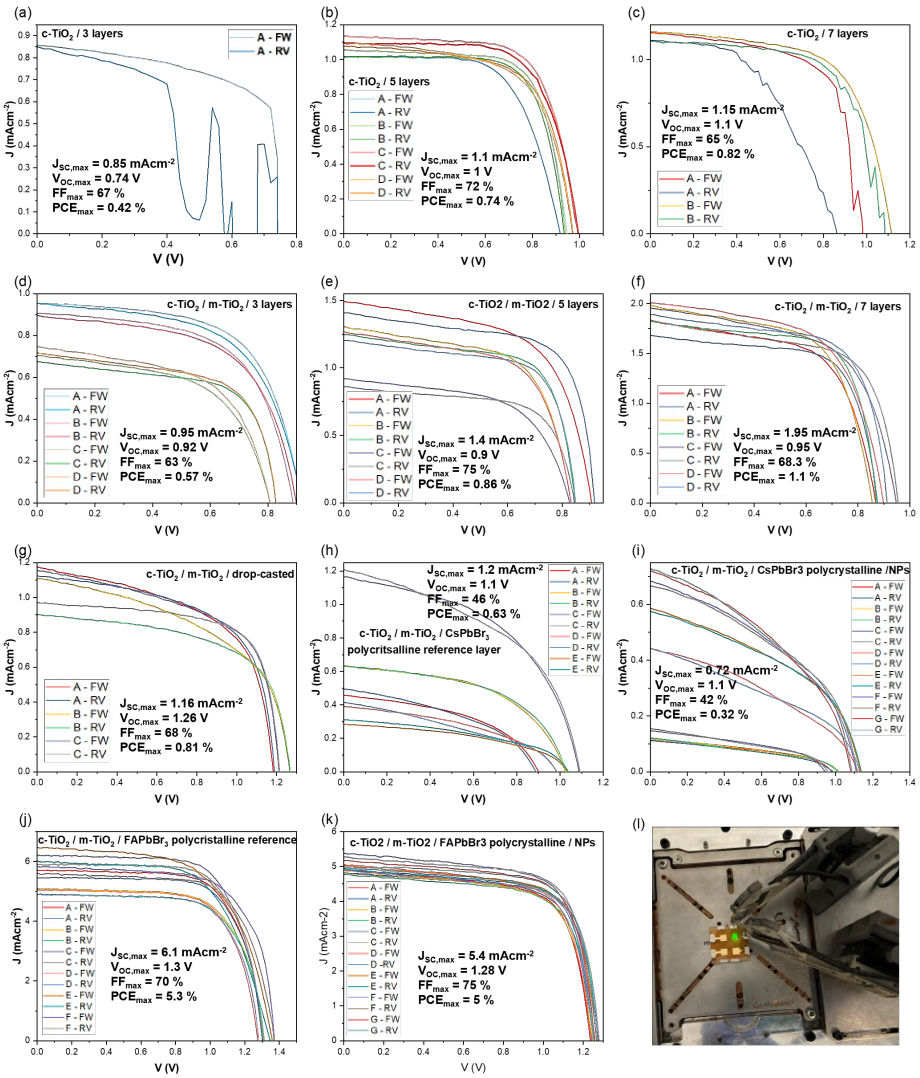

Figure 1.38 Photocurrent density in function of voltage for different cells for (a)-(c) c-TiO_2/3-5-7 layers, (d)-(g) c-TiO_2/m-TiO_2/3-5-7-drop casted layers, c-TiO_2/m-TiO_2/$CsPbBr_3$ polycrystalline reference layer without (h) and with (i) a layer of NPs and c-TiO_2/m-TiO_2/$FAPbBr_3$ polycrystalline reference layer without (j) and with (k) a layer of NPs. (l) Photograph of one cell in a device under illumination.

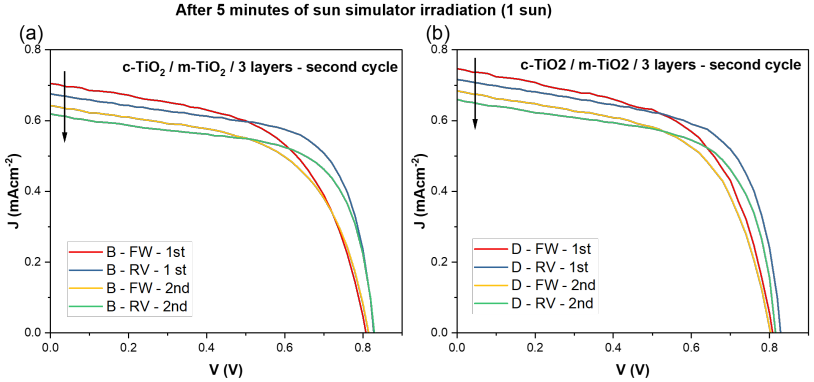

Figure 1.39 Photocurrent density in function of voltage for two different cell of the same device as prepared and after 5 minutes of continuous sun simulator irradiation (1 sun).

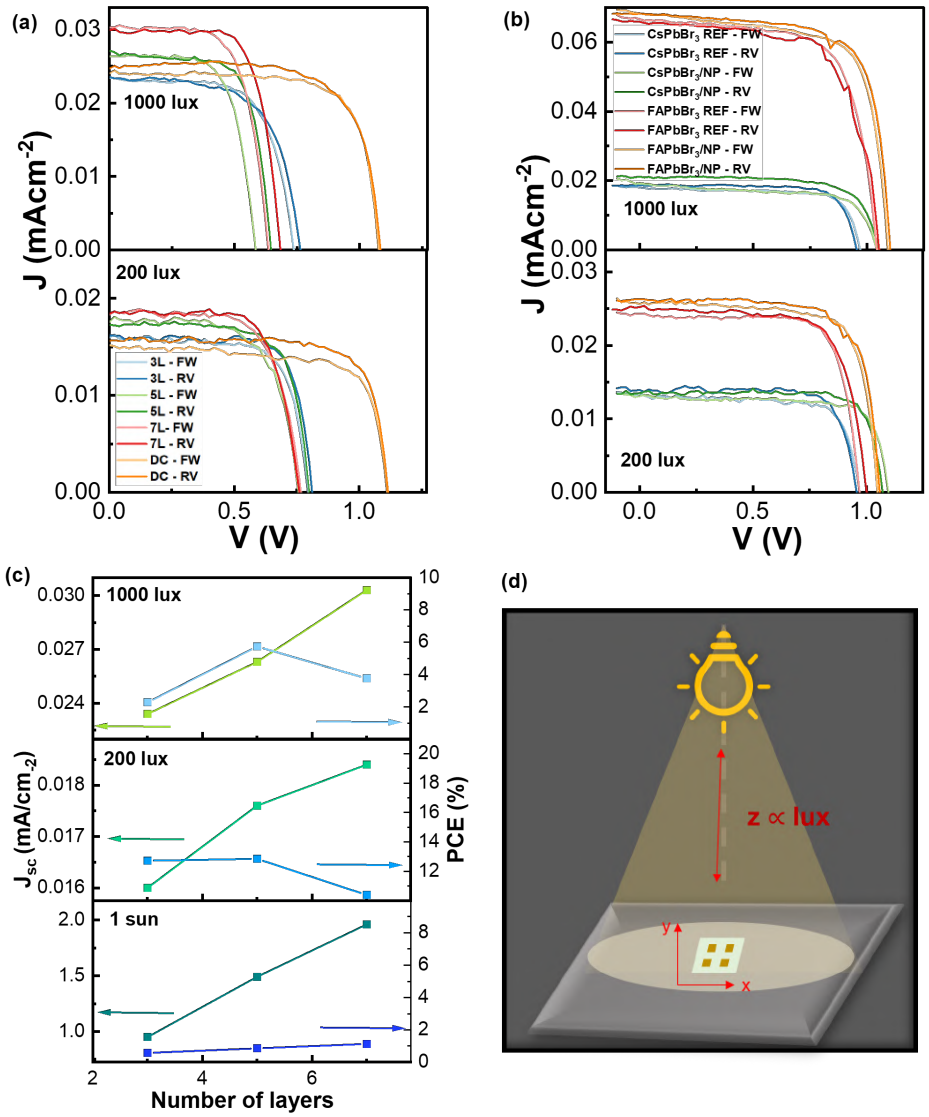

Figure 1.40 Best photocurrent density in function of voltage curves under 200 lux (bottom) and 200 lux (top) of (a) 3, 5, 7 layers and drop casted NPs with c-TiO_2 + m-TiO_2 (top) and only c-TiO_2 (bottom) and (b) reference samples ($CsPbBr_3$ (top) and $FaPbBr_3$ (bottom) polycristalline) alone and with 1 layer of our NPs). (c) Evolution of the short-circuit corrent (green curves and dots) and power conversion efficiency (PCE, blue curves and dots) depending on number of active layer deposited under 1 sun, 200 lux and 1000 lux (respectively from bottom to top).

comparable with the 1 sun one (Figure 1.40(c)). It could suggest that the performances deviation intensifies with the incoming irradiation. Nevertheless, counterintuitively the PCE decreasen between 5 and 7: probably the detrimental parasite effect that scales with irradiance also intensifies with the thickness of active material. The FFs are also improved (between 60 and 75 %) leading to overall conversion efficiencies exceeding 10 % for the spin coated samples and reaching a very remarkable 20.1 % for the drop casted sample (Tabel 1.9). The increase in the irradiance negatively impact all performances, and J_{sc} in particular. The most likely phenomenon affecting the results is charge accumulation, probably due to insulating OAm rich domains. Finally, the behaviour of reference sample with and without our NPs top layer is presented in Figure 1.40(b): in both cases, the presence of our NPs increases V_{oc}, FF and PCE. Statistic under these codnitions is reported

Table 1.9 PCE in different conditions for all tested samples.

Device	1 Sun PCE (%)	200 lx PCE (%)	1000 lx PCE (%)
c-TiO_2 - 3L	$0,42$	$0,9$	$2,02$
c-TiO_2/m-TiO_2 - 3L	$0,57$	$12,7$	$2,28$
c-TiO_2 - 5L	$0,74$	$10,5$	$4,0$
c-TiO_2/m-TiO_2 - 5L	$0,86$	$12,85$	$5,74$
c-TiO_2 - 7L	$0,82$	$4,9$	$2,8$
c-TiO_2/m-TiO_2 - 7L	$1,1$	$10,4$	$03,8$
c-TiO_2/m-TiO_2 - Drop Casted	$0,8$	$20,1$	5
Reference ($CsPbBr_3$)	$0,6$	$15,7$	$3,6$
Reference ($CsPbBr_3$)/NPs-$CsPbBr_3$	$0,3$	$24,3$	$4,3$

in experimental part but follows the trend highlighted for sun irradiation. Efforts are ongoing to reduce the amount of residual OAm In the active layer.

1.8.2 Scintillators

The detection of ionizing radiation is a topic of high relevance in many scientific and technological fields, ranging from particles and high energy physics[82] and medical diagnostics[83] to industrial[84] and environmental monitoring,[85] as well as border security[86] and goods control.[87] There are two types of ionizing radiation detectors: direct ones and scintillator. The former are usually composed by either a stacked layer structure or a planar one that takes advantage on the formation of charges in radiation exposed active materials, eventually collecting them out[88] (Figure 1.41(a)).

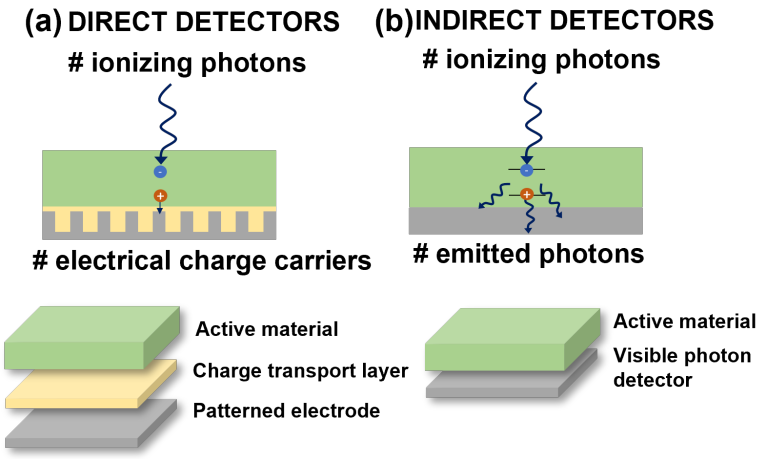

Figure 1.41 Schematic representation of direct (a) and indirect (scintillators)(b) detectors architectures (bottom) and working principles (top).

The number and energy of incident radiations is proportional to measured current and can be thus precisely correlated to extract data. Among the requirements, efficient and fast collection of charges at the contacts, known to be a "tricky" process, is of paramount importance. The indirect radiation detector instead exploits the detection of radiative recombination of generated charges (scintillation process, hence the name) to measure incident radiations.[89] Although the first technology is certainly intriguing and competitive, we firstly focused on the second because more compatible with our as-prepared inks. The active material requirements are thus:

1. elevated high-energy radiation interaction probability, determined by scintillating material effective atomic weight (Z) and density (ρ) according to a power law

$$\mu \propto \frac{\rho Z^4}{E^3} \tag{1.4}$$

   where μ is the radiation absorption coefficient and E the energy of incoming rays. This law makes clear that is better to include in scintillators materials containing heavy atoms.

2. Elevated scintillating efficiency, named radioluminesce (RL) light yield (LY), defined as the number of emitted photons per energy of radiation absorbed.

3. Radiation hardness, that describes the material stability and resistance to high radiation doses. This parameter determines the device duration in operational conditions.

4. Device fabrication that is scalable, low cost and low energy consumption.

5. Extremely fast scintillating emission (under 500 ps).

The last aspect is particularly important for applications in time of flight (TOF) modality. In high energy physics, TOF techniques are employed in high luminescence accelerators,[90] where it's necessary to avoid signal pile-up phenomena and precisely localize the particles decays origin created by collisions. Equally, the time of flight positron emission tomography (TOF-PET), the most important application for everyday impact, is an oncological imaging technique that needs a very fast and precise temporal resolution.[91]

It in fact builds upon collection of two X-rays emitted at 180° one to another after annihilation of a positron with an electron from a tissue. Their detection difference in times is proportional to their pathway and thus contains spatial information about the exact point where annihilation happened. The fast response time of the detector is thus critical to obtain high precision and quality images for diagnostics. Entirely inorganic active layers were already employed[92] but their production is expensive and energy consuming and the resulting device is very heavy and not suitable for portable application. The best way to overcome the former materials drawback is to turn the attention toward plastic matrix embedding the effective active material (nanocomposites). In this way, the fabrication is more industrial-friendly, the costs are reduced and the device can assume limitless shapes, thickness and mechanical properties.[93] However, this asset means that the active material is more "diluted" inside the matrix and thus it must be very efficient in achieving the same performances. The first attempts in these directions were made with encapsulation of specific organic molecules[94].[95] However, even the best ones in light yield show lower radiation hardness than the inorganic counterparts, limiting the stability of the derived device with respect to the expected lifespan of commercial devices. In the last years, along with the fast spread of nanotechnologies, the possibility of embedding inorganic NPs rose and became a very fervent research field.[96] Clearly, LHP were not ignored: the presence of a such heavy atom as lead, the high luminescence efficiency and radiation hardness are surely appealing properties.[97] Moreover, their encapsulation into a polymer matrix partially solves the questions around lead toxicity for humans and environment[98] (moving it from the application itself to production and disposal steps, where different safety protocols can be introduced). Moreover, these materials are renowned to be "fragile" and this characteristic affects performances during the encapsulation**??** (mainly performed by in situ polymerization of the monomer by heat or UV treatment or by slow evaporation of the loaded polymer solution). Post synthesis ligand exchange can improve the stability of scintillating perovskites to the encapsulation step, for example substituting the ligands originally introduced with more stable ones, i.e. dimethyldidodecylammonium bromide - DDAB[99]). Nevertheless, the addition of a

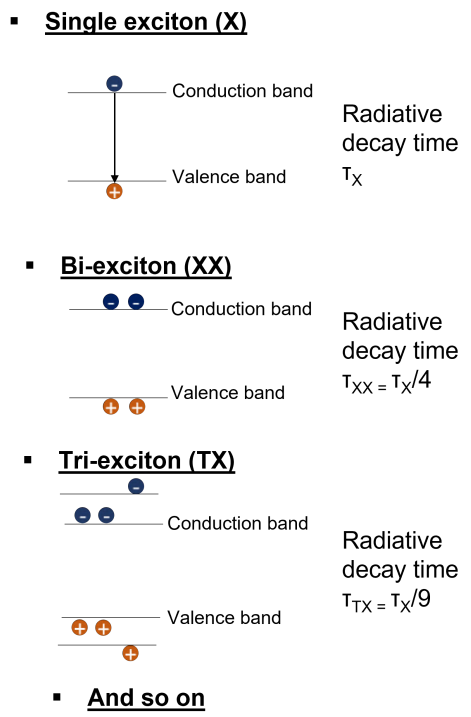

Figure 1.42 Scheme of single, bi- and tri-excitons respect to conduction and valence band and the progressive accelerating of decay times.

post-synthetic treatment limits scalability and industrial appeal. In addition, general procedure employed to obtain this materials are well-established in lab scale but fail when they have to be adapted to an industrial process (as already mentioned in section 1.1 and 1.3). Besides material selection, generally single exciton recombination is exploited: this phenomenon is not fast enough (around tens of ns). Also coupling this process with an organic down-converter, typically characterized by a shorter recombination τ that fastens the process, is not enough (still over 1 ns), and introduces a component very likely not radiation hard. In collaboration with the group of Prof. Sergio Brovelli and Anna Vedda, we developed and patented[100] nanocomposite scintillators with multiple exciton radiative recombination based on our $CsPbBr_3$ NCs that are highly efficient, outstandingly fast and compatible with large scale production. This invention distances from the state of the art devices in two fundamental aspects: the nature of the physical process that leads to scintillating emission, that passes from usual single exciton recombination to multiple ones at NCs band border, and the synthetic process that allows to improve the scintillating properties during polymerization (on the contrary of general protocols), obtaining unprecedented performance, while maintaining RT conditions, low costs and complete scalability (this last is our prevalent contribution). The latter relies on previously reported results (Section 1.3 and 1.4): thanks to turbo-emulsifier, the robustness of our synthesis was undoubtedly proved until 3,6 L scale and the fact that output solid is in a metastable form, which evolves depending on medium conditions, allows practical redispersion of these NCs in the monomers mixture, where the UV slow polymerization makes them grow towards their final form instead of damaging them (section 1.4.1). Briefly introducing the former physical improvement, single and multiple exciton processes are schematized in Figure 1.42. The fundamental difference with the conventional single exciton emission mechanism is the simultaneous co-presence of more electron-hole pairs in the same NC under ionizing irradiation. This phenomenon activates further recombination channels respect to single exciton, resulting in a overall highly accelerated scintillation (<100 ps). Specifically, respect to single excitons recombination time, double excitons show a four-fold acceleration and triexcitons nine-fold, and so on. These processes can be not only radiative, but also non radiative. Remember that the following equation remains true in general:

$$\tau_{tot} = \tau_{radiative} + \tau_{non-radiative}\tau_{tot} = \frac{1}{k_{tot}} = \frac{1}{k_{radiative} + k_{non-radiative}} \tag{1.5}$$

where τ is the recombination time and k is the recombination probability. The former contributions increase the radiative emission rate (intended as the inverse of scintillating radiative decay time that thus becomes very fast), the latters are associated to competitive pathways that increase the decay rate but not the scintillation. An example of non-radiative processes, Auger recombination, speeds up non radiative temporal dynamics but not the luminescence ($\tau_{non-radiative}$). It is reported that the multi-excitonic Auger recombination can be suppressed through NCs well established engineerization strategies. Among these, we can find dimensional control, heterostructuring[101] and engineerization of quantum confinement potential:[102] all these processes are difficult to control either after or during synthesis, and thus not always extendable to industrial workups.[103] Their necessity is due to the fact that NCs defects act as trap sites for charges (both electron and holes). In our case, as deepened ahead, no additional step is needed, as the evolution of the material from its latent stage to the final from during polymerization provides a route to passivate defects. The scintillating device is composed by a nanocomposite matrix (PMMA and NCs), where incident radiation generates multiexcitons in the active material

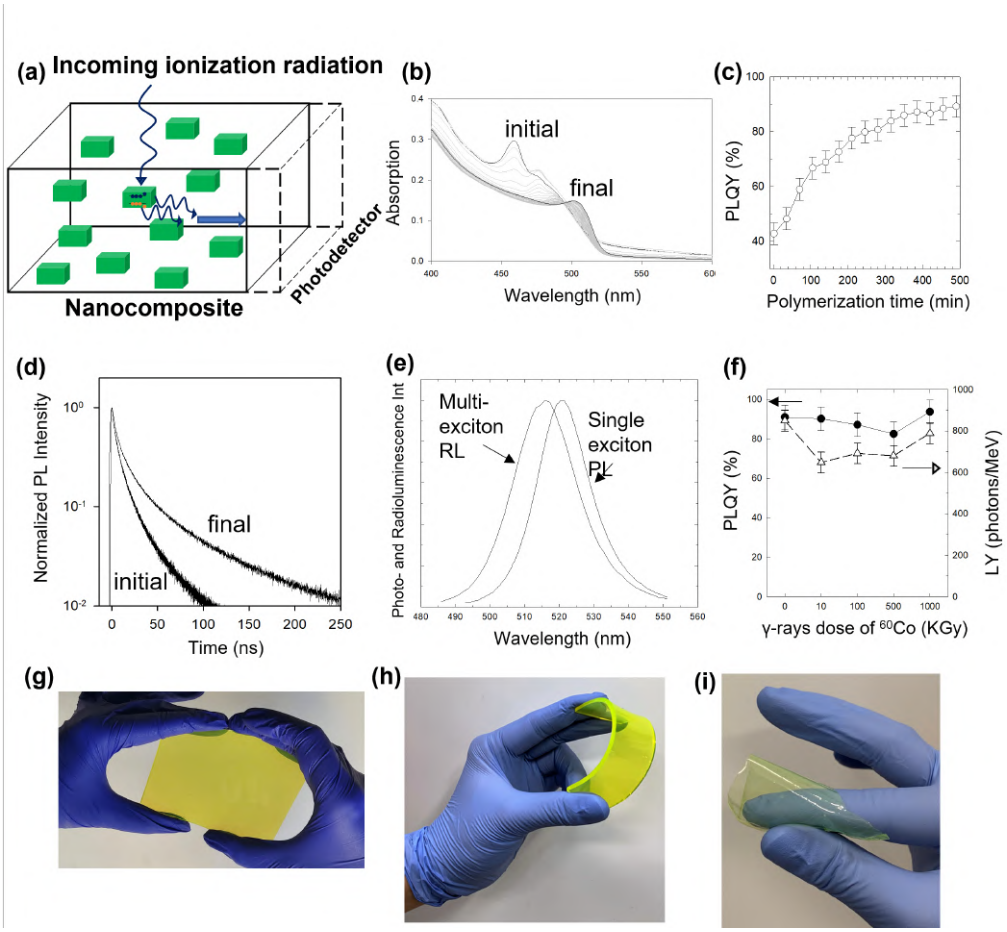

Figure 1.43 (a) Schematic representation of the complete device. (b) ABS spectrum, (c) PLQY and (d) PL decay times evolutions during matrix photopolymerization from initial metastable NPs to final characteristic $CsPbBr_3$ NCs. (e) Single-exciton PL and multi-exciton RL maximum of final nanocomposite. (f) PLQY (black dots) and RL-LY (white triangles) trends in identical nanocomposites irradiated with increasing γ-rays doses (from 60 Co radioactive decay) up to 1 MGy. Photographs of (g) rigid, (h) flexible panel and (i) thin film versions of the nanocomposite.

that efficiently radiatively recombine. These scintillation photons are waveguided towards borders, where high efficiency detectors (i.e. photodiode or photomultiplier) are placed to collect the signal. The preparation of high optical quality nanocomposite where the NCs are homogeneously dispersed and scattering losses are minimal is crucial to obtain high scintillating efficiencies. Literature approaches are based on the cells cast approach, that is the preparation of a solution of the scintillating material in a suitable monomer (mostly acrylates) to be directly polymerized in a mold.[104] This strategy ensures the best possible optical quality for bulk slabs of scintillating nanocomposite. There are two issues limiting the applicability of the cells cast approach to the production of composites of NCs. The first one is the limited solubility of most NCs (including perovskites) in acrylates (inducing nonuniform final slab), the second is the introduction of defects on the NCs by the action of photopolymerization process. In our case, the as-obtained solid $CsPbBr_3$ metastable NCs are directly redispersed in the monomers under magnetic stirring (at concentration ranging from 0,05 to 0,2 wt%), with a small amount of radical photoinitiator. We selected both pure methylamethacrylate (MMA) and mixtures with variable amounts of laurylmethacylate(LMA): acrylates offer high optical quality, low absorption coefficient in visible spectrum (and consequently minimal losses due to matrix absorption even for

large area devices), and good radiation resistance.[105] Moreover, the combination of MMA and LMA allows to tune the mechanical properties from rigid to flexible substrates (Figure 1.43 (g) and (h)). As our as obtained nanocrystals are small and OAm rich, solubility is not an issue. Also, as mentioned above, defectivity is reduced while curing and additional defects possibly induced are also readily passivated. The loaded dispersion is poured into a specifically ideated mould (made with two parallel low-roughness tempered pieces of glass, sticked together by a polyvinyl chloride gasket, see Figure ref in Section 1.45) and put under homogenous LED UV ($\lambda_{exc,maximum} = 365nm$) irradiation for an amount of time dictated by slab dimension (for example, for 80 cm x 80 cm, 8 hours are needed).

Also in this case, we followed absorption features and PLQY during polymerization: the evolution of the former (Figure 1.43(b)) demonstrates that, as previously studied, NCs grow directly along with matrix formation, toward the most thermodynamically stable form (from various population between 2 and 4 nm to bulk-like NCs) compatible with the one we characterized in solution. The PLQY rises over the polymerization time (Figure 1.43(c)). On the contrary to what generally happens when lead halide perovskites are exposed to UV irradiation or when coalescence takes place, intensifying defectiveness, in this case the optical properties improve. The defectiveness suppression is further confirmed by fast part (around 20%) of single-exciton decay time slowing down of 50 times after polymerization (Figure 1.43(d)) respect to initial one: non-radiative competitive pathways are efficiently eliminated. Therefore, the encapsulation step, which is usually the detrimental one, becomes a boost of material properties, without any need of other additive treatments. The proof that multiexcitonic regime is reached is given by different characterizations, first of all by the RL peak energy. It is slightly blue-shifted with respect to single exciton photoluminescence one (Figure 1.43(e)).The difference is around 100 meV, reported in literature to be the characteristic multiexcitonic binding energy.[106] In fact, in addition to energy difference between material bands, the emitted photon also gain the energy released by multi-exciton bond breaking. The study of PLQY and LY trend at increasing γ rays doses corroborates that both values are preserved, leading to properties stability in extreme conditions and the ability to stand long operational times with slower doses. The γ-rays are produced by radioactive decay of ^{60}Co nucleus and the irradiation were performed at Calliope facility at ENEA-Casaccia Research Centre. It's worth to notice that measurement unit for absorbed dose of radiation is grey (Gy): 1 Gy is defined as the dose of radiation that deposits 1 J per material Kg. In our tests, we considered 10, 100, 500 and 1000 kGy, the last one meaning 1 MGy. To have a practical idea, it approximately corresponds to the radiation dose that the internal wall of a nuclear reactor receives in 1 year. These nanocomposites can be produced with different shapes, either slab or thin films (Figure 1.43(i)). Similar radiation hardness and light yield tests are in progress on identical nanocomposites loaded with $CsPbCl_3$ NCs (given their faster PL decay time) and with porous inorganic crystals already renowned for scintillating properties with cavity filled with loaded polymer.

1.9 Conclusion

We developed a synthetic procedure for $CsPbX_3$ NCs which key feature is the use, for the first time in the dedicated literature, of turbo-emulsification as a superior method to avoid concentration profiles in rapid injection methods while working at very large scale. By direct comparison of compositional (XRF, ICP-OES, TGA) optical and morphological (PXRD, TEM) characterizations with a reference sample produced via magnetic stirring, we demonstrated that high shear homogenization employment becomes indispensable when working on more than 1-liter scale. The fundamental assets are:

- remarkable scalability up to the unprecedented production of 8 g of dry material in a single batch;
- improved performances as obtained NCs evolve in different conditions becoming progressively more efficient in a well-defined, reproducible way;
- outstanding generality, enabling access to different halogen composition, morphologies, temperature and ligands;
- versatility towards application field: even if designed for in-solution optical studies, preliminary tests in two completely different devices are promising;
- tackled sustainability issue by developing an efficient method of recycling volatile organic solvents and residual lead ions contaminated nonvolatile residues, showcasing their re-use in synthesis with still high quality output;
- intrinsic easy feasibility, not only for the straightforward conditions, but also because the linear model between output recovered amount of material as function of batch scale we devised originally makes possible to specifically correlate a selected volume to a NCs produced quantity and thus to make a reliable synthetic plan.

Our results provides a dramatic step beyond towards the industrial scalability of LHP nanomaterials. This aspect is a breakthrough for large and efficient plastic scintillator, as demonstrated in section 1.8.2, but work still need to be done in photovoltaic field. Future perspectives for this approach in our group are addressed mainly to substitute OAm with designed "latent" amines (as for aforementioned latent pigment, a portion can be cleaved with mild annealing process in film to compact layers and improve photocarrier conductivity) and further extend the protocol to MA/FA cations to obtain a enhanced overlap with solar spectrum.

1.10 Experimentals

1.10.1 Chemicals

All chemicals and solvents were purchased from Fluorochem, Merck, VWR, Acros Organic and TCI. Isopropanol was dried over CaH_2 for a week and then distilled before use. LiI was anhydrificated heating the powder with direct flame (Bunsen burner) until melting under vacuum and cooling down under nitrogen flux. MMA and LMA were filtered over a silica pad to remove stabilizing agents right before use. All other chemicals were used without any further purification and stored in a dryer. Composition of solvent mixtures are indicated as volume/volume ratios (v/v).

1.10.2 Synthesis of perovksites nanocrystals

1.10.2.1 $CsPbBr_3$ type

Our original standard protocol 3,6 L scale. Solution A is prepared dissolving Cs_2CO_3 (1,95 g, 6 mmol) in propionic acid (6 mL, 79,8 mmol) and then diluting with 3600 mL of heptane/isopropanol 2:1. For preparation of solution B, $PbBr_2$ (22,02 g, 60 mmol) and tetrabutylammonium bromide (19,32 g, 60 mmol) are dissolved under magnetic stirring in a mixture of oleylamine (177,6 mL, 540 mmol), propionic acid (40,2 mL, 540 mmol) and isopropanol (40 mL) at 80 °C. After the complete dissolution of the precursors, the mixture is let cooling down to room temperature. Solution A is put under stirring with a Turbo-emulsifier homogenizer (15k RPM) in a 5 L beaker, then solution B is swiftly added. The mixture is let evolve for 30 s under homogenization. Stirring is stopped, and 1.8 L of isopropanol are added to the crude solution to precipitate the nanocrystals that are thus collected by centrifugation at 4500 rpm for 2 min. The supernatant is gathered for following recycle and the precipitate is dried in a dryer, weighted (8 g) and finally stored in solid state in glove box under argon atmosphere.

Table 1.10 Employed scales and respective quantities.

CsPA (mmol)	Hept/iPrOH 2:1 v/v	$PbBr_2$ (mmol)	TBAB (mmol)	Olam/PA/iPrOH 4,4:1:1 v/v
$0,2$	60	1	1	$4,3$
$0,4$	120	2	2	$8,6$
$0,6$	240	4	4	$17,2$
1	300	5	5	$21,5$
3	900	15	15	$64,5$
4	1200	20	20	86
12	3600	60	60	258

Table 1.11 Characteristics of the two dispersing tools employed.

	Code	Stator (mm)	Rotor (mm)	T_{max} (°C)	Fineness dispersions μm	Fineness emulsions μm	Max rotations	Volume
C	S25N-25G	25	17	180	$15-50$	$1-10$	24k RPM	$0,05-2$ L
D	S50N-G45M	45	$40,5$	180	$25-50$	$5-20$	10k RPM	$0,5-15$ L

The high shear turbo emulsifier employed consists in a motor group (IKA ULTRA-TURRAX 25 (A) or 50 (B) DIGITAL) and a dispersing tool (S25N-25G (C) or S50N-G45M (D), whose characteristics are described in Table 1.11).

Magnetically stirred procedure The reaction was performed as reported for 1.10.2.1, except for using magnetic stirring during addition of solution B into A (1000 RPM),both on 60 mL and 1200 mL scale (for quantites, see Table 1.10).

High viscosity procedure with propionic acid Solution A is prepared dissolving Cs_2CO_3 (32,5 mg, 0,1 mg) in PA (0,1 mL, 1,3 mmol) and then diluting with 60 mL of Octadecene/Dowanol DPnP 2:1. For preparation of solution B, $PbBr_2$ (367 mg, 1 mmol) is dissolved under magnetic stirring in a mixture of Olam (2,9 mL, 9 mmol), PA (0,7 mL, 9 mmol) and Dow (0,7 mL) at 80 °C. After the complete dissolution of the precursor, the mixture is let cooling down to room temperature. Solution A is put under stirring with a Turbo-emulsifier homogenizer (15k RPM) in a 250 mL polypropylene bottle, then solution B is swiftly added. The mixture is let evolve for 30 s under homogenization then stirring is stopped. (Code: SMEPK32)

High viscosity procedure with oleic acid Solution A is prepared dissolving Cs_2CO_3 (65 mg, 0,2 mg) in OA (0,76 mL, 2,4 mmol) and then diluting with 120 mL of ODE/Dow 2:1. For preparation of solution B, $PbBr_2$ (734 mg, 2 mmol) is dissolved under magnetic stirring in a mixture of Olam (4,2 mL, 12,9 mmol), OA (4,2 mL, 13,4 mmol) and Dow (2,5 mL) at 80 °C. After the complete dissolution of the precursor, the mixture is let cooling down to RT. Solution A is put under stirring with a Turbo-emulsifier homogenizer (15k RPM) in a 250 mL polypropylene bottle, then solution B is added. The mixture is let evolve for 30 s under homogenization (this step induces foam formation) then stirring is stopped. (Code: SMEPK24 and 25).

High temperature procedure The reaction was performed as reported for 1.10.2.1, except for the fact that solution A is kept at 180 °C with a silicone bath over an hot plate and solution B is injected after heating at 160 °C. After homogenization is stopped, the mixture is swiftly cooled down with an ice bath and a half of mixture volume of AcOEt is added to the crude solution to precipitate the nanocrystals that are thus collected by centrifugation at 4500 rpm for 2 min. The supernatant is discarded and the precipitate is redisersed in fresh toluene. (Code: LB-XIV-74)

Low temperature procedure Solution A is prepared dissolving Cs_2CO_3 (65 mg, 0,2 mmol) in PA (0,2 mL, 2,6 mmol) and then diluting with 120 mL of hept/iPrOH 2:1. For preparation of solution B, $PbBr_2$ (1 g, 3 mmol) is dissolved under magnetic stirring in a mixture of Olam (5,8 mL, 18 mmol), PA (1,3 mL, 18 mmol) and iPrOH (40 mL) at 80 °C. After the complete dissolution of the precursors, the mixture is let cooling down to room temperature. Solution A is put under stirring with a Turbo-emulsifier homogenizer (15k RPM) in a 250 mL polypropylene bottle while in an ice bath (measured temperature 8 °C), then solution B is swiftly added. The mixture is let evolve for 10 s under homogenization. Stirring is stopped, and 1.8 L of isopropanol are added to the crude solution to precipitate the nanocrystals that are thus collected by centrifugation at 4500 rpm for 2 min. The supernatant is discarded and the precipitate is dried in a dryer, weighted (260 mg) and finally redisperse in fresh toluene (10 mg/mL). (Code: SMEPK13)

Standard procedure with OA Solution A is prepared dissolving Cs_2CO_3 (32,5 mg, 0,1 mmol) in OA (0,42 mL, 1,33 mmol) and then diluting with 60 mL of Hept/iPrOH 2:1.

For preparation of solution B, $PbBr_2$ (367mg, 1mmol) and TBAB (322 mg, 1 mmol) are dissolved under magnetic stirring in a mixture of Olam (2 mL, 6 mmol), OA (1,9 mL, 5,9 mmol) and iPrOH (0,5 mL) at 80 °C. After the complete dissolution of the precursors, the mixture is let cooling down to room temperature. Solution A is put under stirring with a Turbo-emulsifier homogenizer (4k RPM) in a 125 mL polypropylene bottle, then solution B is swiftly added. The mixture is let evolve for 30 s under homogenization. Stirring is stopped, and 30 mL of iPrOH are added to the crude solution to precipitate the nanocrystals that are thus collected by centrifugation at 4500 rpm for 2 min. The supernatant is gathered for following recycle and the precipitate is dried in a dryer, weighted (100 mg) and finally redispersed in fresh toluene (10 mg/mL). (Code: SMEPK29)

Standard procedure with TFA/PA 1:1 mol/mol Solution A is prepared dissolving Cs_2CO_3 (32,5 mg, 0,1 mmol) in TFA (0,1 mL, 1,35 mmol) and then diluting with 60 mL of Hept/iPrOH 2:1. For preparation of solution B, $PbBr_2$ (367 mg, 1 mmol) and TBAB (322 mg, 1 mmol) are dissolved under magnetic stirring in a mixture of Olam (2,9 mL, 9 mmol), PA (0,33 mL, 4,5 mmol), TFA (0,33 mL, 4,5 mmol) and iPrOH (0,7 mL) at 80 °C. After the complete dissolution of the precursors, the mixture is let cooling down to room temperature. Solution A is put under stirring with a Turbo-emulsifier homogenizer (15k RPM) in a 125 mL polypropylene bottle, then solution B is swiftly added. The mixture is let evolve for 30 s under homogenization. Stirring is stopped, and 30 mL of iPrOH are added to the crude solution to precipitate the nanocrystals that are thus collected by centrifugation at 4500 rpm for 2 min. The supernatant is gathered for following recycle and the precipitate is dried in a dryer, weighted (211 mg) and finally redispersed in fresh toluene (10 mg/mL). (Code: SMEPK33)

Standard procedure with BuAm Solution A is prepared dissolving Cs_2CO_3 (65 mg, 0,2 mmol) in PA (0,2 mL, 2,6 mmol) and then diluting with 120 mL of Hept/iPrOH 2:1. For preparation of solution B, $PbBr_2$ (734 mg, 2 mmol) and TBAB (644 mg, 2 mmol) are dissolved under magnetic stirring in a mixture of Buam (1,8 mL, 17,8 mmol), PA (1,33 mL, 17,8 mmol) and iPrOH (1,3 mL) at 80 °C. After the complete dissolution of the precursors, the mixture is let cooling down to room temperature. Solution A is put under stirring with a Turbo-emulsifier homogenizer (15k RPM) in a 125 mL polypropylene bottle, then solution B is swiftly added. The mixture is let evolve for 30 s under homogenization. Stirring is stopped, the mixture is already turbid so 90 mL were directly centrifuged (sample A), indeed at the remaining 30 mL, 15 mL of iPrOH and centrifuged as well (sample B)(in both cases at 4500 RPM for 2 min). The supernatant is discarded and the precipitate is dried in a dryer, weighted (sample A: 220 mg and sample B: 91 mg) and stored in solid state in glove box under argon atmosphere. (Code: PK28)

Standard procedure with recovered reactants and solvents We selected 120 mL scale. Solution A is prepared with 68,8 mL of distillated recovered solvents (iPrOH/Hept 1,3 :1 v/v) and we added only 51 mL of fresh hept to reach the desired ratio of Hept/iPrOH 2:1. We thus employed 57,5% in volume of recycled solvents. The amount of Cs_2Co_3 needed is 62 mg (0,19 mmol) instead of 65 mg, considering the percentage of Cs^+ evaluated with inductively coupled plasma optical emission spectroscopy (ICP-OES, 0,04 wt%) and 0,1 mL of propionic acid (1,3 mmol). Solution B already contains partial lead source, TBAB, OLAM, and PA (respectively 2,25 wt%, approximated 7 %wt and 1:0,86 molar ratio from ICP-OES and ^1H nuclear magnetic resonance -NMR- in solution). We employed

6,6 mL of recovered mixture (6,27 g) and thus added $PbBr_2$ (438 mg, 1,32 mmol), TBAB (205 mg, 0.6 mmol), Olam (1,1 mL, 3,3 mmol) and iPrOH (1 mL). After adding the lacking amount of fresh reactants, we dissolved and homogenized them at 80 °C and followed thus our standard procedure reported before (1.10.2.1). After homogenization stop, the mixture is already turbid so it was directly centrifuged (sample A) and then 60 mL of iPrOH was added to the supernatant and centrifuged again (sample B)(in both cases at 4500 RPM for 2 min).We recovered 272 mg of sample A and 20 mg of sample B, both stored in solid state in glove box under Ar atmosphere.

1.10.2.2 $CsPbCl_3$ type

Our original standard protocol 60 mL scale. Solution A is prepared dissolving Cs_2CO_3 (32,5 g, 0,1 mmol) in PA (0,1 mL, 1,3 mmol) and then diluting with 60 mL of hept/iPrOH 2:1. For preparation of solution B, $PbCl_2$ (278 g, 1 mmol) is dissolved under magnetic stirring in a mixture of Olam (2,9 mL, 9 mmol), PA (0,7 mL, 9 mmol) and iPrOH (0,7 mL) at 80 °C. After the complete dissolution of the precursor, the mixture is let cooling down to room temperature. Solution A is put under stirring with a Turbo-emulsifier homogenizer (15k RPM) in a 125 mL polypropylene bottle, then solution B is swiftly added. The mixture is let evolve for 30 s under homogenization. Stirring is stopped, and 30 mL of iPrOH are added to the crude solution to precipitate the nanocrystals: the process takes 24 hours. After this time, the product is collected by centrifugation at 4500 rpm for 2 min. The supernatant isdiscarded and the precipitate is dried in a dryer, weighted (68 mg) and finally stored in solid state in glove box under argon atmosphere. The reaction has been performed also on 120 mL scale (amount recovered: 125 mg). (Code: respectively PK40-PK57 and PK53-PK56)

Mixed composition: $CsPbBr_{1,5}Cl_{1,5}$ The reaction was performed as reported for 1.10.2.2, except for using $PbCl_2$ (139 mg, 0,5 mmol) with $PbBr_2$ (183,5 mg, 0,5 mmol) for preparation of solution B. Moreover, in this case after homogenization the mixture was turbid, thus was centrifuged directly (sample A) and after 24 h of 30 mL iPrOH addition (sample B). The solids were both stored in glove box under argon atmosphere. Amount recovered: 40 mg of sample A and 38 mg of sample B. (Code: PK41)

Mixed composition: $CsPbBr_1Cl_2$ The reaction was performed as reported for 1.10.2.2, except for adding TBAB (322 mg, 1 mmol) for preparation of solution B. Moreover, in this case after homogenization the mixture was turbid, thus was centrifuged directly (sample A) and after 24 h of 30 mL iPrOH addition (sample B). The solids were both stored in glove box under argon atmosphere. Amount recovered: 67 mg of sample A and 10 mg of sample B. (Code: PK42)

Standard procedure with BuAm The reaction was performed as reported for 1.10.2.2, except for using Buam (0,9 mL, 8,8 mmol)/iPrOH (0,7 mL)/PA (0,7 mL, 9 mmol) for preparation of solution B. Moreover, in this case after homogenization the mixture was turbid: 30 mL of iPrOH were added anyway to finish precipitation and thus we centrifuged the crude directly, without waiting 24 hours. Amount recovered: 110 mg. The solids was stored in glove box under argon atmosphere. (Code: PK43)

1.10.2.3 $CsPbCl_3$ type

Our original standard protocol 60 mL scale. The reaction was performed as reported for 1.10.2.1, except for using PbI_2 (461 mg, 1 mmol) for preparation of solution B. After solution B addition, the mixture becomes immediately intense yellow and after the 30 s of homogenization, pale orange. The mixture is turbid and it is thus immediately centrifuged (4500 RPM for 2 min) After supernatant elimination and resulting solid drying, we obtained 77 mg (difficult to collect, paste-like) intense yellow solid without any sign fluorescence. (Code: PK54)

1.10.3 Post-synthesis treatments

1.10.3.1 $CsPbCl_3$ healing

We adapted Mondal et al. procedure and dispersed the NCs at 0,2 mg/mL in toluene (10 mL scale), then added 10 mg of $CdCl_2$ and let the mixture vigorously stir for 2 hours. The prolonged efficient mixing is necessary because this salt obviously does not dissolve in toluene and the process thus happens in heterogeneous phase. The dispersion is centrifuged to remove solid parts and the output reached a PLQY of 40 % (value relative to quinine solfate 0,1 M in H_2SO_4), one order of magnitude higher than the starter one (4%), without any change in absorption and PL position. This procedure can be performed also in MMA, the monomer of the most common polyacrylate for plastic embedding, for application interest.

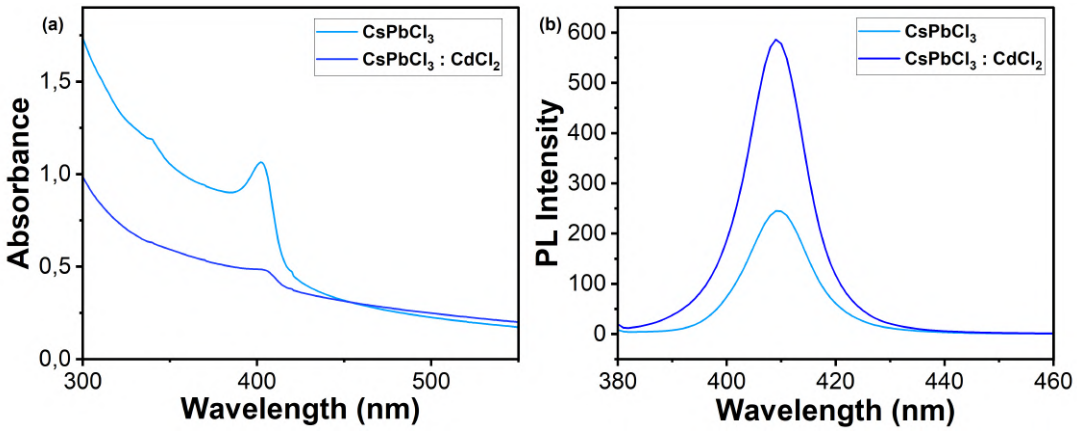

Figure 1.44 (a)Absorbance and (b) photoluminesce spectra of $CsPbCl_3$ as-prepared and after $CdCl_2$ treatment dispersed in MMA (0,2 mg/mL, $\lambda_{exc} = 350$ nm). Both samples show an intense scattering tail due to $CdCl_2$ powder remained. The optical features remain the same but , even if the treated sample absorbs less because partially precipitated in centrifugation step, PL Intensity is strongly increased.

1.10.3.2 Halogen exchange

Treatment with LiI LiI was previously dried out: the solid is heated with direct flame (Bunsen burner) under vacuum until almost melting point and thus cooled down to RT under nitrogen flux. The exchange was carried out in an anhydrous round-bottom flask connected to a Schlenk line, where 3 cycles of vaccum/nitrogen were made, with 20 mg of $CsPbBr_3$ NCs and 20 mL of anhydrous toluene (1 mg/mL). The amount of LiI was added under nitrogen positive flux under magnetic stirring. Specifically, assuming all the 20 mg

of pristine material as composed by unit cells of $CsPbBr_3$ (weight 579,8 g/mol)*, 13,9 mg of LiI are employed for stoichiometric doping (final $\lambda_{em} = 620$ nm) and 2,3 for 1/6 of iodide anions respect to bromide (final $\lambda_{em} = 520$ nm) and 4,6 mg for 1/3 (final $\lambda_{em} = 580$ nm). We initially tested also exchange in an homogeneous medium, previously dissolving LiI in a polar solvent (iPrOH) and then adding the solution to NCS toluene dispersion but abandoned it because the resulting material degrades overnight. (Code: SMEPK20)

Treatment with $SnCl_2$ The exchange was carried out in an anhydrous 20 mL transparent vial where solid anhydrous $SnCl_2$ (45 mg) was added to 3 mL $CsPbBr_3$ toluene dispersion (10 mg/mL). It is let stirring for 2 hours, after which the color has moved from brightly green to intense light blue (Figure 1.29)(final $\lambda_{em} = 450$ nm, exchange not completed)

1.10.3.3 Waste recovery

Scale 240 mL. After performing the reaction and centrifuging, the solid output is stored and the supernatant is distilled under reduced pressure, collecting 245 mL of a first fraction that distillates at 75 °C and 20 mL of a second at 83 °C. Given that hept and iPrOH, the only two solvents employed, have an azeotrope concentration of 46:56 v/v with boiling point at 76,4 °C (celsius) and the two solvents have respectively $T_{bp} = 82{,}5$ °C and 98,4 °C, we recovered 265 mL of Hept/iPrOH 1:1,3 v/v. The dried viscous residue is homogeneous and blue fluorescent and a white solid precipitates overnight. It can be dispersed again with heating under magnetic stirring at 80 °C: this solid is probably composed by $[PbBr6]^{4-}$ aggregates and $CsPbBr_3$ clusters not recovered before for their dimensions under centrifugation limit. This dried residue composition was characterized by ^{1}H NMR in solution (C_6D_6, see Figures 1.48(a), 1.32), XRF (Pb clearly recognizable, cesium very weak - also for its lower x-ray absorption cross section)(see Figure 1.31), ICP-OES (2,25 wt% of Pb and 0,04 wy% of Cs) and TGA (7 wt% of residue at 490 °C, see Figure 1.48(b)). (Code: page of PK24, PK32, PK39, PK51)

1.10.4 Devices preparation

1.10.4.1 Solar cells

Normal glass/FTO (sheet resistance < 15 Ohm/m^2) was purchased from Kintec and patterned via a laser scribing process and cleaned in ultrasonic bath in acetone, iPrOH, and deionised water for 10 minutes each. Ag paste back contacts were brushed, compact TiO_2 was deposited over them and substrates were subdued to UV irradiation for 10 min ($\lambda_{max}400 - 420nm$). When necessary, mesoporous-TiO_2 was deposited by spin-coating. The employed dispersion was obtained diluting 1 g of formulated TiO_2 paste (with terpinol) with 5g of EtOH. An annealing step of few minutes directly on a hot plate at 100 °C to evaporate the solvent is followed by a temperature ramp until 400 °C (to sinter) and then down to 180 °C overnight to avoid mositure deposition. The substrates were UV irradiaten for additional 10 minutes and then carried inside a nitrogen-filled glove box. There, active layers were deposited as follow:

*We evaluated from TGA that there's between 20-30 wt% of ligands; anyway, given that the exchange process is performed in heterogeneous phase and thus only powder grain surfaces are actively partecipating, a slight excess is functional.

1. our $CsPbBr_3$ colloidal dispersion in toluene (10 mg/mL) was spin-coated at 2000 RPM for 45 s, then an annealing step to evaporate the solvent is perform directly on a 90 °C for 2 minutes. We deposited 3, 5 and 7 layer twice both on only c-TiO_2 and c-TiO_2/m-TiO_2 (twice identical devices produced for each type for statistics). The last annealing step was prolonged to 4 minutes, to also "sinter" the NCs. Three devices are also prepared by direct drop-casting 200 μL of stock dispersion.

2. reference $FAPbBr_3$ polycristalline layer was directly obtained in film form depositing precursor solution and then annealing it to promove in-situ crystallization

3. reference $CsPbBr_3$ polycristalline film was produced by spin coating a precursors solution (734 mg of $PbBr_2$ and 30 mg of CsBr in 2 mL of DMSO under magnetic stirring at RT overnight) and successively annealing it to induce in-situ crystallization.

The hole transport layer is formed by spin coating (4000 RPM, 20 s) a solution of PTAA in toluene (10 mg/mL). The energy levels of this polymer are more suitable to $CsPbBr_3$ ones respect to classical employed Spiro-OMeTAD. Finally, a 100 nm thick Au electrode was deposited by thermal evaporation with proper masks and Ag paste is brushed again to complete the contacts. All measurement were performed by Suresh Podapangi, from Prof. Thomas Brown's group, at CHOSE (Polo solare organico della regione Lazio) centre, affiliated with University of Rome-Tor Vergata.

1.10.4.2 Nanocomposite scintillators

Dried solid $CsPBBr_3$ NCs are weighted and directly dispersed in the monomer mixture and along with a radical photoinitiator (Irgacure 651, 0,3 wt% respect to monomers) under magnetic stirring. The homogeneous mixture is poured into a specifically assembled mould generated by two low-roughness parallel tempered glasses stick together by polyvinyl chloride gasket (See Figure 1.45) and placed between both-side equidistant parallel UV LED lamps (λ_{max} around 360 nm) for irradiation homogeneity and to avoid excessive heat accumulation. The process duration depends on nanocomposite dimension: the minimum size (10 cm x 4 cm) takes 30 min, the maximum one (80 cm x 80 cm) 8 hours. After the completion of this procedure, the slabs are removed from the mould and laser cut in pieces of desired sizes. The tested concentration of active NCs in monomers are: 0,05, 0,1 and 0,2 wt%. Higher conentrations gives demixing problems and are now under optimization. Monomers employed are: MMA, LMA and MMA/LMA 80:20 wt/wt. Nanocomposites preparation was performed by Andrea Erroi from Prof. Sergio Brovelli's group.

1.10.5 NCs characterizations

1.10.5.1 Morphological

Transmission electron microscopy (TEM) and selected-area electron diffraction (SAED) Imaging was performed by Prof. Giovanni Maria Vanacore (and in same cases by Dr. Melissa Saibene) at University of Milano-Bicocca Microscopy platform on a JEOL JEM 2100 Plus operating at 200 kV. TEM samples were prepared by drop casting toluene NCs dispersion (0.1 mg/mL) onto a ultrathin lacey carbon TEM grid. High resolution imaging and selected area diffraction analysis were performed in parallel illumination mode using a CMOS Gatan RIO camera. The statistical analysis of dimensions was carried out with ImageJ software, manually measuring short and long side for each NP. On obtained

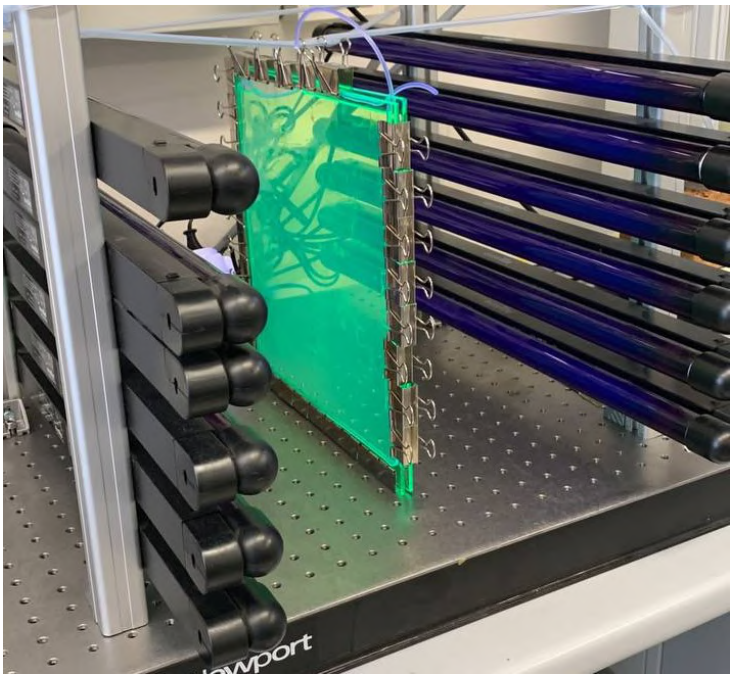

Figure 1.45 Photograph of a nanocomposite under photopolyerization and its set up.

data (usually considering from 50 to 180 NPs), a fit is performed with Fityk function "GaussianA":

$$f(x) = \sqrt{\frac{ln(2)}{\pi}}\frac{a_0}{a_2}e^{-ln(2)(\frac{x-a_1}{a_2})^2} \tag{1.6}$$

where a_0 is function height, a_1 is peak center and a_2 is HFHM ($= \sqrt{2ln2}\sigma$). All mean value are reported as peak center $a_1 \pm \frac{a_2}{\sqrt{2ln2}}$. Note: for non-evoluted sample, the weighted NCs are dispersed in toluene at 10 mg/mL, magnetically stirred for 5 minutes, 15 μL were diluted in 1,5 mL ofr fresh toluene and the 0,1 mg/mL dispersion was immediately deposited. For high viscosity synthesis non-evoluted product, 0,1 mL of crude mixture was diluted in 2 mL of fresh toluene and immediately deposited. For all other samples, the weighted NCs were dispersed in fresh toluene at 10 mg/mL, stirred for 1 hour and then 15 μL was diluted in 1,5 mL of fresh toluene and left under magnetic stirring overnight before deposition. All grids were discarded after measurements.

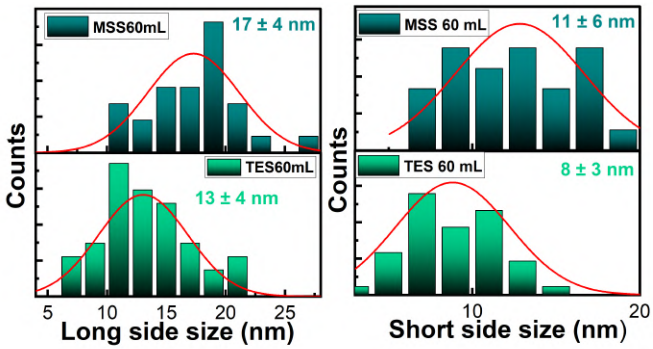

Figure 1.46 Statisical analysis of dimension from TEM images of long (left) and short side size (right) for TESs and MSSs 60 mL.

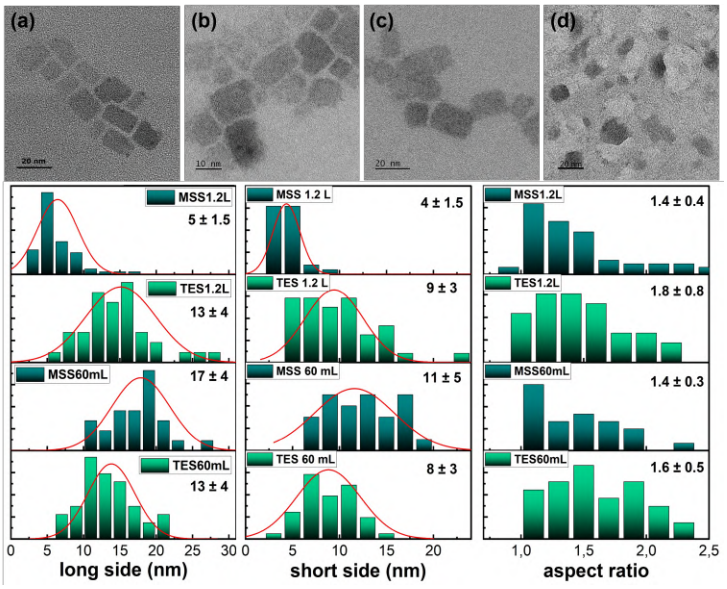

Figure 1.47 TEM images respectively of (a) TES on 60 mL scale, (b) MSS 60 mL, (c) TES 1.2 L, (d) MSS 1.2 and the statistical analysis of long side, short side with gaussian fitting and aspect ratio of the aforementioned samples. (50 NPs)

Scanning electron microscopy Imaging was performed in University of Rome-Tor Vergata on Zeiss Gemini SEM 500 with a field effect source, in high vacuum regime. The electron high tension (EHT) employed is 5 kV. The analysed samples was FTO-glass/c-TiO_2/$CsPbBr_3$NCs and FTO-glass/c-TiO_2+m-TiO_2/$CsPbBr_3$NCs with a different number of active layer, without metallization and putting the substrates directly under the electron beam inside the working chamber.

Powder X-ray diffraction (XRD) Measurements were performed using a benchtop Rigaku MiniFlex 600 operating at 45 kV and 40 mA equipped with a copper radiation source (Kα-Cu 0,154 nm) . Samples were prepared by drop-casting a concentrated NCs toluene dispersion (50 mg/mL) onto glass slides. Diffractograms were collected in laboratory atmosphere and room temperature from 10° to 45° with steps of 0.02 deg and 0.2 deg/min speed. Spectral peak deconvolution was performed using Fityk with "LorentzA" functions:

$$f(x) = \frac{1}{\pi a_2} \frac{a_0}{1 + (\frac{x - a_1}{a_2})^2} \tag{1.7}$$

where a_0 is function area, a_1 is center and a_2 half width at half maximum (HWHM). We connected peaks FWHM (2 x HWHM) to cristallites average dimension with Sherrer equation:[107]

$$D_{hkl} = \frac{K\lambda}{\beta_{hkl} \cos\theta} \tag{1.8}$$

where D_{hkl} is the average cristallite size perpendicular to [hkl] lattice plane direction, K is dimensionless shape factor that depends on different considerations (when in doubt, using 0,9 is recommended), λ is the referred to the X-ray source (Cu Kα, 0,154 nm), β_{hkl} is the FWHM in radiant of [hkl] planes family diffraction signal and θ is the Bragg angle. Note: our sample is not monodisperse in dimensions, thus the results are to be considered as an average indication. The deconvolution is considered only at relatively low Bragg angles, to avoid FWHM(θ) parametrization studies necessary when dealing with higher values.

Dynamic light scattering (DLS) Dynamic light scattering (DLS) analysis were performed using Malvern instrument Nano-S, whose data processing software is Zetasizer. The refractive index (RI) of the material was indicated as 1,9[108] with absorption 0,0 at the laser probe wavelength (633 nm). Dispersant was toluene (RI 1,496). Samples were prepared dispersing the solid product in toluene under magnetic stirring at 10 mg/mL and then diluiting 75 μL of that solution to 1 mL of pure toluene (0,075 mg/mL) and measured as prepared (not-evolved) and after 24h (evolved) under magnetic stirring. Analysis have been performed on 1 mL of solution in a 1 cm quartz cuvettes. Measurements have been collected at 25 °C (equilibration time: 30 seconds), positioning the laser focus in the centre of the cuvette (0,45 mm). Three consecutive measurements have been performed on each sample (each measurement had 17 runs). When data met quality criteria, such measurement were averaged to obtain the final volume distribution through a distribution fit. Given that the instrument collects scattering data only at a fixed angle configuration (175°), the result doesn't consider anisotropy in samples. In this non-spherical case, the output value must be considered thus as the diameter of an approximate sphere around the nanobrick sample, resulting in a bigger value respect to TEM evaluation.

1.10.5.2 Optical/Spectroscopical characterization

Absorption measurements

Classical Steady-state conditions The UV-visible absorption spectra were recorded using a Jasco V-570 UV-Vis-NIR absorption spectrophotometer. Data were collected with 200 nm/min scanning speed in 300-800 nm range (data pitch 1 nm). All in solution samples were prepared by diluting NC dispersions in toluene (from 10 mg/mL to measurements concentration around 0,1-0,05 mg/mL) in 1 cm path length quartz cuvette, if not otherwise stated. The in-film samples were placed into the instrument with the proper sample holder as they was. The peak decovolution was performed with Fityk using GaussianA function (equation 1.6). The Gaussian center was approximately converted in eV from equation

$$\lambda = \frac{hc}{E} \tag{1.9}$$

where λ is the peak center, h is the Planck costant (6.62607015 x $10^{-34}\frac{m^2Kg}{s}$) and E is the corresponding E in eV. The correlation between peak center energy and the expected shortest side dimension (because it's the one that with confinement action affects energy gap) is derived from a theoretical work by Diliberto et al.[34] and can be aprooximated with:

$$D = Nx0,59nm//N = (-6,59)\ln\frac{eV - 2,45}{1,23} \tag{1.10}$$

where D is the shortest dimension, 0,59 nm is the cubic unit cell length (making the hypothesis that the critsalline structure is cubic, on which the calculation that led to this equation is built), N is the number of monolayers in the shortest direction, eV is the energy gap (in this case, approxiamted to the absorption peak maximum absorption). Despite all the approximations, the expected results was comparable with statistical analysis distribution from TEM images.

Absorption over the time To perform in solution evolution characterization, the dried solid is firstly dispersed at 10 mg/mL, magnetically stirred for 5 min and then

diluted to 0,1 mg/mL directly into the 1 cm pathway quartz cuvette placed inside the instrument to start the measurements as soon as possible. For high viscosity procedure output, considering that no solid product was isolated, we dispersed 0,1 mL of the crude mixture in 2 mL of fresh toluene directly inside the cuvette. The measurements were carried out with conditions reported for 1.10.5.2 and the same solution and cuvette is employed to collect al the spectra during time. Usually, after the first spectrum, we collected data minute after minute for the first 5 min and then after 10, 15, 30, 45, 1h and 24h (untill 48 h where necessary).

Photoluminescence measurements

Classical Steady-state conditions The PL spectra of all samples were measured on a Jasco FP-6200 fluorescence spectrofluorometer in a 90° geometry. The samples were excited with 365 nm output of the continuous xenon lamp (Xe900) (if not otherwise stated). The excitation slit width was set at 5 nm, the detection slit width was set at 5 nm, and the spectra were recorded with 1 nm steps and a scanning speed of 250 nm/min. The PL spectra were collected over a 375-600 nm spectral range. In solution and in-film samples were prepared as reproted in 1.10.5.2. The peak deconvolution was performed as reported for 1.10.5.2.

PL over the time PL evolution measurements were always performed rightly after absorption collection, on the same samples. Preparation is thus the same reported in 1.10.5.2 and instrument parameters in 1.10.5.2.

Photoluminescence quantum yield (PLQY)

Relative PLQY The relative QY was calcuated in comparison with fluorescein (free acid in EtOH, $2,7x10^{-4}$ M) for $CsPbBr_3$ related samples and quinine sulfate (1 M in H_2So_4) for $CsPbCl_3$ species. For the former, PLQY was calculated at 430 nm , for the latter at 355 nm. In every case, weighted solid samples were redispersed in an anhydrous 20 mL transparent vial and diluted with anyhdrous toluene to 0,1 mg/mL concentration. Measurement were performed by Andrea Erroi, from Prof. Sergio Brovelli's group.

Absolute PLQY The PLQYs were measured using a FLS920 Edinburgh Instruments spectrofluorimeter equipped with an integrating sphere. The optical density of the NC solution was 0,15-0,20 at the excitation wavelength of 405 nm (3,06 eV, obtained with picosecond laser diodes GaN - Picoquant LDH-P series, 70 ps pulses). The emitted light was collected with a phototube coupled to a Cornerstone 260 VIS-NIR monochromator (ORIEL) and a time-correletad single-photon counting unit (time resolution around 400 ps). Measurement were performed by Andrea Erroi, from Prof. Sergio Brovelli's group.

Radioluminscence measurements

Radioluminescence(RL) Nanocomposite samples were excited by unfiltered X-ray irradiation using Philips PW2274 X-ray tube, with a tungsten target, equipped with a beriullim window and operating at 20 kV. At this operating voltage, a continuous X-ray spectrum is produced by bremsstrahlung mechanism superimposed to the L and M

transition lines of tungsten, due to the impact of electrons generated through thermoionic effect and accellerated onto a tungsten target. Measurement were performed by Francesca Cova, from Prof. Anna Vedda's group.

Lightyield (LY) The LY is obtained by a direct comparison of the RL response of nanocomposite (10 x 5 mm, 3-mm-thick) and commercial 3-mm-thick EJ276 reference scintillator, with a reported LY of 8600 photons MeV^{-1}. The thickness of sample is largely greater than the penetration depth of X-rays, taking into account the X-ray linear attenuation coefficient of 1020 cm^{-1} at the mean X-ray energy of 7,2 KeV.[109] This approach leads to an experimental uncertainty of 30% on the LY values. Measurement were performed by Francesca Cova, from Prof. Anna Vedda's group.

γ rays irradiation measurements A 10 mm x 5 mm (3 mm thick) loaded nanocomposite (0,2 wt%) was laser cut in 5 same dimensions (x cm x x cm) pieces, one for each dose (0, 10, 100, 500 and 1000 kGy). ThThe samples were irradiated in a pool-type γ-ray irradiation chamber equipped with a ^{60}Co (mean energy, 1,25 MeV) γ-source rod array, uniformly irradiating samples at 3,05 $kGy_{air}h^{-1}$ dose rate. Nanocomposites were irradiated at different cumulative absorbed doses up to 1 MGy by varying irradiation time. The irradiation has been carried out at the gamma irradiation Calliope facility at ENEA-Casavvia Reasearch center.[110] No γ-ray-attenuating material was interposed between the source and NC samples. The given dose is in air.

Time resolved photoluminescence intensity (TRPL) TRPL were carried out on toluene solutions of NCs. The samples were excited using a frequency tripled pulsed Nd:YAG laser at 3,49 eV with a 100 Hz repetition rate (pulse duration, 5 ns), and the emitted light was collected with a photon counting unit (resolution better than the pulse duration). Time-correlated single photon counting (TCSPC) measurements are conducted in the same instrument using a pulsed 400 nm laser. TCSPC measurements are performed on diluted NC dispersions (0,1 mg/mL), in a 45° geometry to minimize the self-absorption effects. Measurement were performed by Valerio Pinchetti, from Prof.Sergio Brovelli's group.

Correlation between optical density and concentration of $CsPbBr_3$ NCs through intrinsic extinction coefficient We adopted this procedure from a De Roo et al.,[63] where the following equation was derived:

$$A(\lambda) = \frac{N_A V_{NC} L}{ln10 V_0} c\mu_i(\lambda) = k(c)\mu_i(\lambda) \tag{1.11}$$

where A is sample absorbance at a given concentration (in our case, nominal 0,125 mg/mL); N_A is Avogadro's number (6,022 x 10^{22i3}); V_{NC} is NC unit cell volume (0,2 nm^3, in the hypothesis of cubic crystal structure); L is cuvette length (1 cm = 10^7 nm); V_0 is solvent volume (2 x $10^{21} nm^3$); c is NCs concentration; μ_i is intrinsic extinction coefficient for each wavelength between 320-550 nm reported in reference article.[63] The model based on a linear fit of the absorbance value in function of μ_i suggests that the angular coefficient (k(c)) is proportional to the effective material concentration in sample. Samples produced with both homogenization types (1,2 L batches) are weighted and dispersed directly in toluene at a nominal concentration of 1 mg/mL and stirred overnight. They are then

diluted at nominal concentrations of 0.125 mg/mL and absorption spectra are collected. Absorption values are plotted in function of intrinsic extinction coefficient between 320 and 550 nm with steps of 2 nm and a linear fitting is performed. The results are here reported:

$$TES1,2L : y = (0,006 \pm 0,004) + (6,4 \times 10^{-6} \pm 3 \times 10^{-9})x; R^2 = 0,997 \quad (1.12)$$

$$MSS1,2L : y = (0,03 \pm 0,003) + (5,3 \times 10^{-9} \pm 3 \times 10^{-9})x; R^2 = 0,996 \quad (1.13)$$

k(c) value is higher for TES 1,2 L respect to MSS 1,2 L, suggesting that the effective concentration of active material (despite weight the same) is higher for the former. Morover, if we extract expected concentration from the slope of TES sample and convert the value in mg/mL, we obtaine 0,07 mg/mL, which 56 wt% respect to weighted value of 0,125 mg/mL. This result is slightly slower then TGA measurements (around 65 wt%): this can be due to deviation of our condition to hypotheses made to obtain this formula.

1.10.5.3 Thermal characterization

Thermogravimetrical analysis (TGA) Measurements were carried out on TGA/DSC STARe System (Mettler TOLEDO). Solid state samples (around 15 mg) were directly put inside an allumina crucible. Method: from 30 °C to 600 °C, heating at 10 °C/min, under N_2 flow (50 mL/min).

1.10.5.4 Compositional characterizations

X-ray fluorescence (XRF) Energy-Dispersive X-ray Fluorescence Spectroscopy (XRF). Energy-dispersive XRF analysis was performed with a Bruker Artax 200 EDXRF spectrometer, equipped with an X-ray tube (Mo anode) with a beam collimated down to 0,65 mm in diameter. The induced characteristic X-ray fluorescence passes to a semiconductor detector, which works according to the drift chamber principle (silicon drift detector). A Mo transmission filter (12.5 μ thick) was used. The working conditions were 30 kV and 0.9 mA with an acquisition time of 1800 s for each measurement. Measurement were performed by Porf. Roberto Lorenzi.

In solution ^{1}H nuclear magnetic resonance (^{1}H NMR) ^{1}H NMR measurements were conducted at 300 K on a Bruker Avance NEO 400 MHz spectrometer equipped with BBFO probe. TBAB is directly dissolved in deuterated benzene (C_6D_6). OLAM/PA 1:1 mol ratio are previously mixed under magnetic stirring and then dissolved in C_6D_6. $CsPbBr_3$ samples were dispersed from solid state directly in C_6D_6. The discarded supernatant was dried from iPrOH and Heptane solvents under reduced pressure and then a portion has been dissolved directly in C_6D_6. All samples were analyzed at a concentration of 20 mg/mL in glass NMR tubes. All ^{1}H spectra are referred to the signal of residual nondeuterated solvent (calibrating at 7.16 ppm singlet peak from benzene). Measurement were performed by Giorgio Patriarca.

Note: TBAB is detectable in $CsPbBr_3$ NCs spectrum as well. It is probably embedded into the outer ligands shell.

Inductively-coupled plasma optical emission spectroscopy (ICP-OES) The samples concentration of Pb and Cs ions was detected by an inductively coupled plasma-optical emission spectro-photometer (ICP-EOS OPTIMA 7000 DV Perkin Elmer). Each

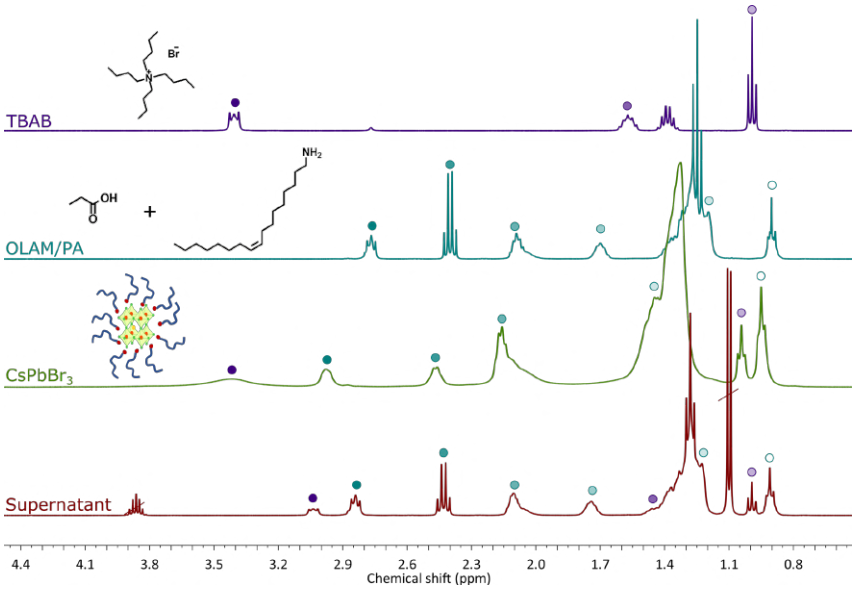

Figure 1.48 ^{1}H NMR in deuterad benzene C_6D_6 of respectively tetrabutylammonium bromide (TBAB), oleylamine(Olam)/propionic acid (PA) 1:1 mol ratio, a $CsPbBr_3$ sample as prepared and dried under reduced pressure supernatant after reaction.

sample was digested in multiwave 5000 (Anton Paar) by adding nitric acid (HNO_3 65%) and hydrogen peroxide (H_2O_2 30%) 8:2 vol. ratio. This process was set in a closed system, to reduce risk of contamination. The system is programmed to reach power of 1000 W to ramp the detected temperature up to 220 °C. Then the instrument kept the vessel at 220 °C for 30 min. Digested samples were diluted with 10 mL of MQ water. After centrifuging and diluting (1:2), samples were ready to be analyzed by ICP-OES. A certified standard reference material of Pb 1000 mg/L and of Cs 1000 mg/L (Perkin Elmer) were used for calibration and quality control. The operating parameters of ICP-OES instrument were set up using emission line at 220,353 nm for Pb and 455,531 nm for Cs in Axial View and sample solution were measured in triplicate. The detection limit (DL) for Pb and Cs is 0,01 mg/L. Considering the different atomic weight of cesium and lead (respectively 132,9 g/mol and 207,2 g/mol), compatible with the ionic form, the Pb/Cs ratio of the two sample is comparable and around 1,2. This value is slightly higher than the stoichiometric expected ratio of 1. This is probably related to $[PbBr4]^{2-}$ terminated surfaces that are abundant in high surface area samples as these nanobricks. Analysis were performed by Maria Tringali, from DISAT facility (department of earth and environmental sciences)

1.10.5.5 Device characterization

J-V measurements on solar cells The current density voltage (JV) characteristics of produced devices were characterized under 1 sun (AM1.5G, 100 mWcm $^{-2}$), 200 lx and 1000 lx at room temperature without any device encapsulation by means of a Keithley 2420 source meter and a ABET sun 2000 solar simulator and LED lamp as light sources. During the measurements, the devices were masked with a black tape with 0.1 cm^2 aperture. The light intensity was calibrated with a silicon reference cell with a spectral mismatch factor of 0.99. For the JV measurement, the voltage step and delay time were 10mV and 10ms, respectively. The forward scan was from 0.5V to 1.8V, while the reverse scan was from 1.8V to 0.5V. Measurement were performed at CHOSE center of University of Rome Tor Vergata.

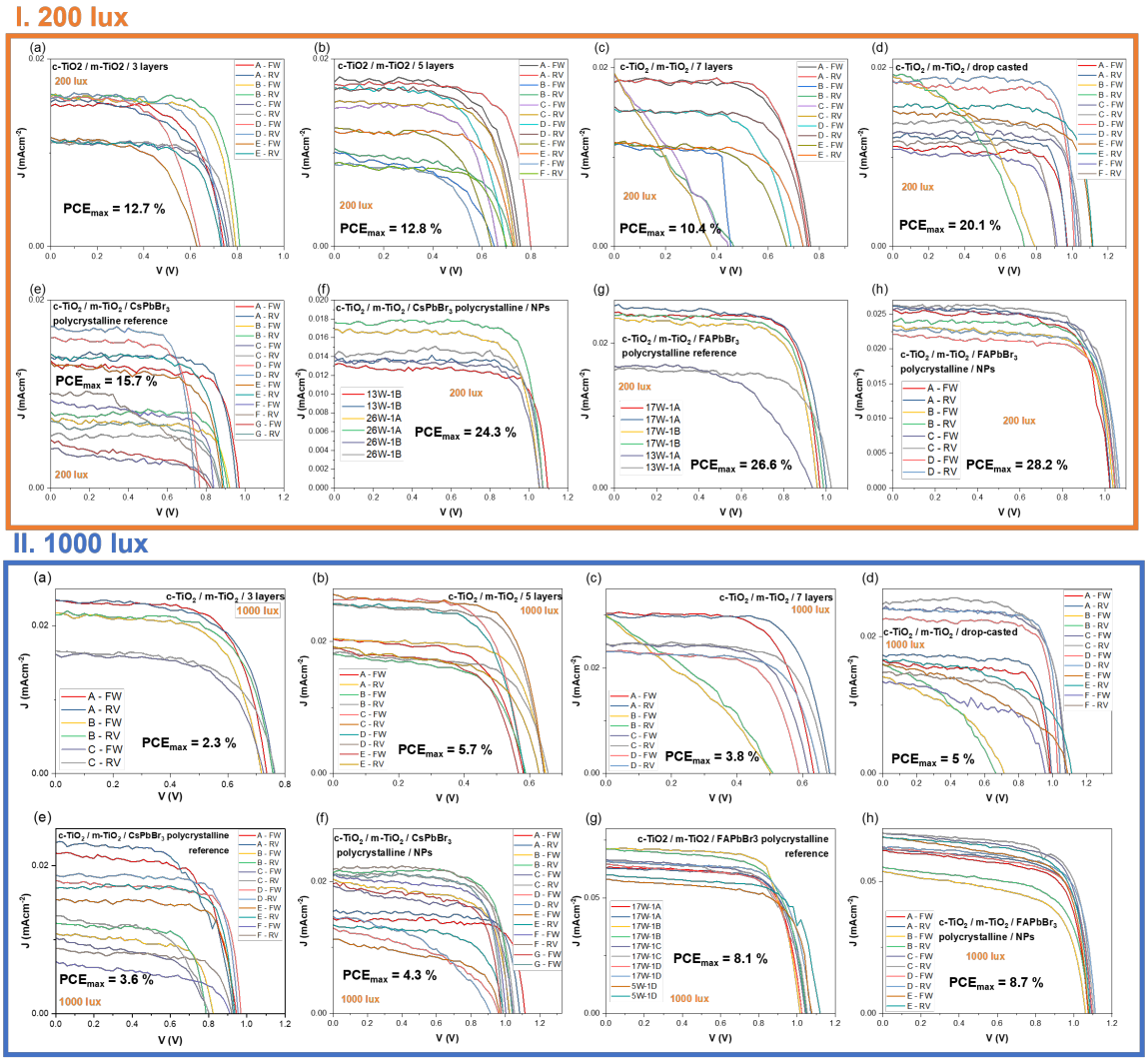

Figure 1.49 Photocurrent density in function of voltage of different cells in different devices for 200 and 1000 lux illumination.

1.10.5.6 Computational calculations

DFT Simulation of Surface Functionalization of $CsPbBr_3$. All calculations were perfomed by Dr Giovanni Diliberto, from Prof. Gianfranco Pacchioni's group. We try to gain some insights on:

- Possible surface termination of CsPbBr3 nanoplatelets
- Effect of functionalization with organic species

Brief summary of what we simulated:

- We prepared three different nanoplatelets models having different terminations. The three models are almost isoenergetic in vacuum (surface energy (E_S) $\propto$ 0.25-0.28 Jm^{-2}).
- We functionalized with i) OleilAmmoniumBromide (OAmBr), ii) OAmBr and Cesium Propionate (PrCs), iii) OAmBr and Cesium Oleate (OACs).

Main Results:

- The functionalization with OAmBr always results into a strong stabilization of the nanoplatelets; the most stable termination is the (001) exposing a CsBr layer.
- The further functionalization with PrCs or OACs provides an additional thermodynamic energy.
- The functionalization with OAmBr and OACs is systematically more favourable when compared to OAmBr and PrCs by around 0.3-0.5 eV. Then, the first should thermodynamically promote in-plane growth of thinner nanoplatelets.
- The (001)-CsBr is the most stable model upon functionalization.

The models are made by $CsPbBr_3$ (001) terminated with CsBr and $PbBr_2$ layers with surface defects to retain stoichiometry and stoichiometric $CsPbBr_3$ (110). Calculations have been performed at the level of Density Functional Theory (DFT) by means of the VASP code. The PBE parametrization of the exchange and correlation functional has been used. Conventional convergence criteria have been applied.

1.11 Acronyms

2D
ABS absorption
BuAm butylamine
Dow dowanol DPnP
FWHM full width at half maximum
Hept heptane
HRTEM high resolution transmission electron microscopy
iPrOH 2-propanol
LARP ligand assisted re-precipitation
LH light yield
LHP lead halide perovskite
NC nanocrystal
OA oleic acid
OACs caesium oleate
ODE octadecene
OAm oleylamine
OAmBr oleylammonium bromide
PA proprionic acid
PL photoluminescence
PLQY photoluminescence quantum yield
PrCs caesium propionate
PVK perovskite
PXRD powder x-ray diffraction
RL radioluminescence
RPM rotations per minute
RT room temperature
SAED single area electron diffraction
TBAB tetrabutylammonium bromide
TFA trifluoroacetic acid
TGA thermogravimetric analysis
TTA-UC triplet-triplet annhilated up-conversion

Bibliography

[1] Roberts, S. *Phys. Rev.* **1947**, *71*, 890–895. doi: 10.1103/PhysRev.71.890.

[2] Smith, G. S. *Chem. Age* **1945**, *53*, 429.

[3] Von Hippel, A. *Reviews of Modern Physics* **1950**, *22*, 221. doi: 10.1103/revmodphys.22.221.

[4] Kieslich, G., Sun, S., and Cheetham, A. K. *Chem. Sci.* **2015**, *6*, 3430–3433. doi: 10.1039/C5SC00961H. Publisher: The Royal Society of Chemistry.

[5] Yu, J., Freeman, A. J., and Massidda, S. *Bonds, bands, charge transfer excitations and superconductivity: yttrium barium copper oxides (YBa2Cu3O7-δ vs. YBa2Cu3O6).* Plenum, p. 367. Copyright © 2022 American Chemical Society (ACS). All Rights Reserved.

[6] Kojima, A., Teshima, K., Shirai, Y., and Miyasaka, T. *Journal of the American Chemical Society* **2009**, *131*, 6050–6051. doi: 10.1021/ja809598r. Publisher: American Chemical Society.

[7] https://www.nrel.gov/pv/cell-efficiency.html.

[8] Jiang, Q., Tong, J., Xian, Y., Kerner, R. A., Dunfield, S. P., Xiao, C., Scheidt, R. A., Kuciauskas, D., Wang, X., Hautzinger, M. P., Tirawat, R., Beard, M. C., Fenning, D. P., Berry, J. J., Larson, B. W., Yan, Y., and Zhu, K. *Nature* **2022**, *611*, 278–283. doi: 10.1038/s41586-022-05268-x.

[9] Shikoh, A. S. and Polyakov, A. *physica status solidi (a)* **2020**, *217*, 2000441. doi: 10.1002/pssa.202000441. Publisher: John Wiley & Sons, Ltd.

[10] Shamsi, J., Urban, A. S., Imran, M., De Trizio, L., and Manna, L. *Chemical Reviews* **2019**, *119*, 3296–3348. doi: 10.1021/acs.chemrev.8b00644. Publisher: American Chemical Society.

[11] Masi, S., Gualdrón-Reyes, A. F., and Mora-Seró, I. *ACS Energy Letters* **2020**, *5*, 1974–1985. doi: 10.1021/acsenergylett.0c00801. Publisher: American Chemical Society.

[12] Nedelcu, G., Protesescu, L., Yakunin, S., Bodnarchuk, M. I., Grotevent, M. J., and Kovalenko, M. V. *Nano Letters* **2015**, *15*, 5635–5640. doi: 10.1021/acs.nanolett.5b02404. Publisher: American Chemical Society.

[13] Jeon, S., Jung, M.-C., Ahn, J., Woo, H. K., Bang, J., Kim, D., Lee, S. Y., Woo, H. Y., Jeon, J., Han, M. J., Paik, T., and Oh, S. J. *Nanoscale Horiz.* **2020**, *5*, 960–970. doi: 10.1039/D0NH00029A. Publisher: The Royal Society of Chemistry.

[14] Umebayashi, T., Asai, K., Kondo, T., and Nakao, A. *Phys. Rev. B* **2003**, *67*, 155405. doi: 10.1103/PhysRevB.67.155405.

[15] Protesescu, L., Yakunin, S., Bodnarchuk, M. I., Krieg, F., Caputo, R., Hendon, C. H., Yang, R. X., Walsh, A., and Kovalenko, M. V. *Nano Letters* **2015**, *15*, 3692–3696. doi: 10.1021/nl5048779. Publisher: American Chemical Society.

[16] Meloni, S., Palermo, G., Ashari-Astani, N., Grätzel, M., and Rothlisberger, U. *Journal of Materials Chemistry A* **2016**, *4*, 15997–16002. doi: 10.1039/C6TA04949D. Publisher: The Royal Society of Chemistry.

[17] Zhang, F., Zhong, H., Chen, C., Wu, X.-g., Hu, X., Huang, H., Han, J., Zou, B., and Dong, Y. *ACS Nano* **2015**, *9*, 4533–4542. doi: 10.1021/acsnano.5b01154. Publisher: American Chemical Society.

[18] Akkerman, Q. A., Rainò, G., Kovalenko, M. V., and Manna, L. *Nature Materials* **2018**, *17*, 394–405. doi: 10.1038/s41563-018-0018-4.

[19] Mooney, J. and Kambhampati, P. *The Journal of Physical Chemistry Letters* **2013**, *4*, 3316–3318. doi: 10.1021/jz401508t. Publisher: American Chemical Society.

[20] Dutta, A., Behera, R. K., Pal, P., Baitalik, S., and Pradhan, N. *Angewandte Chemie International Edition* **2019**, *58*, 5552–5556. doi: 10.1002/anie.201900374. Publisher: John Wiley & Sons, Ltd.

[21] Imran, M., Caligiuri, V., Wang, M., Goldoni, L., Prato, M., Krahne, R., De Trizio, L., and Manna, L. *Journal of the American Chemical Society* **2018**, *140*, 2656–2664. doi: 10.1021/jacs.7b13477. Publisher: American Chemical Society.

[22] Mondal, N., De, A., and Samanta, A. *ACS Energy Letters* **2019**, *4*, 32–39. doi: 10.1021/acsenergylett.8b01909. Publisher: American Chemical Society.

[23] Pan, Y., Zhang, Y., Kang, W., Deng, N., Yan, Z., Sun, W., Kang, X., and Ni, J. *Materials Advances* **2022**, *3*, 4053–4068. doi: 10.1039/d2ma00100d. Publisher: Royal Society of Chemistry.

[24] Chen, J., Du, W., Shi, J., Li, M., Wang, Y., Zhang, Q., and Liu, X. *InfoMat* **2020**, *2*, 170–183. doi: 10.1002/inf2.12051. Publisher: John Wiley & Sons, Ltd.

[25] Cao, M., Xu, Y., Li, P., Zhong, Q., Yang, D., and Zhang, Q. *Journal of Materials Chemistry C: Materials for Optical and Electronic Devices* **2019**, *7*, 14412–14440. doi: 10.1039/c9tc03978c. Publisher: Royal Society of Chemistry.

[26] Huo, C., Liu, X., Song, X., Wang, Z., and Zeng, H. *The Journal of Physical Chemistry Letters* **2017**, *8*, 4785–4792. doi: 10.1021/acs.jpclett.7b02028. Publisher: American Chemical Society.

[27] Cardenas-Morcoso, D., Gualdrón-Reyes, A. F., Ferreira Vitoreti, A. B., García-Tecedor, M., Yoon, S. J., Solis de la Fuente, M., Mora-Seró, I., and Gimenez, S. *The Journal of Physical Chemistry Letters* **2019**, *10*, 630–636. doi: 10.1021/acs.jpclett.8b03849. Publisher: American Chemical Society.

[28] Zhu, Y., Liu, Y., Miller, K. A., Zhu, H., and Egap, E. *ACS Macro Letters* **2020**, *9*, 725–730. doi: 10.1021/acsmacrolett.0c00232. Publisher: American Chemical Society.

[29] Ramasamy, P., Lim, D.-H., Kim, B., Lee, S.-H., Lee, M.-S., and Lee, J.-S. *Chemical Communications* **2016**, *52*, 2067–2070. doi: 10.1039/C5CC08643D. Publisher: The Royal Society of Chemistry.

[30] Parida, B., Yoon, S., Jeong, S. M., Cho, J. S., Kim, J.-K., and Kang, D.-W. *Solar Energy Materials & Solar Cells* **2020**, *204*, 110212. doi: 10.1016/j.solmat.2019.110212. Publisher: Elsevier B.V.

[31] Sichert, J. A., Tong, Y., Mutz, N., Vollmer, M., Fischer, S., Milowska, K. Z., García Cortadella, R., Nickel, B., Cardenas-Daw, C., Stolarczyk, J. K., Urban, A. S., and Feldmann, J. *Nano Letters* **2015**, *15*, 6521–6527. doi: 10.1021/acs.nanolett.5b02985. Publisher: American Chemical Society.

[32] Akkerman, Q. A., Nguyen, T. P. T., Boehme, S. C., Montanarella, F., Dirin, D. N., Wechsler, P., Beiglböck, F., Rainò, G., Erni, R., Katan, C., Even, J., and Kovalenko, M. V. *Science* **2022**, *0*. doi: 10.1126/science.abq3616. Publisher: American Association for the Advancement of Science.

[33] Akkerman, Q. A., Motti, S. G., Srimath Kandada, A. R., Mosconi, E., D'Innocenzo, V., Bertoni, G., Marras, S., Kamino, B. A., Miranda, L., De Angelis, F., Petrozza, A., Prato, M., and Manna, L. *Journal of the American Chemical Society* **2016**, *138*, 1010–1016. doi: 10.1021/jacs.5b12124. Publisher: American Chemical Society.

[34] Di Liberto, G., Fatale, O., and Pacchioni, G. *Physical Chemistry Chemical Physics* **2021**, *23*, 3031–3040. doi: 10.1039/D0CP06245F. Publisher: The Royal Society of Chemistry.

[35] Kostopoulou, A., Sygletou, M., Brintakis, K., Lappas, A., and Stratakis, E. *Nanoscale* **2017**, *9*, 18202–18207. doi: 10.1039/C7NR06404G. Publisher: The Royal Society of Chemistry.

[36] Akkerman, Q. A., Abdelhady, A. L., and Manna, L. *The Journal of Physical Chemistry Letters* **2018**, *9*, 2326–2337. doi: 10.1021/acs.jpclett.8b00572. Publisher: American Chemical Society.

[37] Dey, A., Ye, J., De, A., Debroye, E., Ha, S. K., Bladt, E., Kshirsagar, A. S., Wang, Z., Yin, J., Wang, Y., Quan, L. N., Yan, F., Gao, M., Li, X., Shamsi, J., Debnath, T., Cao, M., Scheel, M. A., Kumar, S., Steele, J. A., Gerhard, M., Chouhan, L., Xu, K., Wu, X.-g., Li, Y., Zhang, Y., Dutta, A., Han, C., Vincon, I., Rogach, A. L., Nag, A., Samanta, A., Korgel, B. A., Shih, C.-J., Gamelin, D. R., Son, D. H., Zeng, H., Zhong, H., Sun, H., Demir, H. V., Scheblykin, I. G., Mora-Seró, I., Stolarczyk, J. K., Zhang, J. Z., Feldmann, J., Hofkens, J., Luther, J. M., Pérez-Prieto, J., Li, L., Manna, L., Bodnarchuk, M. I., Kovalenko, M. V., Roeffaers, M. B. J., Pradhan, N., Mohammed, O. F., Bakr, O. M., Yang, P., Müller-Buschbaum, P., Kamat, P. V., Bao, Q., Zhang, Q., Krahne, R., Galian, R. E., Stranks, S. D., Bals, S., Biju, V., Tisdale, W. A., Yan, Y., Hoye, R. L. Z., and Polavarapu, L. *ACS Nano* **2021**, *15*, 10775–10981. doi: 10.1021/acsnano.0c08903. Publisher: American Chemical Society.

[38] Liu, Y., Wang, Y., Cheng, H., Ma, Z., Li, Q., Wang, G., Pan, D., Wang, L., and Ming, J. *Chemistry - A European Journal* **2022**, *28*, e202104463. doi: 10.1002/chem.202104463. Publisher: Wiley-VCH Verlag GmbH & Co. KGaA.

[39] Akkerman, Q. A., Gandini, M., Di Stasio, F., Rastogi, P., Palazon, F., Bertoni, G., Ball, J. M., Prato, M., Petrozza, A., and Manna, L. *Nature Energy* **2017**, *2*, 16194. doi: 10.1038/nenergy.2016.194.

[40] Li, X., Wu, Y., Zhang, S., Cai, B., Gu, Y., Song, J., and Zeng, H. *Advanced Functional Materials* **2016**, *26*, 2435–2445. doi: 10.1002/adfm.201600109. Publisher: John Wiley & Sons, Ltd.

[41] Montaguti, P., Melloni, E., and Cavalletti, E. *Arzneimittel-Forschung* **1994**, *44*, 566.

[42] Ye, F., Zhang, H., Li, W., Yan, Y., Cai, J., Gurney, R. S., Pearson, A. J., Liu, D., and Wang, T. *Small Methods* **2019**, *3*, 1800489. doi: 10.1002/smtd.201800489. Publisher: John Wiley & Sons, Ltd.

[43] Di Stasio, F., Christodoulou, S., Huo, N., and Konstantatos, G. *Chemistry of Materials* **2017**, *29*, 7663–7667. doi: 10.1021/acs.chemmater.7b02834. Publisher: American Chemical Society.

[44] Sorrentino, R., Gandini, M., Figueroa Tapia, J. M., and Petrozza, A. *Sustainable Energy & Fuels* **2020**, *4*, 171–176. doi: 10.1039/C9SE00502A. Publisher: The Royal Society of Chemistry.

[45] Dai, J., Xi, J., Zu, Y., Li, L., Xu, J., Shi, Y., Liu, X., Fan, Q., Zhang, J., Wang, S., Yuan, F., Dong, H., Jiao, B., Hou, X., and Wu, Z. *Nano Energy* **2020**, *70*, 104467. doi: 10.1016/j.nanoen.2020.104467.

[46] Akkerman, Q. A., Rainò, G., Kovalenko, M. V., and Manna, L. *Nature Materials* **2018**, *17*, 394–405. doi: 10.1038/s41563-018-0018-4.

[47] *The critical issue of using lead for sustainable massive production ...*, **2022**.

[48] Z., M. R. X. Q. Y. C. T. W. Y. *Journal of Hazardous Materials* **2022**, *426*, 127848. doi: 10.1016/j.jhazmat.2021.127848. Publisher: Elsevier.

[49] https://www.epa.gov/lead.

[50] Ke, W., Stoumpos, C. C., and Kanatzidis, M. G. *Advanced Materials* **2019**, *31*, 1803230. doi: 10.1002/adma.201803230.

[51] Park, S. Y., Park, J.-S., Kim, B. J., Lee, H., Walsh, A., Zhu, K., Kim, D. H., and Jung, H. S. *Nature Sustainability* **2020**, *3*, 1044–1051. doi: 10.1038/s41893-020-0586-6.

[52] Jiang, Y., Qiu, L., Juarez-Perez, E. J., Ono, L. K., Hu, Z., Liu, Z., Wu, Z., Meng, L., Wang, Q., and Qi, Y. *Nature Energy* **2019**, *4*, 585–593. doi: 10.1038/s41560-019-0406-2.

[53] Chen, S., Deng, Y., Xiao, X., Xu, S., Rudd, P. N., and Huang, J. *Nature Sustainability* **2021**, *4*, 636–643. doi: 10.1038/s41893-021-00701-x.

[54] Mallick, A. and Visoly-Fisher, I. *Materials Advances* **2021**, *2*, 6125–6135. doi: 10.1039/D1MA00355K.

[55] Venugopalan, V., Sorrentino, R., Topolovsek, P., Nava, D., Neutzner, S., Ferrari, G., Petrozza, A., and Caironi, M. *Chem* **2019**, *5*, 868–880. doi: 10.1016/j.chempr.2019.01.007.

[56] Yang, Y., Qin, H., Jiang, M., Lin, L., Fu, T., Dai, X., Zhang, Z., Niu, Y., Cao, H., Jin, Y., Zhao, F., and Peng, X. *Nano Letters* **2016**, *16*, 2133–2138. doi: 10.1021/acs.nanolett.6b00730. Publisher: American Chemical Society.

[57] Almeida, G., Goldoni, L., Akkerman, Q., Dang, Z., Khan, A. H., Marras, S., Moreels, I., and Manna, L. *ACS Nano* **2018**, *12*, 1704–1711. doi: 10.1021/acsnano.7b08357. Publisher: American Chemical Society.

[58] Ceriani, C., Ghiglietti, E., Sassi, M., Mattiello, S., and Beverina, L. *Organic Process Research & Development* **2020**, *24*, 2604–2610. doi: 10.1021/acs.oprd.0c00285. Publisher: American Chemical Society.

[59] Quarta, D., Imran, M., Capodilupo, A.-L., Petralanda, U., van Beek, B., De Angelis, F., Manna, L., Infante, I., De Trizio, L., and Giansante, C. *The Journal of Physical Chemistry Letters* **2019**, *10*, 3715–3726. doi: 10.1021/acs.jpclett.9b01634. Publisher: American Chemical Society.

[60] Elisabetta, F., Francesca, C., Davide, A., Cinzia, G., Annamaria, P., Leonardo, T., Francesca, P., Nicoletta, D., Roberto, G., Gian Paolo, S., Angela, A., M., L. C., and Marinella, S. *Nano Research* **2019**, *12*, 1155–1166. doi: 10.1007/s12274-019-2371-2.

[61] Li, Y., Huang, H., Xiong, Y., Kershaw, S. V., and Rogach, A. L. *CrystEngComm* **2018**, *20*, 4900–4904. doi: 10.1039/C8CE00911B. Publisher: The Royal Society of Chemistry.

[62] Cho, J., Jin, H., Sellers, D. G., Watson, D. F., Son, D. H., and Banerjee, S. *Journal of Materials Chemistry C* **2017**, *5*, 8810–8818. doi: 10.1039/C7TC02194A. Publisher: The Royal Society of Chemistry.

[63] De Roo, J., Ibáñez, M., Geiregat, P., Nedelcu, G., Walravens, W., Maes, J., Martins, J. C., Van Driessche, I., Kovalenko, M. V., and Hens, Z. *ACS Nano* **2016**, *10*, 2071–2081. doi: 10.1021/acsnano.5b06295. Publisher: American Chemical Society.

[64] Travis, W., Glover, E. N. K., Bronstein, H., Scanlon, D. O., and Palgrave, R. G. *Chem. Sci.* **2016**, *7*, 4548–4556. doi: 10.1039/C5SC04845A. Publisher: The Royal Society of Chemistry.

[65] Pan, A., He, B., Fan, X., Liu, Z., Urban, J. J., Alivisatos, A. P., He, L., and Liu, Y. *ACS Nano* **2016**, *10*, 7943–7954. doi: 10.1021/acsnano.6b03863. Publisher: American Chemical Society.

[66] Boote, B. W., Andaraarachchi, H. P., Rosales, B. A., Blome-Fernández, R., Zhu, F., Reichert, M. D., Santra, K., Li, J., Petrich, J. W., Vela, J., and Smith, E. A. *ChemPhysChem* **2019**, *20*, 2647–2656. doi: 10.1002/cphc.201900432. Publisher: John Wiley & Sons, Ltd.

[67] Correa-Baena, J.-P., Saliba, M., Buonassisi, T., Grätzel, M., Abate, A., Tress, W., and Hagfeldt, A. *Science* **2017**, *358*, 739–744. doi: 10.1126/science.aam6323. Publisher: American Association for the Advancement of Science.

[68] Qi, Z., Gao, H., Yang, X., Chen, Y., Zhang, F.-Q., Qu, M., Li, S.-L., and Zhang, X.-M. *Inorganic Chemistry* **2021**, *60*, 15136–15140. doi: 10.1021/acs.inorgchem.1c02732. Publisher: American Chemical Society.

[69] Yunakova, O. N., Miloslavskii, V. K., and Kovalenko, E. N. *Optics and Spectroscopy* **2012**, *112*, 91–96. doi: 10.1134/S0030400X12010249.

[70] https://www.dow.com/en-us/pdp.dowanol-dpnp-glycol-ether.41173z.html.

[71] Galliani, D., Mascheroni, L., Sassi, M., Turrisi, R., Lorenzi, R., Scaccabarozzi, A., Stingelin, N., and Beverina, L. *Advanced Optical Materials* **2015**, *3*, 1164–1168. doi: 10.1002/adom.201500073. Publisher: John Wiley & Sons, Ltd.

[72] Wang, H., Zhang, X., Wu, Q., Cao, F., Yang, D., Shang, Y., Ning, Z., Zhang, W., Zheng, W., Yan, Y., Kershaw, S. V., Zhang, L., Rogach, A. L., and Yang, X. *Nature Communications* **2019**, *10*, 665. doi: 10.1038/s41467-019-08425-5.

[73] Akkerman, Q. A., D'Innocenzo, V., Accornero, S., Scarpellini, A., Petrozza, A., Prato, M., and Manna, L. *Journal of the American Chemical Society* **2015**, *137*, 10276–10281. doi: 10.1021/jacs.5b05602. Publisher: American Chemical Society.

[74] Imran, M., Ijaz, P., Goldoni, L., Maggioni, D., Petralanda, U., Prato, M., Almeida, G., Infante, I., and Manna, L. *ACS Energy Letters* **2019**, *4*, 819–824. doi: 10.1021/acsenergylett.9b00140. Publisher: American Chemical Society.

[75] Fang, Z., He, H., Gan, L., Li, J., and Ye, Z. *Advanced Science* **2018**, *5*, 1800736. doi: 10.1002/advs.201800736. Publisher: John Wiley & Sons, Ltd.

[76] Liu, F.-W., Biesold, G., Zhang, M., Lawless, R., Correa-Baena, J.-P., Chueh, Y.-L., and Lin, Z. *Materials Today* **2021**, *43*, 185–197. doi: 10.1016/j.mattod.2020.11.024.

[77] Chen, B., Fei, C., Chen, S., Gu, H., Xiao, X., and Huang, J. *Nature Communications* **2021**, *12*, 5859. doi: 10.1038/s41467-021-26121-1.

[78] Green, M. A. and Keevers, M. J. *Progress in Photovoltaics: Research and Applications* **1995**, *3*, 189–192. doi: 10.1002/pip.4670030303. Publisher: John Wiley & Sons, Ltd.

[79] Wang, Z., Zeng, L., Zhang, C., Lu, Y., Qiu, S., Wang, C., Liu, C., Pan, L., Wu, S., Hu, J., Liang, G., Fan, P., Egelhaaf, H.-J., Brabec, C. J., Guo, F., and Mai, Y. *Advanced Functional Materials* **2020**, *30*, 2001240. doi: 10.1002/adfm.202001240. Publisher: John Wiley & Sons, Ltd.

[80] https://lspdd.org/app/en/lamps/2476.

[81] https://dx.doi.org/10.21227/mxr7-p365.

[82] Dujardin, C., Auffray, E., Bourret-Courchesne, E., Dorenbos, P., Lecoq, P., Nikl, M., Vasil'ev, A. N., Yoshikawa, A., and Zhu, R.-Y. *IEEE Transactions on Nuclear Science* **2018**, *65*, 1977–1997. doi: 10.1109/TNS.2018.2840160.

[83] Spahn, M. *PIXEL 2012* **2013**, *731*, 57–63. doi: 10.1016/j.nima.2013.05.174.

[84] Haff, R. P. and Toyofuku, N. *Sensing and Instrumentation for Food Quality and Safety* **2008**, *2*, 262–273. doi: 10.1007/s11694-008-9059-8.

[85] Kim, C., Lee, W., Melis, A., Elmughrabi, A., Lee, K., Park, C., and Yeom, J.-Y. *Crystals* **2021**, *11*. doi: 10.3390/cryst11060669.

[86] Drakos, I., Kenny, P., Fearn, T., and Speller, R. *Crime Science* **2017**, *6*, 1. doi: 10.1186/s40163-016-0062-9.

[87] Duan, X., Cheng, J., Zhang, L., Xing, Y., Chen, Z., and Zhao, Z. *Nuclear Instruments and Methods in Physics Research Section A: Accelerators, Spectrometers, Detectors and Associated Equipment* **2009**, *598*, 439–444. doi: 10.1016/j.nima.2008.08.151.

[88] Datta, A., Zhong, Z., and Motakef, S. *Scientific Reports* **2020**, *10*, 20097. doi: 10.1038/s41598-020-76647-5.

[89] Shevelev, V. S., Ishchenko, A. V., Vanetsev, A. S., Nagirnyi, V., and Omelkov, S. I. *Journal of Luminescence* **2022**, *242*, 118534. doi: 10.1016/j.jlumin.2021.118534. Publisher: Elsevier B.V.

[90] Piroue, P. A. *IEEE Transactions on Nuclear Science* **1966**, *13*, 54–59. doi: 10.1109/TNS.1966.4324330.

[91] Krause, P., Rogers, E., Birowosuto, M. D., Pei, E., Qibing, Vasilev, A. N., and Bizarri, G. *Heliyon* **2022**, *8*, e09754. doi: 10.1016/j.heliyon.2022.e09754.

[92] van Eijk, C. W. E. *Nuclear Instruments & Methods in Physics Research, Section A: Accelerators, Spectrometers, Detectors, and Associated Equipment* **2001**, *460*, 1–14. doi: 10.1016/s0168-9002(00)01088-3. Publisher: Elsevier Science B.V.

[93] Hajagos, T. J., Liu, C., Cherepy, N. J., and Pei, Q. *Advanced Materials (Weinheim, Germany)* **2018**, *30*, n/a. doi: 10.1002/adma.201706956. Publisher: Wiley-VCH Verlag GmbH & Co. KGaA.

[94] Swank, R. K. and Buck, W. L. *Review of Scientific Instruments* **1955**, *26*, 15–16. doi: 10.1063/1.1771230.

[95] Pronko, J., Fisher, T., and Chase, L. *Nuclear Instruments and Methods* **1979**, *163*, 227–235. doi: 10.1016/0029-554X(79)90053-3.

[96] Darukesha, B. H. M., Radhakrishna, V., and Rajanna, K. *Nuclear Instruments & Methods in Physics Research, Section A: Accelerators, Spectrometers, Detectors, and Associated Equipment* **2023**, *1048*, 167922. Publisher: Elsevier B.V.

[97] Heo, J. H., Shin, D. H., Park, J. K., Kim, D. H., Lee, S. J., and Im, S. H. *Advanced Materials (Weinheim, Germany)* **2018**, *30*, n/a. doi: 10.1002/adma.201801743. Publisher: Wiley-VCH Verlag GmbH & Co. KGaA.

[98] Cao, F., Yu, D., Ma, W., Xu, X., Cai, B., Yang, Y. M., Liu, S., He, L., Ke, Y., Lan, S., Choy, K.-L., and Zeng, H. *ACS Nano* **2020**, *14*, 5183–5193. doi: 10.1021/acsnano.9b06114. Publisher: American Chemical Society.

[99] Děcká, K., Pagano, F., Frank, I., Kratochwil, N., Mihóková, E., Auffray, E., and Čuba, V. *J. Mater. Chem. C* **2022**, *10*, 12836–12843. doi: 10.1039/D2TC02060B. Publisher: The Royal Society of Chemistry.

[100] F., B. S. B. L. V. A. M. S. C. and M., Z. *Italy, patent application* **2022**, doi: 06-2022-19.

[101] Hollingsworth, J. A. *Chemistry of Materials* **2013**, *25*, 1318–1331. doi: 10.1021/cm304161d. Publisher: American Chemical Society.

[102] Bae, W. K., Padilha, L. A., Park, Y.-S., McDaniel, H., Robel, I., Pietryga, J. M., and Klimov, V. I. *ACS Nano* **2013**, *7*, 3411–3419. doi: 10.1021/nn4002825. Publisher: American Chemical Society.

[103] Kundu, P., Anumol, E. A., Nethravathi, C., and Ravishankar, N. *Physical Chemistry Chemical Physics* **2011**, *13*, 19256–19269. doi: 10.1039/c1cp22343g. Publisher: Royal Society of Chemistry.

[104] Inagaki, T. and Takashima, R. *Nuclear Instruments and Methods in Physics Research* **1982**, *201*, 511–517. doi: 10.1016/0167-5087(82)90589-0.

[105] Henschel, H., Kuhnhenn, J., and Weinand, U. *Radiation Hard Optical Fibers*. Optica Publishing Group, p. OThI1. Journal Abbreviation: Optical Fiber Communication Conference and Exposition and The National Fiber Optic Engineers Conference.

[106] Vale, B. R. C., Socie, E., Burgos-Caminal, A., Bettini, J., Schiavon, M. A., and Moser, J.-E. *The Journal of Physical Chemistry Letters* **2020**, *11*, 387–394. doi: 10.1021/acs.jpclett.9b03282. Publisher: American Chemical Society.

[107] Scherrer, P. *Nachrichten von der Gesellschaft der Wissenschaften zu Göttingen, Mathematisch-Physikalische Klasse* **1918**, *1918*, 98–100.

[108] Yan, W., Mao, L., Zhao, P., Mertens, A., Dottermusch, S., Hu, H., Jin, Z., and Richards, B. S. *Optics Express* **2020**, *28*, 15706–15717. doi: 10.1364/OE.392246. Publisher: Optica Publishing Group.

[109] https://www.nist.gov/pml/x-ray-mass-attenuation-coefficients.

[110] https://hdl.handle.net/20.500.12079/6838.

Chapter 2

Stabilized micelles

2.1 Introduction

2.1.1 Surface active agents

"Surfactant" is the contraction of "SURFace ACTive AgeNT".[1] As the term itself explains, it refers to compounds that act on surface tension (indicated as γ^*) between two phases. They are amphiphilic species (from ancient greek $\alpha\mu\phi\iota c$ "amphis" = both and $\phi\iota\lambda\iota\alpha$ philia = loving),[3] consisting of two distinct portion covalently linked together: an hydrophilic head and a hydrophobic/lypophilic tail[4†].This intrinsic dual nature assures affinity with both polar and non-polar species, for this reason they are often called tensides or even "schizofrenic molecules" as well. The interface can be between liquid-liquid, liquid-solid or liquid-gas. When these species are dissolved in a biphasic medium, the polar head is prone to wet in water, whereas the tail in the organic solvent: they thus spontaneously accommodate at interphase, reducing the contact area and thus system energy. The process takes place spontaneously, since surfactant molecule free energy decreases respect to solubilzed form. Surfactants can be natural or synthetic: their discovery is uncertain but first reports dates back to ancient Babylon (2800 BC), where animal fats or vegetable oils were heated with wood ash to produce "soaps". In form of lipids, they also build cell membranes.[5] Head and tail nature can be extremely various, outstandingly expanding possible combinations. The former can be either neutral or charged (cationic, anionic, zwitterionic), whilst the latter can be linear, double or branched and chemically composed by hydrocarbons, siloxanes or fluorocarbon chains. The tail length can make them small molecules type or polymeric one. The balance between hydrophilic part respect to the overall surfactant is called HLB (hydrophilic-lypophilic balance) value, and it is a good indicator for system polarity. For nonionic species, it is defined as:[6]

$$HLB = \frac{molar mass of hydrophilic part}{molar mass of surfactant} \times 20 \tag{2.1}$$

It is clear that the intrinsic variability and uniqueness of this class of material make them very attractive for a large number of application field, especially as wetting agents, detergents, foam formers, dispersants and emulsifiers.[7]

*Surface tension of a fluid is defined as the work in mJ necessary to create 1 cm^2 of new surface.[2]

†"Hydrophilic/phobic" and "lypophilic" refer to the fact that they are mostly employed in water/organic molecules compatibilization.

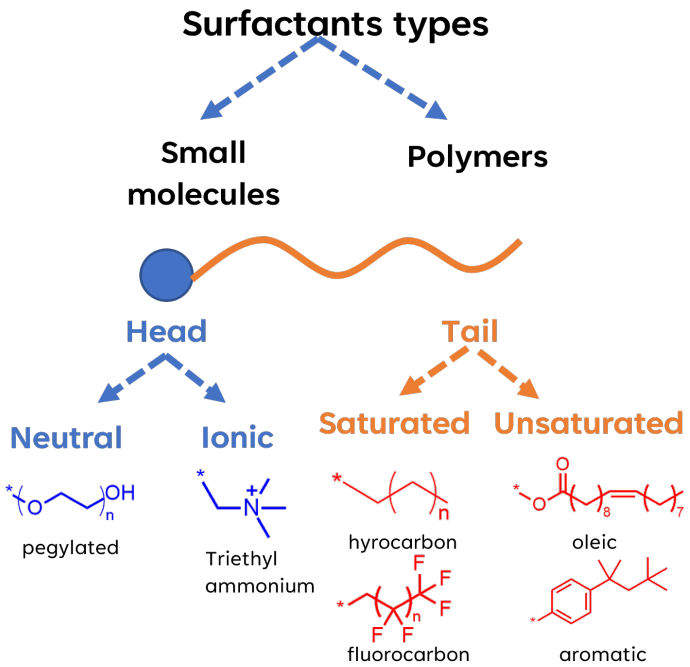

Figure 2.1 Scheme of different types of surfactant and examples of typical species employed as polar head and apolar tail.

2.1.2 Micelles

Surfactants dissolved in water*, at very low concentrations, behave as standard solubilized species. Continuously increasing their concentration, the system reaches a point where energy required to keep the hydrophobic tails in a polar environment is bigger than the loss of entropy that follows the aggregation process. Concentration at which amphiphiles aggregates into self-assembled colloidal structures (micellization process), is called "critical micelle concentration" (CMC) and depends on surfactant properties.[8] The concept of supramolecolar assembly of amiphiphiles was firstly introduced around 1913 by J. W. McBain,[9] studying electrochemistry of sodium palmitate solutions. The "micelle" term (diminutive form of latin word "mica", meaning tiny particle) was borrowed from biology and spread only some years later, by G.F. Hartley.[10] From that moment on, the simplest form of colloid was extensively studied and modelized[11].[12] The ideal micellar shape is represented in Figure 2.3 and it is obviously spherical: this arrangement is the one with the lowest surface area. Apolar tail interacts inside the "core", whilst the polar head protect them from water medium with the fromation of an outer "palysade" layer. This is not the only possible structure: the adopted geometry depends strongly on tenside steric factors. The critical packing parameter (called R), introduced by Israelachvili,[13] is defined as:

$$R = \frac{\nu_H}{a_0 \times \ell} \tag{2.2}$$

where ν_H is the volume % of hydrocarbon chain, a_0 is the area of the polar group and ℓ is the chain length. It can give an useful insight about this aspect: when R ranges between 0-1/3, the associate structure is more probably a sphere, from 3 and 2 is a cylinder and from 1/2 and 1 a vescicle or a lamella. This object is characterized by a micellar aggregation number (a_M), defined as the average number of surfactants that compose

*examples of such behavior are known also in some organic solvents

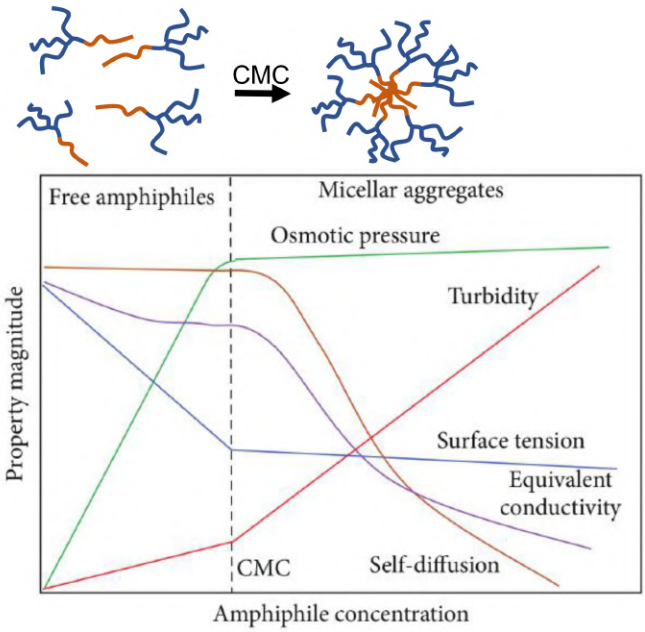

Figure 2.2 Trend of various physical properties as function of amphiphile concentration.[14]

a micelle, from which descends micellar weight, being the product of a_M to surfactant molecular weight. At concentrations around CMC, the system dramatically modifies its structure and consequently numerous physical ensable properties change (Figure 2.2), such as turbidity, surface tension and osmotic pressure. From these variations measurement, it is possible to evaluate CMC for a given surfactant.[15] Micelles formation is in turn affected by different parameters, such as temperature and other species presence (i.e. salts for ionic tensides). Generally, increasing temperature favors solubility, leading to a slight increment in CMC. Indeed, ethoxylated species show opposite behavior. An ethoxylated micellar dispersion above CMC at room temperature is totally clear, but under slow heating, it will become turbid. The temperature (or range of temperature when dealing with mixtures) at which this "demixing" phenomenon takes place is called cloud point.[16] These species in fact curl into hydrophilic coils when at low temperature, moving to a more hydrophobic nature on the average when heated. To give a practical idea of this range of temperature, cloud point of one of the most industrially employed ethoxylated surfactant, Tween 80, is 65 °C.

2.1.2.1 Ideal model versus reality: insight on micellar dynamic nature

Nevertheless, the reported model is useful for computational studies, but reality is a different story. Firstly, they are not so regularly shaped as depicted in cartoons: the effect is due to the fact that the amount of polar heads with respect to the hydrophobic chains is generally not large enough to give a compact surface. Moreover and more importantly, micelles are not stable entities, can't be regarded as nanoparticles, but should be considered dynamical objects: single surfactant is in constant equilibrium between aggregated form and soluted form.[17] They therefore keep on "entering" and "exiting" from micelle to the external medium.[18] Considering micelles as chemical species, this phenomenon can be described as follow:[19]

$$\frac{n-N}{N_A} monomers \rightleftharpoons \frac{N}{a_M N_A} micelles \tag{2.3}$$

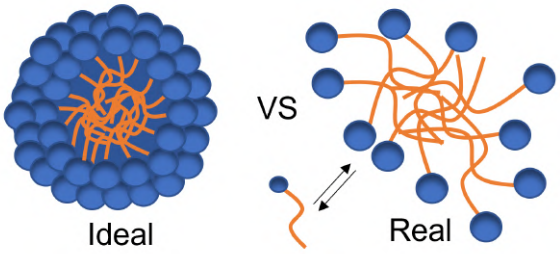

Figure 2.3 Cartoon of an ideal micelle (on the left) versus a more realistic version (on the right): surfactant is in constant equilibrium between the "assembled" and free form.

where n is the total number of surfactant molecules, N is the number of surfactant involved in micelle structure, a_M average micellar aggregation number, N_A Avogadro's number $(6,022 \times 10^{23})$ and the equilibrium can be associated to a k_M constant. The main direct consequences are the generation of percolation pathways for apolar species loading inside the core and, more important, the formation of a pseudophase. They in fact create a new dispersed environment inside the acqueous medium but due to their limited existence they can't be a totally free-standing new phase. This clearly complicates a lot the cards on table, leading to the fact that at the moment no complete model is capable of describe completely the system. Moreover, this new pseudophase is itself composed by different environment depending on localization: palisade layer has different properties respect to core (dielectric constant, polarity).[20] So far, an average description has been adopted, regarding why and how micelles form. Taking into account their dynamic nature, the presence of two different micellar relaxation process were hypothesized:[21]

- surfactant exchange time, τ_1, in the range of milliseconds: it describes the entrance/exit of a single surfactant either from micelle to water or from a micelle 1 to a micelle 2;
- micelle formation/breakdown time, τ_2, from milliseconds to minutes: it resembles the time that a micelle takes to be entirely composed by new surfactants.

They lead to the definition of an average micellar lifetime (T_m),[22] that can be considered as:

$$T_M \sim a_M \times \tau_2 \tag{2.4}$$

valid in the hypothesis that concentration is well above CMC.

2.1.3 Why micelles?

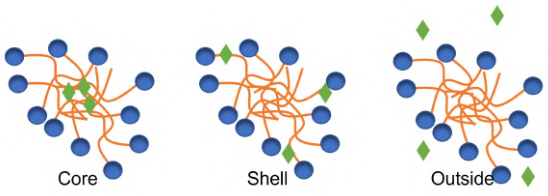

Figure 2.4 Cartoon of different kind of localization of guest species possible in a micelle, depending on their polarity: inside the core, in the shell layer or outside (from left to right).

Chemical industries (and chemical laboratories in far lower extent) produce every year a shocking amount of waste, to which largest contribution (around 80-90 %) is given by organic solvents.[23] They are hazardous for human health, environmentally dangerous, difficult to dispose and their production itself is high polluting. Nevertheless, their demand remains high because this is the only way industrial chemistry knows to obtain drugs and other fine chemicals. This is due to the fact the processes on which it builds upon are the same of 50 years ago, when the world scenario was totally different. Nowadays, a new awareness is raising, pushed also by the fact that change is no more an option, but a necessity.[24] For this reason, all over the world, research is focusing on replacing organic solvents.[25] Some possible options base on solid-state melt reactions or mechanochemistry[26] but they are high energy consuming and not always feasible. Other substituting solvent candidates are supercritical fluids, ionic liquids and bio-solvents.[27] Speaking about the last type, water would be a very turning point: it is the most abundant liquid on earth and its not toxic at all. Unluckily, everyone knows that for the experimental concept of "like dissolves like", it is not compatible with solubilization of the majority of organic species employed. Here micelles came to help us.[28] First reports about surfactants employment in performing reaction appeared in the 1960s.[29] From that moment on, intense work has been made.[30] To gain a deeper insight, we have to remember that the presence of surfactants in water over CMC generates a new pseudophase with compartments showing diverse polarity. This feature allows compatibility of organic compounds in a polar medium such water, at the same time decreasing distance between different species and enhancing reaction rate. In same cases, this localization has been proven to also boost product selectivity.[31] This is mainly due to different localization possibilities depending on reactants polarity outside, in the frontier layer or inside the core of micelles(Figure 2.4). The micellar pseudophase can thus be consider nothing but a nanoreactor.

2.1.4 The advantages of micellar stabilization

We have underlined intrinsic dynamic nature of micellar aggregates. In addition to the fact that they are in constant "living" equilibrium with the surrounding medium, their exsistence is strictly bound to the presence of water. Once solvent is removed (or a dilution under CMC takes place), colloidal objects come back to their "monomeric" form. Some applications are satisfactorily accomplished by temporarily averaged conditions (such as emulsification, anti-foaming, detergent action or standard micellar reactions). In other cases, the lack of stabilization is a limit. Drug delivery, sensing, and template catalysis are the most important examples[32].[33] The former takes advantage of tensides compatibilization of water-insoluble drugs to human circulation system. The cargo is "loaded" and then carried through the human body: the release is triggered only upon desired changes in chemical and physical environments (called stimuli), characteristic of a specific disease. The advantages of these species are good biodegradability, ease of preparation and control. Nevertheless, standard surfactants are too "labile" and often loose their cargo before reaching the target point. Stabilize the colloidal aggregates with stimuli-responsive functionalities can strongly enhance their delivery activity[34].[35] The nanosensing is instead aimed at measuring intracellular

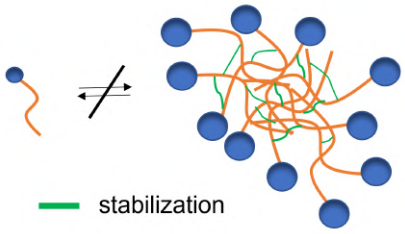

Figure 2.5 Cartoon representing the concept of stabilization: surfactants assemling a micelle are not able to disaggregate anymore.

metabolites and pH.[36] They are principally ratiometric fluorescence based nanosensors composed by polymeric block copolymers. The stabilization allows them to work under CMC, decresing the amount of sensing material needed to detect signal.[37] Finally, as templating agents for synthesis, they can be exploited both for inorganic nanoparticles and for organic compounds. In the first case, their resistance to harsh condition is fundamental (as strong acids are often needed) and the further survival to solvent evaporation imprints colloidal stability to the output materials.[38] The first example of freezing micellar dynamics dates back to 1979: Larrabee and Sprague exploited γ-radiation to polymerize sodium 10-undecenoate.[39] A lot of work arose from that moment on. For example, in 1998, Stahler created a mixed hydrocarbon and fluorocarbon polymerizable block-copolymer surfactant able to solubilized orthogonal species in different micelle portion: this was the first time compartimentalization was introduced in this field.[40] Quantitative studies on polymerization efficiency and its effect on micellar structure were carried on more deeply, through dynamic light scattering (DLS), static light scattering (SLS), and cryogenic transmission electron microscopy (cryo-TEM)[41] and different shapes were obtained, such as cylinders.[42] Going through pertaining literature, stabilization is obtained both via chemical (formation of a covalent bond) or physical methods (taking advantage of H-bonds or interpenetrating networks). Generally, ad-hoc designed, very complex polymeric structures are employed, meaning a lot of reaction steps only to obtain the surfactant. In addition, direct chemical crosslinking of tenside chains results in stiff structures[43].[44] Thinking in direction of an employment as nanoreactors, reactants migration to desired sites and following recover after transformation is thus made very hard. Physically induced freeze of micellar relaxation processes are more straightforward, especially when polymerogenic species is decoupled from surfactant compound. An interesting example is reported by Petrov[45][46]:[47] pluronics micelles (two hydrophilic chains covalently linked to the same lypophilic portion) are stabilized by a photo-induced nanonetwork of penthaerytritol tetraacrylate (PETA). The entanglement is purely physical, there are no chemical bonds between the two species: it is an interpenetrate network (IPN).

2.1.4.1 Interpenetrated polymer networks

IPN are defined as "a broad class of polymer alloys classically defined as materials containing two or more intimately mixed network polymers with at least one being polymerized or crosslinked in the presence of the other."[48] They build upon mechanical entanglement of the two parts, that make them "indivisible" unless chemical bonds are broken. There are a lot of possible categories and the applications span from drug delivery[49] and tissue engineering,[50] to food packaging[51] and more visionary fuel cells(in form of membranes).[52] Among all the possibilities, semi-IPNs relate to architectures where only one compound of the pair is a polymer, generally obtained in-situ to entagle a linear, or better branched, structure. This is the system that triggered our interest: coupling a branched surfactant with a polymerogenic molecule would result in a softer stabilized structure, still not possible to be pulled apart.

2.1.5 A cross-over between micellar and heterogeneous catalysis

2.1.5.1 From standard micellar reaction to miniemulsions

As aformentioned, micellar reactions are gaining great interest both in research and industrial community. When this approach is applied to reagents at low concentrations

(generally 10^{-4}M), there is no perturbation of the micellar environment described before. Neverthless, diluted conditions are not always convenient, especially when involved scales becomes relevant. Increasing species concentration leads to overpassing maximum additive concentration (MAC value): in these conditions, a multiphase inhomogeneous system settles up and it is renowned to lack of reproducibility in most cases. That's the point where the addition of a small amount of an organic co-solvent (usually ranging between 1 and 10 volume to volume %) comes into help. When two immiscible liquids (i.e. water phase and apolar organic solvents, called oil phase) are mixed together, the formation of an emulsion takes place. During mixing, the dispersed oil phase arranges in thermodinamically unstable droplets diffused inside the continuous water medium that tents spontaneously to coalesce and demix. The addition of proper amphiphilic species, naturally lowers the surface tension between the two and lengthens their duration over the time. These droplets can range between tens of nanometers and microns (in the latter case, creating a so called "miniemulsion"). This process spontaneously enlarges micellar dimensions, creating nanoreactors that can dissolve and settle more organic reactive species inside their core. There is thus much more than classical micellar reactions: employing surfactants greatly widens possiblities for well-known reactions. For now, we have considered only the medium where reactions occur: what about the catalytic process? It is an open field for green chemistry approach as well.

2.1.5.2 New frontiers for catalysis: moving towards heterogenous approach

In every chemistry textbook, a catalyst is defined as a chemical able to promote a specific reaction without being consumed at the end of the process: it is reusable many times for definition. It in fact acts on the activation barrier of a transformation, modifying the energy profile and the mechanism. Some reactions can be performed only through its action and some other can be operated in significantly milder conditions. It's easy to understand that this field is of primary interest for many industries, especially pharmaceutical. The most common catalytic species are transition metals and enzymes. A catalyst can be in the same phase of reactants (homogeneous type) or in a different one (heterogeneous type). The former has the advantage to be very efficient and the mechanism through which it acts is known, but it suffers from difficult recovery post-synthesis leading to product contamination. For the second category, it's true the opposite. Neverthless, the reuse of transition metal accounts for their toxicity and high costs and makes worthwhile to focus on this new approach. It's either possible to immobilize over the surface of a support a classical homogeneous catalyst or nanosized metal nanoparticles (NP). The second route is more convenient, given that in the first case leaching and worse performances are unavoidable. Employing the proper support remains still fundamental: zeolites, silica, activated carbons are cheap and inert but less compatible with organic reactants and so limited. Organic species, especially π-conjugated polymer nanopartcles (CPNP), are emerging thanks to their intrinsic tunable nature, coordination capability (in particular in presence of heteroatoms) and possibility to establish specific interaction with the reactive substrates, giving selectivity to the process, since the first successful result reported by Cooper et al. The incorporation of metal clusters makes them perfect candidates for heterogenous catalysis. Catalytic sites can be deposited through a reduction process but they often remain on the surface and consequently the final catalyst suffers of leaching. The most suitable way is the direct incorporation during polymer formation. Moreover, these NPs are poorly dispersible and making them too small to overcome this issue arises difficulty in final recovery. The synergistic cross-over between miniemulsion micellar

reaction, sIPN and heterogenous catalysis can lead to a step beyond in this field. In this stimulating context, in the second part of this chapter I will briefly describe how we thought to synthesize conjugated polymer NPs with miniemulsion technique that retain both surfactants through a sIPN system and embed the same catalyst employed for the reaction to create a stable, intrinsecally dispersible, scalable and directly reusable heterogenous catalyst.

2.2 Aim of the work

Micelles are very simple, yet resourceful, fascinating objects. They enter our everyday life in numerous ways, especially in cleaning and personal care products, to the point that recently the term "micellar" has become market-appealing. However, in the chemistry laboratory, other uses are possible for micellar aqueous dispersions. Micelles capability to generate a new pseudophase in the aqueous environment can be exploited, for example, to carry out chemical reactions in previously inconceivable ways. Reactions in such aqueous media are becoming increasingly attractive especially for the possibility to avoid the need for dangerous solvents, and to open new synthetic pathways otherwise considered challenging. They in fact act as the trait d'union between aqueous and organic media. Thanks to the permeability of the outer water swollen shell, lipophilic species can accommodate within the apolar portion of the association colloid while still being in partial contact with the polar medium (and eventually react with water-soluble species). On the other side, micelles existence is bound to solution state: upon dilution or solvent evaporation, they stop to exist as an association colloid (thus also releasing any embedded cargo). In our constant strive to develop straightforward approaches to produce stable colloids mimicking artificial enzymes, we developed an approach enabling the stabilization of the micellar structure below critical micellar concentration through photopolymerization of the self-assembled original association colloid. In the literature, many examples of such systems exist, however the reported micelles are typically based on complex polymeric designer surfactants stabilized by crosslinking of a polymerogenic unit, resulting in stiff and rigid structures.[53] Aim of our project was to develop a different and more viable approach, based on the combination of commercially available surfactants and simple polymerogenic additives capable of locking the association colloid formed by the surfactants in water through the formation of an interpenetrated polymeric network. Such structures allow us to:

- study the localization of host species, especially during a reaction conducted in that medium;
- exploit this knowledge to create, for example, efficient and reusable reaction medium.

This project builds upon the work of a former PhD student of our group,[54] which will be briefly summarized in the following section.

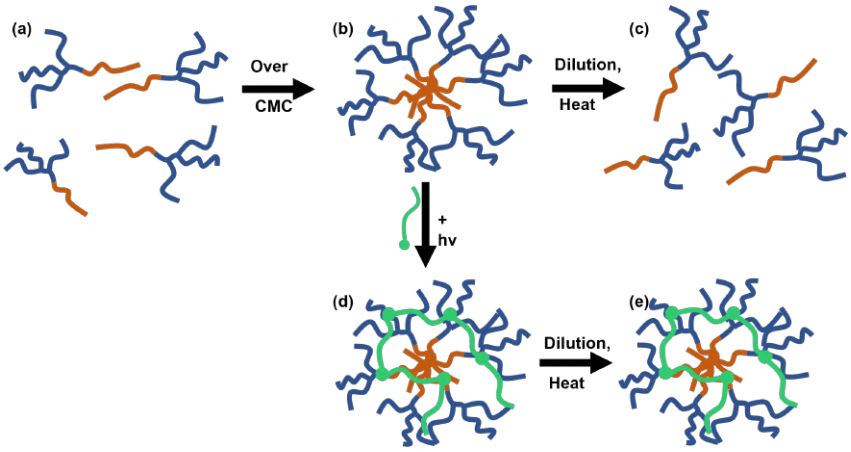

Figure 2.6 Cartoon of branched surfactants dissolved in water at a concentration under cmc (a), micelle formation at increased concentration (b), classic disappearance of miceller structure with dilution or heating (c), a micelle stabilization by photopolimerization of an added co-surfmer (d) and preservation of the stabilized micellar structure upon external stimuli (dilution, heating) (e).

2.3 Summary of preliminary, unpublished work

To study micelles photostabilization via creation of a semi-interpenetrated polymeric network, our research group selected:

- Tween 80 (T80, Figure 2.7(a)) as the surfactant, for its branched structure (that favors chains intertwining), long micellar life time (allowing the polymerization process to be effective), commercial availability, low price and no toxicity (more details in Experimental part).
- APE-4 (2-(tetrahydropyranyl)oxy tetraethylene glycol methacrylate, Figure 2.7(b)) as polymerogenic "co-surfactant" (even if it does not have micellization capability in water). This derivative was specifically designed and synthesized to have a TEG (tetraethyleneglycol) hydrophilic chain, a polymerogenic methacrylate group, and hydrophobic tetrahydropiranyl anchor group to favour its localization inside the micellar PEG-ylated palisade.
- 4-EDMA (tetraethylene glycol dimethylacrylate, Figure 2.7(c)) as crosslinker, for its similarity with APE-4, to generate diluted branched points in the obtained polymer, favoring mechanic interpenetration.

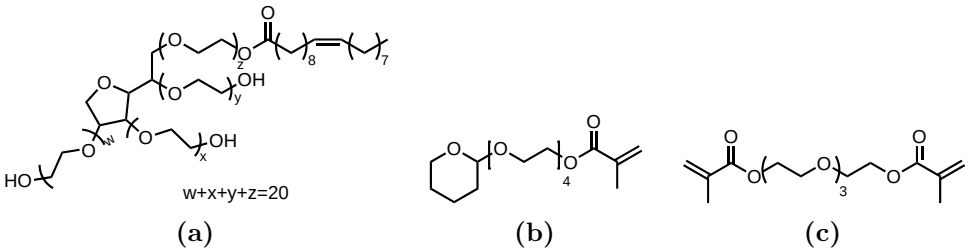

Figure 2.7 (a) Tween 80, (b) co-surfactant APE-4 and (c) cross-linker 4-EDMA.

The reference dispersion is obtained by dissolving T80/APE-4 2:3 mol/mol in a minimum amount of tetrahydrofuran (THF), and by adding this solution under vigorous stirring to

deionized water (final T80 concentration is 0,22 wt%, generally on 20 mL scale). THF is slowly removed within for 1 hour. The as-prepared dispersion has been characterized by DLS, Fourier transform-infrared spectroscopy (FTIR) and ^{1}H NMR both in D_2O and DMSO-d_6. Such measurements revealed that

- the presence of APE-4 induces the formation of secondary micellar aggregates (hydrodynamic radius of species detected moves from 9 nm of pure T80 to 164 nm), due to pre-clouding phenomenon*;
- the tetrahydropyran ring localizes within the micellar core (broadening of the ^{1}H NMR corresponding peaks in D_2O, meaning that protons are not able to fully relax as the molecule is not in solution);
- ester carbonyl group vibration is well recognizable and thus can be diagnostically employed to monitor polymerization occurrence†.

The polymerization procedure was performed both photochemically (with two different UV sources, λ_{exc} 254 nm or 365 nm) and thermally, but only the former approach gave interesting results. In the case of irradiation with 254 nm source (mercury lamp), the introduction of the common photoinitator (PI) 2-hydroxy-2-methylpropiophenone (Ig2, 4 mol% respect to APE-4) allows to complete the photopolymerization in 7 hours. In the case of irradiation with 365 nm source (LED lamp), more problems showed up: between the three different photoinitiators we tested, only 2-di(3-thyenil)-1,2-ethandione (DTE) allowed to obtain 71% conversion of APE-4, at the same time causing tetrahydropyran ring cleavage. The mechanism through which 365 nm photoinitiators generally activate radical polymerization (triplet state sensitized by presence of carbonyl group - ref) induces proton extractions causing tetrahydropyran ring opening and detachment as pentanal (which in water transforms into the tautomer 1-penten-1-ol).[55] The thus formed tetraethylene glycol mono methacrylate ester (AOE4) is water miscible, and do not localize within the micelles, inhibiting polymerization. Employing a phosphate buffer saline (PBS) solution instead of pure water as the reaction medium allowed to control the developed acidity and minimize APE-4 deprotection, at the same time achieving 92% conversion. Once stabilized dispersion was obtained, morphological, dilution and temperature stability, along with loading studies were performed. Firstly, a centrifugation step demonstrated that there still is a small dimension family of objects (11,9 nm) with lower amount of APE-4 that is possible to partially separate (dimension refinement). More importantly, these species show resistance to dilution below CMC (0,0075 wt % in water for T80) and to temperature (up to 60 °C, measurement limit for water), even if above 50 °C a slight small slipping out takes place. Finally, loading of organic species is confirmed by introduction (after the photopolymerization step) of pyrene and di-octyl-quinacridone (5,12-dioctylquinolino[2,3-b]acridine-7,14(5H,12H)-dione): the generalization of this step is an important improvement. Stiff scaffolds don't lose their cargo but at the same time do not allow loading. This means that loading must be performed before the crosslinking step: the production procedure has therefore to be performed in the presence of the cargo. This feature limits applicability only to those molecules that are compatible with the polymerization conditions required to stabilize the colloid. In the literature, the use of

*This event happens when a small molecule substitutes H_2O ones in the outer shell of a micelles, causing their coalescence.

†The ester carbonyl group vibration of the polymer is more energetic than that of APE-4 because of the loss of conjugation, thus the peak shifts from 1720 cm^{-1} to 1730 cm^{-1}

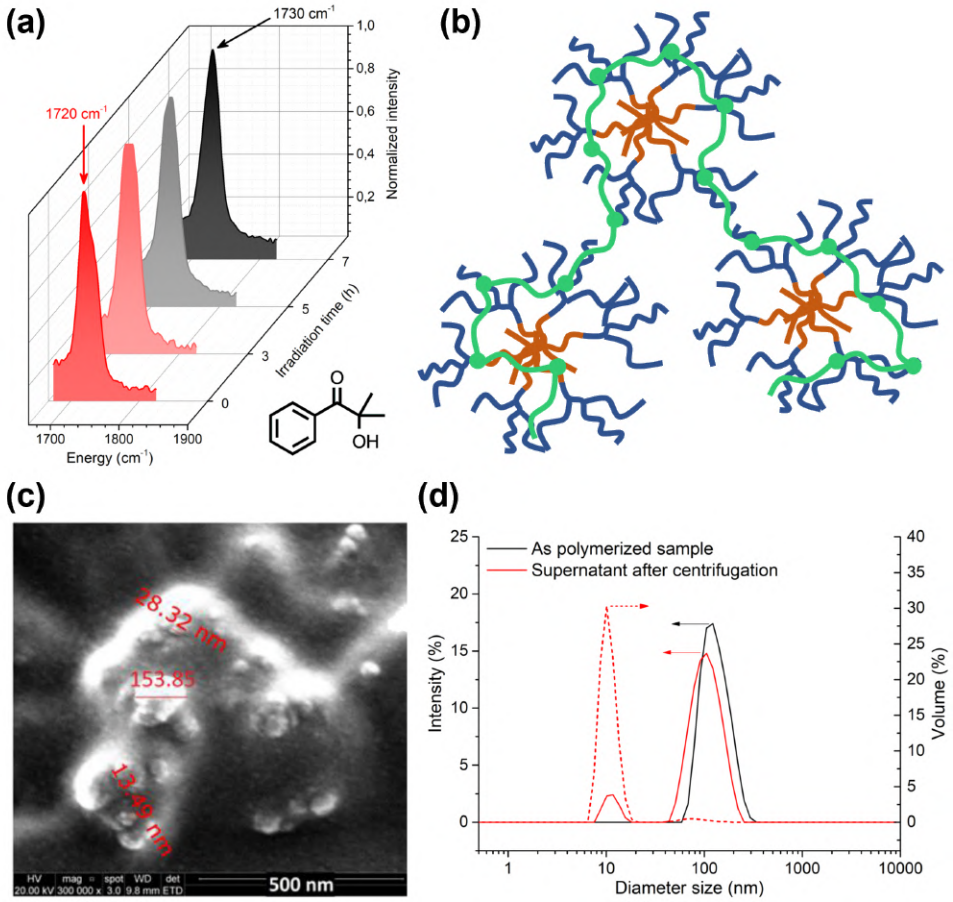

Figure 2.8 (a) Portion of FTIR spectra showing the energy shift of APE-4 carbonyl peak from 1720 cm^{-1} to 1730 cm^{-1} in AP-E4/T80 micellar dispersions with 2-hydroxy-2-methylpropiophenone (Ig2) as photoinitiator (3, 5 and 7 h of irradiation). (b) Cartoon of secondary micellar aggregates induced by photopolymerization of co-surfactant (green lines). (c) Scanning electron microscopy images of stabilized dispersion of APE-4/T80 loaded with N,N'-dioctyl quinacridone: primary and secondary colloidal aggregates are distinguishable. (d) DLS intensity (full lines) and volume distribution (dashed lines) of dimensions of as-polymerized surfactant dispersion before and after centrifugation.

pyrene is reported to gauge information about the polarity of the surrounding medium by the analysis of relative intensity of vibrational replica in emission spectrum. Pyrene was selected also to test load retention after solvent evaporation and redispersion, with and without the presence of crosslinker (in conditions of different "network densities") by comparison of absorption spectra. As expected, the retained pyrene quantity was higher for the crosslinked dispersions. Finally, the slow crystallization of di-octyl-quinacridone within the micelles (12 days) was followed by UV-Vis absorption, specifically monitoring the increase in optical density of the red-shifted peak connected to J-aggregates formation. The nanocrystals presence also allowed to collect scanning electron microscopy images of the dispersion, that confirmed the presence of 150-250 nm aggregates composed by smaller (15-20 nm) objects, as evinced from DLS.

2.3.1 Optimization of 365 nm induced photopolymerization

Some work was still needed to improve the previously developed protocol: we wanted to improve reproducibility (the original method was not always completely reliable), test protocol extension, and try to fix the issue limiting the use of 365 nm light source. This

last aspect was particularly concerning for different reasons. First of all, our 256 nm source was very powerful, and consequently dangerous for the user. Moreover, a dedicated quartz setup is necessary to perform the polymerization: this severely limits the amount of dispersion that can be prepared in every batch, and precludes the possibility of scaling up the procedure. Moving to a 365 nm LED source would be both safer for the user, and easier from the standpoint of the required equipment. However, we knew this was not a straightforward change to implement: preliminary results showed that not only acidity, but also temperature increase as a consequence of prolonged irradiation times, and irradiation by itself are factors favouring tetrahydropyran cleavage in APE-4 co-surfactant. We therefore started the work by optimizing polymerization efficiency to make it faster than the competitive deprotection reaction. Some of the parameters we dealt with to improve photopolymerization efficiency were:

- more sophisticated set-up composed by a flow reactor with enhanced irradiation performances (section 2.3.1.1);
- coupling a photoinitiator working at 254 nm with a 365 nm sensitizer in order maintain the best result of the former while at the same time introducing the 365 nm light source (section 2.3.1.2);
- substituting DTE with a different photoinitiator, more prone to localize in the PEG-ylated shell, where APE-4 is supposed to be (section 2.3.1.3);
- better homogenization of species introducing magnetic stirring: this represents also the first step to scale up the reaction (section 2.3.1.4).

2.3.1.1 Photopolymerization under microflow chemistry conditions

Efficient irradiation is one of the fundamental parameter required by photochemistry.[56] The incoming irradiation penetrates inside the sample with decreasing intensity depending on reaction medium, following Lambert-Beer law:

$$I(x) = I_0 e^{\epsilon_0 M x} \tag{2.5}$$

where I(x) is irradiation intensity at a given distance x from the source, I_0 is source intensity, ϵ_0 is molar extinction coefficient and M molarity of the species dissolved in medium. This equation is exact assuming that both medium and dispersion/solution containing vessel don't absorb irradiation employed. To minimize the distance between the source and the photo-active species, most designer photochemistry setups present thin film or channels geometries. The employed cylindrical quartz vial (suitable for 254 nm protocol, as quartz does not filter the incoming irradiation) limits this aspect, due to limited light penetration, as the optical density of the solution does not change upon irradiation. We thus tested the CORNING lab microfluidic reactor, specifically designed for photoreactions (Figure 2.9(a)). It is composed by a heart-shaped array of glass microchannels (width 400 µm), arranged to ensure maximal light exposition to the content passing through (Figure 2.9(b)). Temperature of the channels can also be controlled through a specific circulator system. The liquid is pumped in the system at a controlled flow rate, then passes through the channels where it is exposed to irradiation, and then comes out from a tube. If the outlet pours the liquid in the same vessel used to pump it in, recirculation can be easily ensured. The instrument is equipped with two LED arrays, one for each side of the reactor plate,

with smallest possible wavelength of 365 nm, and light emitted power density tuneable up to 60 $mWcm^{-2}$. Both recirculation and high irradiation power density together are the key advantage of this reactor, and we were interested to test their effect in our conditions.

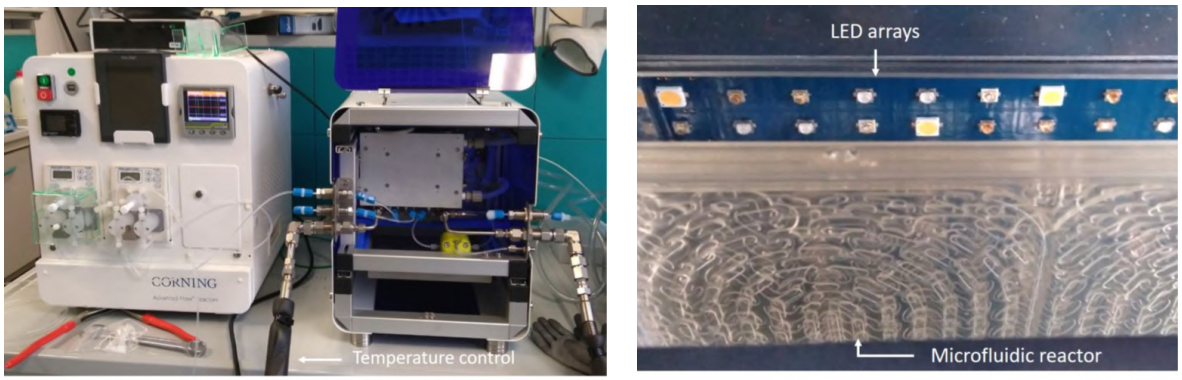

(a) **(b)**

Figure 2.9 (a) CORNING lab microfluidic reactor: pumps and control system unit (left) and operative part (right); (b) zoom on the microchannel disposition and LED array.

We produced a T80/APE-4/4-EDMA dispersion (T80 0,2 wt% with respect to water, T80:APE-4 2:3 molar ratio, crosslinker 4 mol%) and introduced 4,4'-bis(dimethylamino)benzophenone (DABP) as PI: with such conditions, using our standard setup we obtained only 50% APE-4 conversion. We began the circulation employing a flow fate of 8 mL/min, which we decreased to 4 mL/min after a few minutes to reduce the reactor internal pressure. The dispersion was recirculated at room temperature for 2 hours, then stopped to analyse a sample by FTIR.

The amount of recovered dried residue was slightly lower than expected, and no sign of photopolymerization, neither of tetrahydropiranyl detachment was detected (Figure 2.10 (light blue curve)). We decided then to expose the dispersion to 2 additional hours of irradiation, this time increasing the reaction temperature to 40 °C: in fact, with our standard LED light source, heating of the reaction flask was difficult to control, and generally the temperature raised to similar values. However, again no difference in FTIR spectrum was found (Figure 2.10 (dark blue curve)). Having observed such an unexpected result, we tested a totally different but ideally more effective dispersion: T80/4-EDMA 2:3 mol ratio with 4-hydroxybenzophenone (4-HBP) as PI. Substituting APE-4 with 4-EDMA, in fact, essentially allows to double the polymerizable units, thus increasing the probability for the reaction to happen, while at the same time maintaining the system substantially unchanged from the point of view of all the other characteristics. Regarding to the use of 4-HBP as the PI, as discussed in section 2.15, the principal reason is that it is a more effecient and more polar PI than DABP, and we expected it to localize in the PEGylated shell instead of hydrophobic part, similarly to 4-EDMA. This dispersion is irradiated at RT for 2 h while ecirculating at 8 mL/min, but again we observed no polyerization at

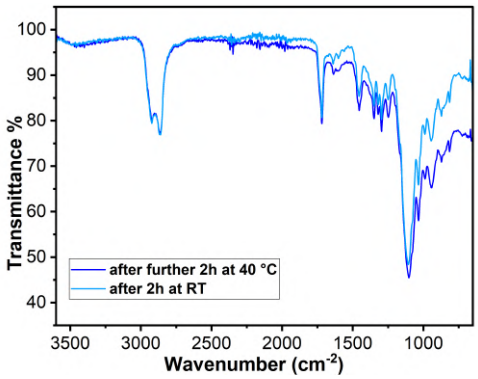

Figure 2.10 FTIR of T80/APE-4/4-EDMA/DABP dispersion after 2h at RT (light blue curve) and 2 additional hours at 40 °C (dark blue curve) in CORNING flux photoreactor (4 mL/min). No difference in spectra are detected and they are compatible with prisitine dispersion.

all. Nevertheless, we also clearly noticed an unexpected increase of internal pressure of the reactor, and recovered an amount of dry material way lower than the expected. At this point, we hypothesized that the set up was quite efficient, but the polymerization did not take place in the aqueous phase. In fact, the PEG-ylated chains can interact well with polar glass surface, creating a film. This also happend in our quartz reactor, but the surface to volume ratio in that case was way more favourable to keep the material in the bulk. In the case of the Corning reactor, instead, probably polymerization occurred only at the surface of the glass, where the irradiation is not filtered. The limited amount of material present in solution prevents channels clogging (altough an increase in the internal pressure is still observable), but the product can't be recovered from the glass surfaces. In conclusion, CORNING flow photoreactor was probably very efficient in terms of promoting the polymerization, but its configuration is not well-suited for this type of dispersion. This result anyway gives us an insight on the fact that photopolymerization efficiency can actually be improved acting on photoinduced process.

2.3.1.2 Sensitization of the photoinitiator

Coming back to our initial setup, we considered the possibility to couple a 254 nm photoinitiator (Ig2) with a 365 nm sensitizer. We selected TPO (diphenyl(2,4,6-trimethylbenzoyl)phosphine oxide) for its compatibility with Ig2, in fact this compination is well-known in the literature.[57] Figure 2.11 shows the sensitization mechanism: TPO absorbs 365

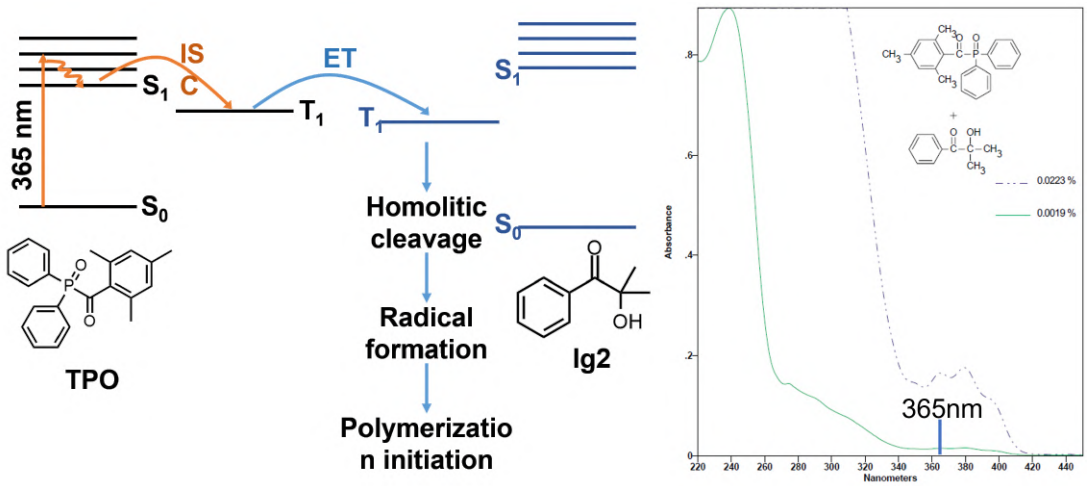

Figure 2.11 Jablonski diagram of expected mechanism between TPO and Ig2 that starts polyerization (right). Absorbance spectrum of TPO/Ig2 1:1 at different concentrations (full and do line) in methanol. From Sigma Aldrich (left).

nm irradiation with higher probability than Ig2 (due to its higher optical density at that specific wavelenght), and an electron is promoted to a S_n excited state. Due to fast relaxation processes (internal conversion, following Kasha rule), it relaxes to the highest singlet unoccupied energy level S_1, from where it converts through inter-system crossing (ISC) to the corresponding triplet state (T_1). If a Ig2 molecule is close enough (few nanometres), energy transfer (ET) between T_1 of the two species can occur. In this way, the 254 nm photoinitiator ends up in the excited triplet state wthout directly absorbing light, andtherefore has the energy sufficient to undergo homolytic cleavage and trigger the radical polymerization reaction. The determining step is the energy transfer between species and thus their proximity is fundamental. We employed a standard T80/APE-4/4-EDMA

dispersion in deionized water with 4 mol% of Ig2 and TPO equimolar. Precise quantities and preparation method are extensively reported in Experimental part.

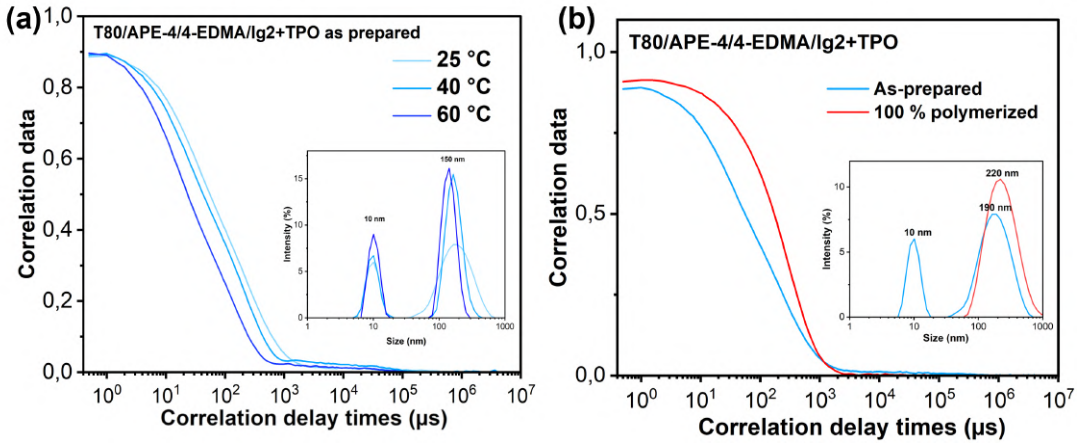

Figure 2.12 DLS correlograms and Intensity % distribution of dimensions (in the inset) of T80/APE-4/4-EDMA/Ig2+TPO dispersion. (a) As prepared dispersion at different temperatures (25 °C, 40 °C and 60 °C) (b) completely polymerized dispersion (with 254 nm source).

We characterized dispersion morphology through DLS: even if we doubled the number of PI molecules, the amount remains too low to affect colloidal distribution of surfactant particles. Correlogram and intensity distribution of dimensions confirm that there's a mix of ∼10 nm and ∼190 nm centered populations (Figure 2.12(a)), as previously seen. Considering that Rayleigh scattering intensity scales as d^6 (where d is the particle dimension), we can confirm that bigger aggregates are a very small percentage (less then 1% from volume distribution). The results of DLS characterization at higher temperatures of 40 °C and 60 °C are important since prolonged irradiation slightly heats the sample. In our case, we only observed minor evolution in the population of the sample, resulting in a slight decrease in polydispersity (Figure 2.12(a)). Firstly, we performed a reference test irradiating 20 mL of dispersion with 254 nm source (mercury lamp) for 4 h (sample A). From both FTIR and ^{1}H NMR (Figure 2.13 and 2.14), acrylate conversion is complete and no tetrahydropyran cleavage is detected: the result is not surprising, since Ig2 alone allows to achieve the same result, as previously demonstrated. Nevertheless, without the sensitizer complete conversion is reached only after 7 h of irradiation (Figure 2.8(a)): adding an equimolar amount of TPO accelerates the photopolymerization rate. DLS of the product at 25 °C shows that only a broad family of object forms, having dimensions centered around 220 nm (99% from volume distribution, Figure 2.12(b)), slightly bigger than starting secondary aggregates. During polymer chains formation, coalescence from different micelles ends up in the creation of such bigger assemblies. We then moved to the 365 nm light source using a commercial nail lamp (sample B, for further details see Experimental part). Firstly, we irradiated the sample in the same quartz tube employed in the previous test (internal diameter = 1,5 cm), obtaining 26% of conversion by NMR, and almost complete tetrahydropyran

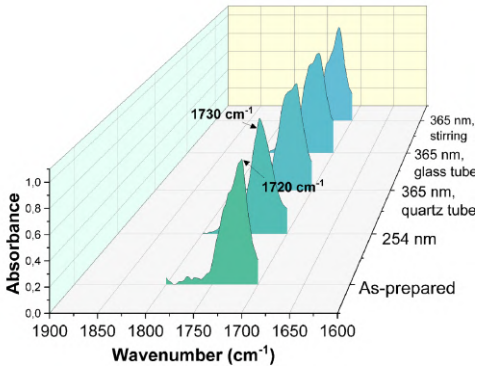

Figure 2.13 Portion of FTIR spectra that show carbonyl peak displacement in different tests on T80/APE-4/4-EDMA/Ig2+TPO micellar dispersions.

cleavage. FTIR exhibits the formation of a peak at 1730 cm^{-1}, although less intense than the starting one at 1720 cm^{-1} one (Figure 2.13). Substituing the first vessel with a glass tube with higher diameter (2,7 cm) (sample C) noticeably reduces the conversion (down to 5%) and the corresponding 1730 cm^{-1} peak, es expected (see also section 2.3.1.4). Finally, employing magnetic stirring during irradiation (sample D) only slightly improves the result (10% conversion). In conclusion, the coupling of a 345 nm sensitizer to a 254 nm working photoinitiator proved to be inefficient. One possible explanation involves the different localization of the two species inside the micellar environment, reducing the probability of energy transfer and inhibiting the formation of radical initiator.

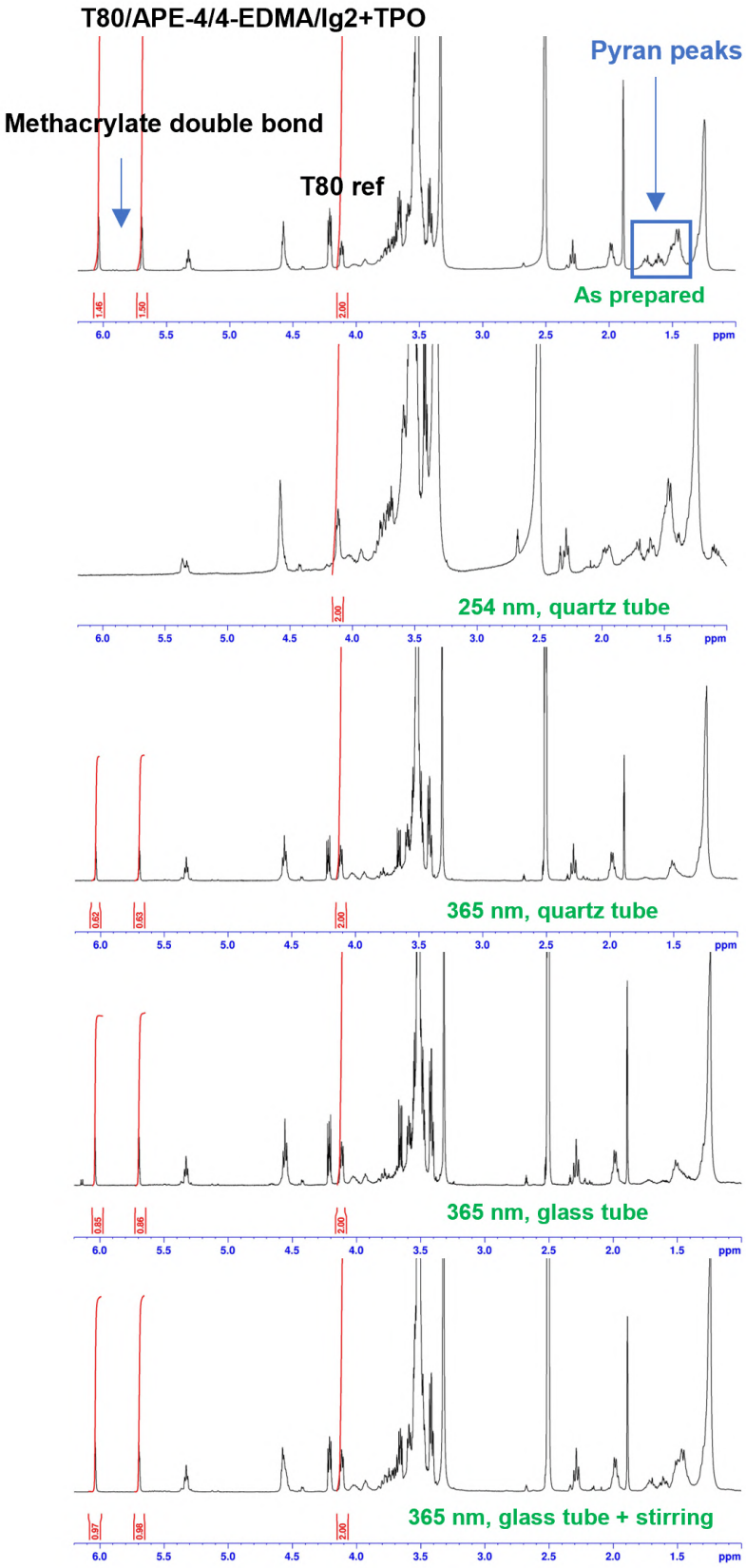

Figure 2.14 ^{1}H NMR spectra comparison in dimethylsulfoxide (DMSO-d_6) of T80/APE-4/4-EDMA/Ig2+TPO dispersions in different conditions. From top to bottom: as prepared; illuminated with 254 nm source; illuminated with 365 nm source in a quartz tube (d = 1,2 cm), in a glass tube (d = 2,7 cm), and while stirring. Reference T80 peak (4,1 ppm, 2H), tetrahydropyran characteristic peaks (between 1 and 2 ppm) and APE-4/4-EDMA double bonds (5,5 and 6,1 ppm, 1H) are highlighted.

2.3.1.3 Use of a more polar PI

Another possibility to improve photopolymerization is to use photoinitiators with polarity better matched with APE-4, to facilitate the reaction. In fact, when working under micellar conditions this strategy should promote the required colocalization of the two species within the same compartment.

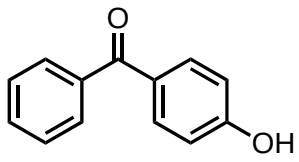

Figure 2.15 Structure of 4-HBP photoinitiator

Previously employed PI suitable for 365 nm light source (DABP, isatin and DTE) are all more lipophilic than APE-4. Going through literature, we found out that 4-HBP is an efficient absorber at 365 nm and bears a -OH group, thus resulting in a more appropriate partitioning between water and oil phase (Figure 2.15). We thus expect this molecule to localized nearer to the PEG-ylated micelle shell, where APE-4 probably accommodates. Firstly, as already done in section 2.3.1.1, we performed a reference experiment, employing only T80/4-EDMA (2:3 mol/mol) dispersion: this choice eliminates the possibility of competitive tetrahydropyran cleavage. Moreover, 4-EDMA is more polar than APE-4. As already said, the starting dispersion exhibits similar morphological characteristic to the one prepared with APE-4, except for the fact that secondary aggregates intensity is low enough to conclude that sample essentially contains only one family of particles with average dimensions of 10 nm (volume distribution ∼99,9%, Figure 2.16(a),left). We irradiated 20 mL of dispersion in a quartz tube using 365 nm light source for 8 hours, after which we checked result by FTIR and NMR: the yield is >95% (Figure 2.17(b)). Even if the number of acrylates groups doubled with respect to to an analogous dispersion containing APE-4, the photopolymerization proves very efficient. In this case, aggregates dimensions measured by DLS increase to ∼250 nm, but polydispersity index (PDI) is very narrow with respect to other stabilized dispersions (i.e. with Ig2/TPO and 254 nm light source, Figure 2.16(b), right). A possible explanation is that the use of a diacrylate, capable to generate many crosslinking points, make the system more stiff and rigidly interconneted, thus reducing variability in the aggregates dimensions. Moving to APE-4 containing dispersion, with the same set up we obtained 79% conversion. Comparing this value with those obtained with DABP, IS and DTE (respectively 50%, 33% and 71%), we can conclude that efficiency is increased even without using buffer solution.

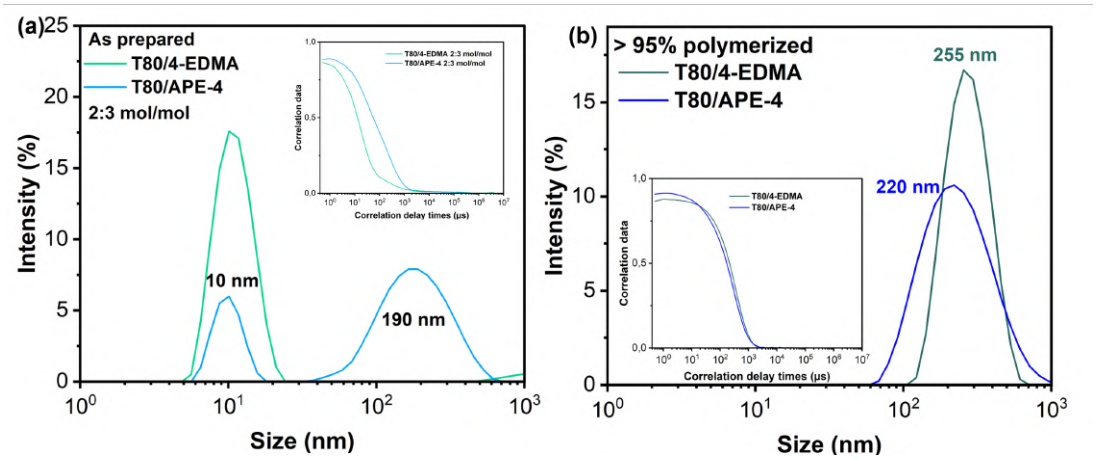

Figure 2.16 Intensity distribution of dimensions from DLS of T80/APE-4 (blue line) and T80/4-EDMA (green line, same concentration) dispersions: as prepared on the left, polymerized on the right. Inset shows the corresponding correlograms.

Since we employed the same set up and the same amount of PI, the more probable reason behind conversion improvement relies on the better localization of PI/co-surfactant couple. To further boost the yield, we repeated the test using glass tube but applying also magnetic stirring (400 RPM). We obtained in this case 100% conversion under 365 nm irradiation, while tetrahydropyran signals are still present. With this combination of PI and set up, the efficiency of photopolymerization overcomes the competitive tetrahydropyran cleavage process.

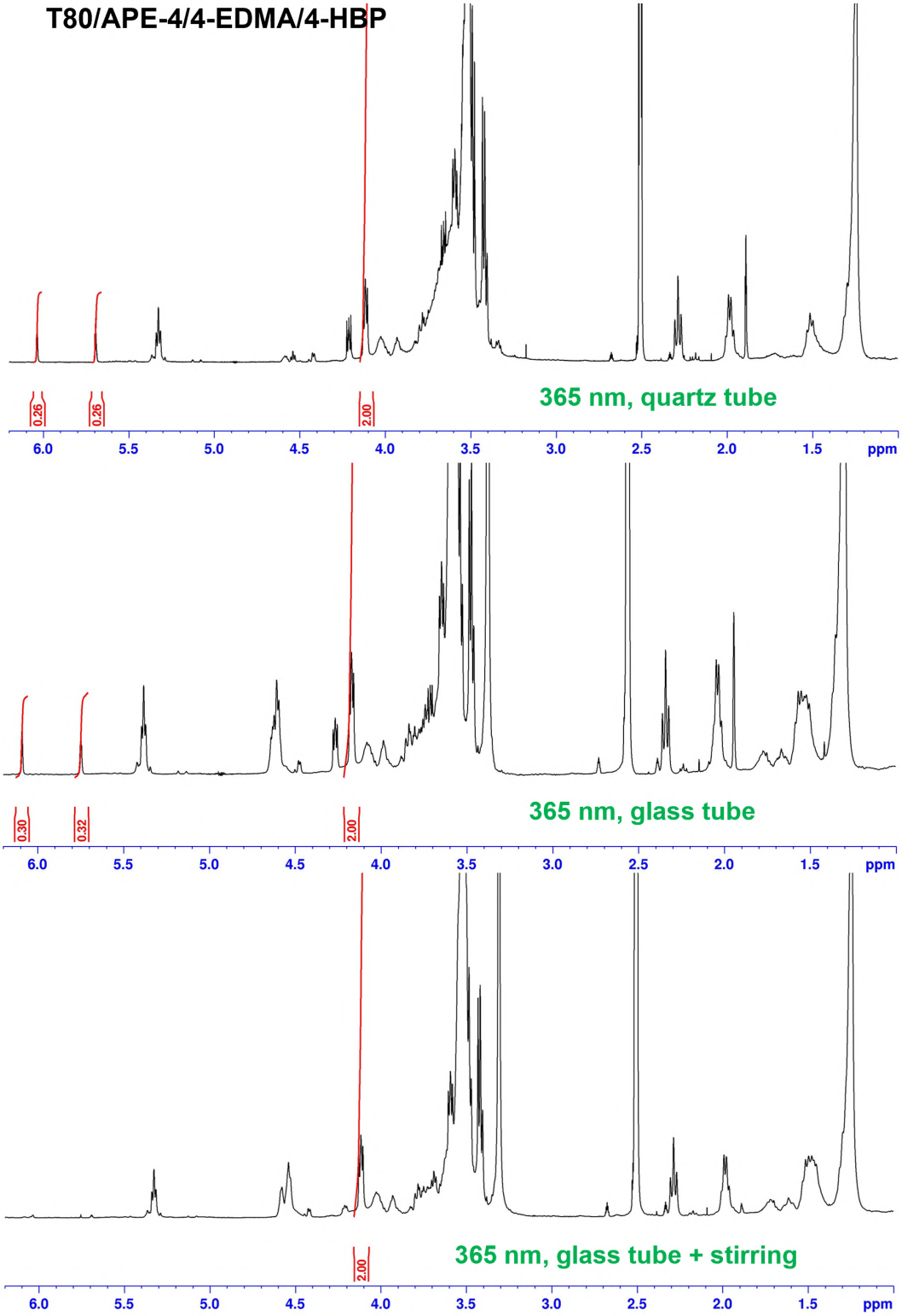

Figure 2.17 ^{1}H NMR spectra comparison (DMSO-d_6) of T80/4-EDMA and T80/APE-4/4-EDMA dispersions irradiated in different conditions at 365 nm. From top to bottom: with quartz tube (d = 1,2 cm), with glass tube (d = 2,7 cm) with and without stirring. Reference T80 peak (4,1 ppm, 2H), tetrahydropyran characteristic peaks (between 1 and 2 ppm) and APE-4/4-EDMA double bonds (5,5 and 6,1 ppm, 1H) are indicated. DA SISTEMARE

Table 2.1 NMR conversion of T80/APE-4/4-EDMA dispersions with different PI in diverse set-up conditions.

PI	quartz tube (%)	glass tube	glass tube + stirring
Ig2/TPO	26	5	10
4-HBP	79	77	100

2.3.1.4 Homogenization

As aforementioned in section 2.3.1.1, efficient irradiation is strongly related to light penetration and thus to employed vessels. This aspect clearly limits the working scale. In fact, for thin channel geometries, even when recirculation is employed, the amount of solution under illumination is limited, and long irradiation times are still required to reach complete conversion. Another possible geometry consists in keeping the light source directly immersed within the reaction solution. Such setups generally allow to increase the reaction volumes, but in many cases at the expenses of thermic control. Proper circulator system outside the vessel can reduce the unwanted heating, but very specific (and expensive) pieces of equipment are needed, which cannot be implemented in home-made setups like the one we were employing. As already stated, apart from the reaction volume, another limit of our setup is the lack of homogeneous irradiation. During the photopolymerization, more secondary aggregates form in the first layers of solution exposed to irradiation, increasing scattering (as aggregates dimensions increase from ∼10 nm to over 200 nm). Particles Brownian motion is not sufficient to make species in the inner layers receive the same irradiation of those in the outer ones. Introducing magnetic stirring seemed to us a convenient and cheap way to overcome these issues: on the average, all objects end up to be irradiated in the same way. Moreover, we had evidence that with constant dispersion homogenization, the formation of secondary aggregates is more uniform, resulting in a smaller polydispersity. Figure 2.18 compares intensity distribution of dimensions from DLS of two polymerized T80/APE-4/4-EDMA/Ig2+TPO dispersions, with and without stirring the dispersion (although in vessels of different material): we can clearly see that secondary aggregates have a sharper distribution in dimensions in the former case than in the latter. Performing reactions in quartz vessels is expensive but unavoidable when working with 254 nm source. Standard borosilicate glass in fact absorbs radiation below 300 nm. When dealing with 365 nm light sources, quartz vessels are not strictly necessary, unless the chosen PI works on higher energy UV tail of the incoming radiation. Selecting the correct PI makes thus possible to employ regular glassware. Table 2.1 clearly shows that, in all cases, Ig2/TPO couple work worse than 4-HBP, probably for localization problems. The passage from quartz to glass vessel is particularly detrimental (conversion decreases from 26% respect to 5%, while in the

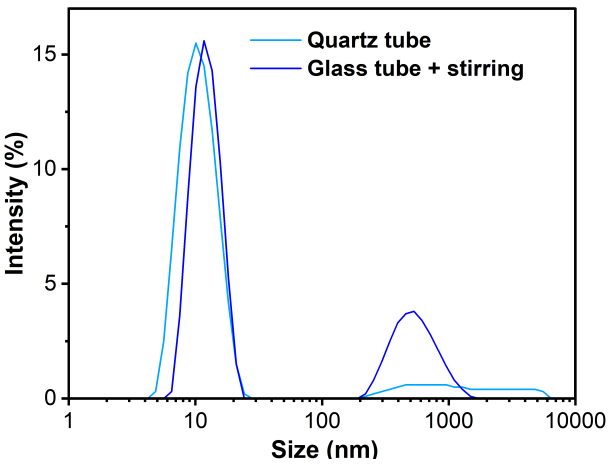

Figure 2.18 Intensity distribution of dimensions from DLS of two T80/APE-4/4-EDMA/Ig2+TPO stabilized micellar dispersions with different set-ups: quartz tube without stirring (light blue line) and glass tube with stirring (400 RPM, dark blue line).

case of 4-HBP it remains nearly unchanged), and neither stirring the dispersion does not really help. Apart from the localization issue, another relevant problem is the different absorption cross section above 300 nm. Figure 2.19 suggests in fact that, since glass absorbs most of the incoming radiation under 300 nm, Ig2+TPO are very poorly active respect to 4-HBP. In conclusion, selecting the correct PI can allow to use less expensive and consuming 365 nm sources coupled with regular glassware instead of quartz, still reaching high polymerization efficiency if the dispersions are properly stirred.

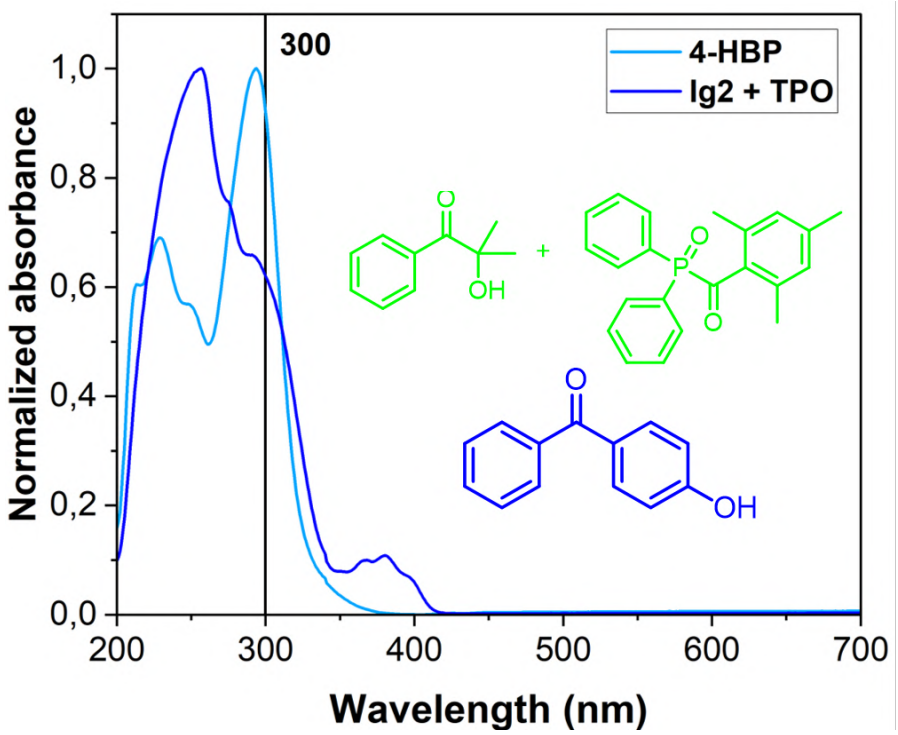

Figure 2.19 Absorption spectra in MeOH from Sigma Aldrich of respectively Ig2+TPO and 4-HBP from left to right. The absorption area over 300 nm is red filled for comparison.

2.3.2 Generality of the method

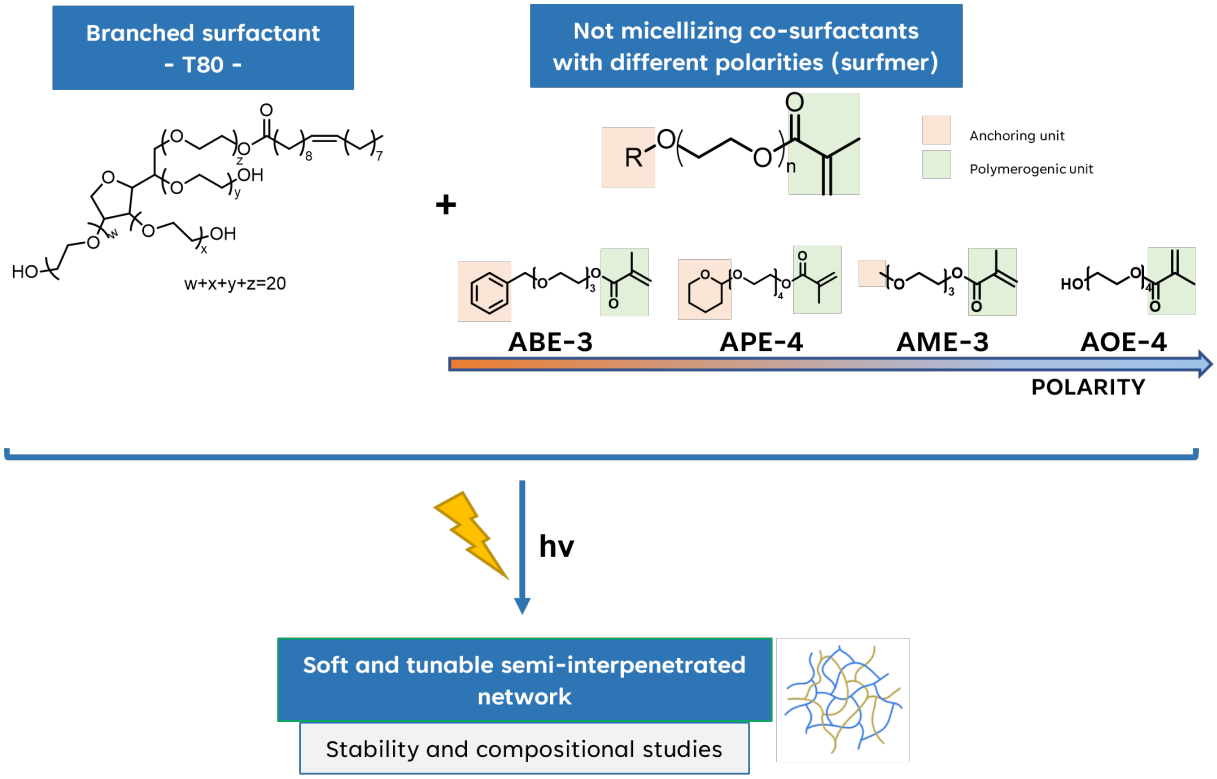

Figure 2.20 Schematic representation of the generalized method.

Part of the intrinsic value of the developed protocol is that is easily extendable to a plethora of co-surfactants. As depicted in Figure 2.20, methacrylic functionality and ethylene glycol chain are maintained but lipophilic portion can be varied. Since anchor group assesses molecule localization, we can exploit a vast spectrum of polarity to tune co-surfactant compartmentalization from core to outer micelle shell, with different effects on softness and morphology of the obtained sIPN. We selected the two representative species:

- benzoxyl triethylene glycol methacrylate (ABE-3), expected to be more lipophilic than APE-4;
- methoxy triethylene glycol methacrylate (AME-3), expected to be less lipophilic than APE-4 (but more respect to its deprotected form, AOE-4).

The different predicted localizations could mean that, potentially, each co-surfactant need to be coupled with a different PI with corresponding polarity, as demonstrated to be fundamental in section 2.15. Further optimization steps would thus be required for each species,somewhat limiting the generality of method. To better understanding the differences between dispersions produced with different co-surfactants, we performed polymerization test using the 254 nm light source, capable to directly activate methacrylate polymerization, without recurring to any PI, and investigate the possibility to use the 365 nm source in the future. Moreover, we systematically measured irradiation power density and employed magnetic stirring to boost reproducibility. We also tested increased dispersion concentration in water of one order of magnitude (from 0,2 wt% to 2 wt% of T80): increasing system efficiency allows us to produce larger quantities of stabilized

colloids in every batch (proof of concept for AME-3 in section 2.3.2.1). Finally, the effective stabilization is demonstrated by purification via dialysis through ultra-centrifugation and by resistance to organic solvent exposure.

2.3.2.1 AME-3

AME-3 is the simplest co-surfactant of the family: it bears a methyl unit as the anchoring group, and it is synthesized from triethylene glycol monomethyl ether with methacrylic acid by Fisher-Speier esterification (details in experimentals). It is less lipophilic than APE-4, but more than the deprotected form (HLB): we consequently expected it to localize in the outer micelle region. First, we tested the effect of increasing the dispersion concentration of one order of magnitude, from 0,2 wt% to 2 wt%. From correlograms and intensity % distribution comparison (Figure 2.21), we can clearly observe that T80/AME-3 system is characterized by similar 10 nm and 190 nm objects, but the smaller population is more abundant. Moving to higher concentration, the concentration of secondary aggregates increases, while still remaining below APE-4 value. Considering that coalescence is unavoidable during the polymerization step, we decided to employ the 2 wt% dispersion. We exposed the dispersion to 254 nm irradiation (3,9 mW cm^{-2}) for 3 hours under magnetic stirring and cooled the system with a stream of compressed air. The ^{1}H NMR (Figure 2.23) and also FTIR confirmed that photopolymerization took place even if conversion was not complete (stopping at 82%). The DLS correlogram evidences the presence of three families of aggregates with distinct dimensions (Figure 2.22): the first one in the tens nanometres range, compatible with starting single micelles, the other two in the hundreds nanometers range. The AME-3 probable localization in the most external part of the PEG-ylated shell can make more probable the reaction between co-surfactants molecules from different starting micelles ("inter-micellar" instead of "intra-micellar"), thus favouring more extended aggregation.

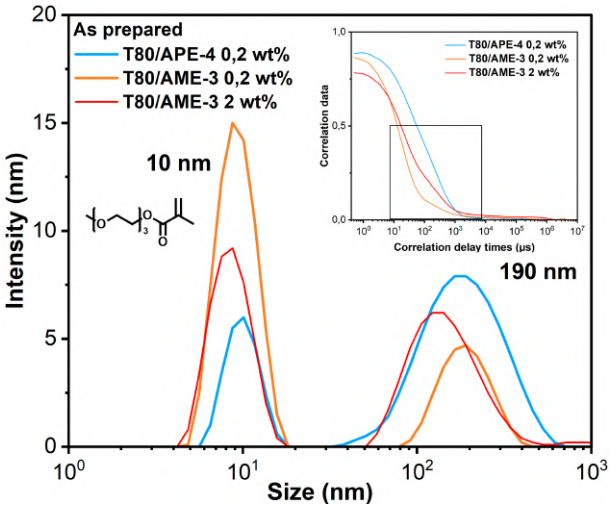

Figure 2.21 Intensity distribution of dimensions and correlograms (in the inset) from DLS of as prepared T80/APE-4 0,2 wt% and T80/AME-3 0,2 and 2 wt% dispersions .

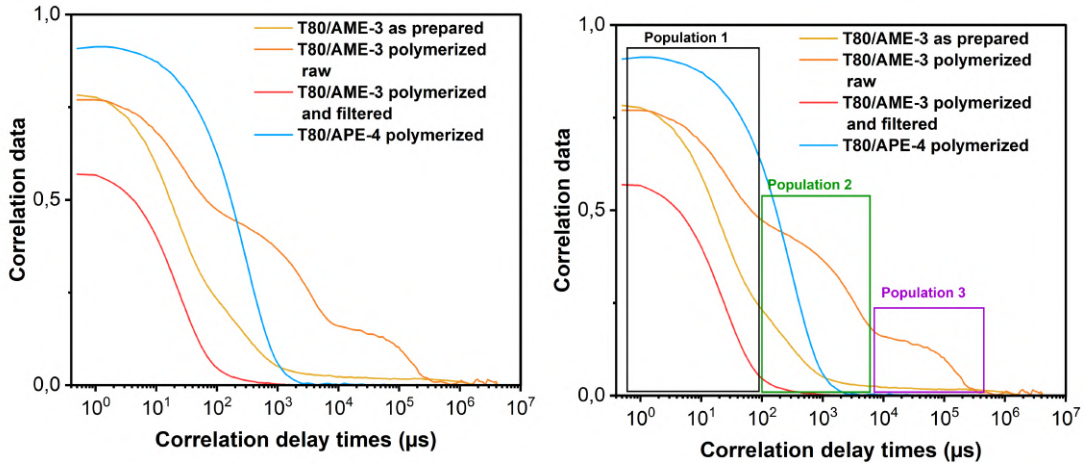

Figure 2.22 Correlograms comparison (with and without highlighted region of different populations) from DLS of as-prepared, photopolymerized raw and filtered (0,2 µm pores) T80/AME-3 2 wt% and T80/APE-4 photopolymerized 0,2 wt% dispersions. (b) ^{1}H NMR in DMSO-d_6 of as prepared and photopolymerized T80/AME-3 samples.

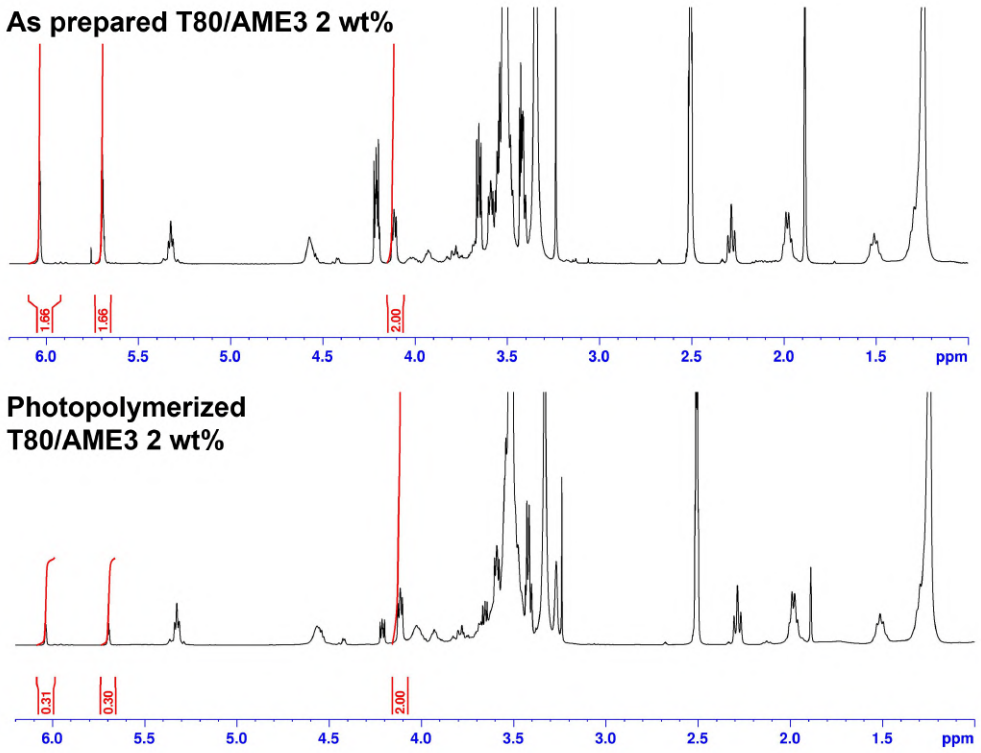

Figure 2.23 ^{1}H NMR in DMSO-d_6 of as prepared and photopolymerized T80/AME-3 samples.

We thus filtered the dispersion through a proper syringe filter (0,2 μm pores) and collected the DLS again. As evidenced in Figure 2.22 (red curve), after filtration only the small population remains. We checked if this dimension refinement was possible with centrifugation as well, treating the dispersion at 8000 RPM for 20 minutes. The DLS of the supernatant (Figure 2.24(a)) is comparable, both for intensity distribution of dimensions and correlogram, to filtered sample, if not a little more refined. Last and foremost, we checked effective stability of this dispersion by drying the polymerized material under

reduced pressure and redispersing it in an organic solvent, N,N'-dimethylformamide (DMF), capable of solubilizing both T80 and AME-3. In both cases dispersion is transparent, but DLS evidences a fundamental difference (Figure 2.24): in the as prepared sample, all species are dissolved (no correlation is detected, yellow curve), while in the photopolymerized sample structured object are still present. This analysis suggests that our micellar aggregates can resist to organic solvent dissolution: this feature distinguishes them from common micelles and widens their applications.

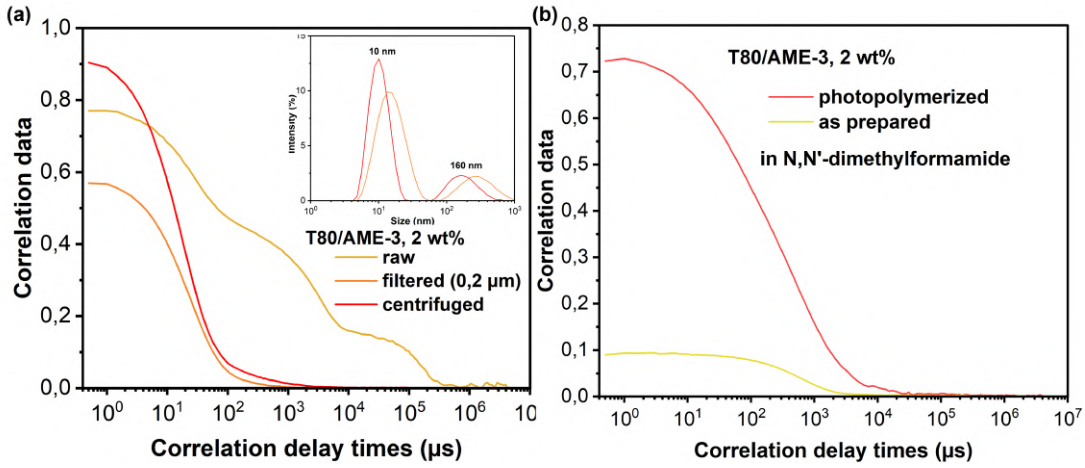

Figure 2.24 (a) Intensity distribution of dimensions from DLS and correlograms comparison in the inset of photopolymerized raw, filtered and centrifuged T80/AME-3 dispersion. (b) Correlograms comparison from DLS of as prepared and photopolymerized T80/AME-3 sample after redispersion in DMF.

2.3.2.2 ABE-3

Benzoxyl triethylene glycol methacrylate (ABE-3) is obtained with the same synthetic protocol of AME-3, employing triethylene glycol monobenzyl ether. The aromatic ring is expected to reduce the HLB value of this species with respect to APE-4, thus imparting a more pronounced lipophilicity, pushing this co-surfactant localization towards the micellar core. As prepared T80/ABE-3/4-EDMA 0,2 wt% dispersion shows intensity distribution of dimensions similar to those observed for APE-4, but secondary aggregates are on the overall bigger (140-390 nm with respect to 190 nm, Figure 2.25(I) light green curve). We thus decided to introduce a pre-treatment strategy: we heated the sample for 2 hours at 50 °C under magnetic stirring. The selected temperature is under T80 clouding point, in order to to maintain micelles structures. Such a treatment facilitates the dispersion of ABE-4 within T80 micelles, thus allowing to a quick equilibration of the system in its thermodynamic state.

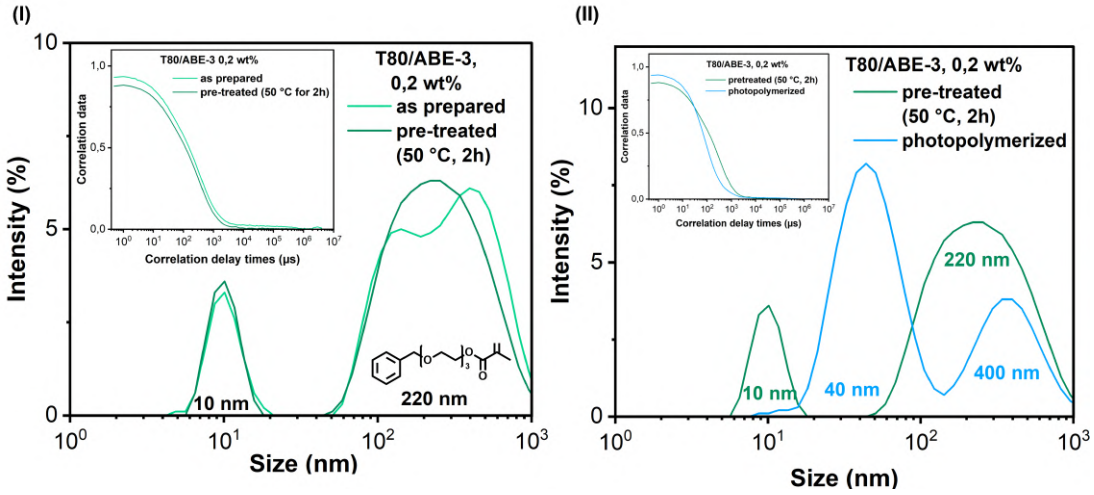

Figure 2.25 Intensity distribution of dimensions from DLS and correlograms comparison in the inset of (I) as prepared (light green curve) and pre-treated at 50 °C for 2h (dark green curve), (II) photopolymerized (blue curve) T80/ABE-3/4-EDMA 0,2 wt% dispersions.

After this step, at RT the dispersion is still limpid, and according to DLS the intensity distribution of the broad bigger ensemble of species reorganized around a single 220 nm peak (Figure 2.25 (II) dark green curve). The polydispersity is still high, but the initial thermally induced equilibration makes the output material more morphologically controlled. We irradiated the dispersion for 1,30 h with 254 nm source under compress air cooling. We significantly decreased irradiation time (usually at least 4 h) as we employed a source with significantly higher power density (31 mW cm^{-2} instead of the previous 3,9 mW cm^{-2}). The ^{1}H NMR conversion evidences that no methacrylate double bonds peaks are present at the end of the treatment, and thus under these conditions photopolymerization is very efficient (complete conversion). According to DLS, the resulting stabilized objects are composed of a principal family having intensity distribution of dimensions around 40 nm, smaller than the initial dimensions of secondary aggregates. This suggests that during photopolymerization process, coalescence is reduced. Since ABE-4 is the most lipophilic species of the family, reasonably the polymerization takes place within micelles instead of at their surface. A "shrinkage" effect can therefore take place (in agreement with the observation that the opposite effect takes place for AME-4). Finally, we tested dialysis and organic solvent resistance of the polymerized dispersion. Dialysis is the

standard purification technique reported in literature for this type of dispersion, for its simplicity and the possibility to remove unreacted species. However, instead of relying on standard procedures based on osmotic pressure differences, we preferred to take adavntage of ultra-centrifugation procedure: the as-obtained dispersion is put inside a centrifuge tube equipped with a dialysis membrane (Figure 2.26(a)), through which the liquid is forced to pass by application of centrifugal force.[58] In this way, the separation driving force is not given by osmotic pressure (slow) but by centrifugal force (fast). This method allows to obtain the same result of a 14-days dialysis in 1 hour. DLS analyses of the

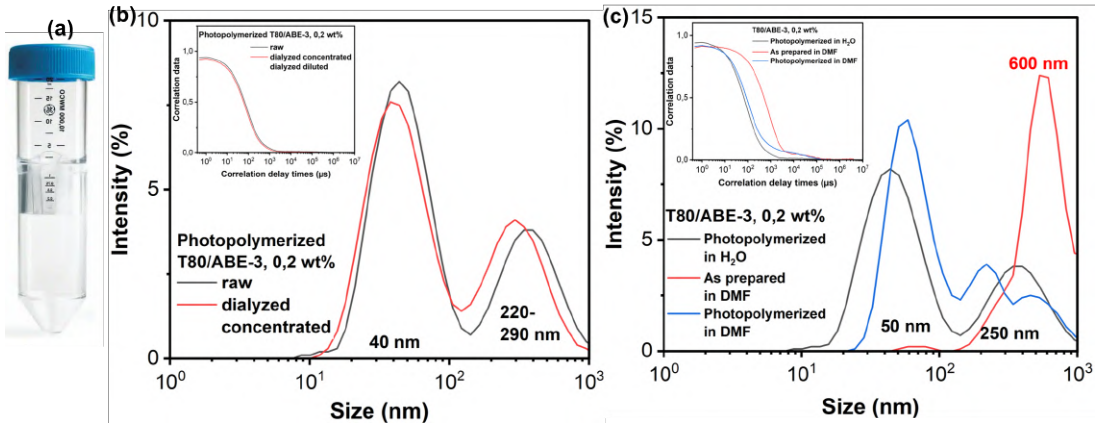

Figure 2.26 (a) Photograph of centrifuge vial for ultra-centrifugation dialysis: in the upper part starting dispersion is placed. This compartment is separated from the above one by a dialysis membrane, through which dispersion is forced to pass due to centrifugal force application: bigger species remains, concentrated. (b) Intensity distribution of dimensions from DLS and correlograms comparison in the inset of photopolymerized raw, dialyzed by ultra-centrifugation concentrated and diluted T80/ABE-3 dispersions. (c) Intensity distribution of dimensions from DLS and correlograms comparison in the inset of as prepared and photopolymerized T80/AME-3 sample after redispersion in DMF and the latter in H_2O.

raw sample as obtained after photopolymerization and of the concentrated sample as obtained after dialysis show the same correlogram and intensity distribution of dimensions (Figure 2.26(b)). These species, once stabilized, can't pass through membrane pores because they can't disaggregate anymore. Finally, we compared the DLS of as prepared and photopolymerized dispersion after drying and redispersion in DMF. Figure 2.26(c) indicates that, in the case of photopolymerized sample, the dimensions distribution is very similar, and the object are thus not affected by the solvent. The non-polymerized sample instead displays a very big peak around 600 nm: either T80/ABE3 starting colloids are not well soluble in DMF, or some water is retained inside the structure even after drying, causing a sort of inverse emulsification. Future lyophilization test on dried dispersion are in progress, to evaluate the second hypothesis. In short, the employment of a more lipophilic co-surfactant, expected to localized more towards micelle core, induce photostabilized micelles aggregates with smaller dimensions. On the contrary, when the polymerogenic species accomodates in the outer PEG-ylated shell, the photostabilized colloids are swollen and bigger. This behaviour supports our localization-polarity speculation and suggests that it can be tailored to obtain nano-object stabilized within specific compartments.

2.4 A preliminary step beyond: semi-interpenetrated surfactant-conjugated polymer nanoparticle network

Considering the previous work as the definition of an hosting system for further micellar catalysis with non-specific interactions, the in-situ formation of a polymer that retains surfactants chains during its growth can be extendend. If the polymer is able also to form specific interactions with reactive substrates, this can be exploited to activate them for specific reactions, as aformentioned in the chapter introduction. One of the most employed C-C coupling reaction both in research lab and more importantly in industry for synthesis of functional drugs and materials is Suzuki-Miyaura. It consists in the cross-coupling

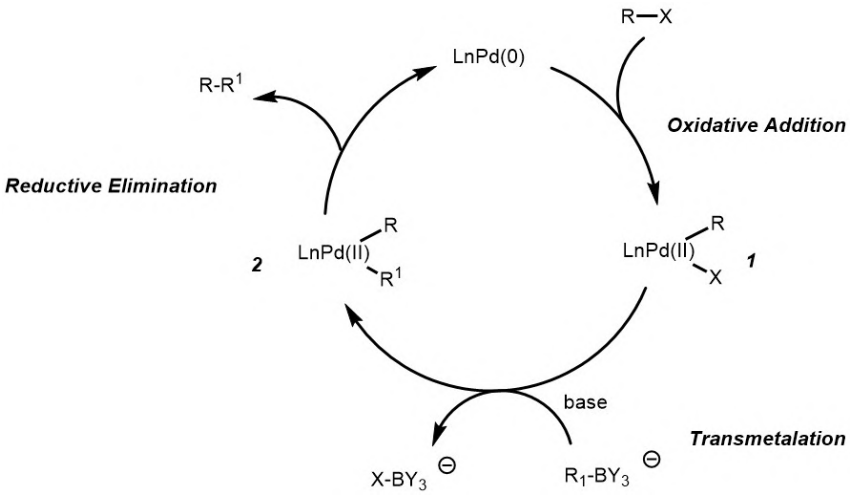

Figure 2.27 Reaction mechanism for Suzuki-Miyaura coupling

between an aryl, akenyl or alkynyl halide and an organoborane (boronic acid or ester) catalysed by a palldium(0) species. The reaction proceeds via three steps: the oxidative addition of the catalyst to the organohalide species to give organopalladium complex, trasmetallation with the boronate that derives from reaction with a base and finally reductive elimination to obtain the product and the restoring of the starting catalyst. The feasibility of this reaction in micellar conditions has been intensively studied and very competitive results have been obtained especially with designer surfactants, thanks to their specific interaction with typically conjugated substrates. We decided to exploit it thus both to synthesize the target supporting conjugated polymer in miniemulsion micellar condition and to further catalysed easier reactions with it, embedding the same palladium source employed for its growth and reusing it without further additions. Setting aside acrylate polymers, we chose Poly(9,9-dioctyl)fluorene (PFO).

2.4.1 Synthesis and characterization of PFO NPs

We firstly borrowed a literature approach by Turner et al.[59] starting from 9,9-dioctyl-2,7-dibromofluorene (1) and 9,9- dioctyl-9-H-fluorene-2,7-diboronic acid bis(pinacol) ester (2) using ($Pd(PPh_3)_4$) and sodium hydroxide (NaOH) as inorganic base (Figure 2.28). The inert atmosphere of nitrogen is required to avoid Pd(0) oxidation. The miniemulsion is created using toluene as disperse phase and a linear ionic surfactant, sodium dodecyl

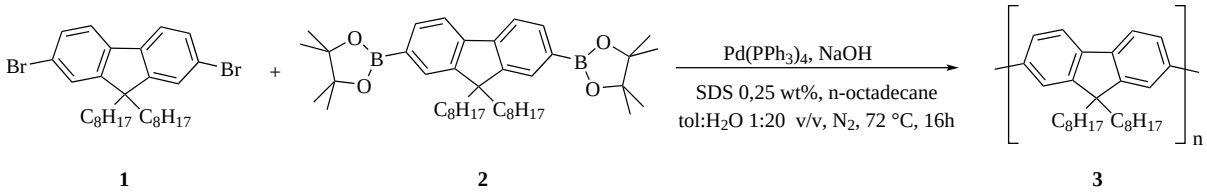

Figure 2.28 Synthesis of PFO NP through miniemulsion reported by Turner et al.[59]

sulfate (SDS, 0.25 wt%). ^{1}H NMR conversion confirmed the presence of short PFO chains along with reagents. This NPs synthetic strategy demonstrated to be not completely effective and moreover is not suitable for our final purpose: a linear ionic surfactant limits the creation of desirable sIPN. We decided to optimize the conditions in accordance to our group previous expertise in micellar catalysis and to our final aim:

- we introduce Aliquat HTA-1 (1 wt % respect to water), which is a renowned water-soluble quaternary ammonium salt designed for phase transfer catalysed reactions. It enables reactions between species dissolved in two immiscible phases through transfer of water-soluble active ions in the organic portion of the system. We were interested in pushing the reaction towards complete conversion of the reactant.
- we substituted SDS with a higher concentration surfactant mixture: T80, Kolliphor EL (K-EL) and Triton X 100 (TX-100). The first one has been already described ahead in the chapter. The second is reported to help preserve disperse species from oxygen[60] (in this case, Pd(0)) and the last one is composed by an aromatic apolar part, compatible with involved species. They are all branched in different way and can thus satisfy easily the requirment of sIPN formation.
- the reaction is performed under milder conditions (50 °C): pegylated species show the presence of a cloud point above that temperature that is detrimental for reaction. The application of such temperature even before base addition, which is the step that triggers reaction start, alongside with 5 minutes in a sonication bath, assures to have the best emulsion conditions.

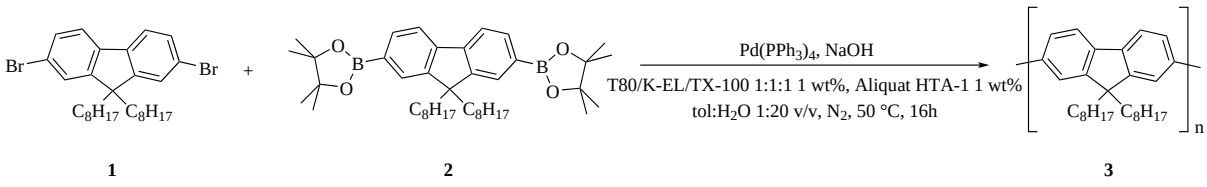

Figure 2.29 Synthesis of PFO NP through optimized miniemulsion.

After 16 hours (Figure 2.29), the presence of the polymer was firstly highlighted by miniemulsion change in colour, from white to yellow and the appearance of a strong blue luminescence typical of PFO. This suggestion is confirmed by ^{1}H NMR: it clearly shows the distinctive broad peak of PFO, whilst reagents peaks are absent. The organic solvent (toluene) is then let evaporate to make the miniemulsion a final nanodispersion (PFO ND): the DLS analysis revealed the presence of a sole family of colloidal objects (Figure2.30).

The average dimension of the aggregates is 180 nm (PdI 0,2). The only purification step is an easy dialysis through ultracentrifugation: it is necessary to remove the salts from the reaction mixture. The concentrated and purified paste is redispersed in the

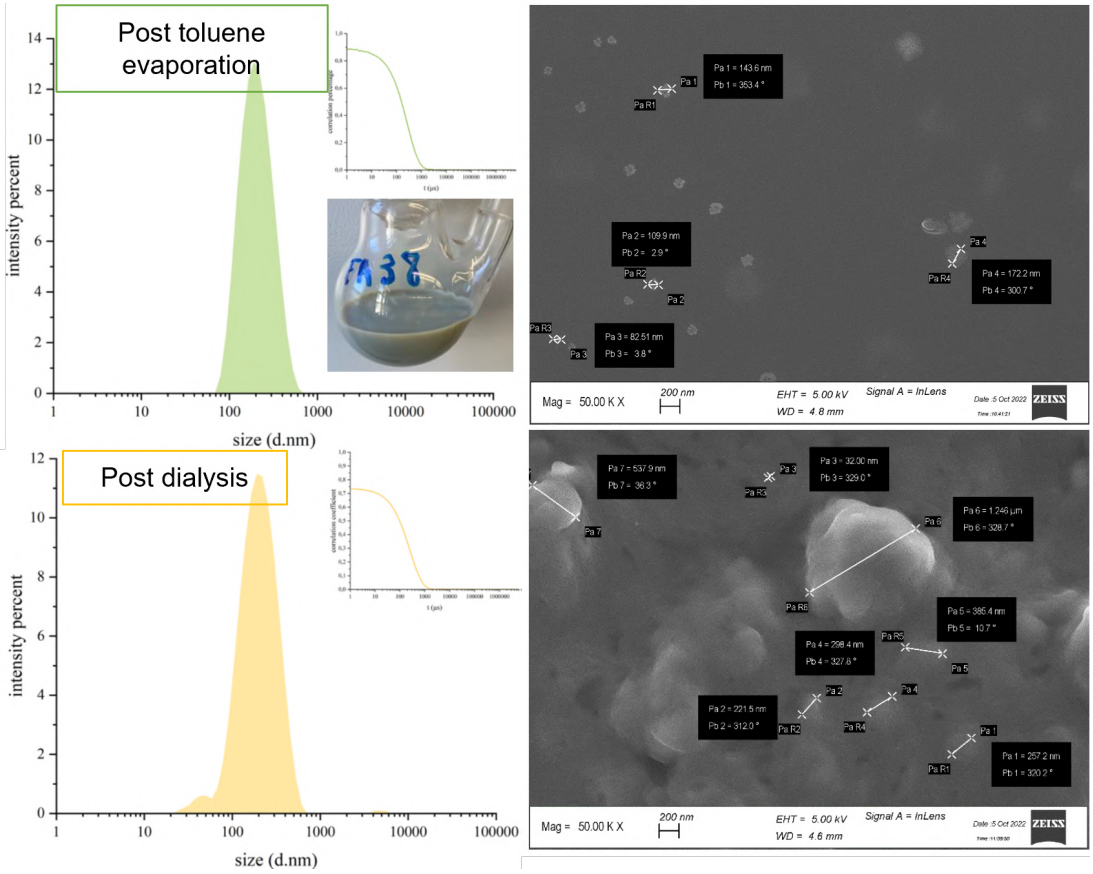

Figure 2.30 DLS derived intensity distribution (on the left) with correlograms in the inset of Pd nanodispersion after toluene evaporation (top, with photograph) and after dialysis (bottom). SEM image (on the right) of PFO ND after dialysis withou (top) and with (bottom)redispersion to the initial concentration with neat water.

same amount of neat water and sonicated with an ultrasound bath for 30 minutes. The discarded water didn't show any absorption peak attributable to Pd species (around 440 nm[61]). After this straightforward purification step, the quality of the dispersion is pretty much maintained (from DLS 170 nm – PdI 0,2), probably because of entangled surfactant contributes. Post-dialysis ^{1}H NMR analysis confirmed the presence of surfactants inside the dispersion, suggesting the presence of desidered sIPN. To deepen morphology of the obtained nanobjects, we performed SEM imaging both on the concentrated and redispersed PFO ND (Figure 2.30, on the left). The samples were prepared by directly drop-casting on a piece of silicon. The analysis confirmed the expected spherical nanometric objects. The surfactant stabilized droplets acted as a template and promoted the formation of spherical polymeric entities (sIPN). The presence of different levels of bigger aggregates is also visible, especially in concentrated sample. Their formation is most likely related to the evaporation of the solvent, causing the accumulation of multiple colloidal objects. The diameter of some of them have also been measured and is coherent with DLS intensity result: the dimensions range between 80 nm and 200 nm, depending on the hierarchical aggregation of the species. We also collected the energy dispersive spectrum (EDS) spectrum of specific area on a more concentrated sample (Figure 2.31), detecting Pd presence even if very diluted. Phosphorous is also detected and its presence is linked to the palladium source phosphine ligands. The phosphines could be in their oxidised form, thus less reactive. Solid state NMR (SS NMR) coupled with X – Rays Photoemission Spectroscopy (XPS)

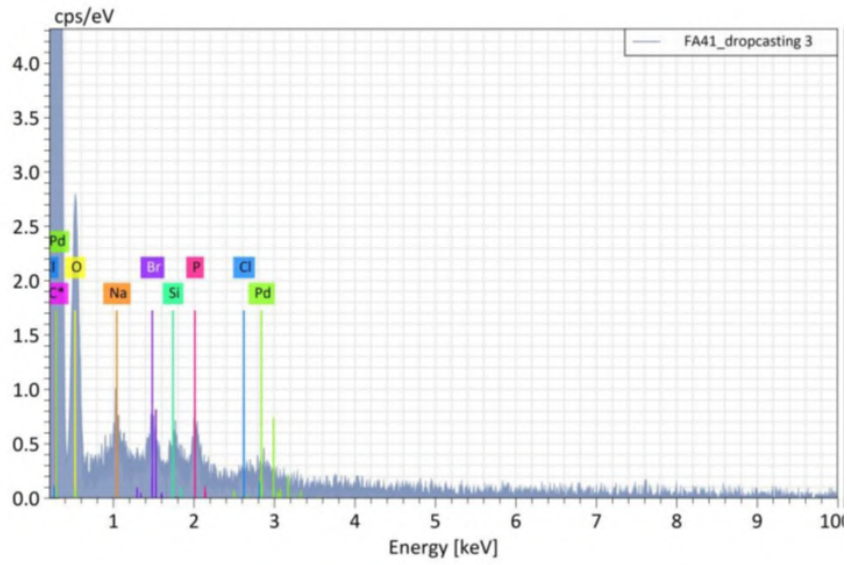

Figure 2.31 Energy dispersive spectrum (EDS) collected on the concentrated sample after purification by dialysis.

could deepen this aspect and are thus in program.

2.4.1.1 Preliminary catalytic tests

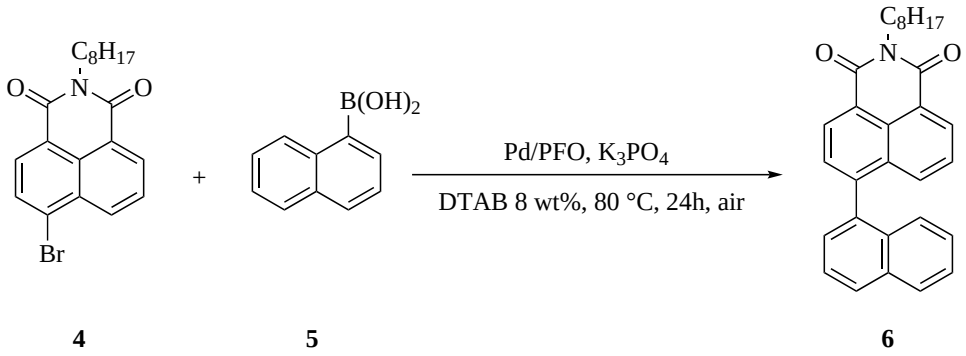

Figure 2.32 Energy dispersive spectrum (EDS) collected on the concentrated sample after purification by dialysis.

We preliminary tested the PFO ND here described on a Suzuki-Miyaura reaction previously investigated inside the research group. The cross-coupling between N-octyl-4-bromonaphthalene-1,8-dicarbimide (7) and 1-napthaleneboronic acid (8) was used as test reaction (Figure 2.32). The reported conditions had been previously optimized by the research group to perform such reaction using Pd/C as heterogeneous catalyst. Given the assonances between the two catalysts, the reaction has been simultaneously pursued using a homemade Pd/C following the same experimental procedure and using nominal 14000 ppm of Pd in both cases. The comparison allowed the relative estimation of the catalytic performance of the novel catalyst. The reaction is simply performed by mixing together the reagents into the PFO ND and the base is added as last. For Pd/C, the powder is mixed with solid reactant and then dispersed in dodecyltrimethylammonium bromide (DTAB) 5 wt% dispersion in deionized water. In the former case, the reaction mixture

appears more homogeneous, both at RT and 80 °Cas consequence of improved dispersion properties of the catalytic NPs allowed by surfactant layer around each colloidal object. DTAB was also employed to maintain the same conditions used for Pd/C, thus making the tests comparable. After 24 h the reaction was stopped. After a filtration step, the crude reaction product was taken up with water to remove both DTAB and salts and ^{1}H NMR was performed. A 100% conversion was obtained as neither reagent nor homocoupling by-product were detected. On the other hand, the Pd/C catalysed reaction conversion settled down to around 63%, and a consisted percentage of homocoupling by-product was also detected (5%) The outstanding result confirmed the benign influence of the enhanced homogeneity of the system but can also be linked to the presence of phosphines, proving that the introduction of the active Pd species from the beginning of the one-pot procedure is advantageous respect to the subsequent deposition by reduction. Reause of the novel catalytic dispersion, further extension of the reaction library, as well as a tune of the conjugated backbone of the supporting polymer is under study.

2.4.2 Conclusions

We started from a preliminary work finalized at photopolymerization of a designer co-surfactant, APE-4, around branched micellar structure of T80. The aim is the formation of a semi-interpenetrated network to freeze micellar dynamics. This could be considered a "box" to study localization of host species depending on their polarity and exploit it as selective reaction medium. We optimized the irradiation protocol based on 365 nm light source,which proved troublesome due to the competitive cleavage of the tetrahydropyran ring moiety. After considering the use of flow reactor and the synergistic effect of a sensitizer, we concluded that photoinitiation localization is the fundamental parameter to achieve best efficiency. In this direction 4-HBP demonstrated to be the most suitable for APE-4. We also investigated the extension of the method toward co-surfactant of the same family: the anchoring unit can be tuned in polarity to enable photopolymerization from micellar core to the external PEG-ylated shell, with differences in obtained aggregates morphology. We synthesized and tested AME-3 and ABE-4: they don't present labile group that can generate parasite processes under irradiation. To make the protocol as general as possible, direct 254 nm methacrylic activation was chosen. Finally, we tested purification via ultra-centrifugation dialysis to refine final dimensions of the particles in the dispersion and proved the resistance of stabilized micelles to a good organic solvent such as DMF. We plan to use our stabilized colloids as artificial enzymes, featuring well defined reaction sites whose structure is independent from the concentration of the surfactant cocktail. We will also study the effect of the localization of the catalysts within the different compartments of the stabilized micelles on the efficiency end selectivity of competitive cross coupling reactions. The concept of an in situ growing polymer that forms a sIPN with surrounding surfactant, as long as the emerging need of efficient heterogeneous catalyst have been taken into consideration for the synthesis of a novel heterogenized catalyst whose supporting counterpart is formed by non-porous π-conjugated organic nanostructures obtained through micellar polymerization. They are designed to be intrinsically stable, water-dispersible and to embed the Pd catalyst involved into their own synthesis so that they could be directly reused as heterogenized catalyst in further micellar cross-coupling reactions. The proof-of-concept of the project has been the optimization of a miniemulsion approach for the synthesis of PFO supporting material. At this stage, polymer growth is directly conduced within nanometric droplets through a one-pot process

to obtain conjugated polymer nanoparticles (CPNPs). Literature examples of CPNPs synthesis always contemplate a purification step, to get rid of surfactants. However, in this case, their entanglement within the colloidal structure is a crucial advantage: they constitute a template in which the polymeric nano-object can grow, and they make it suitable for its final application as catalyst. The synthesis produces dispersed spherical Pd-embedding polymer-surfactant semi-interpenetrated networks (sIPN), as evidenced by ^{1}H NMR, SEM imaging and EDS. Such dispersion is then used as heterogenized catalyst showing complete conversion respect to the classic Pd/C heterogenous catalyst in same conditions. Encouraged by preliminary results both catalysts generalities are currently under investigation and a library of reactions is taking shape broaden their application field.

2.5 Experimental

2.5.1 Chemicals

Tetraethylene glycol, 3,4-dihydropyran, paratoluene sulfonic acid monohydrated and N,N-diisopropylethylamine were purchased from Alfa Aesar. Dichloromethane (then anyhdrificated over $CaCl_2$), N,N-dimethylformamide and toluene were purchased from VWR. 4-(dimethylamino)pyridine, N,N'-Dicyclohexylcarbodiimide, 4-hydroxybenzophenone, tetraethylene glycol dimethacrylate, Tween 80, sodium dodecyl sulfate, Kolliphor EL, triton X 100, Aliquat HTA-1, NaOH, K_3PO_4, dodecyltrimethylammonium bromide and $CDCl_3$ were purchased from Sigma Aldrich. Dimethylsulfoxide-d_6 was purchased from Euriso-top. Triethylene glycol monobenzyl ether was purchased from Fluorochem, triethylene glycol monomethyl ether from Fluka, 2-hydroxy-2-methylpropiophenone and diphenyl(2,4,6-trimethylbenzoyl)phosphine oxide from TCI and 4,4-Bis(dimethylamino)-benzophenone and N-octyl-4-bromonaphthalene-1,8-dicarbimide was synthetized. 9,9-dioctyl-2,7-dibromofluorene, 9,9-dioctyl-9-H-fluorene-2,7-diboronic acid bis(pinacol) ester, $Pd(PPh_3)_4$ and 1-napthaleneboronic acid were purchased from BLD Pharma.
^{1}H NMR measurements were conducted at 300 K on a Bruker Avance NEO 400 MHz spectrometer equipped with BBFO probe. All samples were analyzed at a concentration around 20 mg/mL in glass NMR tubes. All ^{1}H spectra are referred to the signal of residual nondeuterated solvent (calibrating at 7.16 ppm singlet peak from benzene). Measurement were performed by Giorgio Patriarca.

2.5.2 Synthesis of co-surfactants

2.5.2.1 APE-4

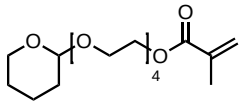

Figure 2.33

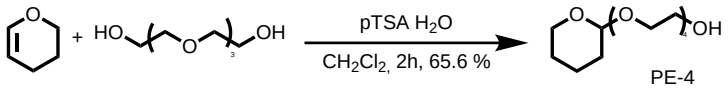

Figure 2.34

PE-4 In a single neck 1 L round bottom flask, 270 g of tetraethylene glycol (1,39 mol, 200 mL) are dissolved in 538 mL of dichloromethane and then 947 mg of paratoluenesulfonic acid monohydrate (5,5 mmol) are added. 15,5 g of 3,4-dihydropyran (0,3 mol, 21,2 mL) are added drop-wise over 1 hour: the solution is colorless. The mixture is let stir for 72 hours. After evaporation under reduced pressure of half solvent volume, the crude solution is washed once with water saturated with $NaHCO_3$ (10 g in 100 mL) and seven times with brine (100 mL). The organic phase is dried over anhydrous Na_2SO_4, filtered and evaporated under reduced pressure, obtaining 58,85 g of a pale yellow liquid (0,2 mol, yield 65,6 %).

^{1}H NMR ($CDCl_3$, 400 MHz): δ 4.57 (q, J=2.8 Hz, 2H), 3.82-3.77 (m, 4H), 3.65-3.53 (m, 29H), 3.1 (s, 1H), 1.8-1.73 (m, 2H), 1.68-1.62 (m, 2H), 1.57-1.43 (m, 8H). See reference[54] for comparison.

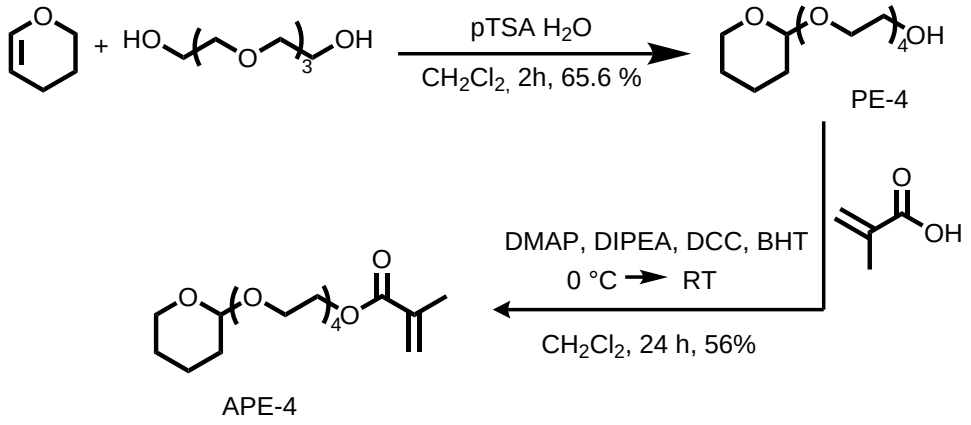

Figure 2.35

APE-4 A 250 mL single neck round bottom flask, a magnetic stirrer and a drying tube filled with $CaCl_2$ are anhydrificated in oven at 120 °Cfor 24 hours. PE-4 (7 g, 25 mmol), methacrylic acid (2,2 g, 2,1 mL, 25,9 mmol), DMAP (400 mg, 3,3 mmol), DCC (5,2 g, 25,4 mmol), DIPEA (423 mg, 3,3 mmol), BHT(Butylated hydroxytoluene) (56 mg, 0,25 mmol) are added. The flask is put inside an ice bath and 161 mL of CH_2Cl_2 are added. The ice bath is removed and the mixture is let stir for 24 hours at RT. After this time, a white precipitate is formed. The crude dispersion is filtered off, the recovered liquid is put in freezer for one night and the rest of the precipitate is filtered off again. The liquid is dried under reduced pressure and taken up with heptane/ethyl acetate 9:1 v/v. After filtration, the solid is recovered as product (1,99 g, 5,7 mmol) and the solution is purified with flash column chromatography (eluents respectively 100 mL of heptane, 100 mL hept/AcOEt 9:1 v/v, 350 mL hept/AcOEt 1:1 v/v). The total amount of product obtained is 4,9 g (14,2 mmol, yield 56,4 %).

^{1}H NMR ($CDCl_3$, 400 MHz): δ 6.11 (m, 1H), 5.55 (m, 1H), 4.6 (t, J=3.7 Hz, 1H), 4.28 (t, J = 4.9, 2H), 3.88-3.82 (m, 2H), 3.73 (t, J= 4.9 Hz, 2H), 3.67-3.63 (m, 10H), 3.61-3.56 (m,1H), 3.50-3.45 (m, 1H), 1.93 (dd, J=1.6 Hz, J=1.0 Hz, 3H), 1.85.1.77 (m, 1H), 1.73-1.66 (m, 1H), 1.61-1.47 (m, 4H). See reference[54] for comparison.

2.5.2.2 AME-3

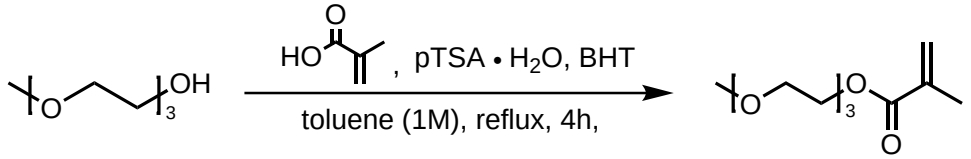

Figure 2.36

In a 100 mL single neck round bottom flask, triethylene glycol monomethyl ether (7 g, 42,6 mmol, 6,8 mL) is dissolved in toluene (42,6 mL). Methacrylic acid (3,67 g, 42,6 mmol,

3,6 mL) is added under stirring, then paratoluenesulfonic acid monohydrated (734 mg, 4,26 mmol) and BHT (93,9 mg, 0,426 mmol) are added too. The reaction is heated at reflux for 4 hours. After that time, the crude mixure is cooled down to RT, filtered on silica pad and completely recovered with hept/AcOEt 1:1 (200 mL). After solvent evaporation, we obtained 5,9 g of viscous liquid (5,9 mmol, yield 60 %). ^{1}H NMR ($CDCl_3$, 400 MHz): δ 6.11 (s, 1H), 5.56 (q, J=1.6 Hz, 1H), 4.6 (t, J=4.9 Hz, 2H), 3.73 (t, J = 4.8 Hz, 2H), 3.68-3.62 (m, 6H), 3.54-3.52 (m, 2H), 3.36 (s, 3H), 1.93 (t, J=1.3 Hz, 3H). See reference[62] for comparison.

2.5.2.3 ABE-3

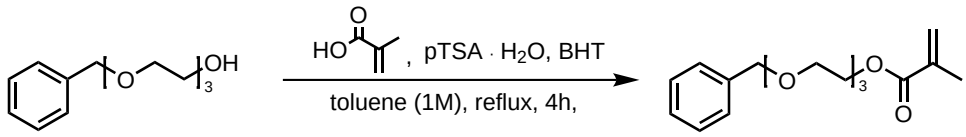

Figure 2.37

In a 50 mL single neck round bottom flask, triethylene glycol monobenzyl ether (2 g, 8,3 mmol) is dissolved in toluene (8,3 mL). Methacrylic acid (0,716 g, 8,3 mmol, 0,7 mL) is added under stirring, then paratoluenesulfonic acid monohydrated (143 mg, 0,83 mmol) and BHT (18 mg, 0,08 mmol) are added too. The reaction is heated at reflux for 4 hours. After that time, the crude mixure is cooled down to RT, filtered on silica pad and completely recovered with hept/AcOEt 1:1 (100 mL). After solvent evaporation, we obtained 1,63 g of viscous liquid (5,3 mmol, yield 64 %). ^{1}H NMR ($CDCl_3$, 400 MHz): δ 7.32-7.23 (m, 5H), 6. 11 (s, 1H), 5.54 (t, J= 1.5 Hz, 2H), 4.55 (s, 2H), 4.28 (t, J=4.9 Hz, 2H), 3.73 (t, J=4.9 Hz, 2H), 3.68-3.63 (m, 6H), 3.62-3.6 (m, 2H), 1.93 (s, 3H).

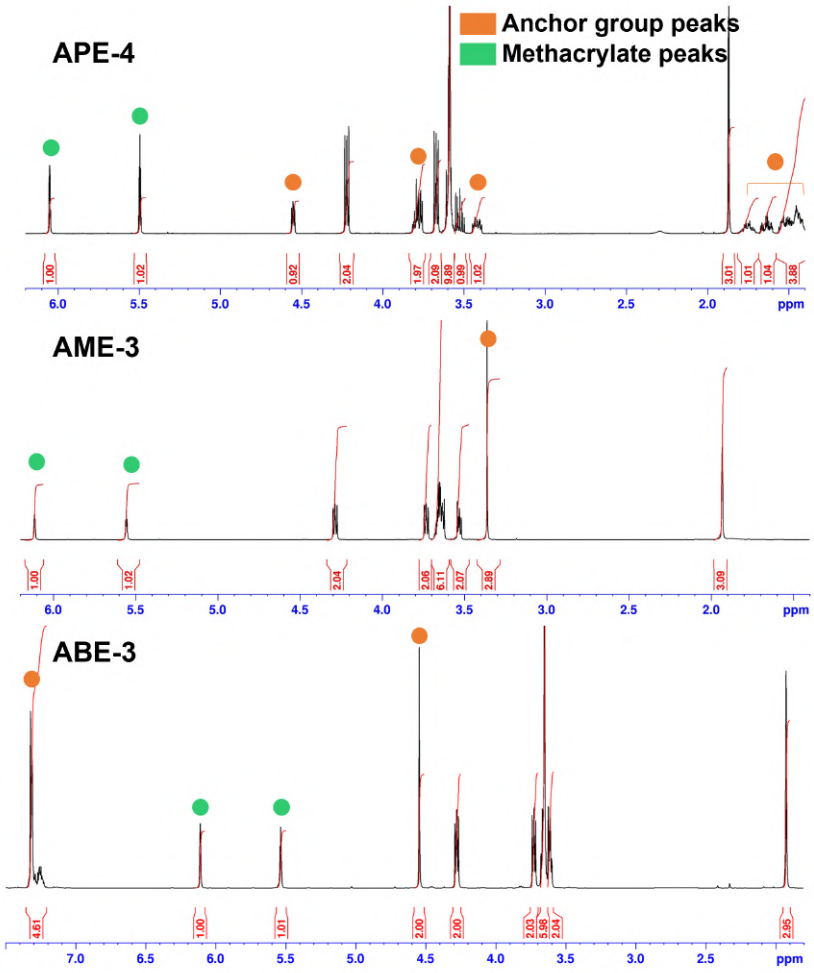

Figure 2.38 ^{1}H NMR comparison in $CDCl_3$ between functional groups of APE-4, AME-3 and ABE-3.

2.5.3 Synthesis of PFO ND by miniemlusion polymerization

2.5.3.1 Literature approach

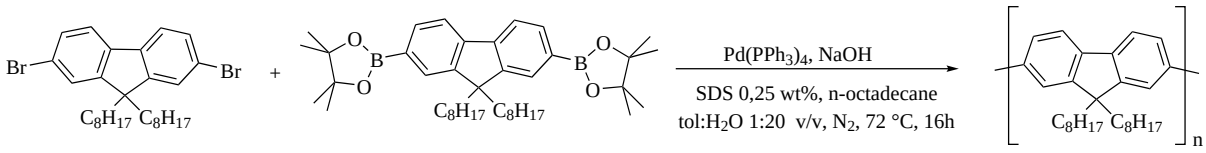

1 **2** **3**

Figure 2.39

Sodium dodecylsulfate (50 mg) and deionised water (20 mL) were degassed by bubbling with N_2 while boiling for 4 hours, then trasferred inside a screw-cap tube filled with nitrogen. 9,9-dioctyl-2,7-dibromofluorene (50 mg, 0.09 mmol), 9,9-dioctyl-9-H-fluorene-2,7-diboronic acid bis(pinacol) ester(58.6 mg, 0.09 mmol), $Pd(PPh_3)_4$ (2.2 mg, 0.02 mmol) and n-octadecane (0.08 mL) were degassed and anhydrous toluene (1 mL) was added under N_2 atmosphere. The solution is transferred to the tube reaction vessel and emulsified by immersion ultrasonication for 2 minute while cooling with an ice bath. The tube was then

Table 2.2 Tween 80 characteristics.

average composition of apolar portion	oleic acid $\geq 58\%$, linoleic, palmitic, stearic acids
average MW	~ 1310
CMC	$0,012mM$ $(0,0016wt\%)$
density	$1,06$ g/mL (25 °C)
clouding point	65 °C
aggregation number	60 (micellar weight ~ 79000 g/mol)
HLB value	15
τ_2	$8-10$ s

filled again with nitrogen, sealed and heated up to 72 °Cunder stirring. At this point, 0.36 mL of 1M NaOH acqueous solution is added and the reaction is stirred for 16 hours. After cooling to room temperature, the residual toluene is let evaporate.

2.5.3.2 Optimized approach

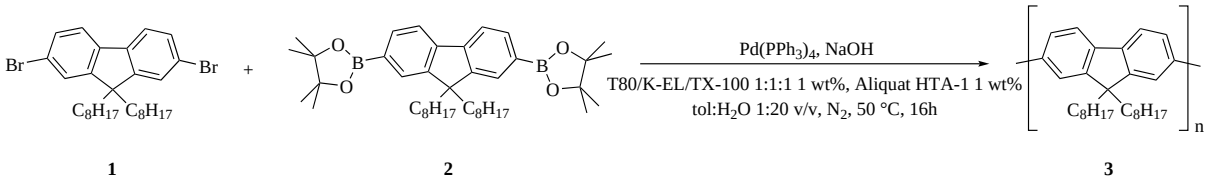

Figure 2.40

Deionised water was degassed by bubbling N_2 for 4 hours. 9,9-dioctyl-2,7-dibromofluorene (120 mg, 0.22 mmol) and 9,9-dioctyl-9-H-fluorene-2,7-diboronic acid bis(pinacol) ester(141 mg, 0.22 mmol) were dissolved together with K-EL, T80 and TX-100 (66 mg each one, 1:1:1 wt/wt, 1 wt% in water) using the minimum THF quantity in a two neck round bottom flask. The solvent was removed form sample by evaporation using rotavap, then both reagents and surfactant are put under N_2 atmosphere through a Schlenk line. Anhydrous toluene (1 mL) containing $Pd(PPh_3)_4$ (14 mg, 0.012 mml) (solution produced in glove box, Ar filled) was added to reagents and surfactant. Deionized water was drop-by-drop added to the oil phase under vigorous magnetic stirring (1100 RPM) keeping the temperature of both phases at 50 °C, followed by 30 minutes ultrasonication bath step allowed for colloids dimension refinement. NaOH (36 mg, 0.9 mmol) is put in a two neck round bottom flask under nitrogen, deionized degassed water is added to reach 1 M concentration and then the solution is added to the reaction. Finally, Aliquat HTA-1 (667 mg) is added with a syringe and the reaction mixture is kept under magnetic stirring at 50 °C. After t24 hours, it is cooled down and characterised through DLS and ^{1}H NMR. The cap of the reaction vessel is then removed and toluene is let evaporate for 5 hours. The colloidal dimension were further checked through DLS. The dispersion was then dialysed by ultracentrifugation (4500 rpm, RT), using a Sigma 3-16PK laboratory centrifuge, to remove the salts from the reaction mixture, then the recovered paste is redispersed in the same amount of neat water and sonicated with an ultrasound bath for 30 minutes. Such purified dispersion was characterised through DLS and SEM analysis.

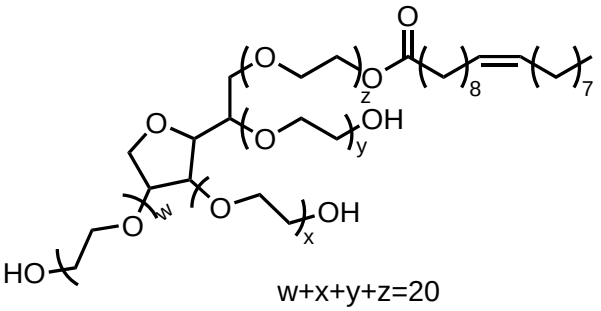

Figure 2.41 Molecular structure of the major component of Tween 80.

Table 2.3 Relative quantities of each derivative employed to obtain T80 0,2 wt% in deionized water micellar dispersions. For each dispersion, one type of co-surfactant and one type of photoinitiator (except for Ig2, used coupled with TPO) are added.

Type	Derivative	MW (g/mol)	Amount (mg)	n (μmol)	Equivalents	V ()mL)
Surfactant	T80	~ 1310	160	$122,2$	$0,67$	
Co-surfactant	APE-4	$346,3$	$63,5$	$183,3$	1	
	4-EDMA	$330,4$	$60,6$	"	"	
	AME-3	$233,3$	$42,8$	"	"	
	ABE-3	$308,4$	$56,5$	"	"	
Photoinitiator	DABP	$220,3$	$1,6$	$7,33$	$0,04$	
	4-HBP	$198,2$	$1,45$	"	"	
	Ig2	$164,2$	$1,2$	"	"	
	TPO	$348,4$	$2,55$	"	"	
Crosslinker	4-EDMA	$330,4$	$3,03$	$9,165$	$0,05$	
THF						1
Deionized water						80

2.5.4 Tween 80

Tween 80 is a mixture derived from reaction of sorbitan with fatty acids and following etoxylation.

2.5.5 Preparation of micellar dispersions

T80, co-surfactant, photoinitiator (if needed) and crosslinker are weighted and dissolved in 1 mL of THF. The solution is swiftly injected in 80 mL of water under vigorous magnetic stirring. THF is let evaporate under stirring for 1 hours, then dispersion is ready to be characterized and employed. The exact quantities for each type of dispersion are reported in Table 2.3 and 2.4

Pre-treatment As prepared T80/ABE-3/4-EDMA micellar dispersion, after THF evaporation, was heated at 50 °Cfor two hours under magnetic stirring. The temperature is under T80 clouding point.

2.5.6 Photopolymerization sources and set up

Photopolymerization was performed on 20 mL micellar dispersion either in quartz tube reactor (25 cm high, 1,5 cm diameter), glass tube reactor (25 cm high, 2,7 cm diameter)

Table 2.4 Relative quantities of each derivative employed to obtain T80 1,5 wt% in deionized water micellar dispersions.

Derivative	MW (g/mol)	Amount (mg)	n (mmol)	Equivalents	V (mL)
T80	~ 1310	400	$0,3$	$0,67$	
AME-3	$233,3$	107	$0,46$	1	
4-EDMA	$330,4$	8	$0,023$	$0,05$	
THF					$0,25$
Deionized water					20

or in specific microchannels. The vessel is put under direct illumination.

2.5.6.1 254 nm

254 nm centered irradiation is obtained with a mercury lamp. The mercury lamp (low pressure, 125 W) and its power supply were purchased from Helios Italquartz Srl.

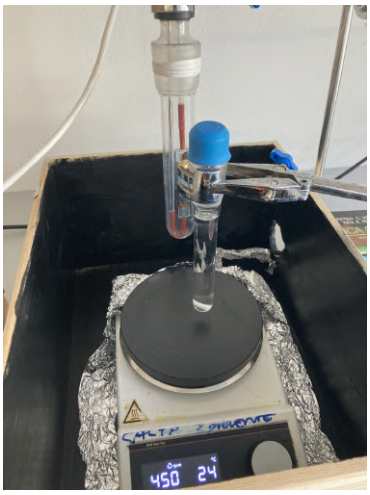

Figure 2.42 Photograph of the home made set up employed for photolymerization under 254 nm irradiation.

2.5.6.2 365 nm

365 nm centered irradiation has been obtained with nail lamp LEDS or with CORNING photoreactor LEDs.

Figure 2.43 Nail lamp employed as UV curing oven for photopolymerization under 365 nm irradiation.

Nail lamp The UV curing oven (shown in figure) was purchased from Proxima Direct® (model number J0202), and it is equipped with four 9 W lamps UV-9W.

CORNING lab reactor The Corning Lab Photo Reactor is a glass-made microfluidic reactor characterized by channels width of $< 500\mu$m. It is equipped with a set of LEDs centered around different wavelengths, the shortest being 365 nm. LED and reactor temperature are controlled through two separate heating circulators. A pump injects the reaction mixture within the reactor at a controlled flow rate, and the mixture comes out from the outlet tubing. If allowed to pour in the inlet vessel, the mixture can be easily recirculated. The main features of this reactor are shown in figure. A 365 nm LED light was selected as irradiation source and was used at 70 % of maximum intensity (radiant flux: 30.5 W); LED temperature was kept at 20 °C. The mixture was recirculated.

Source irradiance evaluation Irradiance of the UV sources was evaluated through a THORLABs S120VC - Standard Photodiode Power Sensor, Si UV extended, wavelength range: 200 - 1100 nm, power range 50 nW-50 mW. Lamps were switched on several minutes before starting measurements in order to reach regime conditions. The photodiode sensor was positioned at the same distance from the lamps as the reaction vessel/channels (3,5 cm in the case of the Corning Lab Photo Reactor, 6 cm in the case of nail and mercury lamps).

2.5.7 Characterizations

Dynamic light scattering (DLS) Dynamic light scattering (DLS) analysis were performed using Malvern instrument Nano-S, whose data processing software is Zetasizer. The refractive index (RI) of the material was indicated as polystyrene latex type (RI 1,59) with absorption 0,10 at the laser probe wavelength (633 nm). Dispersant was water (RI 1,33) or DMF (RI 1,428). Samples were measured directly as prepared, without dilution. Analysis have been performed on 1 mL of solution in a 1 cm disposable polymethylmethacrylate cuvettes for water and 1 cm quartz cuvette for DMF. Measurements have been collected at 25 °C (equilibration time: 30 seconds), positioning the laser focus either in the centre of the cuvette (0,45 mm) or at its side (0,89 mm). Three consecutive measurements have been performed on each sample (each measurement had 12-17 runs). When data met quality criteria, such measurement were averaged to obtain the final correlogram, volume and intensity % distribution through a distribution fit.

Fourier transform infrared spectroscopy (FTIR) FTIR spectra were collected with a PerkinElmer FT-ATR spectrophotometer Spectrum 100 with a KBr crystal. The spectra were acquired and averaged over 16 scans.

Absorption spectroscopy (ABS) The UV-visible absorption spectra of photoinitiator solutions in MeOH were recorded using a Jasco V-570 UV-Vis-NIR absorption spectrophotometer. Data were collected with 200 nm/min scanning speed in 300-800 nm range (data pitch 1 nm) in 1 cm path length quartz cuvette.

2.6 Acronyms

4-EDMA tetraethylene glycol dimethylacrylate
ABE-3 benzoxyl triethylene glycol methacrylate
ABS absorption spectoscopy
AME-3 methoxy triethylene glycol methacrylate
AOE-4 tetraethylene glycol mono methacrylate ester
APE-4 (2-(tetrahydropyranyl)oxy TEG methacrylate
BHT Butylated hydroxytoluene
CMC critical micelle concentration
CPNP conjugated polymer nanoparticle
DABP 4-(dimethylamino)pyridine
DLS dynamic light scattering
DMSO dimethylsulfoxide
DMF N,N-dimethylformamide
DTAB dodecyltrimethylammonium bromide
DTE 2-di(3-thyenil)-1,2-ethandione
EDS energy dispersive spectroscopy
FTIR Fourier-transorm infrared spectroscopy
HLB hydrophilic-lipophilic balance
Ig2 2-hydroxy-2-methylpropiophenone
IPN interpenetrated network
K-EL Kolliphor EL
LED light emitting device
MAC maximum additive concentration
MW molecular weight
NaOH sodium hydroxide
NMR nuclear magnetic resonance
PBS phosphate buffer saline
PDI polydispersion index
PEG polyethylene glycol
PFO Poly(9,9-dioctyl)fluorene
PFO ND palladium nanodispersion
PI photoinitiator
PL photoluminescence spectroscopy
pTSA para-toluenesulfonic acid
RI refractive index
SDS sodium dodecyl sulfate
T80 Tween 80
TEG tetraethylene glycol
THF tetrahydrofuran
TPO diphenyl(2,4,6-trimethylbenzoyl)phosphine oxide
TX-100 Triton X-100

Bibliography

[1] Merianos, J. J. *Disinfection, sterilization, and preservation* **2001**, *5*.

[2] Speight, J. G. *2 - The properties of water* (edited by J. G. Speight). Butterworth-Heinemann, **2020**, pp. 53–89. ISBN 978-0-12-803810-9. doi: 10.1016/B978-0-12-803810-9.00002-4.

[3] *amphiphile*. ISBN: 9780191727641.

[4] Lindman, B. and Alexandridis, P. *Amphiphilic molecules: small and large* (edited by P. Alexandridis and B. Lindman). Elsevier Science B.V., Amsterdam, **2000**, pp. 1–12. ISBN 978-0-444-82441-7. doi: 10.1016/B978-044482441-7/50002-5.

[5] Yèagle, P. L. *The FASEB Journal* **1989**, *3*, 1833–1842. doi: https://doi.org/10.1096/fasebj.3.7.2469614.

[6] Griffin, W. C. *J. Soc. Cosmetic Chem.* **1954**, *5*, 249–256.

[7] Porter, M. R. *Handbook of surfactants*. Springer, **2013**.

[8] Ruckenstein, E. and Nagarajan, R. *The Journal of Physical Chemistry* **1981**, *85*, 3010–3014.

[9] Schryver, S. B., Ramsden, W., Cross, C. F., Schidrowitz, P., Dreaper, W. P., McBain, J. W., Turner, T., Worley, F. P., Martin, C. J., Bousfield, W. R., Morse, H. N., Henri, V., Freundlich, H., The Chairman, Ostwald, W., Chapman, C., and Senter, G. *Transactions of the Faraday Society* **1913**, *9*, 93–107. doi: 10.1039/TF9130900093. Publisher: The Royal Society of Chemistry.

[10] *Hartley G. S. (1936). Aqueous solutions of paraffin-chain salts; a study in micelle formation. Hermann & cie.*

[11] Debye, P. *Journal of Colloid Science* **1948**, *3*, 407–409. doi: 10.1016/0095-8522(48)90025-7.

[12] Israelachvili, J. N., Mitchell, D. J., and Ninham, B. W. *Journal of the Chemical Society, Faraday Transactions 2: Molecular and Chemical Physics* **1976**, *72*, 1525–1568. doi: 10.1039/F29767201525. Publisher: The Royal Society of Chemistry.

[13] Israelachvili, J. N. *Intermolecular and surface forces*. Academic press, **2011**.

[14] Lombardo, D., Kiselev, M., Magazù, S., and Calandra, P. **2015**, .

[15] Mukerjee, P. and Mysels, K. J. *Journal of the American Chemical Society* **1955**, *77*, 2937–2943.

[16] Bae, Y., Lambert, S., Soane, D., and Prausnitz, J. M. *Macromolecules* **1991**, *24*, 4403–4407.

[17] Egger, K. W. and Benson, S. W. *Journal of the American Chemical Society* **1966**, *88*, 241–246.

[18] Cochin, D., Zana, R., and Candau, F. *Macromolecules* **1993**, *26*, 5765–5771.

[19] Aniansson, E. and Wall, S. N. *The Journal of Physical Chemistry* **1974**, *78*, 1024–1030.

[20] Ilya V Berezin, K Martinek, and A K Yatsimirskii. *Russian Chemical Reviews* **1973**, *42*, 787. doi: 10.1070/RC1973v042n10ABEH002744.

[21] Folger, R., Hoffmann, H., and Ulbricht, W. *Berichte der Bunsengesellschaft für physikalische Chemie* **1974**, *78*, 986–997.

[22] Aniansson, G. *The mean lifetime of a micelle*. Springer, **1985**, pp. 2–5.

[23] Raymond, M. J., Slater, C. S., and Savelski, M. J. *Green Chemistry* **2010**, *12*, 1826–1834.

[24] Pörtner, H.-O., Roberts, D. C., Adams, H., Adler, C., Aldunce, P., Ali, E., Begum, R. A., Betts, R., Kerr, R. B., Biesbroek, R., *et al. IPCC Sixth Assessment Report* **2022**, .

[25] Anastas, P. and Eghbali, N. *Chemical Society Reviews* **2010**, *39*, 301–312. doi: 10.1039/B918763B. Publisher: The Royal Society of Chemistry.

[26] Davey, S. G. *Nature Reviews Chemistry* **2022**, , 1–1.

[27] Nanda, B., Sailaja, M., Mohapatra, P., Pradhan, R., and Nanda, B. B. *Materials Today: Proceedings* **2021**, *47*, 1234–1240.

[28] Cortes-Clerget, M., Yu, J., Kincaid, J. R. A., Walde, P., Gallou, F., and Lipshutz, B. H. *Chemical Science* **2021**, *12*, 4237–4266. doi: 10.1039/D0SC06000C. Publisher: The Royal Society of Chemistry.

[29] Duynstee, E. and Grunwald, E. *Journal of the American Chemical Society* **1959**, *81*, 4540–4542.

[30] La Sorella, G., Strukul, G., and Scarso, A. *Green Chemistry* **2015**, *17*, 644–683. doi: 10.1039/C4GC01368A. Publisher: The Royal Society of Chemistry.

[31] Simon, M.-O. and Li, C.-J. *Chemical Society Reviews* **2012**, *41*, 1415–1427. doi: 10.1039/C1CS15222J. Publisher: The Royal Society of Chemistry.

[32] Sabbagh, F. and Kim, B. S. *Journal of Controlled Release* **2022**, *341*, 132–146.

[33] Sporer, E., Poulie, C. B., Bäck, T., Lindegren, S., Jensen, H., Kempen, P. J., Kjaer, A., Herth, M. M., and Jensen, A. I. *Nanotheranostics* **2022**, *6*, 388.

[34] Chen, J., Ouyang, J., Kong, J., Zhong, W., and Xing, M. M. *ACS Applied Materials & Interfaces* **2013**, *5*, 3108–3117. doi: 10.1021/am400017q. Publisher: American Chemical Society.

[35] Yan, L., Yang, L., He, H., Hu, X., Xie, Z., Huang, Y., and Jing, X. *Polymer Chemistry* **2012**, *3*, 1300–1307. doi: 10.1039/C2PY20049J. Publisher: The Royal Society of Chemistry.

[36] Benjaminsen, R. V., Sun, H., Henriksen, J. R., Christensen, N. M., Almdal, K., and Andresen, T. L. *ACS Nano* **2011**, *5*, 5864–5873. doi: 10.1021/nn201643f. Publisher: American Chemical Society.

[37] Kumar E.K., P., Feldborg, L. N., Almdal, K., and Andresen, T. L. *Chemistry of Materials* **2013**, *25*, 1496–1501. doi: 10.1021/cm302922d. Publisher: American Chemical Society.

[38] Liu, S., Weaver, J. V. M., Save, M., and Armes, S. P. *Langmuir* **2002**, *18*, 8350–8357. doi: 10.1021/la020496t. Publisher: American Chemical Society.

[39] Larrabee Jr., C. E. and Sprague, E. D. *Journal of Polymer Science: Polymer Letters Edition* **1979**, *17*, 749–751. doi: 10.1002/pol.1979.130171201. Publisher: John Wiley & Sons, Ltd.

[40] Stähler, K., Selb, J., Barthelemy, P., Pucci, B., and Candau, F. *Langmuir* **1998**, *14*, 4765–4775. doi: 10.1021/la980245d. Publisher: American Chemical Society.

[41] Piogé, S., Nesterenko, A., Brotons, G., Pascual, S., Fontaine, L., Gaillard, C., and Nicol, E. *Macromolecules* **2011**, *44*, 594–603.

[42] Schacher, F. H., Rudolph, T., Drechsler, M., and Müller, A. H. *Nanoscale* **2011**, *3*, 288–297.

[43] Liu, Y., Tian, M., Chang, H., Jiang, J., Yan, X., Liu, Z., and Liu, Z. *Langmuir* **2014**, *30*, 14782–14788.

[44] ten Brummelhuis, N. and Schlaad, H. *Polymer Chemistry* **2011**, *2*, 1180–1184.

[45] Petrov, P., Bozukov, M., and Tsvetanov, C. B. *Journal of Materials Chemistry* **2005**, *15*, 1481–1486.

[46] Petrov, P., Bozukov, M., Burkhardt, M., Muthukrishnan, S., Müller, A. H., and Tsvetanov, C. B. *Journal of Materials Chemistry* **2006**, *16*, 2192–2199.

[47] Petrov, P., Tsvetanov, C. B., and Jérôme, R. *The Journal of Physical Chemistry B* **2009**, *113*, 7527–7533.

[48] Klempner, D. and Sophiea, D. *Interpenetrating polymer networks*. CRC Press, **2020**, pp. 421–444.

[49] Wang, J.-l., Wang, C., Jiao, G.-s., and Wang, Q.-y. *Materials Science and Engineering: A* **2010**, *527*, 2045–2049. doi: 10.1016/j.msea.2009.11.041.

[50] Xiao, W., He, J., Nichol, J. W., Wang, L., Hutson, C. B., Wang, B., Du, Y., Fan, H., and Khademhosseini, A. *Acta Biomaterialia* **2011**, *7*, 2384–2393. doi: 10.1016/j.actbio.2011.01.016.

[51] Farris, S., Schaich, K. M., Liu, L., Piergiovanni, L., and Yam, K. L. *Trends in Food Science & Technology* **2009**, *20*, 316–332. doi: 10.1016/j.tifs.2009.04.003.

[52] Wu, X., He, G., Gu, S., Hu, Z., and Yao, P. *Journal of Membrane Science* **2007**, *295*, 80–87. doi: 10.1016/j.memsci.2007.02.039.

[53] Saito, K., Ingalls, L. R., Lee, J., and Warner, J. C. *Chemical communications* **2007**, , 2503–2505.

[54] S., M. *VARIATIONS ON SELF-ASSEMBLY OF SURFACTANT-BASED CONFINED SYSTEMS*.

[55] Hu, T. Q. and Weller, L. *Canadian journal of chemistry* **1994**, *72*, 1500–1511.

[56] Chen, M., Zhong, M., and Johnson, J. A. *Chemical reviews* **2016**, *116*, 10167–10211.

[57] https://www.sigmaaldrich.com/deepweb/assets/sigmaaldrich/marketing/global/documents/233/907

[58] Guo, L. and Santschi, P. H. *IUPAC Series on Analytical and Physical Chemistry of Environmental Systems* **2007**, *10*, 159.

[59] Behrendt, J. M., Esquivel Guzman, J. A., Purdie, L., Willcock, H., Morrison, J. J., Foster, A. B., O'Reilly, R. K., McCairn, M. C., and Turner, M. L. *Reactive and Functional Polymers* **2016**, *107*, 69–77. doi: 10.1016/j.reactfunctpolym.2016.08.006.

[60] Mattiello, S., Rooney, M., Sanzone, A., Brazzo, P., Sassi, M., and Beverina, L. *Organic Letters* **2017**, *19*, 654–657. doi: 10.1021/acs.orglett.6b03817. Publisher: American Chemical Society.

[61] Rush, R. M., Martin, D. S., and LeGrand, R. G. *Inorganic Chemistry* **1975**, *14*, 2543–2550. doi: 10.1021/ic50152a051. Publisher: American Chemical Society.

[62] Kashyap, S., Singh, N., Surnar, B., and Jayakannan, M. *Biomacromolecules* **2016**, *17*, 384–398. doi: 10.1021/acs.biomac.5b01545. Publisher: American Chemical Society.